DOE/ER-0313/27

Fusion Materials

Semiannual Progress Report for Period Ending December 31, 1999

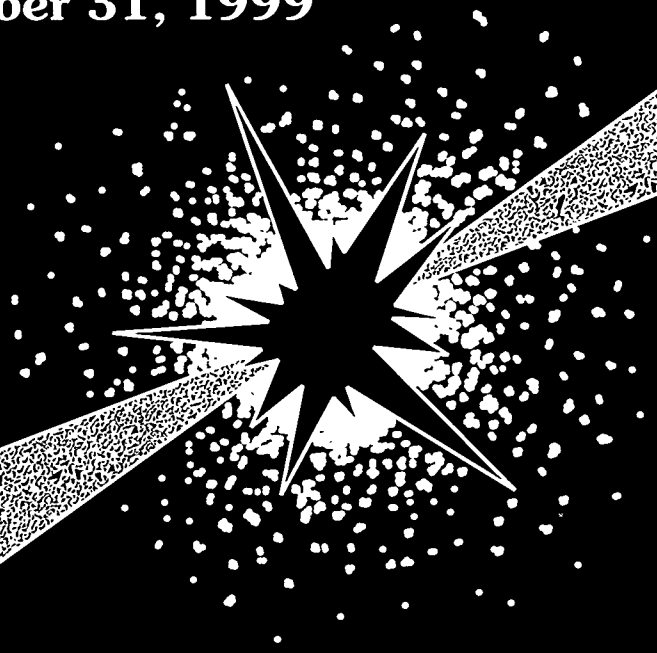

U. S. Department of Energy
Office of Fusion Energy Sciences

This report has been reproduced from the best available copy.

Reports are available to the public from the following source.
National Technical Information Service
5285 Port Royal Road
Springfield, VA 22161
Telephone 703-605-6000 (1-800-553-6847)
TDD 703-487-4639
Fax 703-605-6900
E-mail orders@ntis.fedworld.gov
Web site http://www.ntis.gov/ordering.htm

Reports are available to U.S. Department of Energy (DOE) employees, DOE contractors, Energy Technology Data Exchange (ETDE) representatives, and International Nuclear Information System (INIS) representatives from the following source.
Office of Scientific and Technical Information
P.O. Box 62
Oak Ridge, TN 37831
Telephone 423-576-8401
Fax 423-576-5728
E-mail reports@adonis.osti.gov
Web site http://www.osti.gov/products/sources.html

Reports produced after January 1, 1996, are generally available via the DOE Information Bridge.
Web site http://www.doe.gov/bridge

This report was prepared as an account of work sponsored by an agency of the United States government. Neither the United States government nor any agency thereof, nor any of their employees, makes any warranty, express or implied, or assumes any legal liability or responsibility for the accuracy, completeness, or usefulness of any information, apparatus, product, or process disclosed, or represents that its use would not infringe privately owned rights. Reference herein to any specific commercial product, process, or service by trade name, trademark, manufacturer, or otherwise, does not necessarily constitute or imply its endorsement, recommendation, or favoring by the United States government or any agency thereof. The views and opinions of authors expressed herein do not necessarily state or reflect those of the United States government or any agency thereof.

DISCLAIMER

Portions of this document may be illegible in electronic image products. Images are produced from the best available original document.

DOE/ER-0313/27
Distribution
Categories
UC-423, -424

FUSION MATERIALS
SEMIANNUAL PROGRESS REPORT
FOR THE PERIOD ENDING
December 31, 1999

Prepared for
DOE Office of Fusion Energy Sciences
(AT 60 20 00 0)

DATE PUBLISHED: MARCH 2000

Prepared for
OAK RIDGE NATIONAL LABORATORY
Oak Ridge, Tennessee 37831
Managed by
Lockheed Martin Energy Research Corp.
for the
U.S. DEPARTMENT OF ENERGY
under Contract DE-AC05-96OR22464

FOREWORD

This is the tweny-seventh in a series of semiannual technical progress reports on fusion materials. This report combines the full spectrum of research and development activities on both metallic and non-metallic materials with primary emphasis on the effects of the neutronic and chemical environment on the properties and performance of materials for in-vessel components. This effort forms one element of the materials program being conducted in support of the Fusion Energy Sciences Program of the U.S. Department of Energy. The other major element of the program is concerned with the interactions between reactor materials and the plasma and is reported separately.

The Fusion Materials Program is a national effort involving several national laboratories, universities, and industries. A large fraction of this work, particularly in relation to fission reactor experiments, is carried out collaboratively with our partners in Japan, Russia, and the European Union. The purpose of this series of reports is to provide a working technical record for the use of the program participants, and to provide a means of communicating the efforts of materials scientists to the rest of the fusion community, both nationally and worldwide.

This report has been compiled and edited under the guidance of A. F. Rowcliffe by Gabrielle Burn, Oak Ridge National Laboratory. Their efforts, and the efforts of the many persons who made technical contributions, are gratefully acknowledged.

F. W. Wiffen
International and Technology Division

Reports previously listed in this series are as follows:

DOE/ER-0313/1	Period ending September 30, 1986
DOE/ER-0313/2	Period ending March 31, 1987
DOE/ER-0313/3	Period ending September 30, 1987
DOE/ER-0313/4	Period ending March 31, 1988
DOE/ER-0313/5	Period ending September 30, 1988
DOE/ER-0313/6	Period ending March 31, 1989
DOE/ER-0313/7	Period ending September 30, 1989
DOE/ER-0313/8	Period ending March 31, 1990
DOE/ER-0313/9	Period ending September 30, 1990
DOE/ER-0313/10	Period ending March 31, 1991
DOE/ER-0313/11	Period ending September 30, 1991
DOE/ER-0313/12	Period ending March 31, 1992
DOE/ER-0313/13	Period ending September 30, 1992
DOE/ER-0313/14	Period ending March 31, 1993
DOE/ER-0313/15	Period ending September 30, 1993
DOE/ER-0313/16	Period ending March 31, 1994
DOE/ER-0313/17	Period ending September 30, 1994
DOE/ER-0313/18	Period ending March 31, 1995
DOE/ER-0313/19	Period ending December 31, 1995
DOE/ER-0313/20	Period ending June 30, 1996
DOE/ER-0313/21	Period ending December 31, 1996
DOE/ER-0313/22	Period ending June 30, 1997
DOE/ER-0313/23	Period ending December 31, 1997
DOE/ER-0313/24	Period ending June 30, 1998
DOE/ER-0313/25	Period ending December 31, 1998
DOE/ER-0313/26	Period ending June 30, 1999
DOE/ER-0313/100	Technical Evaluation of the Technology of Vanadium Alloys for Use as Blanket Structural Materials in Fusion Power Systems

CONTENTS

a significant loss of room temperature ductility. Annealing at 950°C was effective in improving ductility at oxygen levels below 1500 ppm. With higher oxygen levels, the anneal was ineffective or further reduced ductility. High resolution analytical electron microscopy was used to examine the oxidized V-4Cr-4Ti microstructure before and after annealing at 950°C. Low ductility before annealing is attributed to fine oxide particles in the matrix inhibiting dislocation movement. Large Ti-rich oxide particles were observed at grain boundaries while the alloy matrix adjacent to the boundary was depleted in Ti.

A systematic study has been conducted to determine the effects of time and temperature on the oxidation behavior of Si-, Al, and Y-modified V-4Cr-4Ti alloys. All samples were from0.80-mm-thick cold-rolled sheets, and each was annealed in vacuum at 1000°C for 1 h prior to high-temperature exposure. Different samples from each alloy were heated in air between 400 and 620°C for times up to a few hundred hours. Weight change data were used to evaluate the kinetics of oxidation process in the modified alloys, and the rate constants were compared with data developed earlier on base alloy.

This project began in June 1999. Initial testing has been performed on AlN + 5% Y_2O_3 at 400-700°C. With increasing temperature, this material was increasingly attached by lithium in 1000 h tests and there was a corresponding increase in the aluminum content of the lithium. These results suggest that the maximum use temperature of AlN in lithium may be 600°C or less. Currently, 1000 h experiments are being completed with yttria-free AlN and CaO specimens at 400, 500, and 700°C.

The purpose of this study was to investigate the interactions between Ti and interstitial solutes over temperature ranges corresponding to thermally activated processes such as precipitation, dislocation recovery and recrystallization, and grain growth. In this study, room temperature electrical resistivity and microhardness measurements were performed on cold-worked (CW) vanadium, CW V-4Cr-4Ti, annealed V-4Cr-4Ti, and the fusion zone of welded V-4Cr-4Ti plate over the isochronal annealing temperature range from 200 to 1200°C. The results suggested that Ti solutes in the vanadium alloys interacted with interstitial O, C, and N solutes at temperatures of 200°C and higher. Below ~400°C, these interactions influenced processes such as solute diffusivity and dislocation atmosphere formation. Above ~400°C, recovery, recrystallization and precipitation processes had the most significant effect on the property measurements.

1.0 VANADIUM ALLOYS

A GENERALIZED CONSTITUTIVE MODEL FOR A V-4Cr-4Ti ALLOY – E. Donahue, G.R. Odette, G.E. Lucas (University of California, Santa Barbara)

OBJECTIVE

The objective of this work is to develop a generalized constitutive equation for a V-4Cr-4Ti alloy that can be used in conjunction with Finite Element Methods to predict crack tip stress and strain fields as a function of temperature and loading rate.

SUMMARY

A physically based constitutive model for low-to-intermediate temperatures, strains and strain rates is derived for the program heat of the V-4Cr-4Ti. The supporting database is based on tensile tests carried out over a wide range of temperatures and strain rates. The overall constitutive model is based on additive yield and post yield strain hardening contributions to the flow stress. The yield stress has both thermally activated and athermal components. The former can be described by a two-mechanism activated dislocation slip model, with contributions from both lattice friction (lower temperature) and interstitial obstacles (higher temperature). The model uses a weighted average of the two mechanisms as a function of a strain rate compensated temperature. Post-yield strain hardening was found to be essentially athermal. Strain hardening can be fit by a two-component modified Voce-type model, which predicts saturating hardening behavior. The constitutive model is used to determine flow stability limits as estimates of uniform tensile strains. The relatively compact, but mechanism-based, model has a number of both fundamental and practical advantages that are briefly outlined. Extensions to directly model compositionally and microstructurally mediated mechanisms, including the effects of irradiation, and key phenomena, such as flow localization, are important objectives of future research.

PROGRESS AND STATUS

Introduction

Constitutive properties are required for design and to measure, apply and obtain a basic understanding of a long list of life-limiting failure-related properties and parameters, such as fracture toughness. In this work we develop a constitutive description of a V-4Cr-4Ti alloy in the *unirradiated* condition for low-to-intermediate temperatures and strain rates (i.e., outside the creep and strain aging regimes). Specifically, we seek a model that accurately and compactly describes the effects of temperature (T), strain rate ($\dot{\varepsilon}$) and strain (ε) on the uniaxial flow stress, $\sigma_{fl}(T, \dot{\varepsilon}, \varepsilon)$ underpinned by dislocation dynamics theories. The research involved three steps: a) measuring and properly reducing the requisite tensile data base; b) analyzing the general data trends in the context of simple, but physically-based, analytical formulations of constitutive models; and c) quantitatively fitting the model equations to the data base.

Experimental Procedures and Data Reduction

Details of the materials and test methods for a wide range of temperatures and strain rates are described elsewhere [1].

Results and Analysis

Representative stress–strain curves have been reported previously [2]. Development of the model equations follow the approach of Armstrong [3]. This model divides flow stress (σ_{fl}) into yield (σ_y) and post yield (σ_ε), strain hardening, contributions. The σ_y is composed of strongly and weakly temperature-strain rate sensitive components as

$$\sigma_y(T, \dot{\varepsilon}) = \sigma_{yt}(T, \dot{\varepsilon}) + \sigma_{ya} \quad (1)$$

The development of post-yield dislocation structures results in a strain hardening component, σ_ε. For bcc single crystal crystals with low dislocation densities, σ_ε also depends on $\dot{\varepsilon}$ and T [4], suggesting a general form:

$$\sigma_{fl}(T, \dot{\varepsilon}, \varepsilon) = \sigma_{yt}(T, \dot{\varepsilon}) + \sigma_{ya} + \sigma_\varepsilon(T, \dot{\varepsilon}, \varepsilon) \quad (2)$$

The (low) temperature-(high) strain rate dependence of σ_y in bcc metals and alloys is attributed to the low mobility of screw dislocations which experience a high Peierls, or lattice friction, resistance to slip [5]. The corresponding trade-off between temperature T and $\dot{\varepsilon}$ can be represented in terms of a strain rate compensated temperature (T') where

$$T' = T\,[1 + C \ln(\dot{\varepsilon}_r / \dot{\varepsilon})] \quad (3)$$

Here T is the actual absolute temperature (K) for the reference strain rate, $\dot{\varepsilon}_r$.

Taking the slowest strain rate of 4×10^{-4}/s as the reference condition, the σ_y data at all three strain rates were plotted on T' scale, using the 'best fit' value for C = 0.030 the T' as shown in Figure 1. For a single underlying thermally activated kink nucleation mechanism the simplest fit form is [6],

$$\sigma_y(T') = \sigma_t[1-(T'/T_c)] + \sigma_a \quad (4)$$

where σ_t and σ_a are the thermal and athermal yield stress contributions at 0°K. However, dispersed barrier strengthening by interstitial solutes is also important, particularly at higher temperatures. T'-weighted averaging and fitting σ_t and T_c for two (1 and 2) activated processes was used to model $\sigma_y(T')$ as

$$\sigma_y(T') = [\sigma_{t1} - (\sigma_{t1} - \sigma_{t2})T'/T_{c2}][1-T'/\{T_{c1} + (T_{c2} - T_{c1})T'/T_{c2}\}] + \sigma_a(1-\beta T) \quad (5)$$

The best fit results are shown as the solid curve in Figure 1 for: a) $\sigma_{yt1} = 780$ and $\sigma_{yt2} = 110$ MPa; $\sigma_a = 255$ MPa; b) $T_{c1} = 188$ and $T_{c2} = 500$°K; and $\beta = 6 \times 10^{-5}$ or

$$\sigma_y(T') = 1035 - 1.32T' + (1.32T' - 780T'/(188 + 0.624T') \text{ (MPa)} \quad (6)$$

The post yield strain hardening contribution was experimentally defined for plastic strain levels of 0.5 to 3.0% in increments of 0.5% and from 3.0 to 14.0% in increments of 1.0% as

$$\sigma_\varepsilon(T', \varepsilon) = \sigma_{fl}(T', \varepsilon) - \sigma_y(T') \quad (7)$$

To a good approximation σ_ε can be treated as being athermal. The corresponding $\sigma_\varepsilon(\varepsilon)$ averaged over T' for the 17 ε levels is shown in Figure 3. Two regimes above and below an ε of about 0.025 are observed. This was fit with a modified two-term Voce type equation [7] with the general form

$$\sigma_\varepsilon(\varepsilon) = \chi_{\varepsilon 1}\varepsilon^{p_1}[1-\exp(-\varepsilon_{s1}/\varepsilon)] + \chi_{\varepsilon 2}(\varepsilon-\varepsilon_t \geq 0)^{p_2}[1-\exp(-\varepsilon_{s2}/\varepsilon)] \quad (8)$$

Here $\chi_{\varepsilon 1}$ and $\chi_{\varepsilon 2}$ represent the magnitude of each strain hardening term, p_1 and p_2 are the corresponding power law, ε_{s1} and ε_{s2} are the flow stress saturation strains, and ε_t is the threshold strain for the second mechanism. The solid line in Figure 3 is a best fit given by the expression for: $\chi_{\varepsilon 1}$ = 865 MPa, $\chi_{\varepsilon 2}$ = 110 MPa; $p_1 = p_2 = 1$; ε_{s1} = 0.07, ε_{s2} 0.23; and ε_t = 0.025.

Equations 3, 6 and 8 define an overall constitutive model,

$$\sigma_{fl}(T, \dot{\varepsilon}, \varepsilon) = 1035 - 1.32T' + \{(1.32T' - 780T')/(188 + 0.624T')\} +$$

$$865\varepsilon[1 - \exp(-0.07/\varepsilon)]+110(\varepsilon-0.025)[1 - \exp(-0.023/\varepsilon)] \text{ (MPa)} \quad (9)$$

Predicted versus measured σ_{fl} at ε of 0.5, 1, 2, 4, 8 and 14% are shown in Figure 3. The overall standard deviation of the predicted versus measured σ_{fl} is ± 9.1 MPa. The model can be applied over the combined T and $\dot{\varepsilon}$ range to 100°C, 2/sec respectively.

Figure 4 shows the ε_u data plotted against σ_y. Except in two cases ε_u ranges from about 0.10 to 0.18. The exceptions were for the highest strain rate case at low temperatures of -132 and -196°C. In this case adiabatic heating may contribute to flow localization and the low ε_u. The constitutive model can be used compute ε_u based on the criteria that $dP/d\varepsilon \leq 0$. The dashed line in Figure 4 is the nominal predicted ε_u. While the trends are reasonable, the simple model over-predicts the measured values. This discrepancy suggests that ε_u is influenced by either defects and other inhomogenieties in the specimens, or an inherent propensity towards flow localization. These effects can be treated by a phenomenologically by increasing the effective rate of reduction in load bearing area per unit strain by a constant factor. The solid line in Figure 4 shows the corresponding results for a factor of 1.6

Discussion, Summary and Conclusions

The σ_{fl} for the program heat of V-4Cr-4Ti alloy has a classical low-temperature activated σ_{yt} regime and athermal contributions to both σ_y and σ_ε. The athermal post-yield σ_ε follows a two component Voce-type hardening law. Overall, the model, which incorporates analytical expressions for these processes that are fit to the tensile database, is broadly consistent with current understanding of deformation in bcc alloys. The relatively simple and compact form of the constitutive model has a number of practical and fundamental advantages as discussed elsewhere [1]. Developing microstructurally based constitutive models, including the effects of irradiation, and key phenomena such as flow localization, is an important objective of future research.

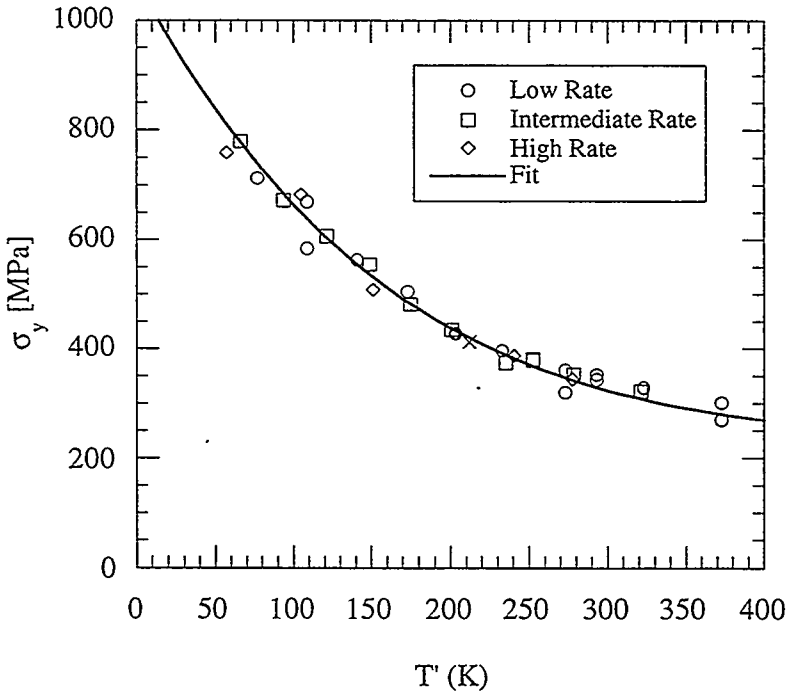

Figure 1. Plot of σ_y versus T' for various strain rates. The two-component fit activate flow model is shown as the solid curve as described in the text.

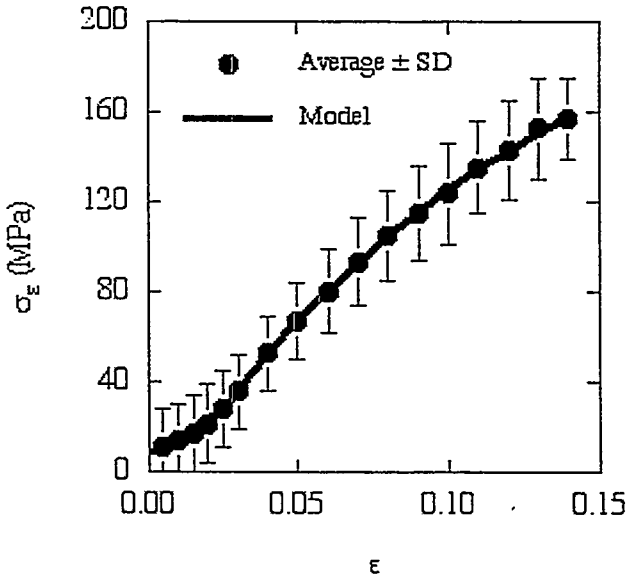

Figure 2. Plot of σ_ε, averaged for all T', versus ε. The two-component Voce-type strain hardening model is shown as the solid curve as described in the text

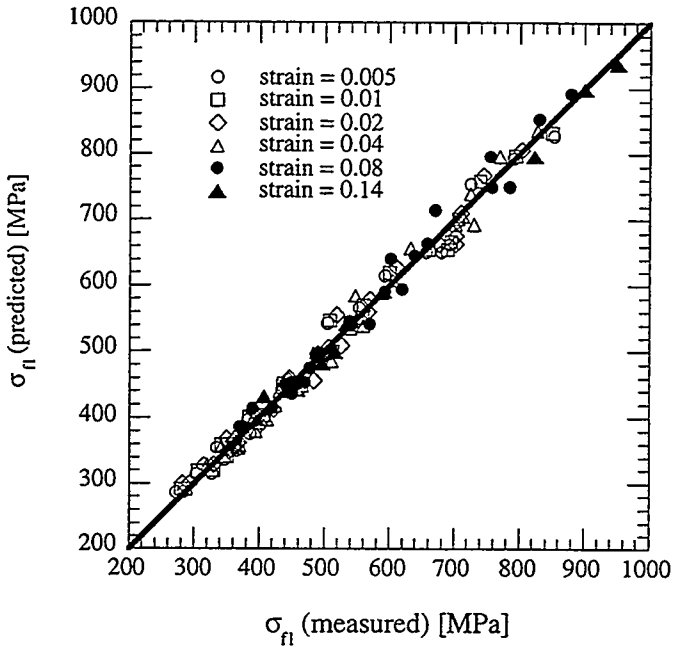

Figure 3. Comparison of the true flow stresses measured with those predicted by the model at true strains of 0.005, 0.01, 0.02, 0.04, 0.08, and 0.14.

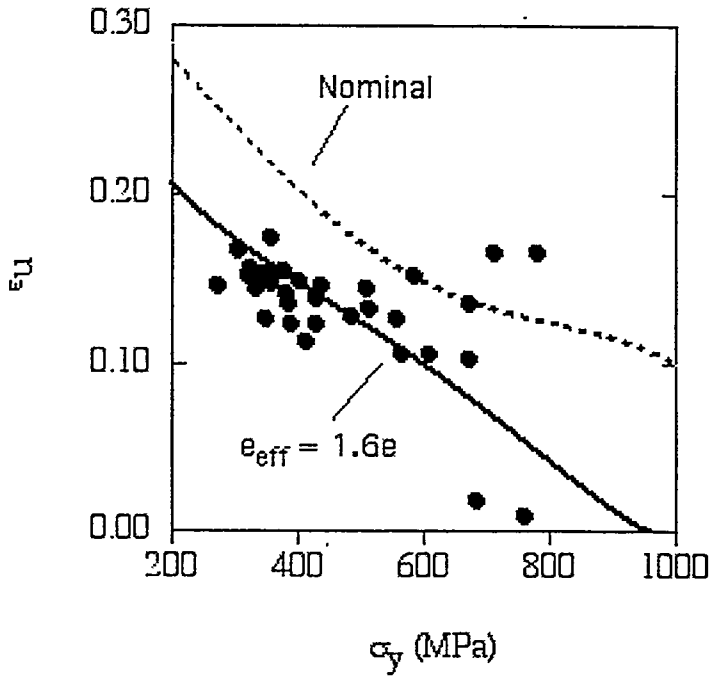

Figure 4. Plot of ε_u versus σ_y. Predictions of ε_u are shown as the solid and dashed curves as described in the text.

REFERENCES

1. E. Donahue, G.R. Odette, G.E. Lucas "A Generalized Constitutive Model For A V-4Cr-4Ti Alloy", J. Nucl, Mat (submitted ICFRM 9 proceedings)
2. H. M. Chung, H.-C. Tsai, D. L. Smith, R. Peterson, C. Curtis, C. Wojcik, R. Kinney, DOE/ER-0313/17, U. S. Department of Energy (1994).
3. M. L. Grossbeck, D. J. Alexander, J. J. Henry, W. S. Eatherly, L. T. Gibson, DOE/ER-0313/18, U. S. Department of Energy (1995).
4. A. N. Gubbi, A. F. Rowcliffe, W. W. Eatherly, DOE/ER-0313/18, U. S. Department of Energy (1995).
5. A. F. Rowcliffe, D. T. Hoelzer, S. J. Zinkle, DOE/ER-0313/26, U. S. Department of Energy (1999).
6. G. R. Odette, E. Donahue, G. E. Lucas, J. W. Sheckherd, DOE/ER-0313/20, U. S. Department of Energy (1996).
7. F. J. Zerilli, R. W. Armstrong, *J. Appl. Phys.*, 61 (1987) 1816.
8. M. Tang, B. Devincre, L. P. Kubin, *Modelling and Simulation in Materials Science and Engineering,* 7 (1999) 893.
9. J. P. Hirth, J. Lothe, *Theory of Dislocations*, McGraw-Hill, Inc., 1968.
10. P. Spatig, G. R. Odette G. E. Lucas, *J. Nucl. Mater.*, 217 (1999) 324.
11. E. Voce, *J. Inst. Metals*, 74 (1968) 537.

ON THE MECHANISMS AND MECHANICS OF FRACTURE IN A V-4CR-4TI ALLOY: MODELING THE EFFECTS OF IRRADIATION, LOADING RATE AND SPECIMEN CONGFIGURATION ON TOUGHNESS-TEMPERATURE CURVES –

E.G. Donahue, G.R. Odette, G.E. Lucas (University of California, Santa Barbara)

OBJECTIVE

The objective of this work is to understand and model the mechanics of fracture as a basis for developing fracture assessment methods for defect tolerant design of vanadium-based fusion reactor structures.

SUMMARY

The fracture behavior of the 500 kg heat of the V-4Cr-4Ti was used to characterize and model of low dose, low-to-intermediate temperature irradiation, loading rate and specimen configuration on toughness-temperature curves. A critical stress–critical stressed area cleavage criteria predicts effective toughness-temperature curves in the cleavage transition regime, including the influence of size and geometry that mediate the loss of triaxial constraint. It appears that cross rolling lowers the cleavage transition temperature. Irradiation and high loading rates result in significant upward shifts in the transition temperature, due to corresponding increases in the yield stress. A simple equivalent yield stress model accurately predicts these effects. Flow localization following irradiation has a profound effect on effective ductile fracture toughness, qualitatively consistent with effects of irradiation on the tensile properties, dominated by reductions in uniform strain. The large cleavage transition temperature shifts and ductile toughness decreases may limit the application of V-4Cr-4Ti alloys for low-to-intermediate temperature irradiation environments.

PROGRESS AND STATUS

Introduction

The objective of this work is to develop physical models for the fracture toughness of a V-4Cr-4Ti alloy that quantitatively treat the effects of: a) specimen/structure size and geometry; b) loading rate; c) metallurgical factors associated with processing and fabrication history; and d) in-service degradation processes such as irradiation embrittlement. Fracture specimens of varying size, geometry, orientation, processing history and irradiation conditions were tested. This study used small to very small specimens, with limited redundancy

Experimental and Data Analysis Procedures

Details of the material fabrication and processing, specimen preparation, and fracture testing conditions are described elsewhere [1]. The effective toughness data were evaluated with both 'standard' elastic-plastic fracture mechanics methods (K_e) [2,3] and by the confocal microscopy-fracture reconstruction (CM-FR) technique (K_δ) [4,5]. Both CM-FR and scanning electron microscopy (SEM) were also used to characterize the local fracture processes and mechanisms.

In selected cases, the K_e data were constraint corrected to provide estimates of K_{Jc} based on a critical stress (σ^*)/critical area (A^*) local fracture model coupled with three dimensional finite element method (FEM) calculations of crack tip stress and strain fields. Details of this model are described elsewhere [6-8]. The σ^*–A^* model can be used to compute mean $K_e(T)$ curves for a given specimen and constitutive law [6]. In the limiting case of SSY the $K_{Jc}(T)$ curve is unique. The

K_e data outside the SSY regime, can be corrected to K_{Jc} based on FEM calculations of the K_e/K_{Jc}-ratio needed to produce the same stressed area.

Irradiation and loading rate induced shifts in the cleavage transition temperatures ($\Delta T_{\phi t/P}$) were compared to predictions of the equivalent yield stress model (EYSM) [9]. A key assumption is that σ^* is independent of irradiation, loading rate and temperature.

Corresponding reductions in the maximum load toughness can be crudely predicted based on a decohesion model proposed for irradiated stainless steels [10]. In its simplest form, the ratio of the irradiated (i) to unirradiated (u) toughness can be estimated from tensile properties as given by

$$K_{maxi}/K_{maxu} \approx \{[(\sigma_{yi} + \sigma_{ui})/(\sigma_{yu} + \sigma_{uu})](\varepsilon_{ui}/\varepsilon_{uu})\}^{1/2} \qquad (1)$$

where σ_u are the ultimate tensile stresses and ε_u are the uniform strains.

Results

Figure 1 shows toughness data from MPCC tests from rolled versus crossrolled plate in the LT orientation. The crossrolled material exhibited higher toughness associated with a downward shift of $K_e(T)$ data by about 20°C. The effects of specimen orientation was investigated in two different plates. These comparisons suggest a slightly higher toughness for the TL orientation versus LT for bend bars from the thin plate. However, there was essentially no difference in toughness between the two orientations of 0.26T CT specimens taken from the thick plate.

Figure 2 shows the raw K_e data (open symbols), the constraint corrected K_{Jc} data (filled symbols) for each MPCC specimen, and the SSY $K_{Jc}(T)$ curves (lines) for both rolled and crossrolled plates. A value of $A^* = 10^{-8}$ m^2 was used for both sets of specimens. The σ^* were 1750 (rolled) and 1900 (crossrolled) MPa. The constraint corrected data lie close to the SSY line.

Since σ_y increases with increasing strain rate [11], higher loading rates shift $K_e(T)$ curves to higher temperature as reported previously [12]. The measured shifts associated with rate increases by factors of 10^5 (low-dynamic) and 10^6 (intermediate-dynamic) were about 60 and 70°C, respectively.

Irradiation at low-to-intermediate temperatures also results in significant elevations of σ_y, even at relatively low dose [13-15]. Data for smooth-sided MPCC specimens irradiated to ~ 0.4 dpa at 200°C [13] shows a shift of about 165°C with a corresponding $\Delta\sigma_y$ ~ 330 MPa [16]. As discussed in more detail elsewhere [12], CM-FR and SEM show that irradiated versus unirradiated cleavage fracture surfaces and processes are generally similar. However, there is abundant evidence of irradiation enhanced flow localization in the form of coarse slip steps; and, in some cases, even extrusions bridging transverse cracks that penetrate into the fracture surface. Large scatter in the cleavage K_e is also evident. Indeed the largest values of cleavage toughness are higher than the values of maximum load ductile toughness, K_{max}. The irradiated K_{max} toughness of about 95 MPa$\sqrt{m}$ was much lower than for the unirradiated material and, in contrast to the blunting-only behavior in the latter case, involved tearing and sliding-off along slip bands of highly concentrated deformation. Figure 3 shows that irradiations to ~ 0.1 dpa at 160 and 255°C [14] produced even larger reductions in the K_{max}. CM-FR and SEM also indicated more pronounced tearing and crack sliding-off. Significant elevations of the cleavage transition temperature were also observed. However, since the maximum load and cleavage toughness are of the same order, only about 60±10 MPa$\sqrt{m}$ at 160°C, it is difficult to define a cleavage transition temperature shift. The reductions in maximum load toughness are smaller for the 0.1 dpa irradiations at higher irradiation

temperatures of 390 and 295°C, and the increases in the cleavage transition temperature more obvious.

Figure 4 shows that the measured shifts in cleavage transition temperature ($\Delta T_{\dot{\varepsilon}t,P}$) due to irradiation and loading rate are in excellent agreement with predictions of the EYSM and the corresponding elevations in σ_y ($\Delta\sigma_y$). Details of the method for estimating shifts due to loading rate differences are described elsewhere [6]. Figure 4 also includes results from Alexander et. al. [13]. The apparent success of the EYSM in predicting cleavage transition temperature shifts is somewhat puzzling, in view of the severe flow localization which occurs in this alloy, particularly after irradiation. Figure 5 compares the the predictions of the ratio of the irradiated to unirradiated toughness estimated by Equation 1 using tensile data from the literature [14,15] with the experimental estimates of the K_{max}.

The dominant effect of irradiation on K_{max} is associated with reductions in the uniform strain (ε_u) from ε_{uu}~ 0.15 to ε_{ui} as low as 0.001. While Equation 1 is consistent with the observed trends, it underpredicts K_{max} at lower irradiation temperatures. Indeed, tensile tests show substantial post-uniform strains prior to fracture, as well as significant reductions in area [14]. An illustration of the effect of using higher irradiated strains in Equation 1 is shown as the filled diamond symbols in Figure 5, where ε_{ui} has been replaced by $\varepsilon_{ui} + 0.01$. Although somewhat arbitrary, this modest adjustment produced much better agreement with the experimental estimates. Another observation that may seem puzzling is also qualitatively consistent with this model. That is in the irradiation temperature range of 150 to 250°C, the lowest dose 0.1 dpa irradiation produce similar or even larger reductions in K_{max} than irradiations to 0.4 dpa at 200°C. This can be understood by the competing effects of ε_{ui} and σ_{yi}. Specifically, ε_{ui} decreases and the propensity for localization increases more rapidly than the corresponding increases in σ_{yi}.

Developing more rigorous fracture models will require detailed characterization of the underlying physical processes. Fractographic evidence of the flow localization and its consequences is seen in the form of coarse slip steps, transverse microcracks, flat-bottomed voids and extrusion-type features on the fracture surfaces. Further quantification of these phenomena to guide the development of new fracture models for the range of fracture modes from cleavage to decohesion will be the focus of future research.

Summary and Conclusions

A micromechanical model based on a critical stress-critical stressed area, σ^*-A^*, cleavage criteria provides a basis for predicting effective toughness-temperature, $K_e(T)$, curves in the cleavage transition regime, including the effects of size and geometry pertinent to the use of small specimen data to estimate the fracture limits of structures. The cleavage transition temperature of the as-fabricated alloy is high due to its relatively low strength (e.g., lower than typical steels) combined with a high σ^* (comparable to typical steels). It appears that crossrolling lowers the transition temperature. The effects of low strength on toughness is amplified in small specimens by the loss of triaxial constraint.

Irradiation and high loading rates result in significant upward shifts in the cleavage transition temperature. The shifts are largely due to corresponding increases in the yield stress. Notably, the σ^*-A^* concept also provides the basis for an apparently effective way to predict these effects using the simple equivalent yield stress model (EYSM). However, the reason for this success is not fully understood, in view of the severe flow localization observed in irradiated alloys.

Flow localization following irradiation has even more profound effects on effective ductile fracture toughness, K_{max}, defined in this work as the K_J at maximum load in the load-displacement curve. The trends in the experimental estimates of K_{max} are qualitatively consistent with a simple model based on effects of irradiation on the tensile properties, as dominated by reductions in uniform strain. However, more realistic models reflecting the complexities of the underlying physics are needed and are under development.

Finally, it is clear that the large cleavage transition temperature shifts and ductile toughness decreases may limit the application of V-4Cr-4Ti alloys for low-to-intermediate temperature irradiation environments.

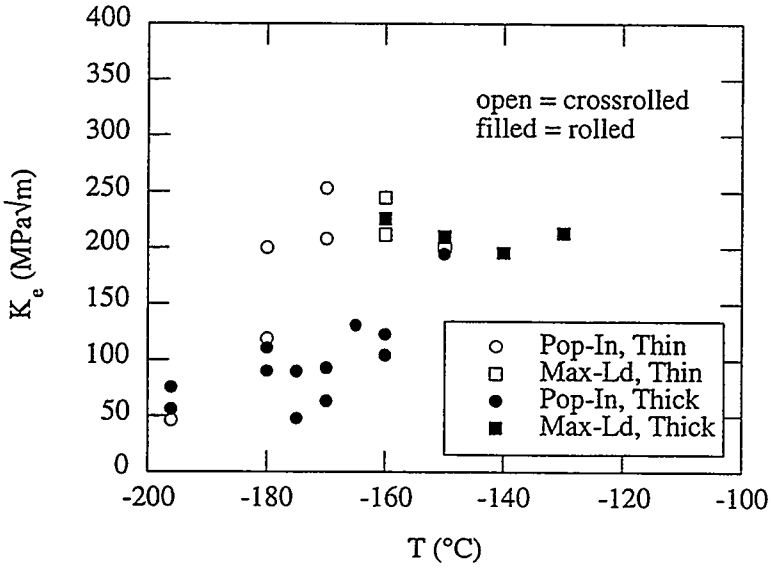

Figure 1. $K_e(T)$ data from MPCC tests from rolled and crossrolled plate. Both sets of specimens were in LT orientation with respect to the last rolling direction. The crossrolled material exhibited higher toughness associated with a downward shift in the $K_e(T)$ curve.

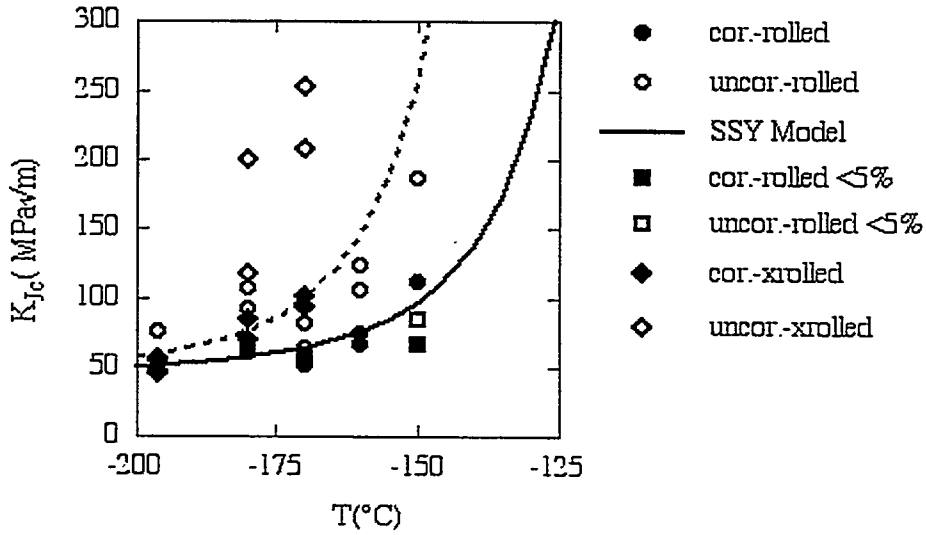

Figure 2. Constraint correction to K_{Jc} data for each MPCC specimen, and the SSY $K_{Jc}(T)$ curves for both rolling conditons, rolled and crossrolled (xrolled). The σ^*/A^* criteria used for each rolling condition differed slightly which accounts for the difference in SSY $K_{Jc}(T)$ curves.

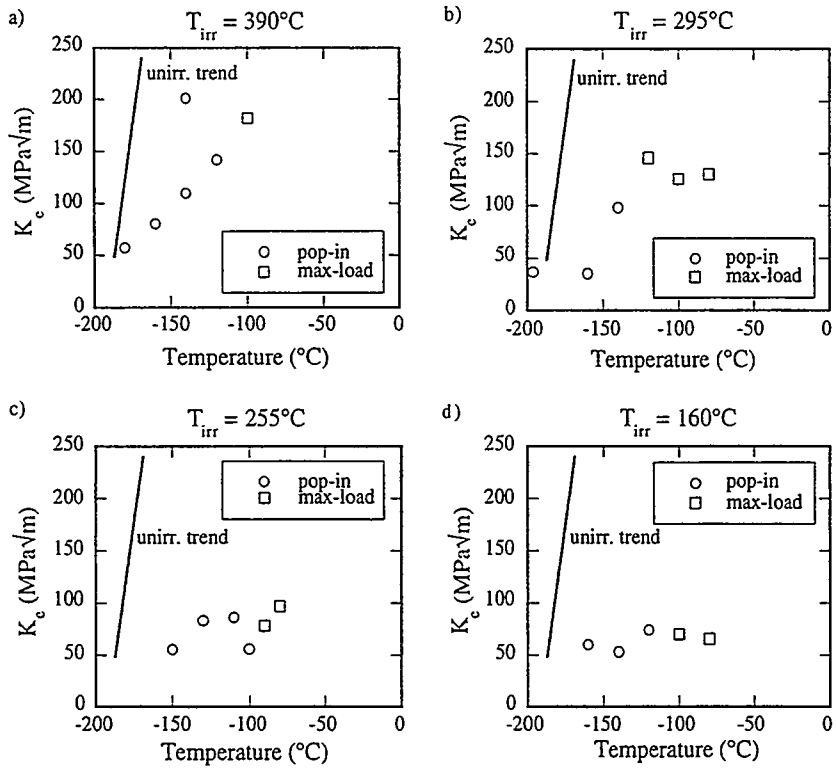

Figure 3. $K_e(T)$ data for side-grooved MPCC specimens irradiated to 0.1 dpa at (a) 390°C, (b) 295°C, (c) 255°C, and (d) 160°C.

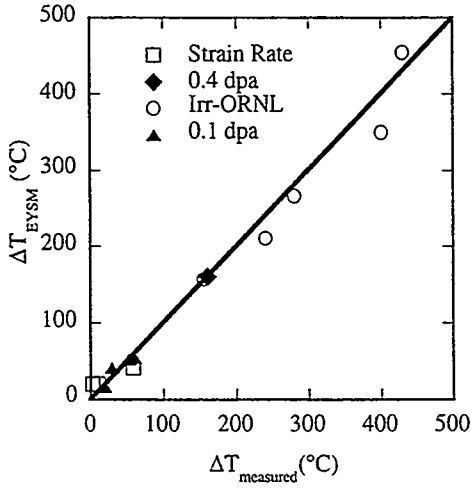

Figure 4. Comparison between measured ΔT and ΔT as predicted by the EYSM are shown showing good agreement.

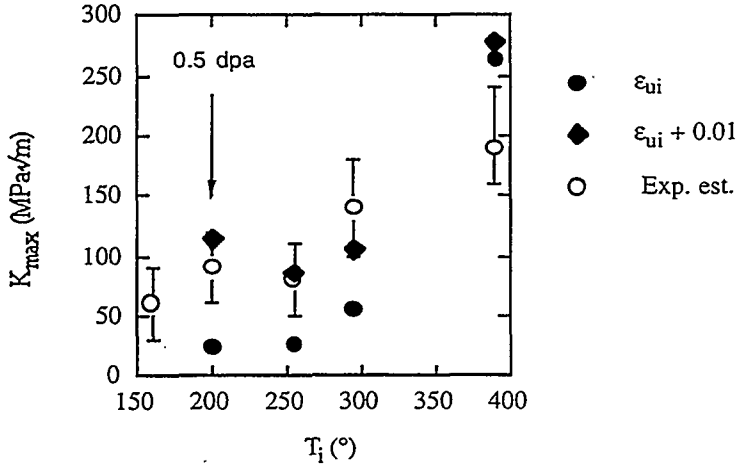

Figure 5. Comparison of the predictions of the ratio of the irradiated to unirradiated toughness estimated by Equation 1 (filled circles) using tensile data from the literature [14,15] with the experimental estimates of the K_{max} (open circles).

REFERENCES

1. E.G. Donahue, G.R. Odette, G.E. Lucas, "On The Mechanisms and Mechanics of Fracture in a V-4Cr-4Ti Alloy: Modeling the Effects of Irradiation, Loading Rate, and Specimen Configuration on Toughness-Temperature Curves", *J. Nucl. Materials, (submitted to ICFRM9 proceedings).*
2. ASTM E399-90, "Standard Test Method for Plane-Strain Fracture Toughness of Metallic Materials," *Annual Book of ASTM Standards*, American Society for Testing and Materials (1996) 407-437.
3. ASTM E813-89, "Standard Test Method for Jlc, A Measure of Fracture Toughness," *Annual Book of ASTM Standards*, ASTM (1996) 633-647.
4. K. Edsinger, "Fracture Reconstruction and Advanced Micromechanical Modeling of Structural Steels," Ph.D. Thesis, Department of Chemical and Nuclear Engineering, University of California, Santa Barbara (1995).
5. K. Edsinger, G.R. Odette, G.E. Lucas, *Proceedings of the IEA International Symposium on Miniaturized Specimens for Testing Irradiated Materials*, KFA Julich, September 22-23, 1994 (1995) 150–159.
6. G.R. Odette, K. Edsinger, G.E. Lucas, E. Donahue, "Developing Fracture Assessment Methods for Fusion Reactor Materials with Small Specimens," *Small Specimen Test Techniques, ASTM STP-1329*, American Society for Testing and Materials, 1998.
7. G.E. Lucas, G.R. Odette, J.W. Sheckherd, K. Edsinger, B. Wirth, *Effects of Radiation on Material, 17 International Symposium*, ASTM-STP 1270, ASTM (1996) 790.
8. G.R. Odette, E. Donahue, G.E. Lucas, J.W. Sheckherd, DOE/ER-0313/20, (1996) 11.
9. G.R. Odette, DOE/ER-0313/20, U.S. Department of Energy (1996) 283-298.
10. G.R. Odette, *Journal of Nuclear Materials* 212–215 (1994) 45.
11. E. Donahue, G.R. Odette, G.E. Lucas, J.W. Sheckherd, "Effect of Irradiation on Toughness-Tempeature Curves in V-4Cr-4Ti," *Proceedings of the 8th International Conference on Fusion Reactor Materials* (1998).
12. G.R. Odette, E. Donahue, G.E. Lucas, J.W. Sheckherd, "A Micromechanical Model of the Effect of Irradiation on Cleavage Fracture in Vanadium Alloys," *Effects of Radiation in Materials:*

18th International Symposium, ASTM STP-1325, ASTM 1997.

13. D.J. Alexander, L.L. Snead, S.J. Zinkle, A.N. Gubbi, A.F. Rowcliffe, E.E. Bloom, "Effects of Irradiation at Low Temperature on V-4Cr-4Ti," DOE/ER-0313/20 (1996) 87.
14. L.L. Snead, S.J. Zinkle, D.J. Alexander, A.F. Rowcliffe, J.P. Robertson, W.S. Eatherly, DOE/ER-0313/23 (1997) 81.
15. S.J. Zinkle, L.L. Snead, A.F. Rowcliffe, D.J. Alexander, L.T. Gibson, DOE/ER-0313/24 (1998) 33.
16. D.J. Alexander, L.L. Snead, *Effects of Radiation in Materials: 18th International Symposium*, ASTM STP-1325, ASTM 1997.

UNIAXIAL CREEP BEHAVIOR OF V-4Cr-4Ti Alloy*

K. Natesan, W. K. Soppet, and D. L. Rink (Argonne National Laboratory)

OBJECTIVE

The objectives of the creep test program are to (a) to establish time/temperature relationships for creep properties, such as creep rupture strength, 1% creep in 10,000 hr, onset of third-stage creep, etc., all of which are key parameters in designing structural components for service at elevated temperatures; (b) provide a basis to establish the upper-use temperature associated with creep limits for application of V-base alloys; and (c) evaluate the influence of variations in the concentrations of substitutional and interstitial elements on the creep properties of fusion-reactor-relevant V-base alloys.

SUMMARY

A systematic study is currently being conducted at Argonne National Laboratory (ANL) to evaluate the uniaxial creep behavior of V-Cr-Ti alloys as a function of temperature in the range of 650-800°C and at applied stress levels in the range of 75-380 MPa. At present, the principal effort has focused on the V-4Cr-4Ti alloy of Heat 832665; however, another heat of a similar alloy from General Atomics (GA) will also be used in the study.

INTRODUCTION

Refractory alloys based on V-Cr-Ti are being considered for use in first-wall structures in advanced blanket concepts that involve liquid Li as a coolant and breeding material. Furthermore, advanced concepts that involve He as a coolant also require structural alloys such as V-Cr-Ti, which can withstand thermal loading at high temperature. It is important that for advanced fusion systems, design concepts establish the upper temperature limits for structural components based on various design criteria. At temperatures above 600°C, the time-dependent creep properties of V alloys must be considered when evaluating performance limits.

The long-term creep properties of the V-base alloys will be influenced by the time-dependent nucleation and growth of precipitates that involve nonmetallic elements such as O, N, and C. Several of the microstructural studies of V-base alloys have identified precipitates such as face-centered-cubic Ti(O, N, C) with variable O, N, and C ratios. To correlate microstructual development with creep properties, It is essential to establish the time-dependent evolution of type, number, and location of precipitates in V-base alloys. Furthermore, development of several of these precipitates can be influenced by the exposure environment during creep testing. Over the long term, creep data are needed for environments with a wide range of chemistry and that encompass high vacuum to low partial pressures of O and H, and He of various purities.

---

*This work has been supported by the U.S. Department of Energy, Office of Fusion Energy Research, under Contract W-31-109-Eng-38.

SCOPE OF WORK

In the near term, the program will experimentally evaluate uniaxial creep properties of V-Cr-Ti materials in high-vacuum environments at temperatures of 650-800°C, with emphasis on baseline creep behavior of the alloys and correlations between microstructures and properties. Another aspect of the program will be creep tests on heats of V-base alloys that represent a range of variations in the concentrations of both substitutional and interstitial elements to provide an understanding of the effects of these variables on creep behavior.

EXPERIMENTAL PROGRAM

The effort is focused on the ANL-procured large heat of nominal composition V-4Cr-4Ti and on the GA heat of a similar composition.[1] Four uniaxial creep-test machines have been allocated for this program. All of the machines are equipped with high-vacuum systems and furnaces capable of 900°C. Flat creep specimens, 1 mm in thickness (see Fig. 1 for details), were fabricated according to ASTM Standard E8-69 and used in the initial phase of the program. A few specimens with cylindrical cross sections will be tested to validate the effects, if any, of specimen geometry on creep properties. Initial tests were conducted on specimens annealed at 1000°C for 1 h in vacuum. During this reporting period, several tests were conducted at 650, 725, and 800°C. The specimens were wrapped in Ti foil to minimize contamination of the sample, especially by O.

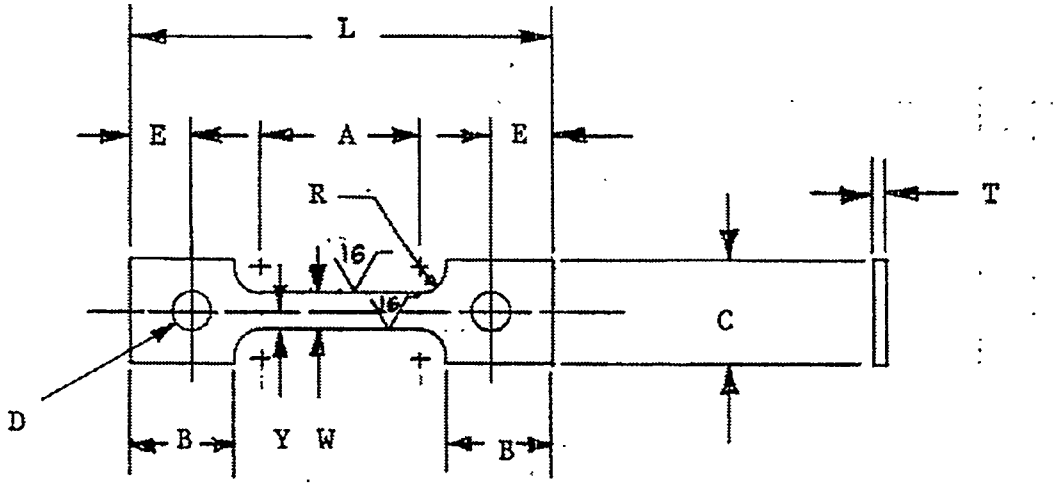

Dimensions in mm

A = 19 ± 0.50	Y = 2.2
B = 12.7	W = 4.5
C = 12.7	T = 1.0
D = 4.0	R = 3.175
E = 7.6	L = 50.8

Fig. 1. Schematic diagram of creep specimen designed according to ASTM Standard E8-69.

Creep strain in the specimen is measured by a linear-variable-differential transducer (LVDT), which is attached between the fixed and movable pull rods of the creep assembly. Displacements of 5×10^{-3} mm could be accurately determined with the LVDT. Before each test, the LVDT was calibrated by measuring its output for displacements that were set manually on a micrometer. The linear portion of the calibration curve is used to measure strain in a specimen during creep testing. The strain measurements are made at sufficiently frequent intervals during a test to define the creep strain/time curve.

A three-zone resistance-heated furnace is used in each testing machine to conduct creep tests at elevated temperatures. Chromel-Alumel thermocouples with small beads are used to measure specimen temperature. Ceramic insulators are used on the thermocouples in the hot zone. In general, three thermocouples are fed through the specimen chamber, one spot-welded onto each end of the grips on the specimen near the shoulder region, the third, held in the vacuum environment adjacent to the gauge-length portion of the specimen. Temperature is maintained within 2°C of the desired value for each test. The specimens are loaded at a constant rate to full load at the test temperature.

A detailed microstructural evaluation of the tested specimens is planned to characterize the morphologies as a function of exposure temperature and time and to establish the mechanisms of creep failure. The test program is aimed at obtaining the steady-state creep rate, onset of tertiary creep, rupture strain, and rupture life. At least four stress levels are planned at each temperature to obtain sufficient data to develop Larson-Miller correlations between time, temperature, and applied stress. The information will be used to assess the upper-use temperature for the material, based on appropriate design criteria and as a basis for alloy improvement.

RESULTS

During this period, several creep tests were conducted at 650, 725, and 800°C. Furthermore, a test was initiated at 700°C to complement and compare the data generated in the biaxial creep test program at 700°C conducted at Pacific Northwest National Laboratory (PNNL).[2] Figure 2 shows the creep strain/time plot for a V-4Cr-4Ti alloy specimens that were tested in vacuum at 650, 725, and 800°C at ANL. The data indicate that the primary creep period is negligible for all tests and the secondary, or linear, creep portion of the curve is small. The curves show an accelerating creep behavior over the range of the present tests, especially at 725 and 800°C. The creep strain/time curves have been analyzed in detail to extract data on the onset of tertiary creep, creep strain at the onset of tertiary creep, minimum creep rate (linear portion of the curve), and time and strain at rupture. Data are listed in Table 1 for tests that have been completed.

To examine the extent of O contamination, if any, in the creep specimen, cross sections of the tested specimen were mounted and polished, after which Vickers hardness measurements were made along the thickness direction. Figure 3 shows the hardness profile for several specimens after testing at 650, 725, and 800°C. Hardness values ranged from 145 to 195, with negligible variation in hardness within a given specimen, indicating that the contamination is minimal over the range of the

current study. Examination of the fracture surfaces of tested specimens showed a ductile mode of fracture in all of the specimens. The specimens tested at 800°C showed rupture strains of 30-61%, with significant thinning of the cross section in the fracture zone. Detailed examination of the tested specimens by scanning and transmission electron microscopy is planned for the future.

A comparative analysis was attempted I order to correlate the uniaxial creep data developed at ANL and the biaxial creep data developed at PNNL. At the common test temperature of 800°C, ANL tests were conducted at applied stress levels of 174, 150, and 130 MPa. PNNL tests were conducted at effective stress levels of 136.8, 117.7, 92.6, and 70.6 MPa. Figure 4 shows a comparative correlation of the data between time-to-rupture and applied or effective stress developed at 800°C in ANL and PNNL programs. The data developed at 800°C can be correlated as follows:

$$\text{Time to rupture (h)} = 1.5 \times 10^{12} [\text{Applied or effective stress (MPa)}]^{-4.58}$$

$$\text{Applied or effective stress (MPa)} = 565.85 \times [\text{Time to rupture (h)}]^{-0.2548}$$

Additional tests are in progress at 650, 700, 725, and 800°C; results will be reported as they become available. Furthermore, the creep curves will be analyzed in detail to evaluate the time for accumulation of 1 and 2% strain and to develop correlations that relate stress with 1 and 2% strain in 10,000 h.

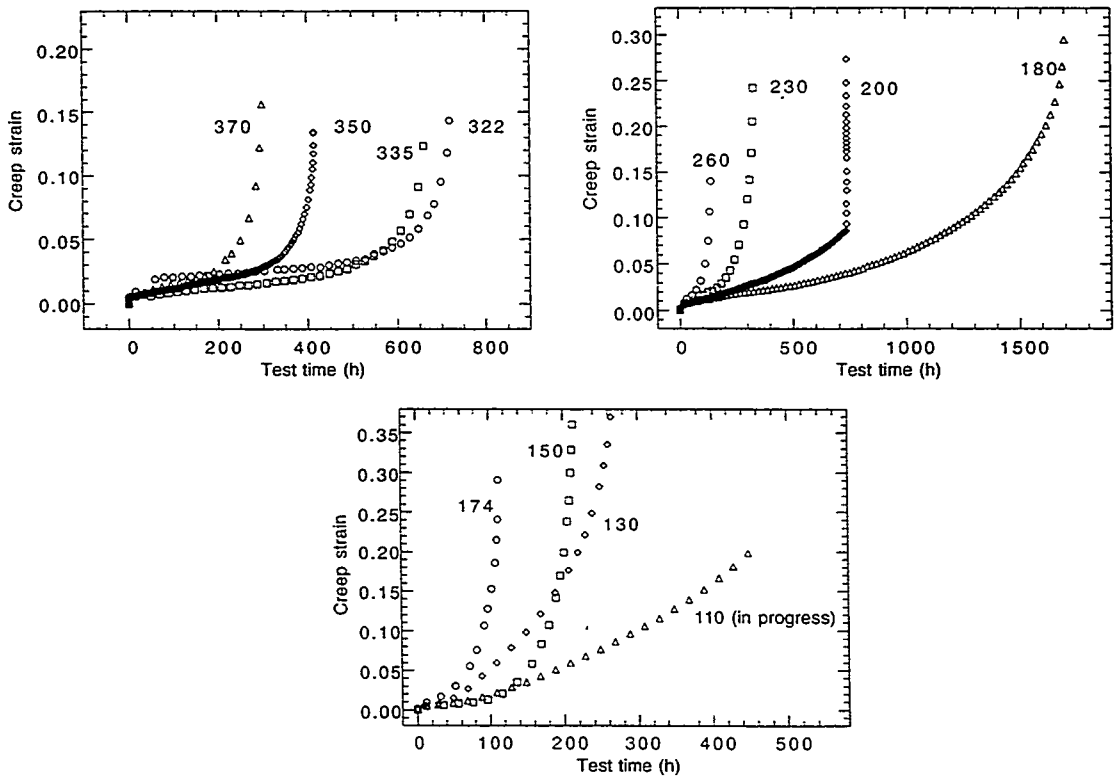

Fig. 2. Uniaxial creep strain-vs.-time plot for V-4Cr-4Ti alloy tested at 650 (top left), 725 (top right), and 800°C (bottom) in vacuum environment. Numbers next to the curves indicate applied stress in MPa.

Table 1. Creep test data obtained for V-4Cr-4Ti alloy at 650-800°C

Temperature (°C)	Applied stress (MPa)	Time to rupture (h)	Rupture strain	Minimum creep rate (s^{-1})	Time-to-onset of tertiary (h)	Strain-to-onset of tertiary
650	370	300	0.18	2.2×10^{-8}	210	0.029
	350	414	0.14	2.0×10^{-8}	280	0.029
	335	661	0.15	9.3×10^{-9}	450	0.028
	322	718.5	0.16	7.0×10^{-9}	515	0.029
	280[a]	-	-	-	-	-
700	250[a]	-	-	-	-	-
725	260	139.2	0.17	7.2×10^{-8}	80	0.024
	230	329	0.25	3.3×10^{-8}	160	0.024
	200	737.4	0.27	2.2×10^{-8}	380	0.033
	180	1701.4	0.32	1.0×10^{-8}	530	0.029
800	174	112.2	0.30	1.1×10^{-7}	45	0.036
	150	214.9	0.46	2.3×10^{-8}	85	0.015
	130	275	0.61	$\approx 10^{-8}$	40	0.012
	110[a]	-	-	-	-	-
	90[a]	-	-	-	-	-

[a]In progress.

REFERENCES

1. K. Natesan, W. K. Soppet, and D. L. Rink, Uniaxial Creep Behavior of V-Cr-Ti Alloys, Semiann. Progress Report for Period Ending June 30, 1999, DOE/ER-0313/26, Sept. 1999, p. 20.

2. R. J. Kurtz and M. L. Hamilton, Biaxial Thermal Creep of V-4Cr-4Ti at 700 and 800°C, ibid, p. 3.

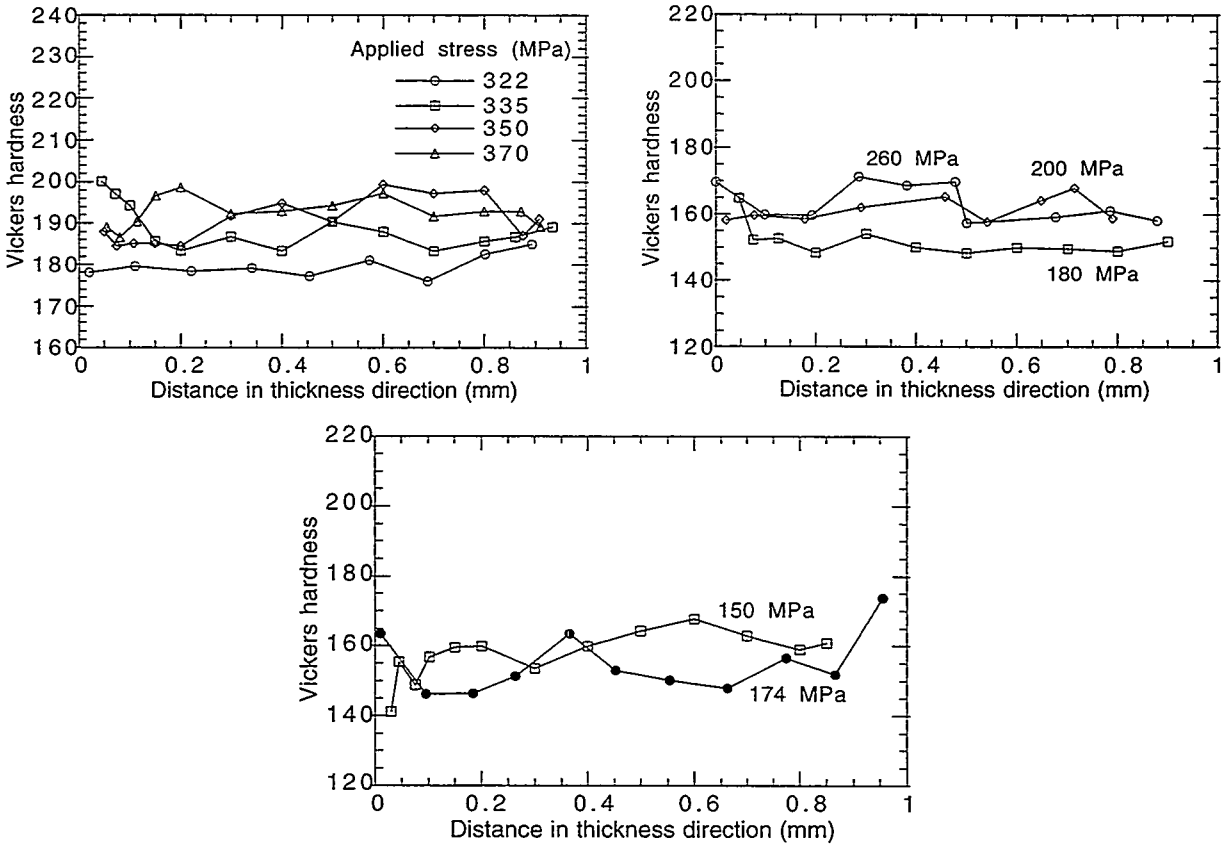

Fig. 3. Vickers hardness profiles in thickness direction for V-4Cr-4Ti specimens, after creep testing at various stress levels at 650 (top left), 725 (top right), and 800°C (bottom) in vacuum environment. Numbers next to curves indicate applied stress in MPa.

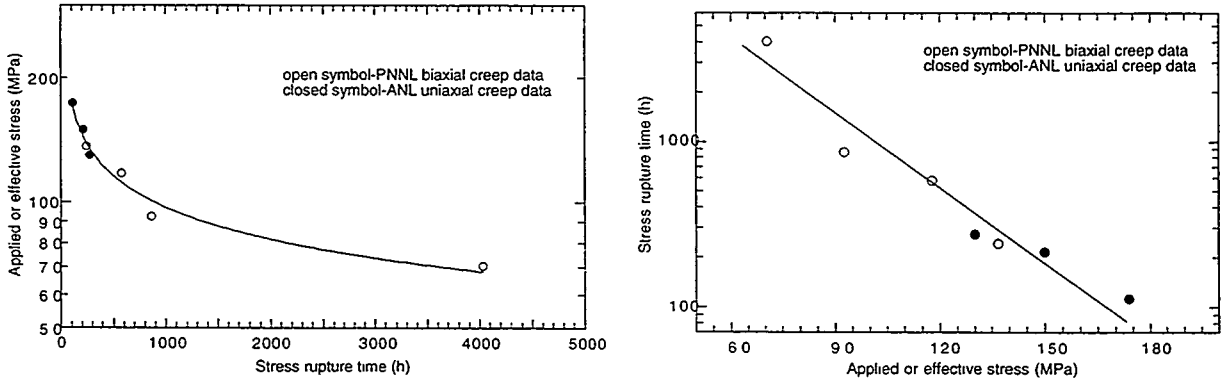

Fig. 4. Two correlations between time-to-rupture and applied stress, where independent variable is time-to-rupture (left) and applied stress (right). Curves represent best fit of data at 800°C obtained in both ANL and PNNL programs.

MICROSTRUCTURAL EXAMINATION ON V-4Cr-4Ti RODS AND CREEP TUBES

- Y. Yan, H. Tsai, and D.L. Smith (Argonne National Laboratory)

OBJECTIVE

The objective of this task is to determine whether the V-4Cr-4Ti bars from the extruded 832665 and swaged 832864 heats are suitable feedstock for the upcoming creep tubing fabrication campaign.

SUMMARY

Extruded V-4Cr-4Ti bar stock from ANL's 500-kg 832665 heat and swaged rod stock from GA's 1000-kg 832864 heat were examined using optical microscopy and transmission electron microscopy to determine whether they are suitable feedstock for the upcoming creep tubing fabrication campaign. To compare microstructure, 832665-heat creep tubing from the last fabrication campaign was also examined. The results of this study show a banded (stringer) structure, consisted of fine Ti-rich particles, exists in both the 832665 and 832864 bars. In the finished creep tubing, remnant of Ti-rich secondary phase particles could also be found although the imhomogeneity is less pronounced than in the feedstock. A homogenization treatment (e.g., annealing at 1200°C for 2 h) may remove the banded structure and this will be tested on small pieces of the 832665 and 832864 bars in the near future.

EXPERIMENTAL PROCEDURE

Specimens were prepared in directions both parallel and perpendicular to the extrusion direction of the bars in order to elucidate the microstructure, particularly the distribution of the banded structure. After mechanical polishing and electropolishing, optical microscopy examinations were conducted to delineate the grain sizes and the microstructural imhomogeneity. Transmission electron microscopy (TEM) studies were carried out to identify the secondary phase particles using a Philips-CM30 microscope, and high resolution electron microscopy (HREM) observations were performed using a JEM-4000EX microscope with a point-to-point resolution of 0.17 nm at Argonne National Laboratory.

RESULTS AND DISCUSSION

There are significant differences in microstructure, including grain sizes between the extruded 832665 and swaged 832864 rods, as shown in the low-magnification micrographs in Figs. 1 and 2. The microstructure of the extruded 832665 material, as shown in Fig. 1(a), consists of an inhomogeneous mixture of small (5-20 μm) and coarse grains (25-50 μm). The grains are mostly equiaxed. For the 832864 material, as shown in Fig. 2(a), the grains are elongated parallel to the extrusion direction and the average grain size is larger than that of the 832665 material.

A banded structure parallel to the extrusion direction, as reported by Rowcliffe et al [1], was observed in both materials. The average grain size in the banded region is considerably smaller than that in the un-banded region, particularly for the as-extruded materials from heat no. 832665 (see Fig. 1(a)). The "dark-field" imaging (i.e. using the scattering light illuminating in optical microscopy), as shown in Figs 1(b)-(c) and 2(b)-(c), was used in our examinations to enhance the contrast of the grain boundary structure and the secondary particles. Figs. 1(b) and 2(b) are higher magnification micrographs showing the banded structure in specimens from heat nos. 832665 and 832864, respectively. Detail analyses indicate that the width of the bands and the distances between them are varied from region to region. The typical width of the bands ranges

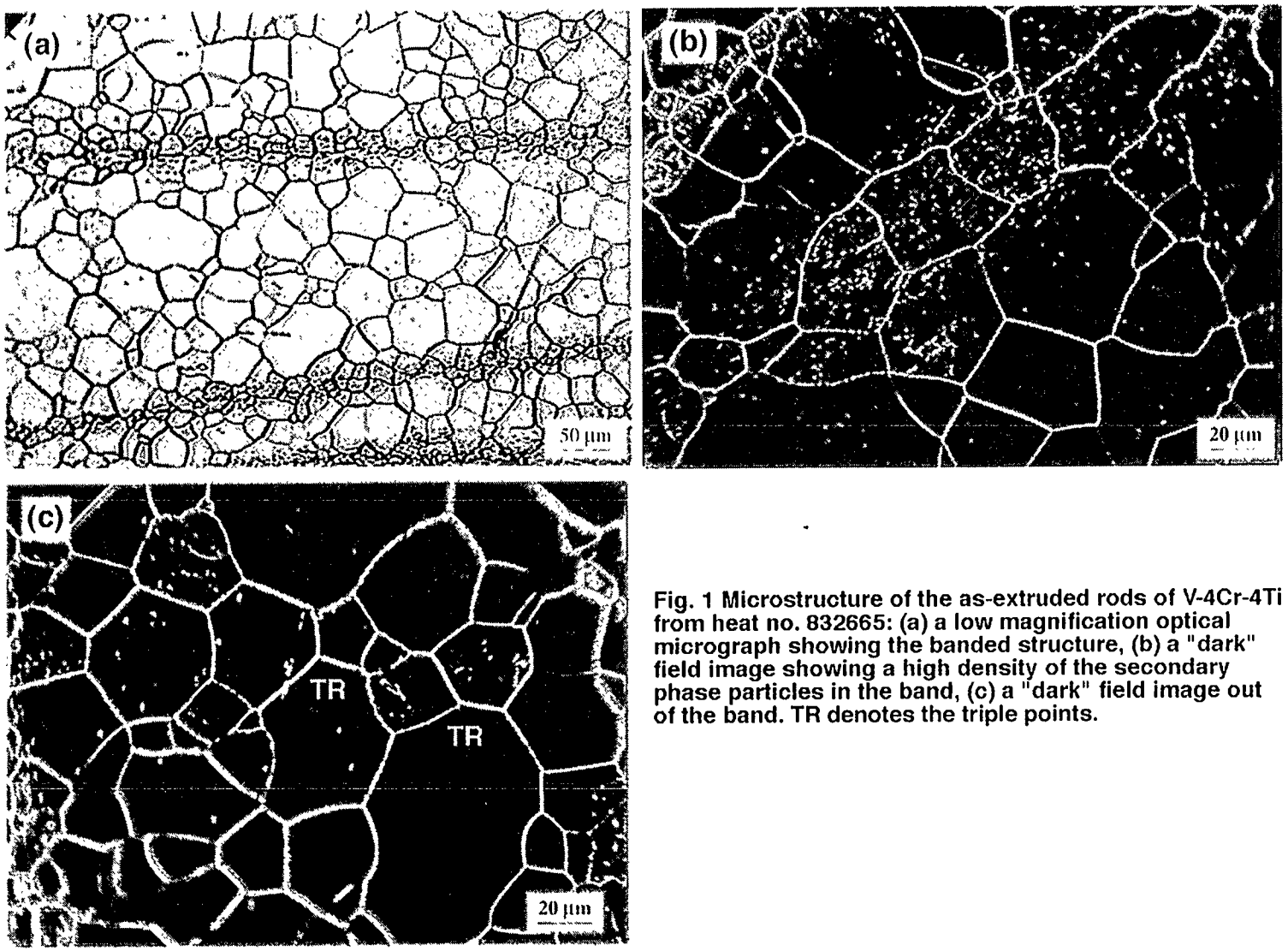

Fig. 1 Microstructure of the as-extruded rods of V-4Cr-4Ti from heat no. 832665: (a) a low magnification optical micrograph showing the banded structure, (b) a "dark" field image showing a high density of the secondary phase particles in the band, (c) a "dark" field image out of the band. TR denotes the triple points.

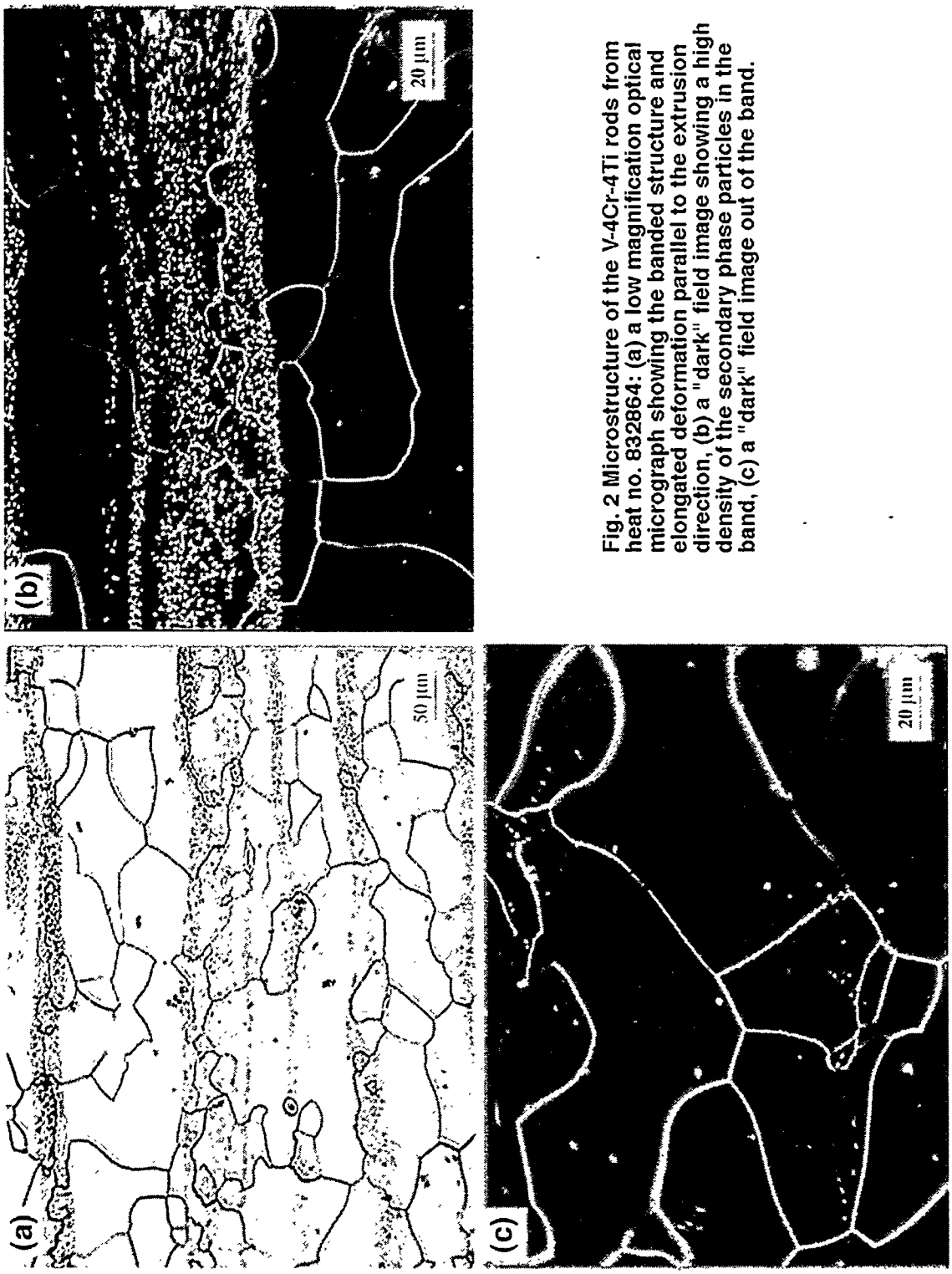

Fig. 2 Microstructure of the V-4Cr-4Ti rods from heat no. 832864: (a) a low magnification optical micrograph showing the banded structure and elongated deformation parallel to the extrusion direction, (b) a "dark" field image showing a high density of the secondary phase particles in the band, (c) a "dark" field image out of the band.

from 25 to 100 μm, and the distances between the bands are ≈ 50-150 μm in the specimens examined.

Figs. 1(c) and 2(c) are higher magnification micrographs showing local areas without the banded structure in the extruded 832665 and swaged 832864 materials. There is a strong tendency for grain boundary interfaces to be faceted for as-extruded rods from heat no. 832665 (see Fig. 1(c)). The faceted planes are presumably some low index crystallographic plans, which are usually in favor of formation energy for grain boundaries. At the triple points (marked as TR in Fig. 1(c)) the grain boundaries likely joint together at some special angles, such as ~90°, ~120°, or ~135°. The tendency to be faceted onto low index plans is decreased for the grain boundaries in the sample from heat no. 832864 due to the deformation induced in swaging processing of round bars from the original materials. It has also been found that the grain sizes are not uniform in the banded areas. Although the average of the grain sizes in the banded area are smaller than that in the un-banded areas, some large grains (>30 μm) were also observed occasionally in the banded areas, as shown in Fig. 1(b).

TEM micrograph of Fig. 3(a) shows a secondary phase particle in the 832864 specimen. According to other investigators [1,2], the globular-shaped secondary particles in V-4Cr-4Ti consist of Ti-oxycarbonnitrides (Ti-OCN). Our preliminary TEM examinations confirmed the predominant composition of Ti in the secondary phase particles. However, it appears that there is no significant increment of the C and O peaks in the energy dispersive spectrum of the secondary phase particle examined in our sample. A typical energy dispersive spectrum for the impurity phase is shown in Fig. 3(c) and can be compared with the reference spectra obtained from the V-4Cr-4Ti matrix, shown in Fig. 3(b). A more detailed analysis on the secondary phase particles will be conducted in the near future.

Electron diffraction studies did not reveal any preferred orientation of the discrete Ti-rich particle inclusions with respect to the V-4Cr-4Ti matrix. TEM microscopy indicates further that the interface between the V-4Cr-4Ti and secondary phase particles is predominantly non-faceted, as can be seen from Fig. 3(a). High-resolution electron microscopy (HREM) was used to examine the interface structure. The lattice disorder, indicated by the non-uniform contrast in the HREM image (see Fig. 4(a)) of the V-4Cr-4Ti phase around the second phase, was observed, although the spatial distribution of the defects is better viewed at low magnification using the diffraction contrast techniques. The lower magnification using a zone-axis bright-field image shown in Fig. 4(b) reveals the form and distribution of the stress field associated with the secondary phase particle. In the area examined, the dislocations are non-uniformly distributed, with high density near the Ti-based particles. The dislocations appear to extend to distances of up to hundreds of nanometers from the interface of the V-4Cr-4Ti and secondary phase particles.

Limited microstructural characterization on creep tubing from the previous fabrication campaign was conducted to determine whether there are residual imhomogeneity from the feedstock. Optical microscopy, conducted along both longitudinal (see Fig. 5) and transverse (see Fig. 6) directions, shows that the grain sizes are from ≈10 to 70 μm with elongated deformation parallel to the longitudinal (i.e. drawing) direction (see Fig. 5). The secondary phase particles in the creep tubes distribute more uniformly, as shown in Fig. 5(c), than in the as-extruded feedstock, but the banded structure can still be observed (see Fig. 6(c)).

FUTURE PLAN

A homogenization treatment (e.g., annealing at 1200°C for 2 h) will be performed on small pieces of the 832665 and 832864 bars, and microstructural examinations on the treated materials will be conducted to determine whether the treatment will re-dissolve the secondary phase particles.

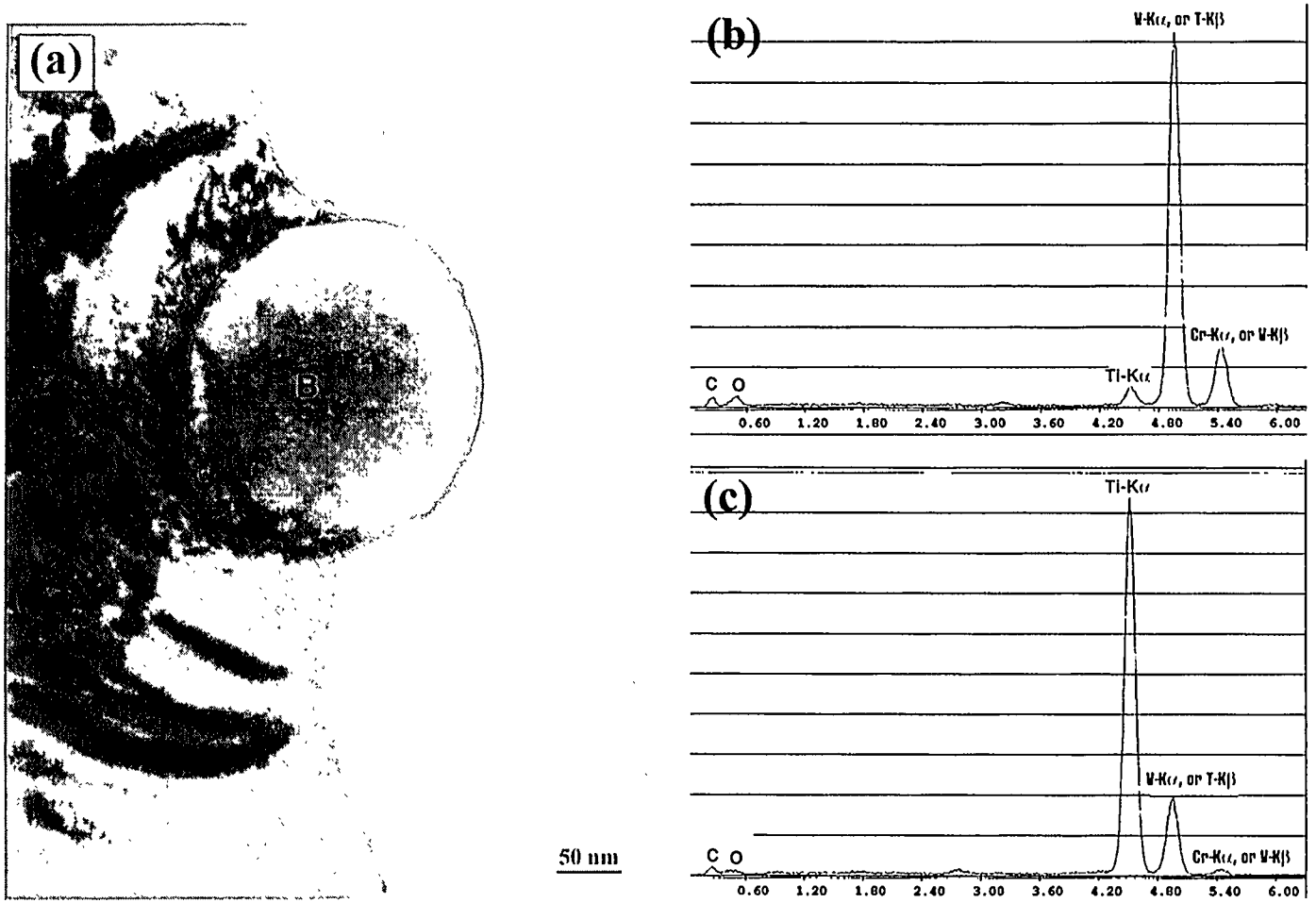

Fig.3 (a) A TEM image showing a secondary phase particle (labeled as B) in the V-4Cr-4Ti rods from heat no. 832864. (b) Energy dispersive spectrum obtained from the V-4Cr-4Ti matrix. (c) Energy dispersive spectrum obtained from the secondary phase particle. Note the lack of noticeable increase in C and O peaks in the spectrum of the particle B.

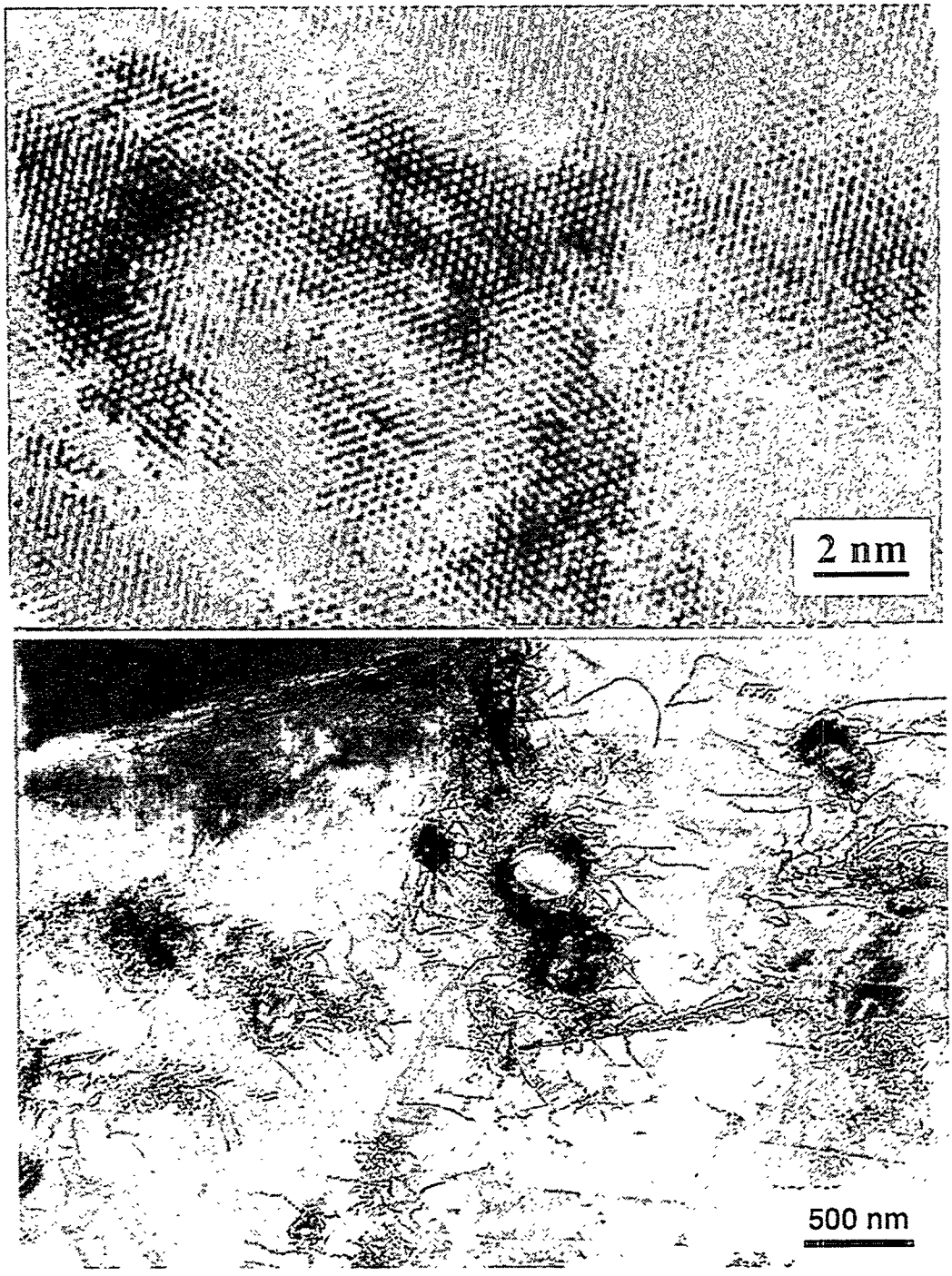

Fig.4 (a) HREM image showing the lattice disorder of the V-4Cr-4Ti phase around the second phase particles. (b) A low magnification TEM micrograph showing the microstructure in the band of the V-4Cr-4Ti rods from heat no. 832864.

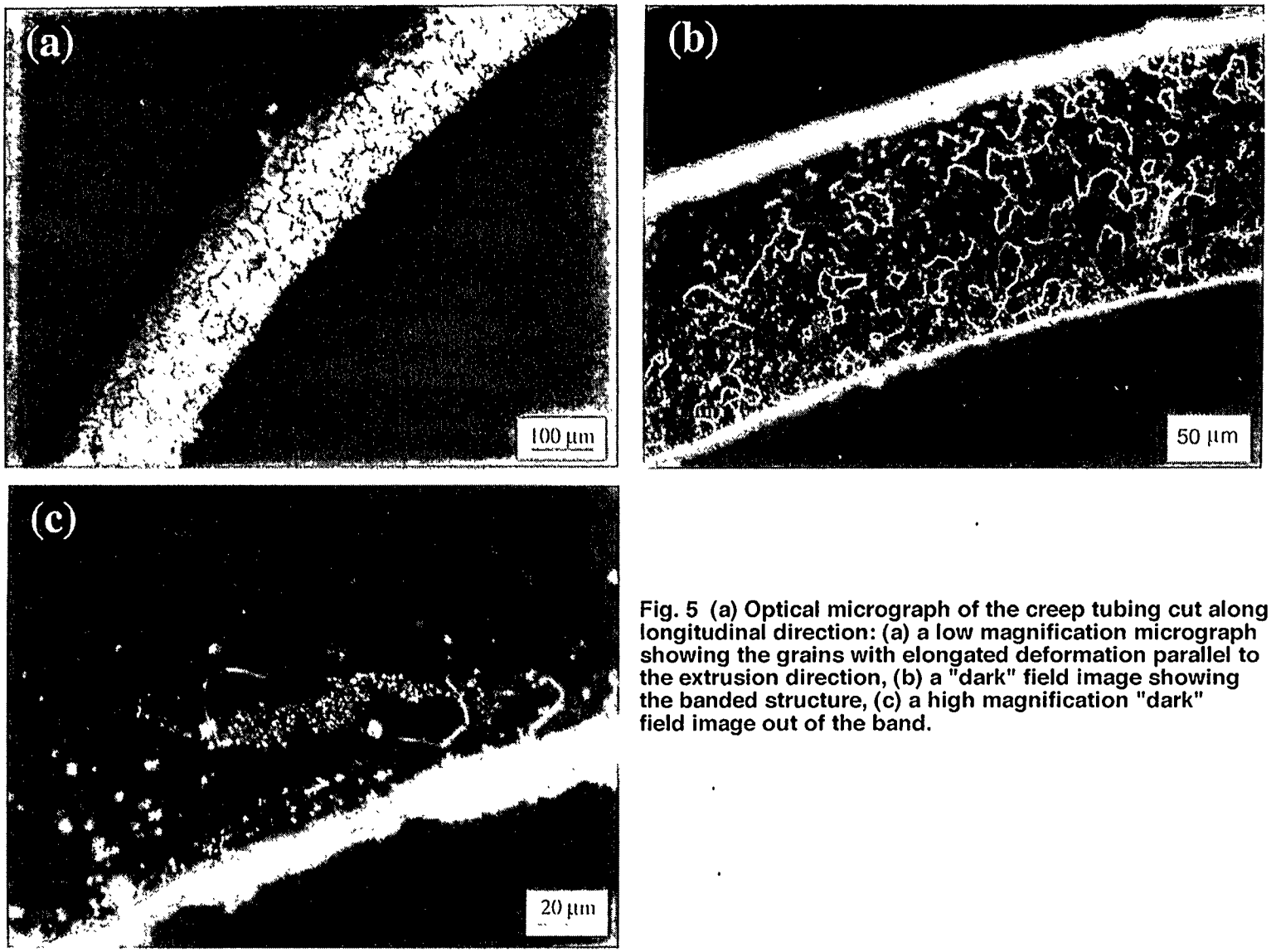

Fig. 5 (a) Optical micrograph of the creep tubing cut along longitudinal direction: (a) a low magnification micrograph showing the grains with elongated deformation parallel to the extrusion direction, (b) a "dark" field image showing the banded structure, (c) a high magnification "dark" field image out of the band.

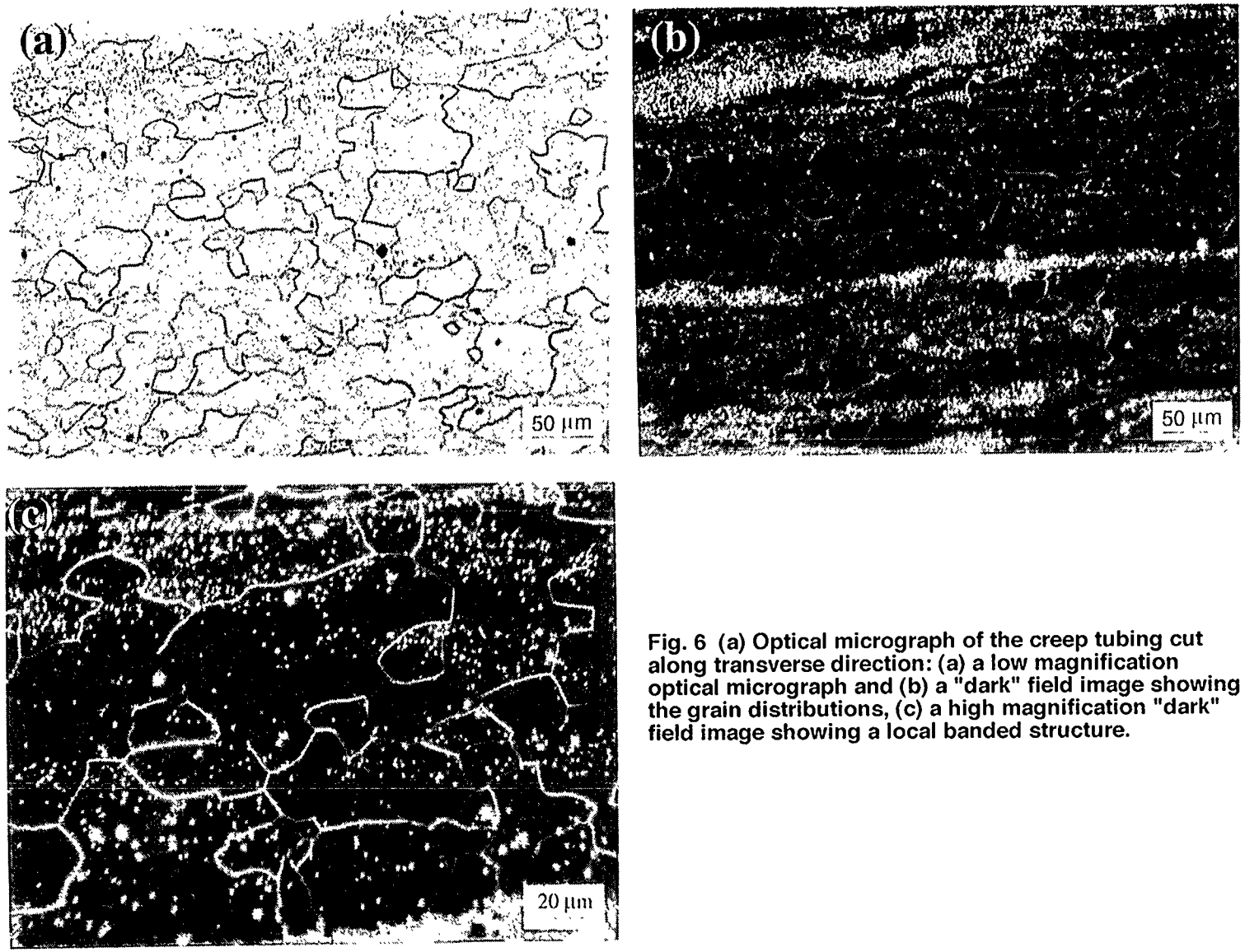

Fig. 6 (a) Optical micrograph of the creep tubing cut along transverse direction: (a) a low magnification optical micrograph and (b) a "dark" field image showing the grain distributions, (c) a high magnification "dark" field image showing a local banded structure.

ACKNOWLEDGEMENTS

We are grateful to Dr. R. Cook and Mr. B. Kestel for helping with the sample preparing. We also acknowledge the support of Dr. M.A. Kirk of Electron Microscopy Center, Argonne National Laboratory, for the provision of laboratory facilities.

REFERENCES

1. F. Rowcliffe and D. T. Hoelzer, Fusion Materials Semiannual Progress Report, DOE/ER-0313/25, December 1998, pp42-58.

2. D. T. Hoelzer, Fusion Materials Semiannual Progress Report, DOE/ER-0313/25, December 1998, pp. 59-63.

EFFECT OF OXYGEN ON THE CRACK GROWTH BEHAVIOR OF V-4CR-4TI AT 600°C –

R. J. Kurtz (Pacific Northwest National Laboratory)*

OBJECTIVE

The objective is to determine the effect of oxygen on the subcritical crack growth behavior of V-4Cr-4Ti alloys. Constant load compact tension tests are being performed to determine the propensity for stress-assisted, oxygen-induced embrittlement of V-4Cr-4Ti.

SUMMARY

Exploratory experiments were performed to evaluate the effect of oxygen on the crack growth response of V-4Cr-4Ti at 600°C under constant load. Tests were run in gettered argon, argon containing 2000 ppm oxygen, and laboratory air using fatigue pre-cracked compact tension specimens. Crack growth was measured primarily by post-test fracture surface examination, but also by in-test compliance measurements. Crack growth rates measured in air and gettered argon were about 2-3x10^{-3} mm/h at a stress intensity factor of about 40 MPa$\sqrt{m}$. The crack growth rate in argon with 2000 ppm oxygen was about 7x10^{-2} mm/h at the same stress intensity level. The crack growth rates were very sensitive to the stress intensity factor. Over a limited range of stress intensity values the crack growth rate in argon plus 2000 ppm oxygen appears to be power-law dependent on stress intensity with an exponent of about 8.9. The fracture mode in air and gettered argon was transgranular cleavage with 20 to 30% intergranular fracture. In the oxygenated argon environment crack growth occurred predominantly by transgranular cleavage.

PROGRESS AND STATUS

Introduction

The mechanical properties of vanadium alloys being developed for fusion power system structures are sensitive to interstitial impurities such as oxygen, nitrogen and carbon. Previous studies [1-7] have shown the profound effect these impurities have on the tensile and fracture behavior of these materials. Effects include loss of ductility, increases in the ductile-to-brittle transition temperature, and a propensity for mechanical failure by low-energy modes such as cleavage or grain boundary fracture. The severity of the effect largely depends on the concentration and distribution of interstitials in the microstructure, but the details of how properties are degraded are not well understood. Relatively few studies have been performed to evaluate the effect of environment on the sub-critical crack growth and fracture behavior of candidate structural materials [8]. The objective of the present investigation is to examine the effect of oxygen on the propensity for stress-assisted dynamic embrittlement in V-4Cr-4Ti.

Dynamic embrittlement is a type of brittle fracture that occurs by quasi-static decohesion, usually along grain boundaries, caused by the stress-driven diffusion of a surface-adsorbed embrittling element. This type of embrittlement has been observed in a number of alloy systems. Oxygen is found to embrittle nickel-base superalloys and intermetallics [9-11], as well as in a precipitation strengthened Cu-Be alloy [12]. Tin will embrittle bronze [13] and in steels sulfur is the deleterious element [14]. Crack growth rates are between 0.1 – 100

*Pacific Northwest National Laboratory (PNNL) is operated for the U.S. Department of Energy by Battelle Memorial Institute under contract DE-AC06-76RLO-1830.

mm/h which is many orders of magnitude slower than conventional brittle fracture. The growth rate is determined by the diffusivity of the embrittling species, the stress profile ahead of the crack tip (assumed to be time-dependent), and the concentration of the embrittling element need to cause local fracture. Excellent review papers have appeared in recent years describing dynamic embrittlement and quantitative models based on a modification of Fick's second law of diffusion [15,16]. In the present report, the results of exploratory experiments to study the effect of oxygen partial pressure and stress intensity level on the crack growth behavior of V-4Cr-4Ti at 600°C are presented.

Experimental Procedure

Compact-tension (CT) specimens 30.5 mm wide by 3.8 mm thick were machined from warm-rolled V-4Cr-4Ti alloy (Heat No. 832665) plate in the T-L orientation. The CT specimens were cut according to the dimensions specified by the ASTM standard test method for plane-strain fracture toughness of metallic materials [17]. After machining, specimens were annealed at 1000°C for one hour in a vacuum furnace at a pressure $\leq 10^{-7}$ torr. This heat treatment produced a recrystallized microstructure with an average grain size of 25 μm. Specimens were fatigue pre-cracked in room temperature air and then tested at 600°C in an appropriate environment.

Three environments were utilized 1) flowing (0.4-0.5 l/min) purified argon, 2) flowing argon doped with 2000 ppm oxygen, or 3) laboratory air. Table 1 summarizes test conditions for the experiments performed to date. An oxygen gettering furnace was used to purify the argon gas before passing it once through the test chamber. The oxygen concentration of the purified argon leaving the gettering furnace was much less than ~1 ppm oxygen as measured by a zirconia-cell oxygen meter. To create an environment consisting of argon containing 2000 ppm oxygen a gas mixing apparatus was used. Details of how the gas mixing system operates have been described previously [18].

Table 1. Test conditions employed.

Specimen ID	Total Test Time, h	Test Environment
CT44-01	407	Gettered Ar
CT44-02	529	Air
CT44-05	241	Air
CT44-08	171	Ar + 2000 ppm O_2
CT44-09	212	Gettered Ar

All experiments were performed in a controlled atmosphere furnace, with quartz windows on two opposite sides, attached to a rigid, electromechanically controlled, load frame. The CT specimens were loaded via Inconel 625 pin and clevis grips. These grips extended out of the furnace hot zone and were, in turn, connected to water-cooled, stainless steel loading rods inside the controlled atmosphere chamber. The loading rods passed through stainless steel bellows and were connected to the load frame.

The samples were loaded to a nominal constant load by cycling the load 1 N above and below a desired value at a crosshead speed of 0.05 mm/min. The load-line displacement of the specimen notch was measured with a laser extensometer, Figure 1. The extensometer transmitter scanned a laser beam vertically through one of the quartz windows on the

furnace. The extensometer receiver collected the resultant signal after it had passed through the furnace chamber. The sample was arranged so that the laser beam could only be transmitted through the notch of the sample. The resolution of the extensometer is 0.5 μm.

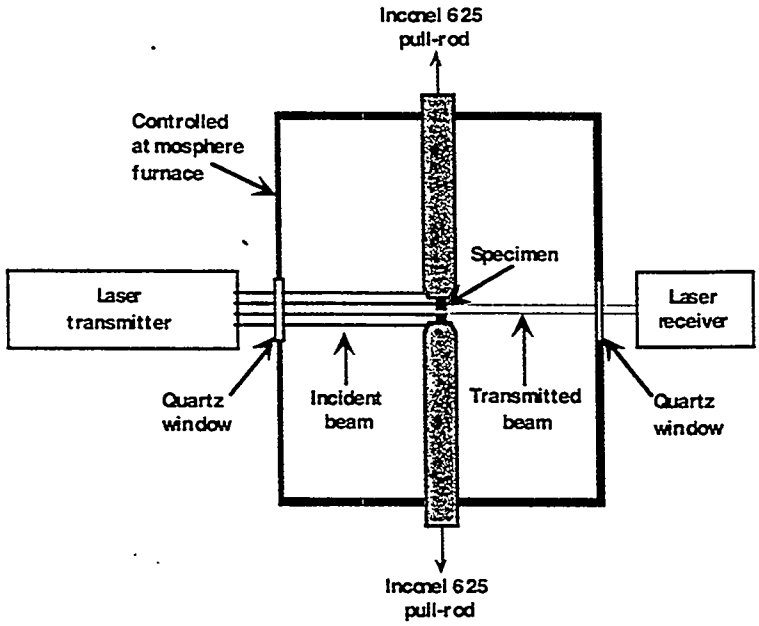

Figure 1. Schematic of experimental test set-up for constant load crack growth testing.

The load-line displacement and load were recorded once a minute by a computer data acquisition system. Periodically the specimen compliance was measured by unloading to 80% of the current load level. During unloads the data acquisition rate was increased to once a second. The specimen compliance was used as an indication of crack growth at a particular load level. At the end of a test the extent of environmentally induced crack growth was marked by causing additional fatigue crack growth in room temperature air. Specimens were then broken open and the fracture surfaces examined both optically to measure crack extension, and in a scanning electron microscope (SEM) to characterize fracture mode.

Results

Figure 2 gives a representative plot of the load and load-line displacement as a function of time for specimen CT44-08 tested in argon plus 2000 ppm oxygen. The load-line displacement measurement includes displacements from several sources. Increasing displacement may be attributed to either crack growth or to creep of the material in the vicinity of the highly stressed crack tip. A decrease in load-line displacement may be caused by growth of an oxide film on the surfaces of the notch. All of these effects occurred during our tests. As noted above the specimen compliance was measured in an effort to separate crack growth from specimen creep and oxide film growth. Reliable measurements of the specimen compliance were not obtained under low stress intensity and severe oxidation conditions. Build up of oxide at the crack tip wedged the crack open preventing complete unloading. Thus, crack growth measurements were based primarily (but not entirely) on

post-test visual and SEM examination of the fracture surface. These results suggest that another crack growth measurement technique, such as the DC potential drop method, may provide better crack growth monitoring capability. The crack growth data are summarized in Table 2. The dependence of the crack growth rate on stress intensity factor is shown in Figure 3. It is evident from Figure 3 that the crack growth rate in air and gettered argon are similar at a stress intensity of about 40 MPa$\sqrt{m}$. In contrast, the crack growth rate in argon with 2000 ppm oxygen is one to two orders of magnitude higher at similar stress intensity levels and appears to be power-law dependent on the applied stress intensity. The data gathered under other conditions are too few to make conclusive statements about the dependence of the crack growth rate on stress intensity factor.

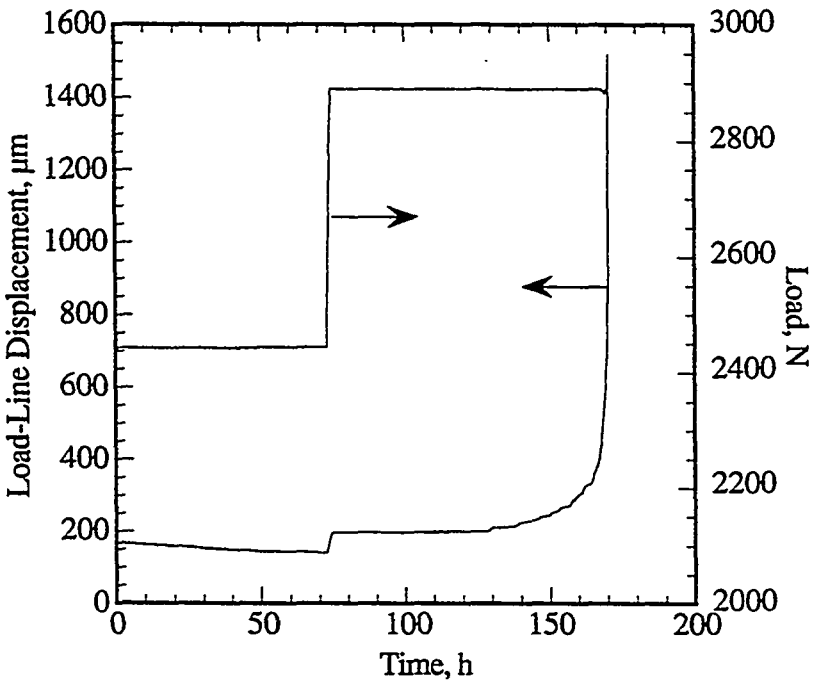

Figure 2. Time dependence of the applied load and load-line displacement for specimen CT44-08 tested in 2000 ppm oxygen at 600°C.

SEM fracture surface examinations were performed on all specimens. For specimens tested in air the fracture surfaces were heavily oxidized. Attempts to remove the scale by ultrasonic cleaning in an acetone bath were partially successful, but this treatment did not reveal the details of the fracture process since the surfaces were severely corroded. The oxide scale did not interfere with optical measurements of the extent of crack propagation, however due to clear differences in surface roughness between fatigue crack growth regions and environmentally assisted crack growth. On the other hand, the fracture surfaces of specimens tested in gettered argon or oxygen doped argon were less severely oxidized, so only brief ultrasonic cleaning was needed prior to SEM examination. For these specimens it

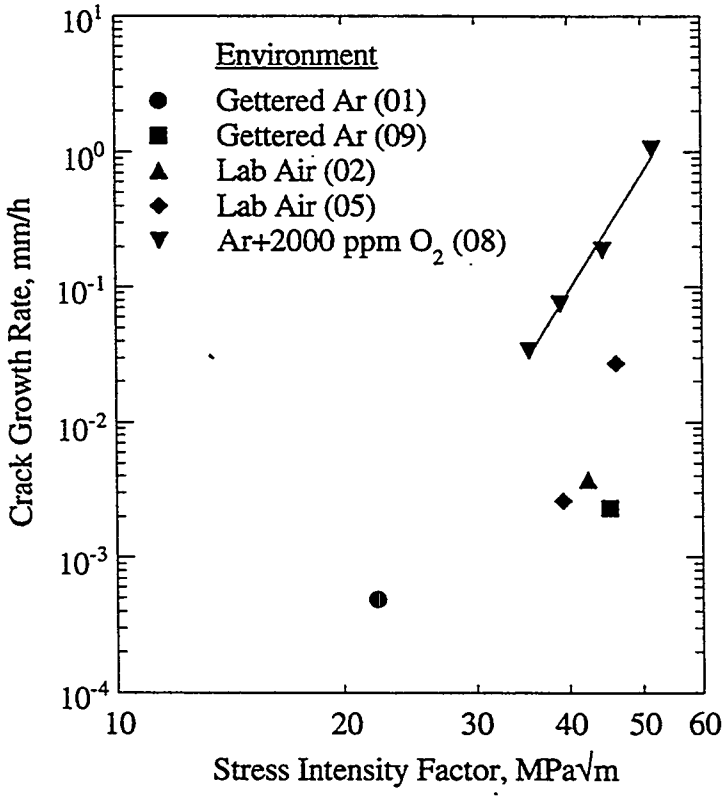

Figure 3. Crack growth rate as a function of stress intensity factor for unirradiated V-4Cr-4Ti tested in gettered Ar, laboratory air, or Ar + 2000 ppm oxygen at 600°C.

was not difficult to determine the fracture mode. Transgranular cleavage and intergranular fracture were the principal fracture features observed on specimens tested in gettered argon, Figure 4. About 20 to 30% of the fracture features are considered intergranular in these specimens. For the specimen tested in argon containing 2000 ppm oxygen the fracture mode was predominantly transgranular cleavage with some evidence of tear ridges separating cleavage patches, Figure 5.

Table 2. Summary of crack growth results.

Specimen ID	Δa, mm	Δt, h	Δa/Δt, mm/h	K, MPa√m
CT44-01	0.20	407	4.91×10^{-4}	22.2
CT44-02	1.00	266	3.76×10^{-3}	42.4
CT44-05	0.55	210	2.62×10^{-3}	39.2
"	0.83	30.7	2.71×10^{-2}	46.2
CT44-08	0.66	19.5	3.38×10^{-2}	35.4
"	1.40	18.5	7.57×10^{-2}	39.0
"	1.07	5.70	1.88×10^{-1}	44.4
"	1.78	1.70	1.05×10^{0}	51.7
CT44-09	0.38	164	2.32×10^{-3}	45.3

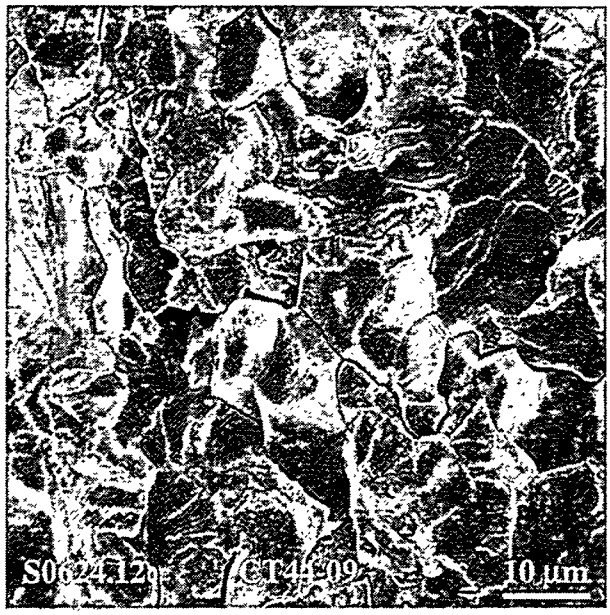

Figure 4. SEM image of the fracture surface of specimen CT44-09 tested in gettered Ar at 600°C.

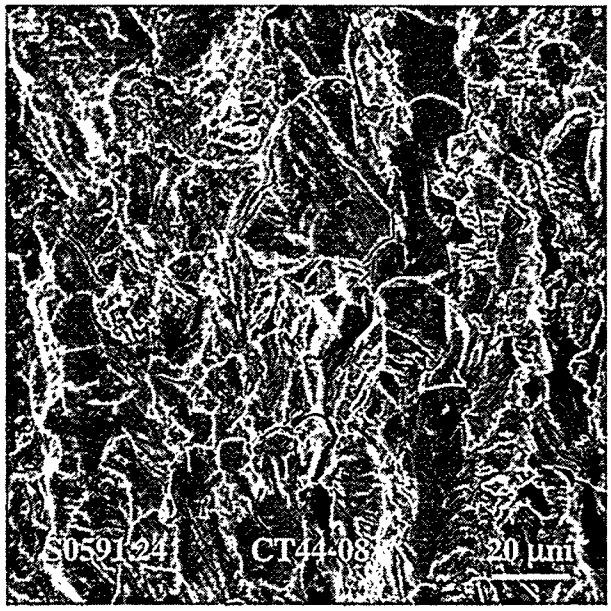

Figure 5. SEM image of the fracture surface of specimen CT44-08 tested in Ar+2000 ppm oxygen at 600°C.

Discussion

A clear difference in crack growth behavior was found for specimens tested in air or gettered argon compared to tests conducted in oxygenated argon. The diffusion coefficient of oxygen in V-4Cr-4Ti at 600°C is about $3x10^{-5}$ mm^2/h [1]. The distance oxygen must diffuse in order to cause the observed crack growth rates may be computed from

$$x = \frac{D}{\dot{a}} \qquad (1)$$

where $\dot{a}$ is the crack growth rate in mm/h and D is the diffusion coefficient in mm^2/h. For tests conducted in air or gettered argon the required oxygen diffusion distance is between 8 and 61 μm depending on the specific environment and stress intensity level. These diffusion distances are on the order of the grain size in this material. This suggests that the cracking process in air or gettered argon is intermittent. In a low oxygen environment such as gettered argon a relatively long time is needed for oxygen to diffuse into the material and elevate the oxygen concentration to a value high enough to cause local fracture. It is interesting to note that the fracture mode observed during tensile testing of pre-charged specimens seems to differ from that found here. The primary fracture mode seen by Natesan et al. [3] and DiStefano et al. [2] following tensile testing was intergranular rather than transgranular cleavage. In contrast, Fujiwara et al. [5] observed transgranular cleavage in specimens exposed to air for one hour at 500 or 700°C. Air has been found to be a more aggressive oxidation environment than low partial pressure oxygen [2,3]. In air it appears that formation of a relatively thick oxide scale inhibits oxygen transport to the crack tip relative to the oxygen doped argon environment. For the argon with 2000 ppm oxygen the characteristic diffusion distance ranges from 0.03 to 0.4 μm. In other words, the depth of penetration is 10 to 1000 times smaller than the crack tip opening displacement. Thus, oxygen must be embrittling the material at or very near the surface. There is very little time for protective oxide film to form, as should be the case for a continuous cracking process. These results indicate that under certain conditions of stress intensity and oxygen partial pressure the near surface region is easily embrittled and rapid crack growth occurs.

Conclusions

The crack growth rate in gettered argon and laboratory air was similar at a stress intensity factor of about 40 MPa√m. The crack growth rate in argon containing 2000 ppm oxygen was more than one order of magnitude faster than for tests run in laboratory air or gettered argon at similar stress intensity factors. The crack growth rates were very sensitive to the stress intensity factor. Over a limited range of stress intensity values the crack growth rate in argon plus 2000 ppm oxygen appears to be power-law dependent on stress intensity with an exponent of about 8.9. The fracture mode in air and gettered argon was transgranular cleavage with 20 to 30% intergranular fracture. In the oxygenated argon environment crack growth occurred predominantly by transgranular cleavage.

REFERENCES

[1] M. Uz, K. Natesan, and V. B. Hang, J. of Nucl. Mater. 245 (1997) 191.

[2] J. R. DiStefano and J. H. DeVan, J. of Nucl. Mater. 249 (1997) 150.

[3] K. Natesan, W. K. Soppet and M. Uz, J. of Nucl. Mater. 258-263 (1998) 1476.

[4] H. D. Roehrig, J. R. DiStefano and L. D. Chitwood, J. of Nucl. Mater. 258-263 (1998) 1356.

[5] M. Fujiwara, M. Satou, H. Hasegawa and K. Abe, J. of Nucl. Mater. 258-263 (1998) 1507.

[6] K. Natesan and M. Uz, in: Fusion Materials: Semiannual Progress Report for Period Ending June 30, 1998 (1998) 73.

[7] B. A. Pint, P. M. Rice, L. D. Chitwood, J. H. DeVan and J. R. DiStefano, in: Fusion Materials: Semiannual Progress Report for Period Ending June 30, 1998 (1998) 77.

[8] B. G. Gieseke, C. O. Stevens and M. L. Grossbeck, J. of Nucl. Mater. 233-237 (1996) 488.

[9] R. W. Hays, D. F. Smith, E. A. Wanner and J. C. Earthman, Mater. Sci. and Eng. A177 (1994) 43.

[10] C. T. Liu and C. L. White, Acta Metall. Vol 35 (1987) 643.

[11] C. A. Hippsley and J. H. DeVan, Acta Metall. Vol 37 (1989) 1485.

[12] R. C. Muthiah, A. Guha and C. H. McMahon, Jr., Mater. Sci. Forum 207-209 (1996) 585.

[13] D. Bika and C. J. McMahon, Jr., Mater. Res. Soc. Symp. Proc. 238 (1992) 399.

[14] D. Bika, J. A. Pfaendtner, M. Menyhard and C. J. McMahon, Jr., Acta Metall. Mater. Vol 43, No.5 (1995) 1895.

[15] D. Bika and C. J. McMahon, Jr., Acta Metall. Mater. Vol 43, No.5 (1995) 1909.

[16] J. A. Pfaendtner, R. C. Muthiah, C. T. Liu and C. J. McMahon, Jr., Mater. Sci. and Eng. A260 (1999) 1.

[17] ASTM E399-90, American Society for Testing & Materials, Philadelphia, PA (1992).

[18] C. H. Henager, Jr. and R. H. Jones, J. Am. Ceram. Soc. 77 [9] (1994) 2381.

OXIDATION OF V-4Cr-4Ti AT LOW PRESSURES -- B. A. Pint, J. R. DiStefano, J. Bentley and L.D. Chitwood (Oak Ridge National Laboratory)

OBJECTIVE

The objective of this task is to assess the high temperature oxidation behavior of V-4Cr-4Ti in low oxygen pressure environments and any related effect on mechanical properties. Many reactor designs involve vanadium alloys in high temperature environments such as vacuum or helium which will contain some level of oxygen and hydrogen impurities. Testing is being conducted in vacuum with low oxygen pressures, 10^{-3}-10^{-6}Pa (10^{-5}-10^{-8}Torr), and in high-purity helium at 400-700°C. Recent emphasis has been on determining kinetics of oxidation at 600-700°C.

SUMMARY

To complement previous work on V-4Cr-4Ti at 400-500°C,[1] similar oxidation experiments were conducted at 600-700°C. In general, the rates were linear with time. However, at higher oxygen pressures, e.g. 10^{-3}Pa (10^{-5}Torr), specimen surfaces became slightly discolored indicating the formation of a surface oxide and rates were linear-parabolic. The addition of more than 1000ppm oxygen resulted in a significant loss of room temperature ductility. Annealing at 950°C was effective in improving ductility at oxygen levels below 1500ppm. With higher oxygen levels, the anneal was ineffective or further reduced ductility. High resolution analytical electron microscopy was used to examine the oxidized V-4Cr-4Ti microstructure before and after annealing at 950°C. Low ductility before annealing is attributed to fine oxide particles in the matrix inhibiting dislocation movement. Large Ti-rich oxide particles were observed at grain boundaries while the alloy matrix adjacent to the boundary was depleted in Ti.

PROGRESS AND STATUS

Experimental Procedure

All of the experiments were conducted on V-4Cr-4Ti (Heat#8326). Prior to exposure, the specimens were annealed at 1050°C to produce a uniform grain size. Low pressure exposures were conducted in an ultra high vacuum system with a base vacuum of 10^{-7}Pa (10^{-9}Torr). A leak valve is used to achieve oxygen partial pressures of 10^{-3}-10^{-6}Pa (10^{-5}-10^{-8}Torr). Specimens were 0.76mm thick tensile specimens. Oxygen content was determined by weighing the samples before and after exposure. Select samples were then annealed for 4h at 950°C in vacuum, which has been shown to restore room temperature ductility to O-loaded vanadium[1]. Mechanical properties were measured at room temperature. TEM samples were prepared in parallel near the center of the specimen using electropolishing.

Results and Discussion

Reaction Kinetics 600°-700°C

The oxidation rate of V-4Cr-4Ti was measured from 10^{-3}-10^{-5}Pa (10^{-5}-10^{-7}Torr) at 600°C and from 10^{-3}-10^{-6}Pa (10^{-5}-10^{-8}Torr) at 700°C. Results to date are summarized in Table I (mass gain data in Table I are based on either 2 or 3 test specimens). Mass gains in ppmw O are shown for

Table I. Oxidation data for V-4Cr-4Ti at low pressure.

Temp.	Pressure (Pa)	Time (h)	Mass Gain (mg/cm^2)	Rate of Mass Gain (mg/cm^2h)	Mass Gain Rate Ave. Normalized to 10^{-5}Torr	power law fit (n)	Fitted Linear Rate (mg/cm^2h)
600°C	10^{-3}	8	0.35	$4.4x10^{-2}$	1	1.63	$2.0x10^{-2}$
		24	0.73	$3.0x10^{-2}$			
		48	1.04	$2.2x10^{-2}$			
	10^{-4}	8	0.11	$1.4x10^{-2}$	0.4	0.98	$1.4x10^{-2}$
		24	0.34	$1.4x10^{-2}$			
		48	0.67	$1.4x10^{-2}$			
	10^{-5}	24	0.06	$1.3x10^{-3}$	0.04	1.00	$1.5x10^{-3}$
		48	0.11	$1.2x10^{-3}$			
		100	0.07	$6.8x10^{-4}$			
		242	0.35	$1.4x10^{-3}$			
700°C	10^{-3}	8	1.06	$1.3x10^{-1}$	1	1.44	$7.2x10^{-2}$
		24	2.22	$0.9x10^{-1}$			
		48	3.70	$0.8x10^{-1}$			
	10^{-4}	8	0.2	$2.5x10^{-2}$	0.19	1.38	$1.6x10^{-2}$
		24	0.34	$1.4x10^{-2}$			
		48	0.81	$1.7x10^{-2}$			
	10^{-5}	8	0.021	$2.6x10^{-3}$	0.016	1.23	$9.5x10^{-4}$
		24	0.016	$0.7x10^{-3}$			
		48	0.092	$1.9x10^{-3}$			
		250	0.256	$1.0x10^{-3}$			
	10^{-6}	48	0.042	$8.7x10^{-4}$	0.004	2.85	$1x10^{-4}$
		100	0.036	$3.6x10^{-4}$			
		250	0.058	$2.3x10^{-4}$			
		500	0.058	$1.2x10^{-4}$			

10^{-3} and 10^{-4}Pa in Table II. A power law was used to fit the data at each pressure and temperature where n=1 is linear reaction kinetics and n=2, parabolic. In general, the results showed near linear behavior at 10^{-4}-10^{-6}Pa (10^{-6}-10^{-8}Torr) but deviations were observed at 10^{-3}Pa. The linear-parabolic behavior at 10^{-3}Pa (10^{-5}Torr) was attributed to the formation of a surface oxide which then inhibited oxygen uptake into the substrate. Under these conditions, specimen surfaces became discolored as weight increases exceeded 0.5–2%. For the data at 10^{-6}Pa (10^{-8}Torr), the mass gains were so low and scattered that they are difficult to reliably interpret. In order to compare the various results, a linear rate was fitted in all cases. At 10^{-4}-10^{-6}Pa, the change in oxidation rates was proportional to the oxygen partial pressure. However, comparing the rates at 10^{-3}Pa and 10^{-4}Pa the rates were less than an order of magnitude different and thus did not scale with the oxygen pressure. At 700°C, the rates at 10^{-6}Pa, averaged about 4X less than at 10^{-5}Pa, but the linear rate fit over all of the data points was almost exactly one order of magnitude lower.

No single mathematical relationship likely describes the oxidation rate over the range of temperature and pressures of interest. However, if the assumption is made that the data generated thus far fits an equation of the form:

$$r = k \bullet P_{O_2}, \text{ and } k = k_0 \bullet e^{-Q/RT}$$

where:

r = rate in mg/cm^2h
k_0 = constant
R = gas constant
P_{O_2} = oxygen partial pressure in Pa
T = temperature in Kelvin

then the data yields:

$$r = 4.7 \times 10^6 \bullet e^{-821/T} \bullet P_{O_2}$$

This equation can be used to calculate the approximate oxidation rate of V-4Cr-4Ti at 600–700°C for partial pressures of oxygen in vacuum between 10^{-3}-10^{-6}Pa (10^{-5}-10^{-8}Torr). These levels correspond approximately to the total residual oxygen pressures in vacuum between 10^{-1}-10^{-3}Pa. Previous work indicated that at 500°C, the oxidation rate was independent of pressure at 10^{-2}-10^{-4}Pa (~4 x 10^{-3} mg/cm^2h).

Testing in helium also has been initiated at 600° and 700°C. Samples will be exposed to ultra pure (<1 ppmw O) and impure (10 ppmw O) helium to determine oxidation rates and effects on tensile properties.

Room Temperature Mechanical Properties

The room temperature tensile properties were measured as a function of oxygen pick-up by the V-4Cr-4Ti. Tests have been completed on the specimens exposed at 10^{-3} and 10^{-4}Pa at 600° and 700°C, Table II. Unexposed specimens generally have a room temperature elongation of ~30% and a yield strength of 350MPa. Most of the 10^{-3}Pa exposures at both temperatures resulted in

Table II. Room temperature mechanical properties of V-4Cr-4Ti after exposure

			No Anneal			with 950°C Anneal		
Temp.	Pressure (Pa)	Time (h)	Oxygen Content (wppm)	Yield Strength (MPa)	Elong-ation (%)	Oxygen Content (wppm)	Yield Strength (MPa)	Elong-ation (%)
600°C	10^{-4}	8	723	475	10.3	522	354	29.0
		24	1806	590	2.3	1993	383	9.1
		48	3613	520	3.6	3741	604*	0
	10^{-3}	8	1991	502	12.6	1856	394	4.3
		24	4012	402	6.0	4029	513	1.4
		48	5647	399	6.3	5793	640	0.3
700°C	10^{-4}	8	1065	421	6.6	1092	390	12.3
		24	1704	456	4.4	2005	395	2.8
		48	4466	533*	0	4381	688*	0
	10^{-3}	8	6048	343	4.2	5580	666*	0
		24	12312	219	1.2	11862	537*	0
		48	20408	broke	0†	20606	257	0.2

* no yield, ultimate strength
† broke during preparation

severe embrittlement and the 950°C anneal did not improve performance. In most cases, the anneal reduced the ductility further. This negative effect is attributed to the higher temperature anneal allowing the diffusion of oxygen throughout the specimen. For example, the oxygen uptake (1991ppm) after 8h at 600°C in 10^{-3}Pa was likely concentrated at the specimen surface, resulting in a total elongation of 12%, Table II. When a similarly exposed specimen (1856ppm O) was annealed at 950°C, thus allowing more oxygen diffusion throughout the cross-section, its ductility dropped to 4.3%. Specimens with 1000ppm of oxygen or less showed improved ductility when annealed. Further tensile testing is being completed to determine mechanical properties at 600°C.

Microstructural Characterization of V-4Cr-4Ti After Oxidation

Previous TEM work on large-grained V-4Cr-4Ti after exposure to 10^{-4}Pa at 500°C (1434ppmw O addition) and a 100h vacuum anneal at 600°C revealed a uniform matrix microstructure with ultra fine oxide precipitates.[2] At every grain boundary there was a 100-200nm denuded zone adjacent to the boundary and large precipitates along the boundary. The same TEM specimen was analyzed recently with electron energy loss spectroscopy (EELS) to examine the chemical composition of the precipitates and the matrix near the grain boundaries. A typical EELS spectrum from a large area of the specimen has clear peaks for V, Cr and Ti, Figure 1a. The grain boundary region was then mapped by energy-filtered TEM (EFTEM) imaging to produce fully quantitative maps of elemental concentrations of Ti and V, Figures 1c and 1d, respectively. This technique uses electrons with characteristic energy losses like those in regions marked 3 in Figure 1a and then adjacent regions, marked 1 and 2, as a relative background. A 'zero loss'image of the region is shown in Figure 1b. As expected, the precipitates were denuded in V and were likely TiO_x but may contain some level of N and C. Figure 1e combines the information in Figures 1c and 1d and shows the Ti/V atomic ratio generated with calculated ionization cross-sections. Analyzing a 50-pixel wide region across the boundary, Figure 1e, showed that the matrix adjacent to the boundary was depleted in Ti, Figure 1f. Away from the boundary, the Ti/V was close to the bulk composition of 0.042 and at the boundary the Ti/V ratio showed a peak. These results suggest that the majority of Ti near the boundary was incorporated into the large oxide precipitates.

Grain boundary precipitates were observed before and after annealing so their presence does not appear to affect ductility.[2] The denuded zone adjacent to the boundaries has been proposed to be an important factor in reduced ductilities observed in refractory metals.[3] However, based on these observations, the low ductility in V-4Cr-4Ti is attributed to the fine oxide particles in the matrix preventing dislocation movement. The 950°C anneal improved the room temperature alloy ductility from near 0% to 15-20% by coarsening the fine matrix oxide particles into large precipitates similar in size to those on the grain boundaries.[2] Further work is being conducted on lower O content specimens prepared under similar conditions to assess the importance of the particles and denuded zone at the alloy grain boundaries.

REFERENCES

1. J. R. DiStefano and J. H. DeVan, J. Nucl. Mater. 249 (1997) 150.
2. B. A. Pint, P. M. Rice, L.D. Chitwood, J. H. DeVan and J. R. DiStefano, DOE/ER-0313/24 (1998) 77.
3. C. T. Liu, H. Inouye, R. W. Carpenter, Met. Trans. 4 (1973) 1839.

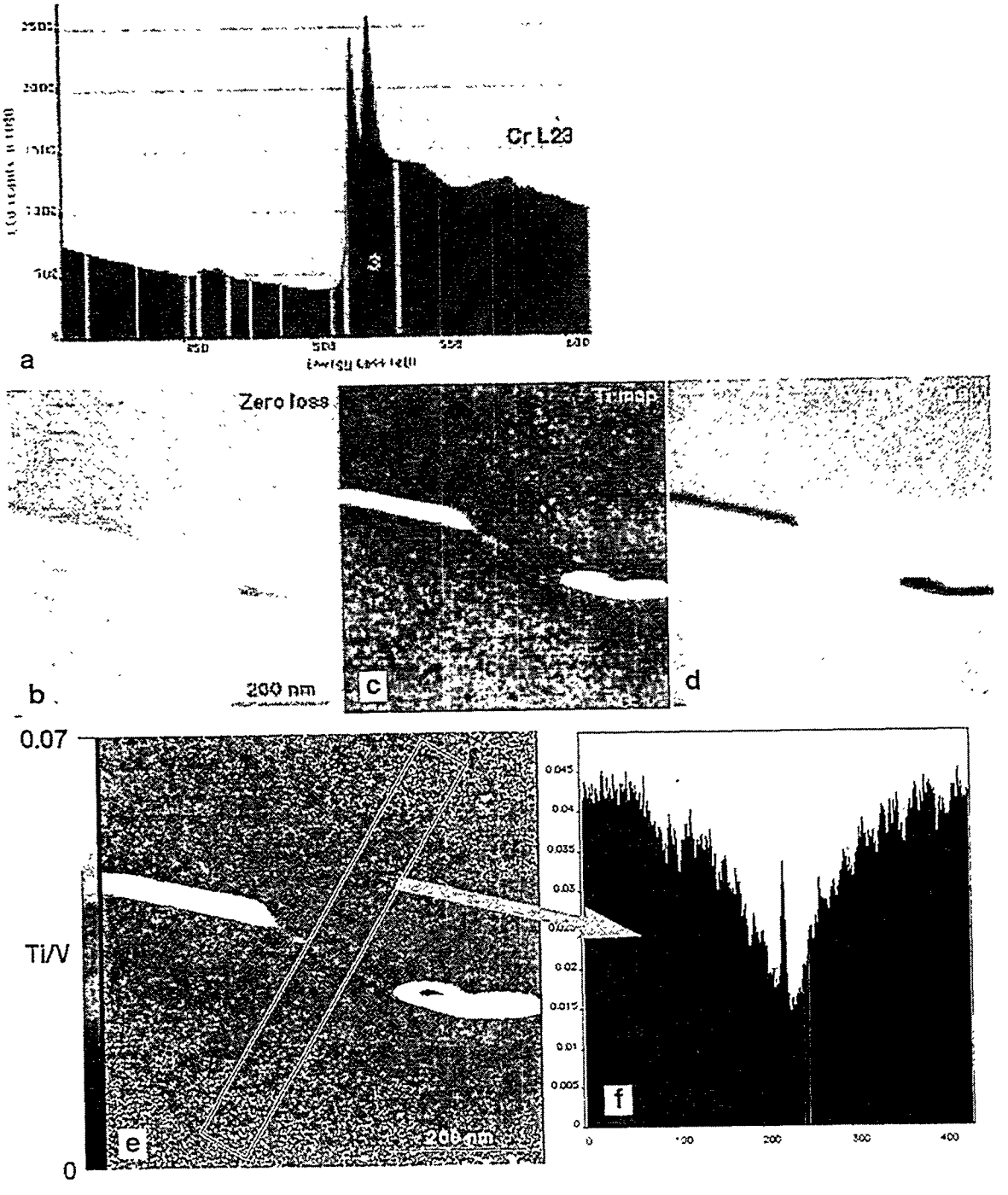

Figure 1. TEM/EELS analysis of V-4Cr-4Ti after the addition of 1434ppmw O at 500°C and annealing for 100h at 600°C. Fine oxide precipitates are observed in the matrix and larger precipitates at the grain boundary (b) which is surrounded by a precipitate denuded zone. A typical EELS spectra is shown in (a). The peak (3) and background (1&2) regions are used to construct EFTEM maps (c,d) of the region showing the particles rich in (c) Ti and denuded in (d) V. Images (c) and (d) were used to create a Ti/V distribution in (e) and analyzing a region across the boundary (box in (e)) showed that the boundary region was depleted in Ti (f).

OXIDATION OF V-4Cr-4Ti ALLOYS CONTAINING Al, Si, and Y*

M. Fujiwara (Tohoku University) and K. Natesan (Argonne National Laboratory)

OBJECTIVE

The objectives of this task are to (a) evaluate the oxygen uptake of several V-4Cr-4Ti alloys with additions of 0.5 wt.% Si, or Al, or Y as a function of temperature and oxygen partial pressure in the exposure environment and compare the uptake with that of the base alloy without alloying additions; (b) examine the microstructural characteristics of oxide scales and oxygen trapped at the grain boundaries in the substrate alloys; and (c) evaluate the influence of alloy composition on oxygen uptake and develop correlation(s) between alloy composition, exposure environment, and temperature.

SUMMARY

A systematic study has been conducted to determine the effects of time and temperature on the oxidation behavior of Si-, Al-, and Y-modified V-4Cr-4Ti alloys. All samples were from 0.80-mm-thick cold-rolled sheets, and each was annealed in vacuum at 1000°C for 1 h prior to high-temperature exposure. Different samples from each alloy were heated in air between 400 and 620°C for times up to a few hundred hours. Weight change data were used to evaluate the kinetics of oxidation process in the modified alloys, and the rate constants were compared with data developed earlier on base alloy.

INTRODUCTION

Refractory alloys based on V-Cr-Ti are being considered for use in first-wall structures in advanced blanket concepts that employ liquid Li as a coolant and breeding material. Further, advanced concepts that use He as a coolant also require structural alloys such as V-Cr-Ti alloys that can withstand the thermal loading at high temperature. Interstitial impurity atoms such as oxygen can affect both irradiation behavior and baseline properties of the alloys. Therefore, oxidation performance of V-4Cr-4Ti alloy with simultaneous additions of Si, Al, and Y has been examined in air at 300-700°C. Alloying additions of 0.1, 0.3, and 0.5 wt.% of each of the three elements have been included in the study [1]. The base and modified alloy specimens of 0.22-mm thickness exhibited negligible weight changes after 1 h oxidation at 300°C. The change in Vickers microhardness number was ≈5. After oxidation at 500°C, the specimens exhibited some increase in weight, and the hardness number increased by ≈60 and was similar for both the base and the modified alloys. After oxidation at 700°C for 1 h, all alloys exhibited significant weight increase, and the modified alloys showed more uptake of oxygen than the base alloy. Furthermore, the results showed that oxygen uptake increased as the concentration of the alloying elements increased from 0.1 to 0.5 wt.%, but the difference was small when compared with the total weight change. The Vickers hardness number

---

*This work has been supported by the U.S. Department of Energy, Office of Fusion Energy Research, under Contract W-31-109-Eng-38.

increased by ≈325 for the base alloy after oxidation and it was reported that the modified alloy surfaces were too rough to allow reliable measurement [1].

The purpose of the present work is to evaluate the oxidation behavior of V-4Cr-4Ti alloys with individual additions of Si or Al or Y over longer time periods and to compare their performance with that of the large heat of V-4Cr-4Ti alloy fabricated by Argonne National Laboratory.

EXPERIMENTAL PROGRAM

The alloys selected for evaluation included V-4Cr-4Ti alloy from Heat #832665 (from ANL) and V-4Cr-4Ti alloys with additions of 0.5 wt.% Si, or Al, or Y (from Tohoku University, Japan). The modified alloys were obtained in ≈0.8-mm-thick sheets. Samples measuring about 0.8 x 10 x 10 mm were cut from each alloy. Before any further treatment or testing, all samples were annealed for 1 h at 1000°C in vacuum at $<10^{-6}$ torr. The samples were wrapped in titanium foil to protect them from contamination during this heat treatment process. Samples from each alloy were heated in a thermogravimetric test apparatus (TGA) in air at different temperatures to determine oxidation kinetics as a function of temperature. The TGA experiments were carried out at 400, 500, and 620°C. Weight gain was recorded continuously on a strip chart throughout each experiment [2,3]. All samples were also weighed separately before and after any high-temperature exposure to determine the resulting total weight change. We plan to measure the hardness variation in the thickness direction in several of the oxidized specimens. Also, metallographic examination of the exposed specimens and X-ray diffraction analysis of the oxide scales on several of the specimens are planned.

RESULTS

Extensive studies were conducted on the oxidation kinetics of V-4Cr-4Ti and V-5Cr-5Ti alloys over a temperature range of 300-650°C; the results were reported earlier [2-4]. The current oxidation study on the modified V-Cr-Ti alloys supplements the data developed earlier on those two alloys. Figure 1 shows normalized weight changes (in mg/mm^2), obtained by TGA, of the modified V-Cr-Ti alloys in air at temperatures of 400-620°C. Data obtained earlier on V-4Cr-4Ti base alloy are also shown in this figure for comparison [3]. The curves show that oxidation follows parabolic kinetics at all temperatures. The data also show that Al and Y additions seem to decrease the oxidation rate of the alloy when compared with that of base alloy. The effect of Si addition on oxidation is negligible at 400°C, probably because Si is present in both the base alloy (≈750 wppm Si) and modified alloy (≈5000 wt.%). However, at 500 and 620°C, the modified alloy showed significant reduction in rate when compared with those of base alloy. The results also showed that additions of any of the three elements improved oxidation resistance in air.

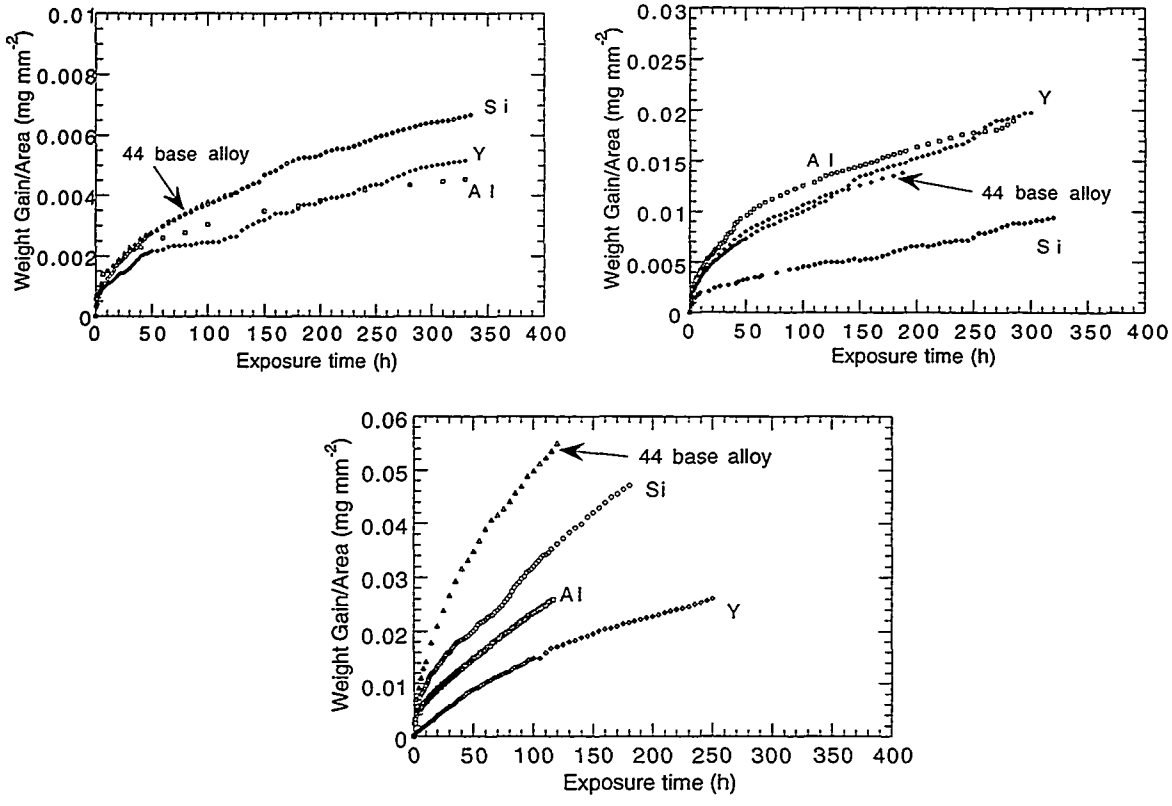

Figure 1. Thermogravimetric weight change data for Si-, Al-, and Y-modified V-Cr-Ti alloys exposed to air at 400 (top left), 500 (top right), and 620°C (bottom).

Figure 2 shows replots of weight change data as a function of square root of exposure time. In general, the data can be fitted by straight lines, indicating a parabolic kinetics. Table 1 lists the parabolic rate constants derived from the present data for the modified alloys along with data reported earlier for the base alloy. Additional oxidation experiments are in progress in low-pO_2 and in high-purity He environments at 500°C, to evaluate the role of reduced pO_2 in the oxidation process.

Table 1. Parabolic rate constants for base and modified alloys derived from air-oxidation data

Alloy	Parabolic rate constant (mg/mm^2) at		
	400°C	500°C	620°C
V-4Cr-4Ti	3.8×10^{-4}	1.1×10^{-3}	5.0×10^{-3}
V-4Cr-4Ti-0.5 Si	3.8×10^{-4}	4.8×10^{-4}	3.2×10^{-3}
V-4Cr-4Ti-0.5 Al	2.8×10^{-4}	1.2×10^{-3}	2.2×10^{-3}
V-4Cr-4Ti-0.5 Y	2.8×10^{-4}	1.1×10^{-3}	1.5×10^{-3}

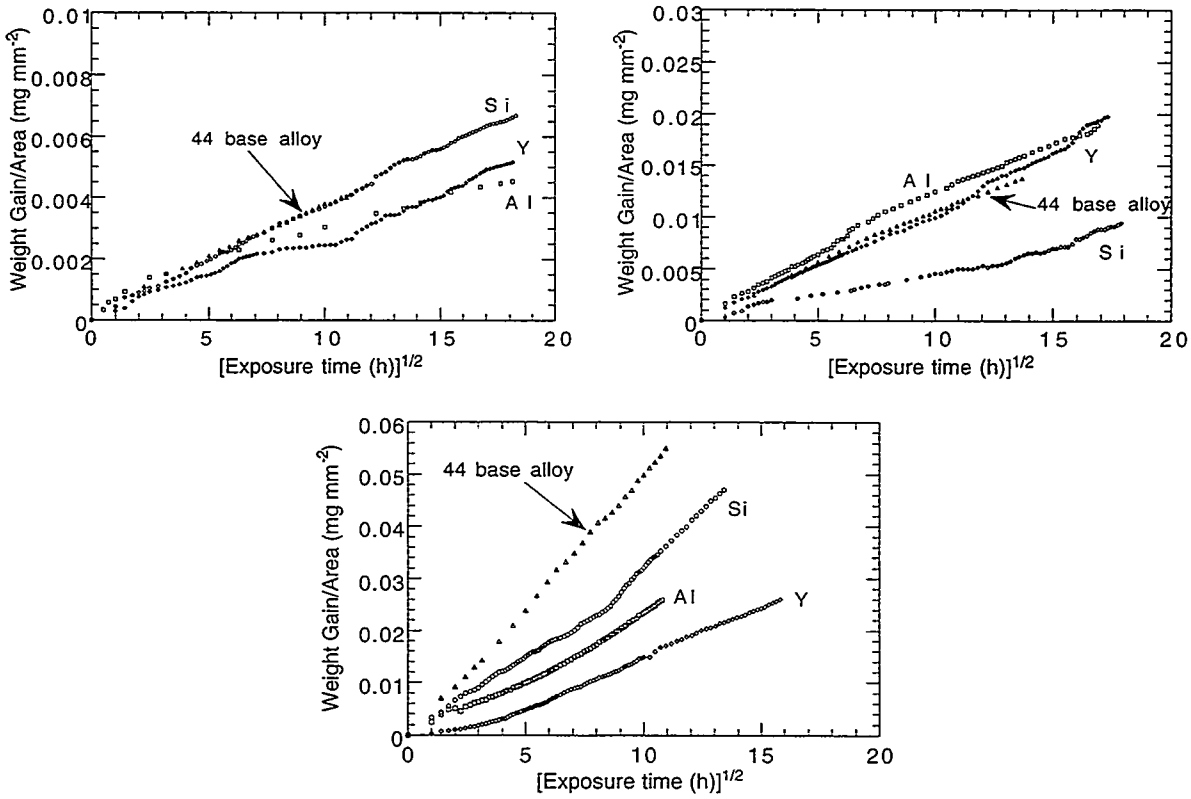

Figure 2. Weight change data plotted against square root of exposure time for Si-, Al-, and Y-modified V-Cr-Ti alloys exposed to air at 400 (top left), 500 (top right), and 620°C (bottom).

REFERENCES

[1] M. Fujiwara, M. Satou, A. Hasegawa, and K. Abe, "Rapid oxidation and its effects on mechanical properties of V-Ti-Cr-Si type alloys," J. Nucl. Mater. 258-263, 1507, 1998.

[2] K. Natesan and W. K. Soppet, "Effect of Oxidation on Tensile Properties of a V-5Cr-5Ti Alloy," Proc. 2nd Intl. Conf. Heat-Resistant Materials, eds. K. Natesan, P. Ganesan, and G. Lai, ASM International, Sept. 11-14, 1995, Gatlinburg, TN, 375.

[3] M. Uz, K. Natesan, and V. B. Hang, "Oxidation Kinetics and Microstructure of V-(4-5) wt.%Cr-(4-5) wt.% Ti Alloys Exposed to Air at 300-650°C," J. Nucl. Mater. 245, 191, 1997.

[4] K. Natesan, W. K. Soppet, and M. Uz, "Effect of oxygen and oxidation on tensile behavior of V-4Cr-4Ti Alloy ," J. Nucl. Mater. 258-263, 1476, 1998.

STUDY OF THE LONG-TERM STABILITY OF MHD COATINGS FOR FUSION REACTOR APPLICATIONS -- B. A. Pint, L.D. Chitwood, J. H. DeVan and J. R. DiStefano (Oak Ridge National Laboratory)

OBJECTIVE

The objective of this task is to assess the long-term, high-temperature compatibility of high electrical resistance coatings with lithium at high temperatures. So-called magnetohydrodynamic (MHD) coatings on the first wall of magnetic confinement reactors are essential to reduce the MHD force that would otherwise inhibit the flow of the lithium coolant. Initial experimental work is being conducted on bulk ceramics to determine maximum-use temperatures of candidate ceramics such as AlN and CaO.

SUMMARY

This project began in June 1999. Initial testing has been performed on AlN+5%Y_2O_3 at 400°-700°C. With increasing temperature, this material was increasingly attacked by lithium in 1000h tests and there was a corresponding increase in the aluminum content of the lithium. These results suggest that the maximum use temperature of AlN in lithium may be 600°C or less. Currently, 1000h experiments are being completed with yttria-free AlN and CaO specimens at 400°, 500° and 700°C.

PROGRESS AND STATUS

Experimental Procedure

A welded capsule system was used to test bulk specimens, Figure 1. Capsules were loaded in glove boxes in a controlled environment. An inner vanadium (V-4Cr-4Ti) capsule was used to better simulate the environment that the ceramic will see in operation. Because vanadium is not oxidation resistant, the vanadium capsule was then placed into a stainless steel capsule prior to exposure. These capsules were then tested in 3 calibrated box furnaces for 1000h. After allowing the lithium to melt, the capsules were inverted to submerge the specimen in lithium. At the end of 1000h, the capsule was again inverted to allow the lithium to drain away from the specimen. After opening, the specimen was cleaned by distilling off any remaining lithium followed by a final cleaning in alcohol. Initial tests were conducted at 400°, 500°, 600° and 700°C on AlN+5%Y_2O_3 with dimensions of 0.6x10x10mm. Because of extensive attack of the AlN, the only characterization that was performed was specimen mass change and measurement of the composition of the lithium by Lockheed Martin Energy Systems (Y12) in Oak Ridge, TN. In future tests, measurements also will be made of electrical resistivity and the microstructure will be examined.

Results and Discussion

Initial testing of AlN with 5%Y_2O_3 showed increasing attack over the range 400°-700°C. Whereas previous work showed a 0.02% mass loss after 100h at 400°C[1], there was a 0.08% mass loss after 1000h at 400°C and a 1.92% mass loss after 1000h at 600°C. After 1000h at 700°C, only tiny fragments of the specimen were recovered. This material had a starting thickness of only

Table I. Lithium composition determined by spectrographic analysis.

Conditions	Nitrogen	Aluminum
Starting Lithium	244 wppm	<10 wppm
After 1000h at 400°C	292 wppm	800 wppm
After 1000h at 600°C	232 wppm	1500 wppm
After 1000h at 700°C	258 wppm	>4000 wppm

0.6mm, subsequent tests used specimens at least 2mm thick in an attempt to prevent the complete loss of the coupon. After testing, the lithium showed an increase in aluminum content with test temperature indicating some dissolution of AlN at all temperatures and a major dissolution at 700°C, Table I. The nitrogen did not significantly increase during the test. This may indicate that the V-4Cr-4Ti capsule walls gettered some of the nitrogen. Nevertheless, the high Al levels in the lithium suggest that some reaction is taking place and that the maximum use temperature of AlN in Li may be 600°C or less.

It is believed that the high (5%) yttria content of the AlN likely contributed to the extent of the attack because of selective attack of the Y_2O_3 by lithium. Previous work showed higher attack of Y_2O_3 than AlN in lithium at 400°C.[1] Because Y_2O_3 is generally a grain-boundary phase in AlN, selected attack may have increased the disintegration of the specimen at 700°C. Pure AlN may perform differently. Therefore, subsequent tests were conducted on yttria-free AlN and high-purity CaO. Exposures of these materials will be complete at the end of January 2000.

REFERENCES

1. R. J. Lauf and J. H. DeVan, J. Electrochem. Soc. 139 (1992) 2087.

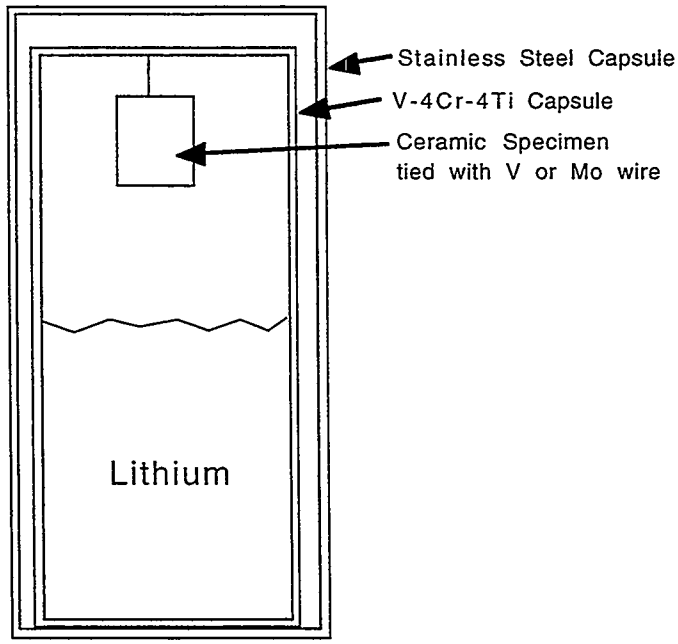

Figure 1. Schematic of the ORNL Li capsule test. After melting the Li, capsule is inverted to submerge the specimen. At the end of the test, the capsule is again inverted to free the specimen from the Li for removal.

ELECTRICAL RESISTIVITY AND MICROHARDNESS MEASUREMENTS OF VANADIUM AND V-4Cr-4Ti ALLOY - D.T. Hoelzer, S.J. Zinkle, and A.F. Rowcliffe (Oak Ridge National Laboratory) and M.K. West (University of Tennessee)

SUMMARY

The purpose of this study was to investigate the interactions between Ti and interstitial solutes over temperature ranges corresponding to thermally activated processes such as precipitation, dislocation recovery and recrystallization, and grain growth. In this study, room temperature electrical resistivity and microhardness measurements were performed on cold-worked (CW) vanadium, CW V-4Cr-4Ti, annealed V-4Cr-4Ti, and the fusion zone of welded V-4Cr-4Ti plate over the isochronal annealing temperature range from 200°C to 1200°C. The results suggested that Ti solutes in the vanadium alloy interacted with interstitial O,C, and N solutes at temperatures of 200°C and higher. Below ~400°C, these interactions influenced processes such as solute diffusivity and dislocation atmosphere formation. Above ~400°C, recovery, recrystallization and precipitation processes had the most significant effect on the property measurements.

INTRODUCTION

Vanadium alloys with compositions near V-4Cr-4Ti are candidate structural materials for first wall/blanket applications in fusion energy reactors because of their attractive low activation characteristics and combinations of good thermal conductivity, strength, and low ductile-to-brittle transition temperature (DBTT) in the unirradiated condition. The current fabrication practices used for producing plate and sheet products from the large heats of V-4Cr-4Ti (500 kg heat #832665 and 1200 kg heat #832864) have typically resulted in cumulative interstitial O, C, and N solute concentrations ranging from 400 to 700 appm. In general, some of the interstitial solutes react with Ti atoms to form globular-shaped Ti-oxycarbonitride (Ti-OCN) precipitates and possibly other phases such as platelet-shaped Ti-oxides and the unreacted interstitial content remains in solution in the bcc vanadium matrix. However, both the precipitates and the interstitial solutes in solution can affect the thermomechanical processing and the mechanical properties of vanadium alloys. For example, the formation of an inhomogeneous distribution of Ti-OCN precipitates during thermomechanical processing was related to formation of banded grain structures in plate products[1] and increases in DBTT[2] and observation of the dynamic strain aging[3] (DSA) phenomena has been attributed to interstitial solutes in solution.

The purpose of this report is mainly to provide the measured microhardness and electrical resistivity data, since a detailed discussion of the results from this study was presented at ICFRM-9, which will be published as a conference proceeding in the Journal of Nuclear Materials.

EXPERIMENTAL PROCEDURE

The microhardness and electrical resistivity measurements were performed on type SS-3 sheet tensile specimens with nominal lengths of 25.4 mm and gage dimensions of 0.76 x 1.52 x 7.6 mm. The specimens were electro-discharge machined from 50% CW unalloyed vanadium plate (heat #820642), 40% CW V-4Cr-4Ti (heat #832665) plate, and fusion zone of a gas tungsten arc welded V-4Cr-4Ti (alloy) plate. Half of the 40% CW V-4Cr-4Ti specimens were annealed at 1000°C for 2 hours in a vacuum of $<\sim 3\times10^{-7}$ torr.

The isochronal annealing experiment was performed with six specimens of the CW vanadium, CW alloy, and annealed alloy and three specimens of the welded alloy. Measurements were performed at room temperature after each isochronal annealing was performed at temperatures ranging from 200°C and 1200°C for 1 hour. The specimens were wrapped in tantalum foil and

the annealings were performed in a vacuum of ~(0.7-1.2)x10^{-6} torr using a constant heating rate of 10°C/min and furnace cooling. A four-point probe technique covered in ASTM Standard Method of Test for Resistivity of Electrical Conductor Materials, ASTM B 193-87 (reapproved 1992) and described by Zinkle et al.[4] was used to make five measurements per specimen, which were averaged and corrected to a reference temperature of 20°C. The typical standard error (SE) of the mean for the five measurements was ±0.5 nΩ-m. The SE of the mean ranged from ±0.3 to ±1.4 nΩ-m for resistivity measurements of specimens within each category. A Vickers pyramidal indenter with a 1 kg load was used to make 2 to 4 indents per specimen near the end tab region of the SS-3 tensile specimens. The CW and annealed alloy specimens consistently showed less scatter in hardness values compared to the CW vanadium and welded alloy specimens. The typical SE of the mean was ±3 DPH for the CW and annealed alloy, ±5 DPH for the CW vanadium, and ±8 DPH for the welded alloy specimens.

RESULTS AND DISCUSSION

Chemical Analysis

The chemical analysis of the interstitial O, C, and N contents on selected specimens before the isochronal annealing and after the final annealing temperature of 1200°C is shown in Table 1. The results obtained for the CW vanadium and welded V-4Cr-4Ti specimens indicated that no substantial uptake of O, C, and N impurities occurred during the isochronal annealing and property testing. The interstitial content measured in these specimens are more representative of the testing conditions since chemical analysis was conducted on SS-3 tensile specimens before and after the testing. This was not the case for the CW V-4Cr-4Ti and annealed V-4Cr-4Ti specimens. The SS-3 tensile specimens of these material showed substantial increases in O, N and C content compared to interstitial contents reported for the ingot (heat #832665). It is possible that much of the contamination occurred during thermomechanical processing of the ingot into plate and then into the SS-3 tensile geometry.

Hardness and Electrical Resistivity Measurements

Figure 1 shows the room temperature hardness and electrical resistivity measurements of the CW vanadium specimens. The significant points shown in this Figure are, the increase in hardness of ~26 DPH and decrease in electrical resistivity over the initial temperature range from 200°C to ~400°C; the decrease in hardness above temperatures of 400°C, minima at ~1000°C,

Table 1. Chemical analysis of specimens used in the property measurement study.

Material	Annealing	Specimen	O (wppm)	N (wppm)	C (wppm)
50% CW Vanadium	Before	SS-3	340	177	198
	After	SS-3	320	222	157
40% CW V-4Cr-4Ti	Before	Ingot*	310	85	80
	After	SS-3	492	109	196
Annealed V-4Cr-4Ti	Before	Ingot*	310	85	80
	After	SS-3	390	102	165
Welded V-4Cr-4Ti	Before	SS-3	457	95	235
	After	SS-3	484	108	225

* Chemical analysis has not been performed on SS-3 tensile specimens of the V-4Cr-4Ti alloy.

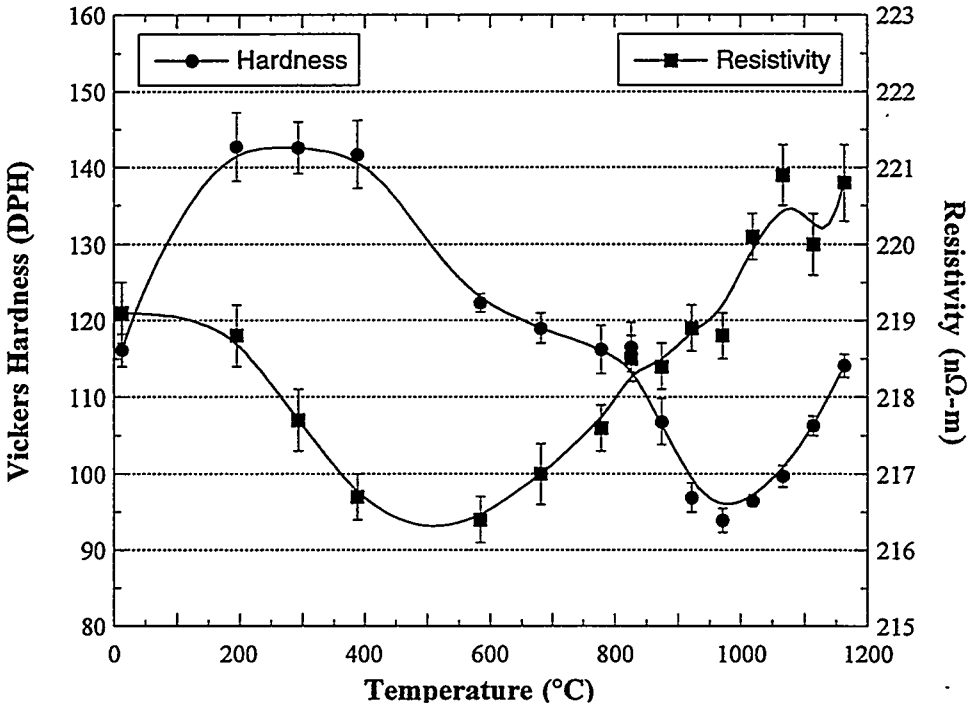

Figure 1. Hardness and electrical resistivity measurements of the 50% cold-worked vanadium specimens over the isochronal annealing temperature range from 200°C to 1200°C.

and subsequent increase in hardness above 1000°C; and the minima in electrical resistivity between ~400°C to 600°C and subsequent increase at higher temperatures.

Figure 2 and 3 show the measured hardness and electrical resistivity for CW V-4Cr-4Ti and annealed V-4Cr-4Ti specimens, respectively. The room temperature measurements indicated that cold-working caused a significant increase in hardness and only a small increase in electrical resisitivity as observed by comparing Figure 2 (CW) to Figure 3 (annealed). For the annealed specimens, the measured hardness was 139.7 DPH and electrical resistivity was 285.1 nΩ-m. Compared to the cold worked specimens, the measured hardness increased by 71 DPH to 210.7 DPH while the resistivity increased by 1.1 nΩ-m to 286.3 nΩ-m.

The most significant result observed for the annealed specimens shown in Figure 3 was the positive change in electrical resistivity compared to room temperature over the entire isochronal annealing temperature range from 200°C to 1200°C. A initial increase in electrical resistivity of ~5 nΩ-m was measured after annealing at 200°C where it then remained positive up to 1200°C. However, no significant change in hardness was observed over this temperature range except for a small peak between 600°C and 900°C. The measured properties for the CW specimens shown in Figure 2 showed considerable departure from those measured for the annealed specimens (Figure 3). Although the electrical resistivity initially increased with annealing temperature, reaching a maximum of 3.6 nΩ-m at 300°C, it then decreased at higher annealing temperatures. The electrical resistivity then reached a minima between 700° to 800°C and subsequently increased up to 1200°C. The hardness showed no appreciable change from the room temperature value until a small peak occurred near 700°C followed by a steady decrease above 700°C. A minimum in hardness was measured near 1050°C to 1100°C which was followed by a small increase at the highest temperatures.

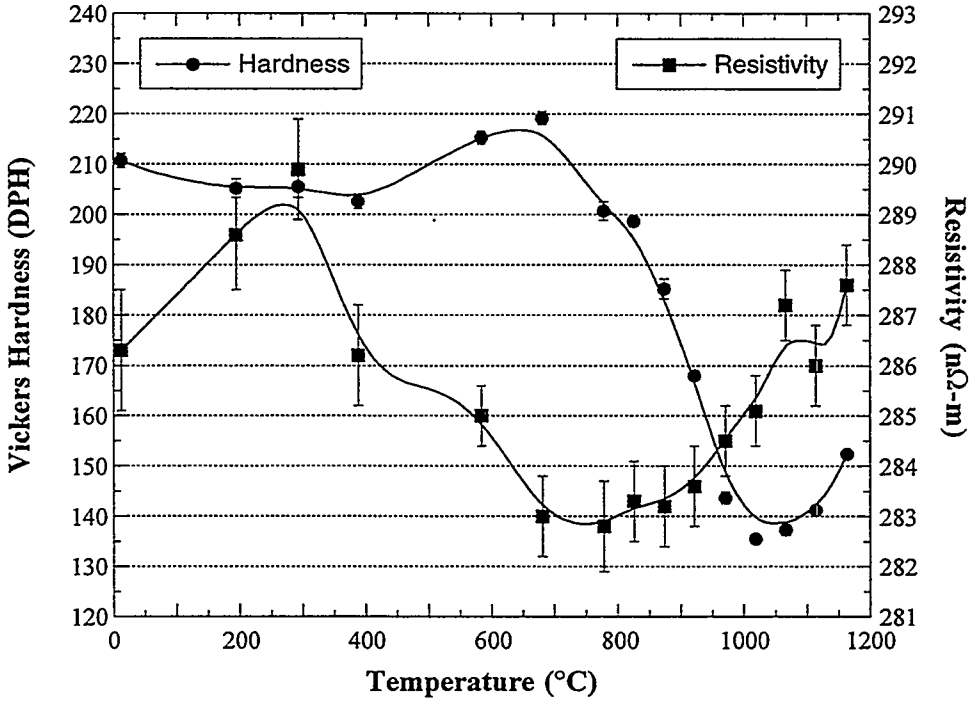

Figure 2. Hardness and electrical resistivity measurements of the 40% cold-worked V-4Cr-4Ti specimen over the isochronal annealing temperature range from 200°C to 1200°C.

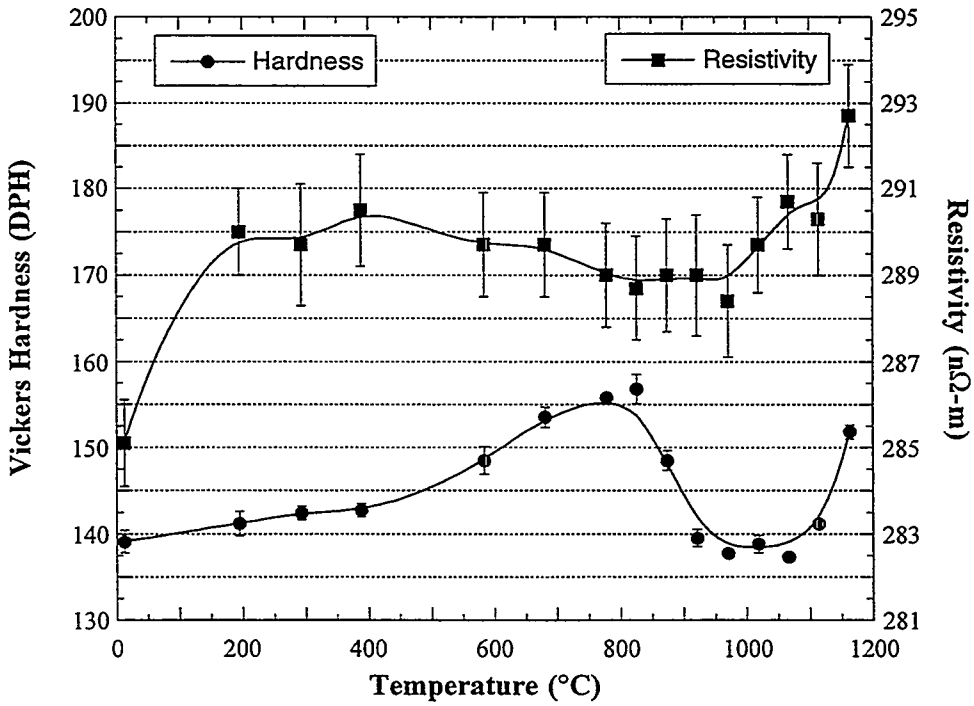

Figure 3. Hardness and electrical resistivity measurements of the annealed V-4Cr-4Ti specimen over the isochronal annealing temperature range from 200°C to 1200°C.

The temperature dependence of hardness and resistivity measured for the GTA weld specimens is shown in Figure 4. The measurements at room temperature showed that the hardness was 213.4 DPH and resistivity was 294.2 nΩ-m. The results showed that isochronal annealing caused the formation of a minor and major hardness peak near 200°C and 700°C, respectively, a minimum in hardness near 1100°C, and a continuous decease in resistivity from the room temperature value to a minimum of ~283.5 nΩ-m that remained nearly constant from 800°C to 1200°C.

The results showing the exostence of the hardness maxima from ~700°C to 800°c in the CW alloy (Figure 2) and weld alloy (Figure 4) specimens was attributed to a precipitation reaction. This precipitation reaction is believed to be associated with formation of Ti-oxide phase. In general, the electrical resistivity decreases over this temperature range and is consistent with the idea that interstitial solutes are being removed from the matrix by the precipitation reaction. However, recrystallization is occurring at temperatures above 700°C. This process also causes a decrease in the electrical resistivity since the dislocation density rapidly decreases during this process. Further work is in progress in order to clarify whether precipitation is occurring along with recrystallization in this temperature range.

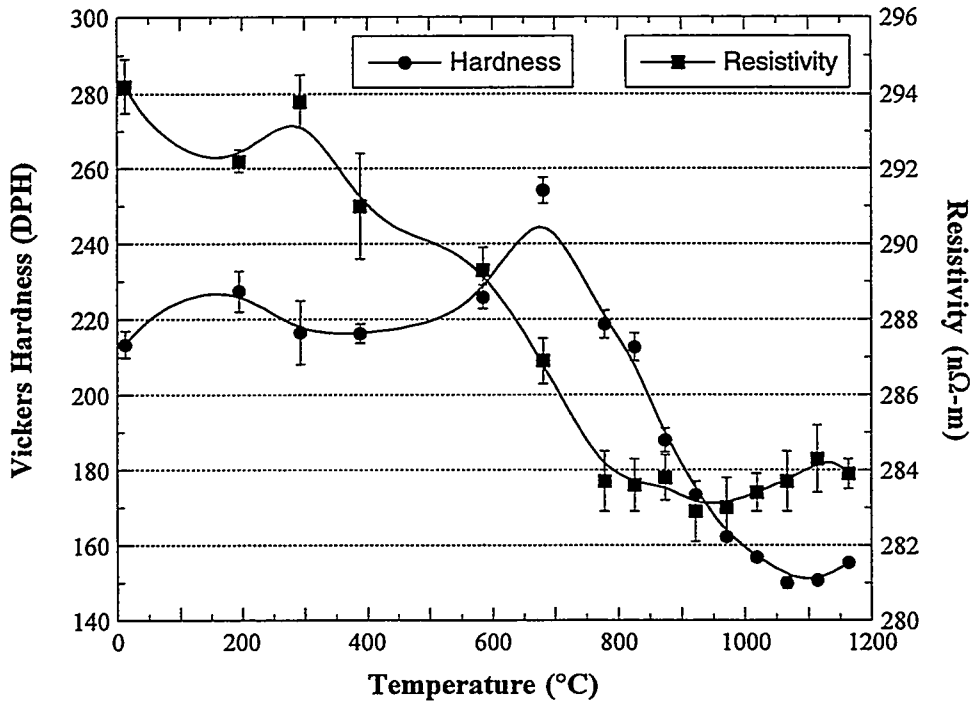

Figure 4. Hardness and electrical resistivity measurements of the welded V-4Cr-4Ti specimen over the isochronal annealing temperature range from 200°C to 1200°C.

REFERENCES

1. A.F. Rowcliffe and D.T. Hoelzer, in Fusion Materials Semiannual Progress Report for Period Ending December 31, 1998, DOE/ER-0313/25, (1999), 42.
2. R.J. Kurtz. M.L. Hamilton and H. Li, in Fusion Materials Semiannual Progress Report for Period Ending December 31, 1997, DOE/ER-0313/23, (1998), 111.
3. A.F. Rowcliffe, D.T. Hoelzer, and S.J. Zinkle, in Fusion Materials Semiannual Progress Report for Period Ending June 30, 1999, DOE/ER-0313/26, (1999), 25.
4. S.J. Zinkle, A.N. Gubbi and W.S. Eatherly, in Fusion Materials Semiannual Progress Report for Period Ending December 31, 1996, DOE/ER-0313/21, (1997), 15.

RESISTANCE WELDING OF V-4Cr-4Ti ALLOY*

Z. Xu, D. L. Smith, and C. B. Reed (Argonne National Laboratory)

OBJECTIVE

The goal of this task is to further investigate the potential of resistance welding for joining of vanadium-base alloys and to develop a better understanding of the effects of the machine parameters on the weld characteristics.

SUMMARY

More resistance weld samples were prepared on 3.8-mm thick V-4Cr-4Ti alloy plate on a 50 KVA welder with more optimal process parameters. The microstructure of the weld regions were characterized and correlated with the weld parameters. Simplified torque tests were conducted on the test samples to provide a preliminary assessment of the shear strength and ductility of the test welds. Fractography results for the torque samples indicated that the fracture surfaces of resistance welds exhibit ductile characteristics.

BACKGROUD

Continuous resistance welding potentially offers several advantages for fabrication of vanadium alloy for first wall/blanket systems. Current blanket designs for vanadium/lithium systems provide for joining of ~4 mm thick sheet with long weld joints. Previous investigations on resistance welding of vanadium-based alloy [1] indicated that sound welds with minimal restructuring and limited extent of heat-affected zone could be achieved for a range of process parameters. This approach may also reduce the stringent environmental control required to avoid excessive oxygen contamination effects frequently observed in more conventional weld processes.

EXPERIMENTAL PROGRAM

Weld specimens were prepared from 3.8-mm thick V-4Cr-4Ti alloy (heat #832665) in the annealed condition. Specimens were surface polished with a Scotch Brite pad and cleaned with acetone before joining. Lap-type resistance welds on these sheet specimens were produced on a 50 KVA welder at ANL. The process parameters, such as transformer tap settings, preweld squeeze time, weld time, power setting, and post-weld hold time were chosen based on previous experience [1]. All the specimens were made with a pair of weld tips of 5/8" in diameter.

Resistance weld specimens were metallurgically prepared and etched to reveal the microstructural features of the welds. The fractography of torque-broken specimens were obtained. A Nikon MSZ-B stereomicroscope, a Nikon optical microscope and a COHU high performance CCD camera were used for the microstructural evaluation.

---

* This work has been supported by the U.S. Department of Energy, Office of Fusion Energy Research, under Contract W-31-109-Eng-38.

A simplified torque test was used to provide a preliminary evaluation of the weld strength and ductility characteristics. A deflecting beam torque wrench (0 – 150 ft-lbs. torque range) was used to shear the weld joints. The maximum torque as a function of twist angle to fracture was recorded and an estimation of the shear strength was calculated based on the fracture surface area.

RESULTS AND DISCUSSION

The process parameters used to prepare the resistance weld specimens for the microstructural evaluation and torque test are presented in Table 1. Compared to the previous investigations [1], the transformer tap fine setting of the welder was decreased from 7 to 5, which decreased the output power level of the machine. The cross-sectional microstructure of the welds are shown in Figure 1, 2, and 3 for test no. 991203-3, -6, and –7, respectively. The weld zone and heat-affected zone varies considerably for the range of weld parameters shown in Fig. 1 – 3. The maximum torque and twist angles from the torque test for specimens 991203-6 and –9 are listed in Table 2. The large amount of distortion before fracture indicated substantial ductility weld joints. Photographs of the corresponding shear fracture surfaces are shown in Fig. 4 and 5. The fractography results for test no. 991203-6 and –7 show a ductile fracture feature, which is further verified by the large recorded twist angle. A weld specimen with test no. 991203-3 was separated using a wedge. The fractured surface of this weld (Figure 6) indicated some ductile fracture character. An attempt to estimate the shear stress in the welds based on the weld area and the torque values indicated considerably higher than expected values. Calculated results for similar test welds on steel gave reasonable values, although slightly higher than reported shear strength for the base metal. The higher than expected shear strength for the vanadium welds are attributed to some random bonding effects observed outside the primary weld region. Surface roughness created by these effects contribute to the higher torque; however, they should not affect the deformation character of the joint. Additional resistance welds will be prepared with attempts to avoid the observed random bonding effects noted above. Based on results from these types of tests, weld parameters that produce the best weld performance will be used to prepare additional weld specimens for more conventional mechanical tests including Charpy impact tests. Chemical analyses are also being performed on the weld material to determine the extent of any contamination. Those results will be presented in the next report.

Table 1. Resistance welding parameters of V-4Cr-4Ti alloy

Test No.	Transformer tap fine setting	Squeeze (Cycles)	Weld time (Cycles)	Heat (%)	Hold time (cycles)
991203-3	5	30	50	80	30
991203-6	5	30	70	80	30
991203-7	5	30	50	90	30

Table 2. Maximum torque and twist angle to fracture of welds

Test No.	Max. Torque, N-m, (ft-lbs)	Twist angle (degree)	Diameter of fractured and bonded area (mm)
991203-6	67.8, (50)	175	6.5
991203-7	80, (59)	95	6.17
991203-3	Weld join separated by a wedge		

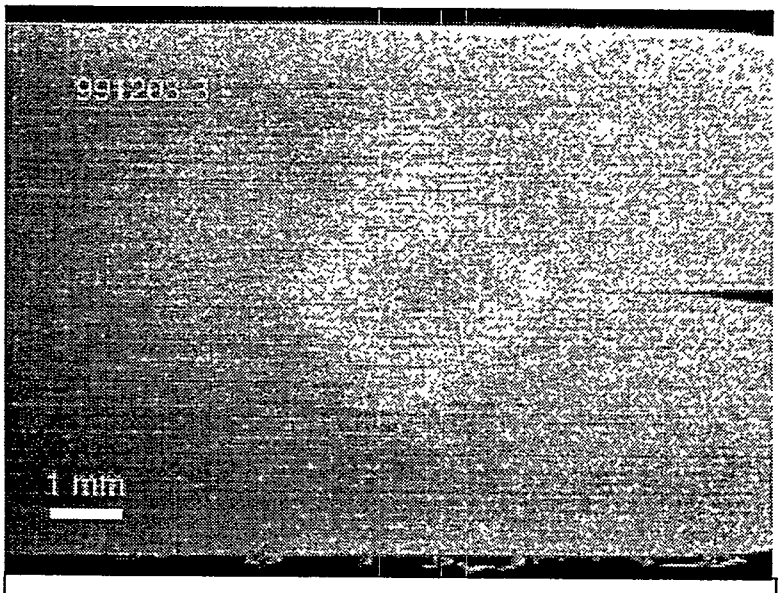

Figure 1 Cross sectional view of resistance weld of V-4Cr-4Ti alloy (Test No. 991203-3 in Table 1) showing minimal structure change of the bond

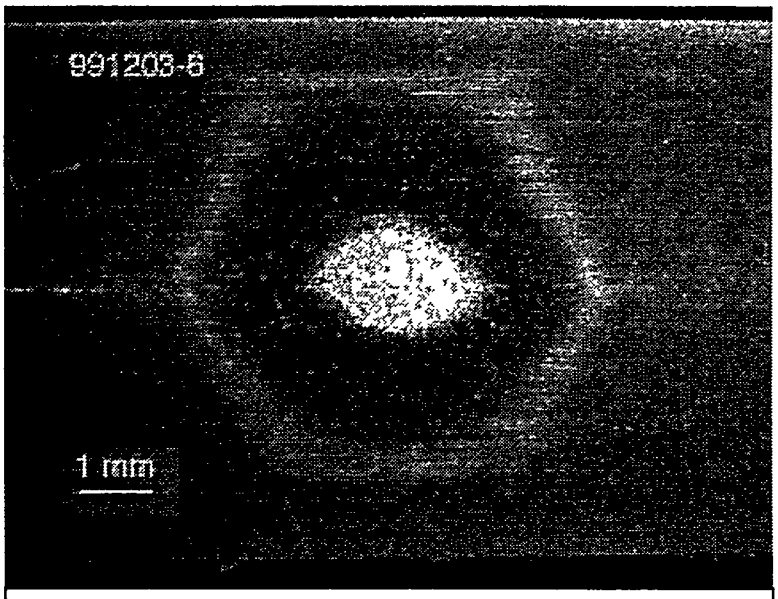

Figure 2. Cross sectional view of resistance weld of V-4Cr-4Ti alloy (Test No. 6 in Table 1) indicating small restructuring zone (white area)

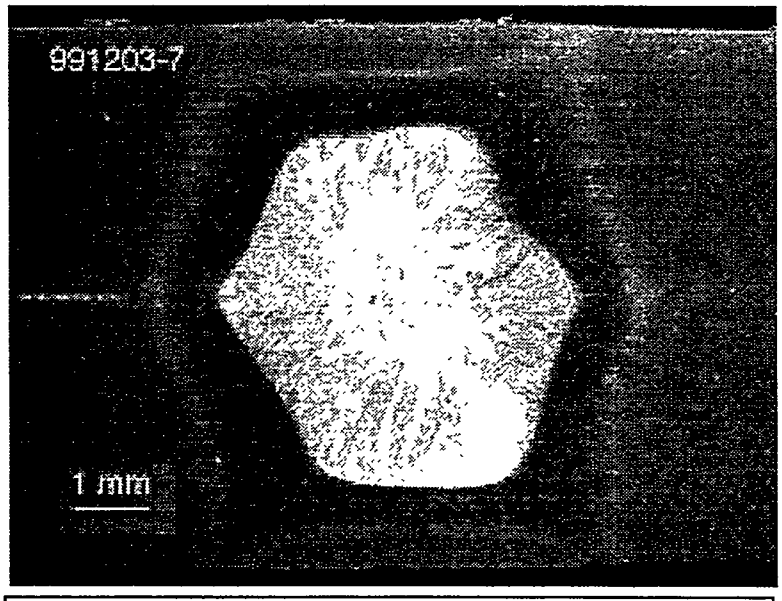

Figure 3. Cross section view of resistance weld of V-4Cr-4Ti alloy (Test No. 991203-7 in Table 1) showing extensive restructuring zone (white area)

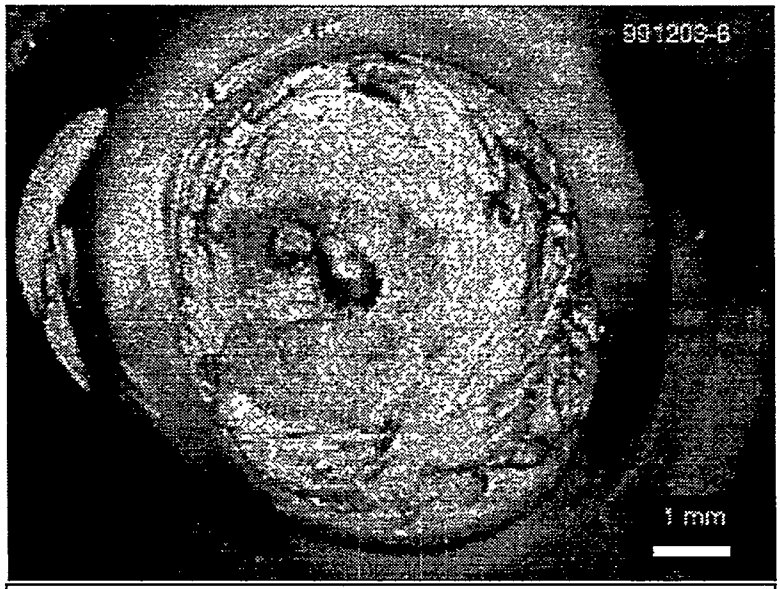

Figure 4. Fractography of torque tested weld (test No. 991203-6) revealing a ductile fracture surface and total bonded area.

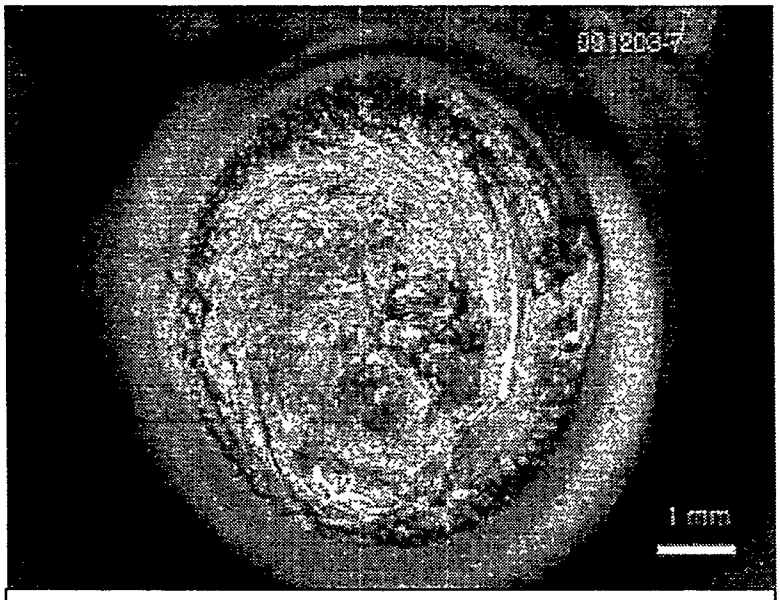

Figure 5. Fractography of torque tested weld (Test No. 991203-7)

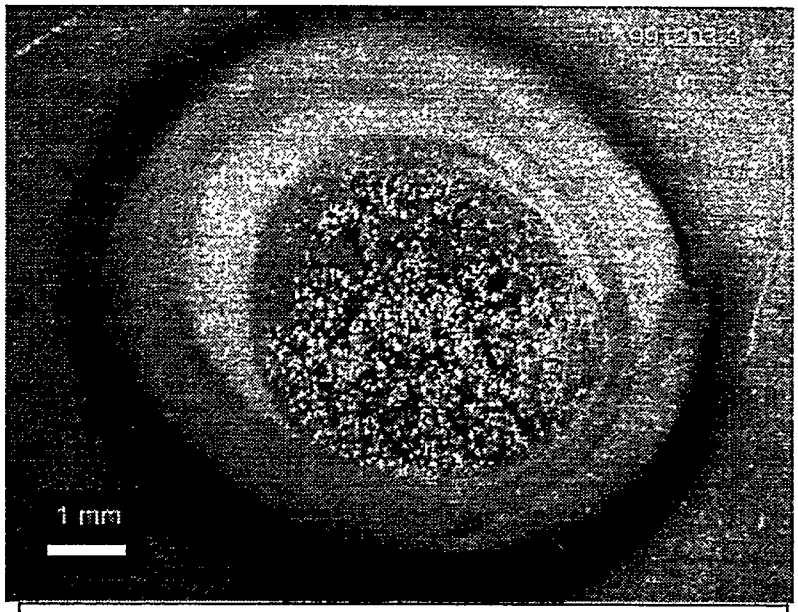

Figure 6. Fractography of the weld (Test No. 991203-3), separated by using a wedge.

REFERENCE

1. Z. Xu, D. L. Smith, and C. B. Reed, "Diffusion Bonding of Vanadium Alloys", Fusion Reactor Materials Progress Report for the Period Ending June 30, 1999, DOE/ER-0313/24.

HYDROGEN SOLUBILITY IN VANADIUM ALLOYS, LiCa ALLOYS, AND SnLi ALLOYS*

D.L. Smith (Argonne National Laboratory), R.E. Buxbaum (REB Research), and C.B. Reed (Argonne National Laboratory)

OBJECTIVE

The objective of this program is to provide baseline solubility data for hydrogen in selected vanadium-base alloys, LiCa alloys and SnLi alloys which will provide a basis for determining the equilibrium distribution and hydrogen/tritium inventories in candidate structure/breeder materials systems.

SUMMARY

A systematic study is currently being conducted by Argonne National Laboratory with support from REB Research to provide baseline data on the solubility of hydrogen in selected LiCa, SnLi, and VCrTi alloys. The experimental approach involves charging and degassing of vanadium alloys and vanadium alloy encapsulated LiCa and SnLi specimens to various hydrogen partial pressures while maintaining the system at constant temperature. With this procedure one avoids the problems associated with the rapid redistribution of hydrogen that is typically observed during cool-down of the specimens. Initial tests have been conducted on solid cylindrical specimens of a vanadium alloy. The liquid metal alloys will be contained in vanadium alloy capsules. Preliminary results for the V-4Cr-4Ti alloy (Heat #832665) are reported.

INTRODUCTION

The self-cooled lithium system with a vanadium alloy structure offers a potential for a high performance, environmentally attractive first-wall/blanket system for fusion applications. One of the key issues associated with this system relates to the development of an electrically insulating coating on the vanadium alloy channel walls to mitigate the magnetohydrodynamic (MHD) – induced pressure drop in the recirculating lithium coolant. Calcium oxide-based coatings are a leading candidate for this insulator application. Since tritium production in the lithium is essential for the fuel cycle, hydrogen transmutations will occur in the vanadium alloy structure, and hydrogen isotopes are highly mobile in most materials at elevated temperatures; tritium/hydrogen interactions are an important safety related issue and effects of hydrogen isotopes on the stability of the coating and integrity of the structure are important performance considerations for the V/Li system.

---

* This work has been supported by the U.S. Department of Energy, Office of Fusion Energy Sciences, under Contract W-31-109-Eng-38.

The Sn-Li alloy has recently been proposed as a possible liquid metal coolant for fusion applications, primarily because of low vapor pressure considerations. An important consideration regarding the potential of this system involves hydrogen/tritium solubility.

A procedure previously used at both ANL and REB Research to accurately determine the hydrogen solubility in metals and alloys involves quantitatively charging and degassing of specimens to various hydrogen partial pressures while maintaining the system at constant temperature. This procedure avoids the difficulties of obtaining accurate data caused by rapid redistribution of the hydrogen during cooling.

This task involves the accurate determination of hydrogen as a function of temperature and pressure in selected vanadium alloys, LiCa alloys and a SnLi alloy. Results for the vanadium alloys are important for evaluating the performance of these alloys in a fusion system, as baseline data for the distribution of hydrogen/tritium in the DHCE experiment to evaluate He effects in neutron irradiation tests, and to provide an accurate blank for the vanadium alloy capsules used for the hydrogen solubility tests for LiCa and SnLi. The effects of Ca in Li on the solubility of hydrogen/tritium are important to evaluate tritium inventory, tritium recovery, and the stability of the CaO coatings in lithium cooled systems. The measurements of hydrogen solubility in SnLi will provide baseline data for further evaluation of this alloy system for fusion applications.

EXPERIMENTAL PROCEDURE

Test specimens are exposed at constant temperature to flowing helium gas containing varying concentrations of hydrogen. Initially the specimens are exposed to pure helium (no hydrogen) to purge the system and degas any hydrogen in the test specimen. The gas exiting the test section is analyzed with a gas chromatograph. Purging of the system is continued until impurities in the helium are reduced to negligible levels.

In the current series of tests cylindrical specimens (~4.75 mm dia x 100 mm long) are used. The test specimens are contained in a cylindrical chamber so that the gas flows axially in an annular region surrounding the test specimen. The test specimens are pre coated with a thin (~1 micron) coating of palladium to facilitate absorption and desorption of hydrogen and to avoid possible surface oxidation of the vanadium during the initial purging of the system. The vanadium alloy specimens are solid cylinders to maximize the volume and the liquid metals (LiCa and SnLi) are contained in thin-walled vanadium alloy capsules of approximately the same geometry.

After the test specimens are completely degassed in the pure helium, a specified H/He mixture is introduced and the concentration of hydrogen exiting the test section is continuously measured. Flow conditions are controlled such that initially most of the hydrogen entering the test section is absorbed by the test specimen. As the test specimen becomes saturated at the set hydrogen pressure, the hydrogen concentration exiting the text section increases until no further absorption

of hydrogen by the test specimen occurs. The total concentration in the test specimen is determined by the difference. This value is then checked by quantitatively degassing the hydrogen from the specimen in pure helium. The reversibility of this process assures an accurate measurement. Subsequent charging/degassing runs on the same specimen can be used to further verify the results. The hydrogen solubility in the test specimens is determined directly from the weight of the specimen. For the cases of the liquid metals, the total hydrogen absorption is corrected by adjusting for the hydrogen concentration in the vanadium alloy capsule.

RESULTS

Preliminary results have been obtained on the solid vanadium alloy (V-4Cr-4Ti). Figure 1 shows a desorption curve for this specimen after equilibration at 360°C in He containing ~400 ppm H. In this particular case the test was prematurely terminated with a small concentration of hydrogen remaining in the specimen as indicated by discontinuity at an elapsed flow of ~130,000 cm^3·s.

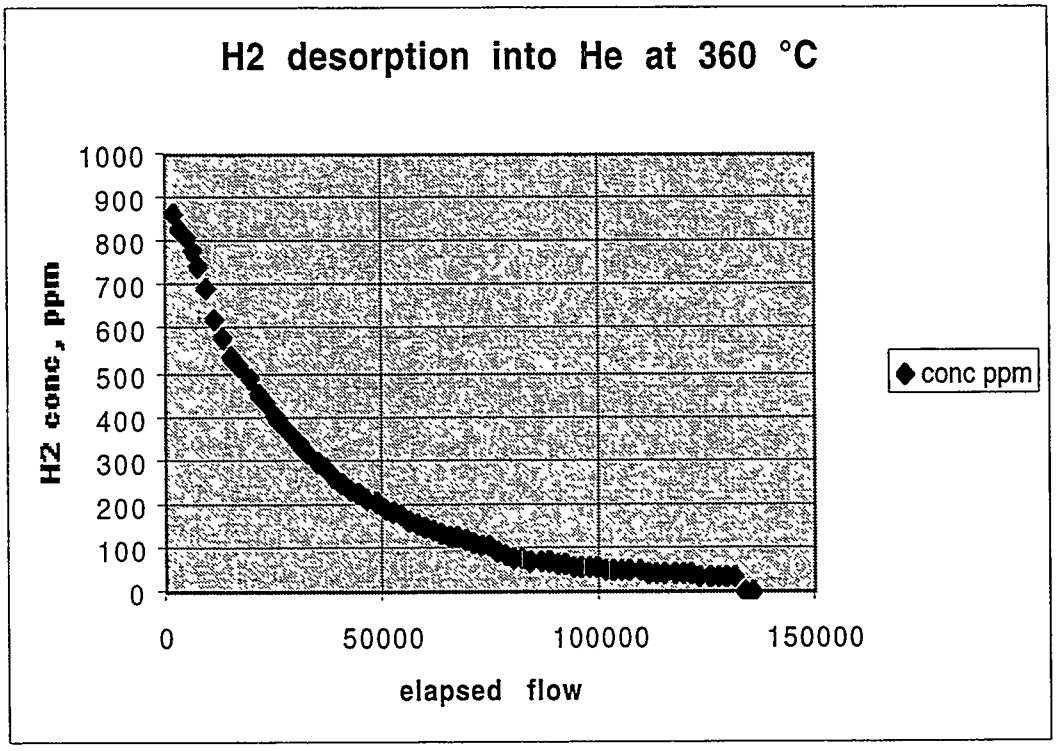

Figure 1. Desorption curve for V-4Cr-4Ti alloys at 360°C.

FUTURE DIRECTIONS

Additional runs will be made on the V-4Cr-4Ti alloy at selected temperatures and pressures. Tests on the LiCa and SnLi specimens will then be tested.

STUDY OF IRRADIATION CREEP OF VANADIUM ALLOYS,[1] H. Tsai, R. V. Strain, M. C. Billone, T. S. Bray, and D. L. Smith (Argonne National Laboratory), M. L. Grossbeck (Oak Ridge National Laboratory), K. Fukumoto and H. Matsui (Tohuku University, Japan)

SUMMARY

Pressurized-tube specimens made from V-4 wt.% Cr-4 wt.% Ti (832665 heat) thin-wall tubing were irradiated in the HFIR RB-12J experiment to study creep under neutron-damage conditions. The calculated dose for the specimens ranged from 5.5 to 6.0 dpa and the calculated irradiation temperatures ranged from 400 to 500°C. The results show the creep rate to be linearly dependent on stress. The 12J data, when combined with the previous ATR-A1 data set, indicate the creep rates could be significant even at moderate stress and dpa levels.

OBJECTIVE

Vanadium alloys are candidate structural materials for fusion first-wall/blanket because of their attractive high-temperature properties and low activation. Many of the properties have been extensively studied; however, irradiation-induced creep has not. Data on irradiation creep is important because creep may be one of the principal contributors to deformation and is potentially performance limiting. The objective of this task is to determine the creep rate at 500°C under a range of stres loading conditions.

CREEP SPECIMEN FABRICATION

The creep specimens used in the RB-12J experiment are pressurized tubes, 25.4 mm long x 4.57 mm OD x 0.25 mm wall, with welded end plugs, as shown in Fig. 1. The tubing[1] was fabricated by drawing of an extruded bar stock. Each 25.4-mm-long tube section was nondestructively examined with radiography and profiled with a coordinate measurement machine to determine the wall thickness, ID and OD roundness and concentricity. The circumferential plug-to-tube welds were made with an electron-beam welder in vacuum. The specimens were then vacuum annealed at 1000°C for 1.0 h while wrapped in Ti getter foils. The tubes were then pressurized through a 0.25 mm-dia. hole in the top end plug with high-purity helium in a pressure chamber. The final closure weld of the 0.25 mm-dia. hole was made with a laser through the quartz window in the chamber. Six specimens, with at-temperature hoop stresses ranging from 0 to 200 Mpa, were prepared for irradiation in the RB-12J experiment. The dimensions of the creep specimens were measured with a precision laser profilometer before and after the pressurization. The measurements were made at 5 axial (x/L=0.1, 0.3, 0.5, 0.7 and 0.9) and 19 azimuthal locations (9° apart). The accuracy of the measurements were 10^{-4} mm, or ≈0.01% strain.

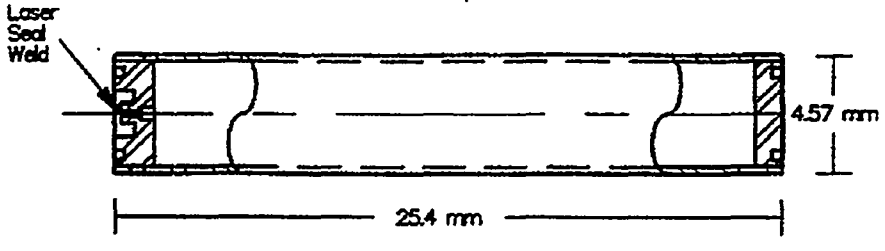

Figure 1. Schematic of the Creep Specimens

[1] This work has been supported by the U.S. Department of Energy, Office of Fusion Energy Research, under Contract W-31-109-Eng-38.

IRRADIATION SUMMARY

To mitigate gaseous impurity uptake, the six creep specimens were loaded in two sealed thin-wall Zircaloy capsules, which acted as an impurity getter. The inside dimensions of the Zircaloy tubing were 81.3 mm long x 5.05 mm ID and the wall thickness was 0.10 mm. A pinhole was provided in the capsule end plug prevent pressure build-up in case of an unexpected specimen failure.

The irradiation of RB-12J was completed in ten HFIR cycles, from Cycle 352 (February 7, 1997) through Cycle 361 (January 17, 1998). The irradiation location was RB-5B.

The calculated temperature and neutron damage[2] for the six samples are shown in Table 1. The temperature shows a range instead of being constant because of the following reasons:

- changes in HFIR power levels during operation,
- 180° capsule rotation at the end of each cycle,
- movement of the HFIR control plates,
- uncertainties in the relationship between specimen temperatures and thermocouple temperatures, and
- variations in individual thermocouples over the course of the 10 cycles.

In Cycle 353, an attempt to recover from a computer failure led to three separate high-temperature excursions. The total duration was about 4 minutes. The peak temperatures during these times were estimated to be ≈40°C above those shown in Table 1.[2]

Table 1 Creep Specimens for the HFIR-12J Experiment

Specimen No.	Calculated Temp.(°C)	Calculated Dpa
B1 (0 MPa)	496±22	5.96
B12 (50 MPa)	399±21	5.96
B11 (100 Mpa)	496±22	5.75
B3 (150 MPa)	476±22	5.45
B9 (150 MPa)	496±22	5.75
B5 (200 MPa)	476±22	5.45

MEASUREMENT RESULTS AND DATA EVALUATION

The diameters of the specimens were measured after the irradiation with the same laser profilometer for the pretest measurements. The 19 azimuthal readings were averaged to yield the mean diameter for each axial location. To exclude end effects from the welded end plugs, only the middle three diameters were used to determine the average diameter and effective creep strain.

To facilitate a general stress analysis, the specimen's internal pressure loading and the measured diametral strain were converted to the wall-averaged effective von Mises stress and effective strain according to the following formulas:

$$\sigma_e = (0.5)(3)^{0.5}(r_m/t)\Delta P, \text{ and}$$

$$\varepsilon_e^C = 2\,(3)^{-0.5}(r_o/r_i)(\varepsilon_{dia}^C)\,,$$

where σ_e is the effective stress; r_i, r_m, r_o are the internal, midwall and external radii, respectively; ΔP is the difference in internal and external gas pressure at temperature; ε_e^C is the effective creep strain; and $\varepsilon_{dia}^C = (\varepsilon_{dia}^C - \varepsilon_e^{stress\text{-}free})$ is the component of the measured OD hoop strain associated with creep. To obtain the creep coefficient (A), the assumed form of the irradiation creep law is

$$\varepsilon_e^C = A\,\sigma_e D,$$

where D is the neutron damage in dpa. Using this method, the effective creep strains and creep coefficients are determined and the results are summarized in Table 2.

Ovality in specimens after the irradiation was generally small, indicating uniform stress loading in the tube wall. The transverse cross-sectional profile of the highest-stress specimen B5 after the irradiation is illustrated in Fig. 2.

Table 2. Summary data for the six creep specimens irradiated in the HFIR 12J experiment

Spc. ID	ID (in.)	OD (in.)	Irr T. (°C)	ΔP at temp (MPa)	von Mises Stress (MPa)	Preirr. D_o	Postirr. D_o	Avg. $\Delta D/D$ (%)	Creep Strain (%)	dpa	Strain Rate (%/dpa)
B1	.1591	.1800	496	-0.06	-0.45	.18000	.18011	0.0585	0.0000	6.0	0.00
B12	.1591	.1800	399	5.46	38.33	.17979	.18019	0.2238	0.2160	6.0	0.04
B11	.1590	.1800	496	12.77	89.26	.17982	.18073	0.5044	0.5830	5.8	0.10
B3	.1591	.1800	476	18.62	130.83	.18001	.18111	0.6061	0.7154	5.5	0.13
B9	.1590	.1800	496	19.18	134.05	.17988	.18144	0.8603	1.0483	5.8	0.18
B5	.1591	.1800	476	24.93	175.16	.17996	.18183	1.0293	1.2684	5.5	0.23

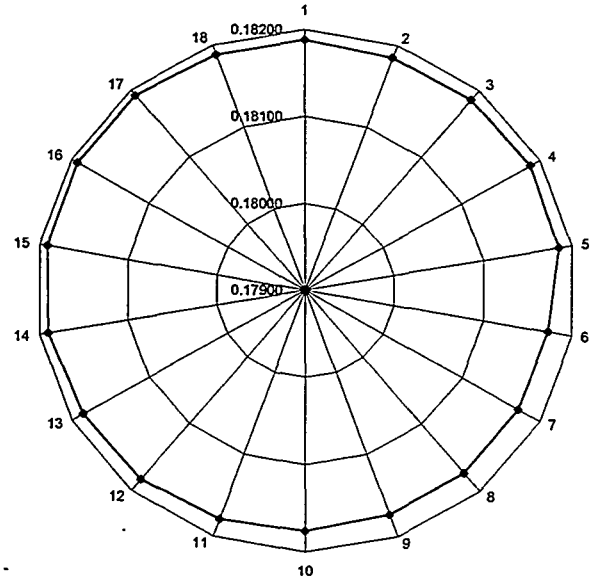

Fig. 2 Cross-sectional profile of Specimen B5 after the irradiation showing little ovality. The diameter was 0.1800 in. prior to the irradiation.

DISCUSSION

Available irradiation creep data for V-base alloys are scarce. For the recent- vintage V-Cr-Ti alloys, data are limited to those from this study, the ATR-A1 experiment in ATR, and an experiment performed by Troyanov et al. In BR-10. The ATR-A1 experiment utilized pressurized tubes (as in the 12J), whereas the BR-10 experiment utilized a single torsional tube [3]. The results from these three studies thus form a preliminary data set for evaluating the irradiation creep of V-4Cr-4Ti alloy. This data set is shown in Fig. 3.

Within the scatter of data, the results from this study, in conjuntion with those from the ATR-A1 experiment, show a trend of increasing strain rate with stress. Part of the data scatter is due to the relatively low attained neutron damage, low measured strains, and limited number of test specimens. This limited HFIR/ATR data set indicates possibly significant creep rates even at modest stresses and dpa levels. Within the data resolution, the HFIR/ATR data set appears not to show the bilinear behavior – sharply increased strain rate at stress >≈120 Mpa – that were observed in the BR-10 torsional experiment. Reducing the data uncertainty, including determining whether a bilinear behavior exists for the vanadium-base alloy, would be an important objective for the future irradiation creep experiments.

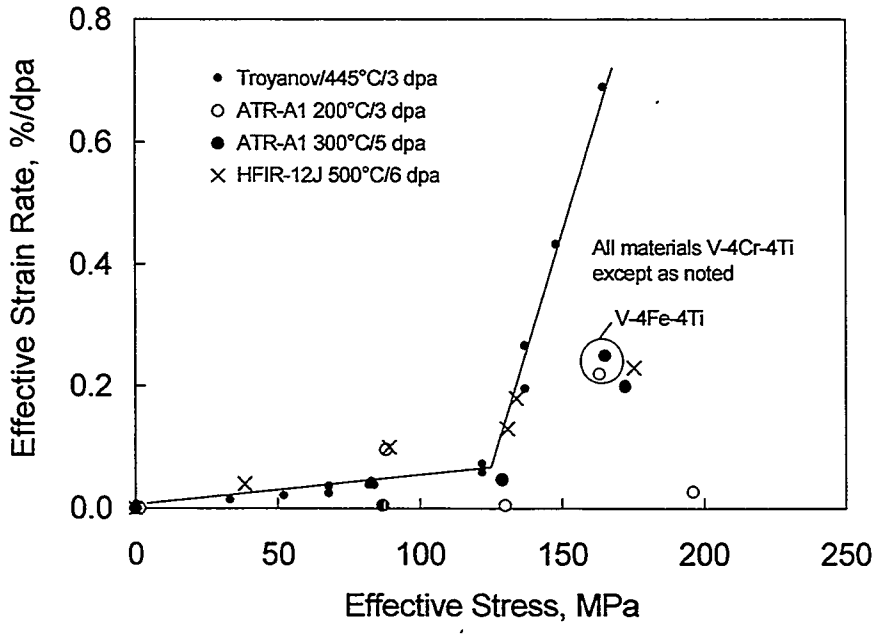

Fig. 2 Summary creep data set from the BR-10, ATR and HFIR experiments.

CONCLUSIONS

A set of six pressurized-tube creep specimens was irradiated in the HFIR-12J experiment. The results show a consistent dependency of creep rate on applied stress. Because of the limited data set, however, uncertainty in irradiation creep is still a major issue. Additional experiments would be necessary to establish a credible irradiation creep database for fusion system design using the V-Cr-Ti alloys.

REFERENCES

1. H. Tsai, R. V. Strain, and D. L. Smith, "Study of Irradiation Creep of Vanadium Alloys," Fusion Materials Semiannual Progress Report, DOE/ER-0313/22, June 1997, pp. 57-60.
2. K. E. Lenox and M. L. Grossbeck, "Operating History of the HFIR MFE-RB-11J and –12J (P3-2 and P3-3) Experiments," Fusion Materials Semiannual Progress Report, DOE/ER-0313-25, December 1998, pp.307-323.
3. V. M. Troyanov et al., "Irradiation Creep of V-Ti-Cr Alloy in BR-10 Reactor Core Instrumented Experiment," Journal of Nuclear Materials, 233-237 (1996), pp.381-384.

TENSILE PROPERTIES OF V-(CR,FE)-TI ALLOYS AFTER IRRADIATION IN THE HFIR-12J EXPERIMENT - K. Fukumoto, H. Matsui (IMR/Tohoku Univ.), Y. Yan, H. Tsai, R. V. Strain and D. L. Smith (Argonne National Laboratory)

OBJECTIVE

The objective of this work is to determine the tensile properties of V-(Cr,Fe)-Ti alloys after the irradiation at 500°C to ≈6 dpa in HFIR-12J experiment.

SUMMARY

Postirradiation tensile tests at room temperature and 500°C were performed on V-(Cr,Fe)-Ti alloy specimens irradiated in the HFIR-12J experiment. The specimens were of the SSJ design with overall dimensions of 16.0x4.0x0.2 mm and gauge dimensions of 5.0x1.2x0.2 mm. The irradiation temperature was ≈500°C and the attained neutron damage was ≈6 dpa. Results from these tensile tests show all specimens retained respectable elongation and irradiation hardening was modest. The properties of the V-(3-5)Cr-(3-5)Ti alloys appears not to be strongly affected by the Ti and Cr composition variations. For the V-(3-4)Fe-4Ti-(0-0.1)Si alloys, significantly, the uniform elongation was nearly 10%. The reduction-in-area in all specimens was high, >85%, indicating ductile behavior. These findings show good mechanical properties of V-(Cr,Fe)-Ti alloys after the 500°C neutron irradiation to 6 dpa.

INTRODUCTION

Data on mechanical properties for V-base alloys are needed to establish guidelines for the design and operation of fusion devices utilizing this class of materials for in-vessel structures. Recently two irradiation experiments, RB-11J and RB-12J, were performed in HFIR to investigate the mechanical properties at the temperatures of 300 and 500°C, respectively[1]. These experiments were conducted under the auspices of the Japanese Monbusho, the Japan Atomic Energy Research Institute (JAERI), and the U.S. Fusion Energy Sciences Program.

In this study, ten V-base alloys, six with Cr, Ti and Si additions and four with Fe,Ti, and Si additions, were included. Whereas the reference alloy has been V-(3-5)Cr-(3-5)Ti, replacement of Cr with Fe is being explored because it is perceived that iron atoms may be a more effective trap for the helium atoms produced in transmutation by neutron reaction [2]. The goals of the present work were to evaluate the mode of fracture and the reasons of irradiation hardening and loss of ductility should it occur.

EXPERIMENTAL PROCEDURES

Six ingots of V-(4-5)Cr-(3-5)Ti-(0-0.1)Si and four ingots of V-(3-4)Fe-4Ti-(0-0.1)Si alloys were produced by arc melting. Chemical analyses of the heats are shown in Table 1. The SSJ tensile specimens (16 x 4 x 0.2 mm) were punched from 0.2 mm-thick as-rolled sheets with the longitudinal direction parallel to the final sheet rolling direction. All specimens were vacuum degassed at 600°C for 0.5 h and then vacuum annealed at 1100°C for 2h. An impurity getter made of Zr and Ta foils was used to protect the specimen at temperature. According to previous studies, mechanical properties of these materials, in terms of yield stress, uniform elongation and ultimate tensile stress, are not strongly influenced by the annealing temperature in the range of 950 to 1100° [3].

In the 12J experiment, the specimens were irradiated at 497 ± 22°C and attained a peak dose of 5.7 dpa. Details of the operating history are given in a previous report [1].

Table 1. Composition of the Alloys Studied

Heat	Nominal Comp.	Cr (wt%)	Fe (wt%)	Ti (wt%)	Si (wppm)	O (wppm)	N (wppm)	S (wppm)
VM9401	V-4Cr-4Ti-0.1Si	4.43	-	4.07	640	240	5.5	3
VM9402	V-4Cr-4Ti	4.39	-	4.08	5	595	305	3
VM9403	V-5Cr-4Ti	5.56	-	4.05	7	515	4.5	2
VM9404	V-4Cr-3Ti	4.35	-	3.05	6	515	10	3
VM9405	V-5Cr-3Ti	5.53	-	3.07	4	490	5.5	3
VM9406	V-5Cr-5Ti	5.43	-	5.06	5	495	7	9
VM9407	V-4Fe-4Ti-0.1Si	0.06	3.94	4.03	210	370	7.5	4
VM9408	V-4Fe-4Ti	0.05	3.92	3.99	8	470	7.5	3
VM9409	V-3Fe-4Ti	0.05	3.01	3.97	6	515	7.5	2
VM9502	V-3Fe-4Ti-0.1Si	-	2.92	3.96	400	1478	21	8

The postirradiation tensile tests were conducted using the facilities in the Irradiation Materials Laboratory of the Argonne National Laboratory. The tests were conducted at room temperature and 500°C. All tests were performed at a strain rate of 6.67×10^{-4}/s (0.2mm/min). The 500°C tests were performed in a high-purity (99.999%) flowing argon environment with the specimen protected in a Ti getter foil. After the tensile tests, fractography was performed with a SEM in the ANL's Alpha-Gamma Hot Cell Facility. For the reduction-in-area determinations, specimens were mounted in a vertical clip holder and oriented with cross-section parallel to image plane. For the side view observations, specimens were tilted. TEM examinations were performed in Tohoku University with specimens punched out from the deformed tensile gauge sections and polished with a Tenupole-3 machine.

RESULTS

Table 2 summarizes the tensile test results: 0.2% offset yield stress (YS), ultimate tensile strength (UTS), uniform elongation (UE) and reduction-in-area (RA). Also shown in the table are the sums of weight percentages of the major alloying components, Ti plus Cr or Fe.

Table 2. Summary results of the 12J tensile tests

Heat/ Material	(Cr, Fe) +Ti (wt%)	Spec. No.	Test Temp. (°C)	0.2% YS (MPa)	UTS (MPa)	UE (%)	RA (%)
VM9401 V-4Cr-4Ti-0.1Si	8.65	TH13	RT	491	577	3.4	91
		TH18	500	368	449	2.3	95
VM9402 V-4Cr-4Ti	8.62	TH21	RT	420	519	4.8	92
		TH24	500	399	439	1.5	93
VM9403 V-5Cr-4Ti	9.73	TH34	RT	435	530	6.7	91
		TH36	500	355	435	3.2	90
VM9404 V-4Cr-3Ti	7.49	TH46	RT	395	491	9.1	93
		TH41	500	330	428	5.7	89
VM9405 V-5Cr-3Ti	8.66	TH50	RT	460	558	8.0	93
		TH58	500	374	443	4.5	NA
VM9406 V-5Cr-5Ti	10.67	TH65	RT	385	477	4.3	93
		TH63	500	368	449	2.3	92
VM9407 V-4Fe-4Ti-0.1Si	7.86	TH73	RT	635	745	10.6	90
		TH76	500	555	660	2.7	89
VM9408 V-4Fe-4Ti	7.80	TH80	RT	490	657	9.4	87
		TH81	500	505	608	5.3	85
VM9409 V-3Fe-4Ti	6.95	TH92	RT	518	600	9.2	89
		TH95	500	530	608	3.0	89
VM9502 V-3Fe-4Ti-0.1Si	6.78	TB05	RT	663	750	4.9	88
		TB07	500	462	575	4.5	90

Figure 1 shows a typical example of stress – strain curve on tensile tests for unirradiated and irradiated vanadium alloys, VM9407 with a nominal compositiion of V-4Fe-4Ti-0.1Si. The yield stress and ultimate strength of unirradiated V-Cr-Ti and V-Fe-Ti alloys at RT are ≈350 and 450 MPa, respectively. The ultimate tensile strengths of the irradiated materials were found to have increased over those of the unirradiated. However, the magnitude of hardening was limited, <≈66%. There were noticeable losses of ductility in the irradiated samples, but they still retain elongations up to 10% at RT. Even in 500°C tests, about 5% of elongation could be seen in some alloys.

Fig. 2 shows the dependence of strength and uniform elongation on the amount of major alloying components, measured in wt% of (Cr,Fe) + Ti. From the figures, it can be seen that the V-Fe-Ti alloys are more susceptible to irradiation hardening than the V-Cr-Ti alloys. In these experiments, the production of helium and hydrogen is negligibly small, <1 ppm. Therefore, the greater increase in irradiation hardening in the V-Fe-Ti alloys than in the V-Cr-Ti alloys might not be due to a trapping effect of helium at undersized solute atoms. At low levels of (Cr,Fe) + Ti alloy addition, both V-Fe-Ti and V-Cr-Ti alloys show good uniform elongation, up to ≈10% in RT tests.

Figure 3 shows the dependence of alloying component weight on the yield stress, ultimate tensile strength and uniform elongation in 500°C tests. The tendency in the 500°C tests is comparable to that in RT tests, with the uniform elongation decreased to about 5%. After the stress reached to ultimate tensile strength in 500°C tests, serration on stress-strain curve can be seen until the onset of crack extension.

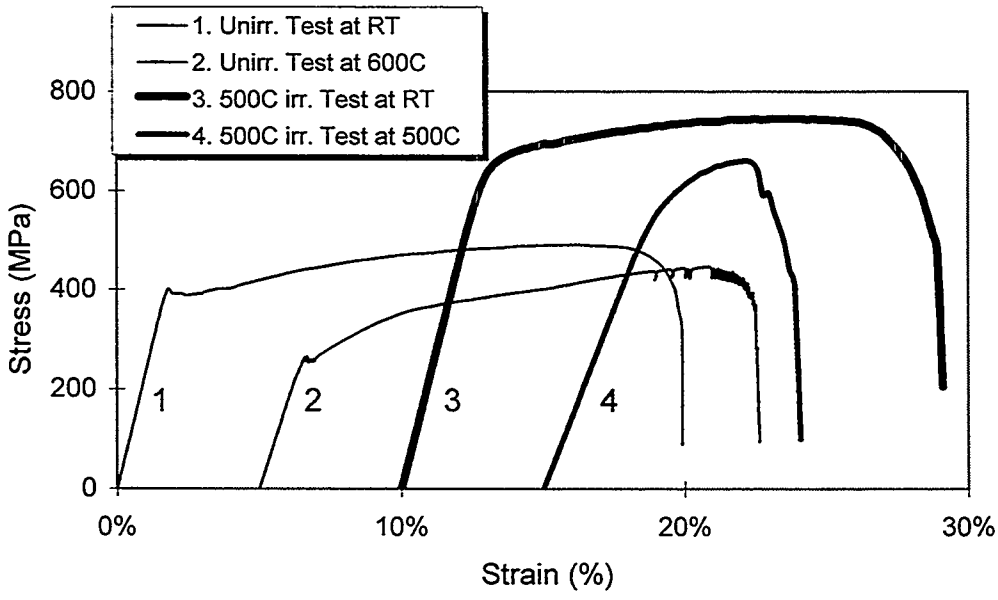

Fig.1 Stress-strain curves for VM9407/V-4Fe-4Ti-0.1Si.

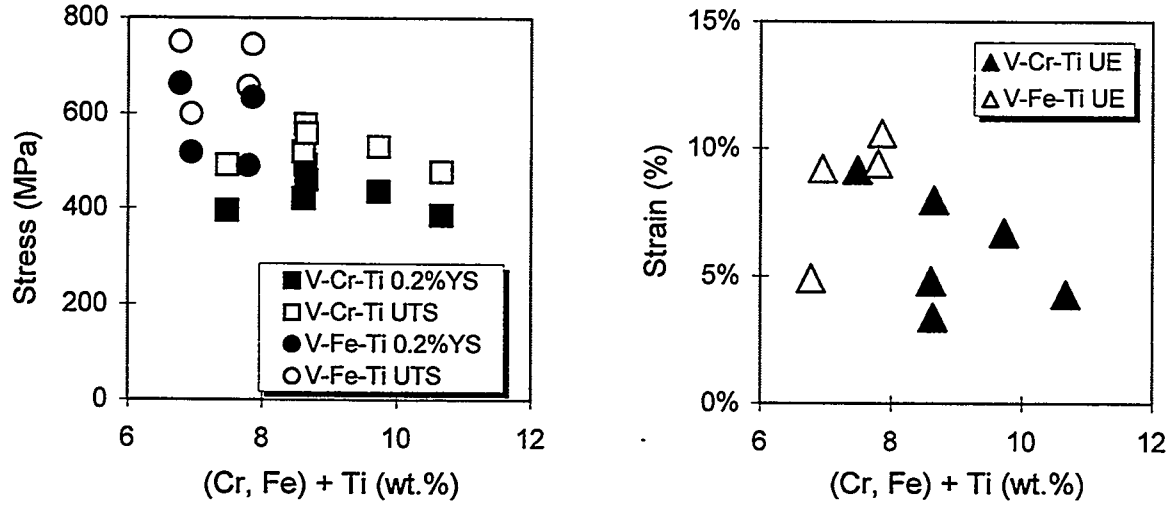

Fig. 2. Comparison of tensile strength of V-Cr-Ti and V-Fe-Ti alloys in room temperature tests. Left figure shows dependence of yield stress and ultimate tensile strength on (Cr,Fe)+Ti addition. Right figure shows the dependence of uniform elongation on (Cr,Fe)+Ti addition.

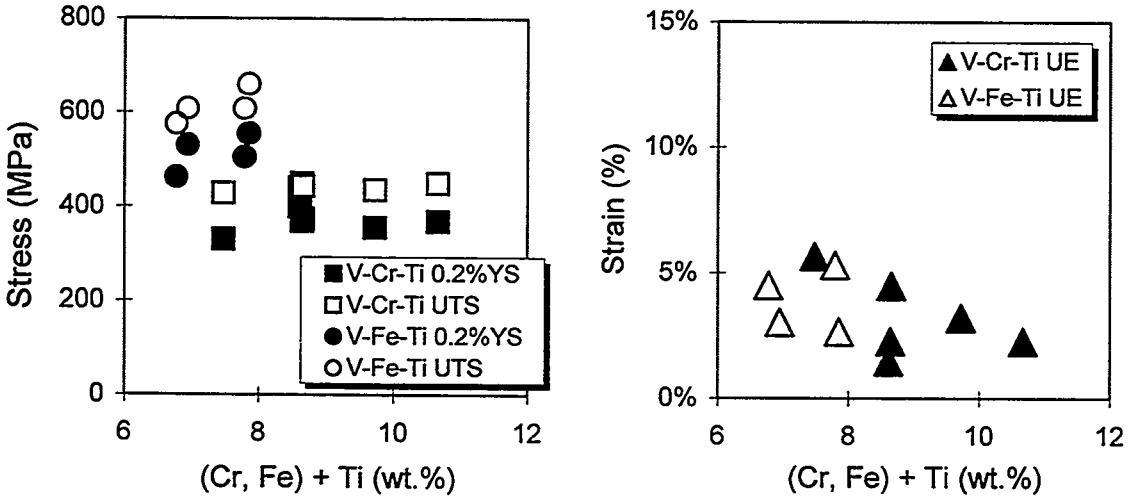

Figs.3 : Comparison of tensile strength and ductility of V-Cr-Ti and V-Fe-Ti alloys in 500°C tests. Left figure shows dependence of yield stress and ultimate tensile strength on (Cr,Fe)+Ti addition. Right figure shows the dependence of uniform elongation on (Cr,Fe)+Ti addition.

A perspective view of the fractured tip of a representative specimen, TH36 (VM9403/V-5Cr-4Ti), is shown in Fig. 4. Necking at the fracture part can be seen. The reductions in area in all specimens were >80%, which corroborated with the ductile features noted in the SEM fractography. A typical example is shown in Fig. 5. There are no intergranular fractures and

clevage patterns on the fracture surfaces. Surface cracks are visible; however, these cracks and slip bands are observed only in the necked region. This localized structure might be related to plastic instability.

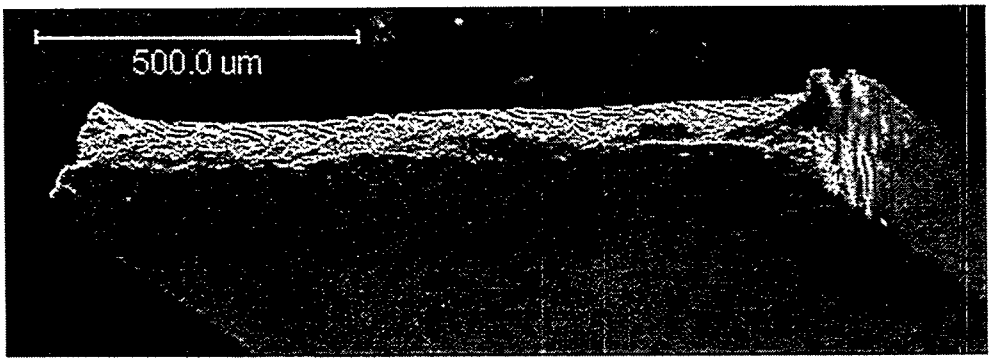

Fig.4 A perspective view of the tip of fractured tensile specimen TH36 with a nominal composition of V-5Cr-4Ti. Both the irradiation and test temperatures were 500°C.

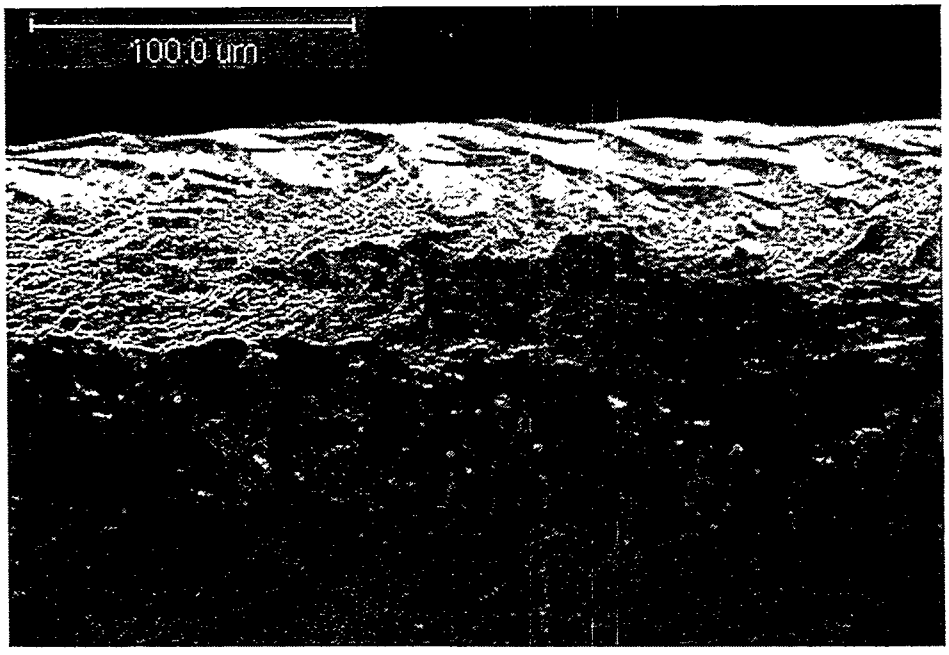

Fig.5 Higher magnification SEM fractograph of the same TH36 specimen showing ductile features at the fracture.

Fig. 6A shows the TEM micrograph of irradiated specimen TH13 (VM9401/V-4Cr-4Ti-0.1Si). The features seen are typical in other specimens. Dislocation network and dislocation loops formed in the matrix at high density. Also formed were precipitates, which have an average size of 30nm. While there were no detectable cavities in the grains, they could be seen close to

and/or on the grain boundaries, as shown in Fig.6B. These microstructural features are consistent with the previous data [4,5] obtained from FFTF and EBR-II irradiation in temperature regimes of 430 or 500°C. The relationship between the tensile behavior and microstructure in this work are therefore in good agreement with the previous work in FFTF or EBR-II.

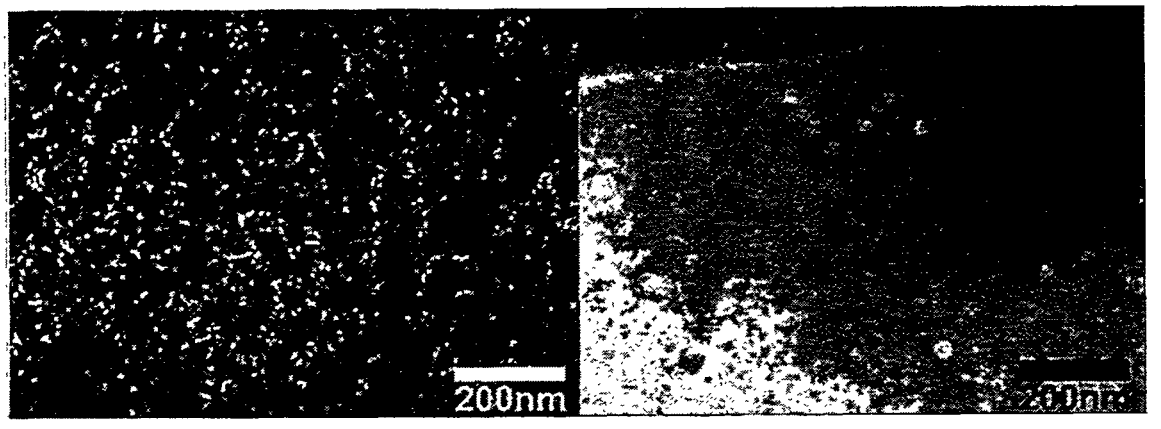

Fig. 6A (left) TEM weak-beam dark-field micrograph of sample TH13 (VM9401/V-4Cr-4Ti-0.1Si). High density of dislocation can be seen.
Fig. 6B (right) TEM bright-field image of the same sample TH13. Cavities can be seen close to and on the grain boundary.

FUTURE WORK

TEM observations at the necking parts of tested tensile specimens will be completed to determine the mechanisms of irradiation hardening. As well as subsequent experiments of HFIR-12J, a series of examination for specimens irradiated at 300C in HFIR-11J is undergoing.

REFERENCES

[1] Operating history of the HFIR MFE-RB-11J and 12J (P3-2 and P3-3) experiments, K.E.Lenox and M.L.Grossbeck; Fusion Materials Semianual Progress Report for Period Ending December 31, 1998 (DOE/ER-0313/25) p.307
[2] Effects of implanted helium on the mechanical properties of vanadium-based alloys, M.Tanaka and H.Matsui; Materials Transactions, JIM, Vol. 34 (1993) 1083
[3] Mechanical properties of vanadium based alloys for fusion reactor, K.Fukumoto, T.Morimura, T.Tanaka, A.Kimura, K.Abe, H.Takahashi and H.Matsui; J.Nucl.Mater., 239 (1996) 170
[4] H.M.Chung, B.A.Loomis and D.L.Smith; J.Nucl.Mater., 239(1996) 139
[5] K.Fukumoto, A.Kimura and H.Matsui; J.Nucl.Mater. 263-268 (1998)

Effect Of Low Temperature Irradiation In ATR On The Mechanical Properties Of Ternary V-Cr-Ti Alloys - M. L. Hamilton, M. B. Toloczko, B. M. Oliver and F. A. Garner (Pacific Northwest National Laboratory)*

OBJECTIVE

This experiment was designed to allow the relationship between shear punch and tensile data to be established for vanadium alloys irradiated at low temperatures in the ATR-A1 experiment.

SUMMARY

Tensile tests and shear punch tests were performed on a variety of vanadium alloys that were irradiated in the Advanced Test Reactor (ATR) at temperatures between 200 and 300°C to doses between 3 and 5 dpa. Tests were performed at room temperature and the irradiation temperature. The results of both the tensile tests and the shear punch tests show that following low temperature irradiation, the yield strength increased by a factor of 3-4 while the ultimate strength increased by a factor of approximately 3. Uniform elongation and tensile reduction in area show that the ductility diminishes following irradiation. The correlation between uniaxial ultimate strength and effective shear maximum strength was in excellent agreement with previous studies on other materials. Using the room temperature test data, the correlation between uniaxial yield strength and effective shear yield strength was in excellent agreement with previous studies on other materials. The yield strength data obtained at the irradiation temperature did not fit the room temperature correlation.

PROGRESS AND STATUS

Introduction

Vanadium-base alloys are considered to be attractive candidates for low activation structural materials in future fusion power devices. Most attention is currently focused on V-Cr-Ti alloys because of their relatively attractive mechanical properties after irradiation at relatively high temperature and because these alloys are resistant to void swelling. [1] Recent studies at lower temperatures, however, have shown significant degradation in mechanical properties during radiation, with large increases in strength and large decreases in ductility observed following irradiation at temperatures below 400°C. [2] The purpose of the current work is to provide further data on the change in mechanical properties of V-Cr-Ti alloys following low temperature irradiation. Mechanical properties were determined from tensile tests and shear punch tests; the latter is a TEM disk-based test developed to provide strength and ductility information. [3-9] This experiment is the first in which the tensile-shear punch correlation work has been extended to a bcc material, and it is the first time that the viability of the correlation has been evaluated at elevated test temperatures.

Experimental Procedure

The alloys of interest were V-3Cr-3Ti, V-4Cr-4Ti, V-5Cr-5Ti and V-6Cr-3Ti. These alloys will be referred to as V33, V44, V55, and V63, respectively. All were annealed at 1000°C prior to the irradiation for either one hour (V44 and V55) or two hours (V33 and V63). These

---

*Pacific Northwest National Laboratory (PNNL) is operated for the U.S. Department of Energy by Battelle Memorial Institute under contract DE-AC06-76RLO-1830.

alloys were irradiated as both tensile and TEM specimens in the ATR mixed spectrum reactor in the A1 experiment at nominal temperatures of 200 and 300°C to doses between 3 and 5 dpa. [10] The specimens were irradiated in lithium-bonded subcapsules that were shielded to reduce the number of thermal neutrons. The details of the temperature and dose history for each alloy and specimen type are given in Table 1. As shown in Table 1, tensile specimens of V63 were not available for irradiation.

Table 1. Temperature and dose history of each combination of alloy and specimen geometry.

Alloy	Tensile Specimens		TEM Specimens	
	Actual Irradiation Temp. (°C)	Dose (dpa)	Actual Irradiation Temp. (°C)	Dose (dpa)
V33	205	3	205	3
	295	3	293	4.7
V44	229	3.5	205	3
	293	4.7	293	4.7
V55	229	3.5	205	3
	293	4.7	293	4.7
V63			205	3
			293	4.7

The tensile specimens, cut from sheet stock by electro-discharge machining (EDM), were S1 miniature specimens with nominal gauge dimensions of 5 mm x 1.2 mm x 0.25 mm (0.2 in. x 0.05 in. x 0.010 in.). Specimen thickness ranged from 0.25 to 0.36 mm (0.010 to 0.014 in.) between the alloys , but for any one alloy, the specimen thickness was uniform across the specimen to within 0.01 mm (0.0005 in.). Tensile tests were performed at a crosshead speed of 0.127 mm/min (0.005 in./min), yielding an initial strain rate of 4×10^{-4} sec^{-1}. For each irradiation condition, tests were performed at the actual irradiation temperature and at room temperature. Room temperature tests were performed in air. Specimens tested at elevated temperature required about 90 minutes for heatup and stabilization prior to testing in static argon. One test was performed for each alloy/irradiation condition.

Reduction of area (RA) measurements were obtained using SEM photomicrographs taken from each of the tensile specimen fracture surfaces. RA measurements were obtained on both irradiated and unirradiated test specimens using calibrated digital image analysis software.

Shear punch tests were performed using standard 3 mm diameter TEM disks of the same thickness as the tensile specimens. TEM disks were also cut from sheet stock by the EDM method. Nominal specimen thickness varied from alloy-to-alloy, but for any one alloy, the specimen thickness was uniform across the TEM disk to within 0.005 mm (0.0002 in). Tests were performed at a crosshead speed of 0.127 mm/min (0.005 in./min). Specimen displacement during a test was assumed to be equal to crosshead displacement. For each irradiation condition, tests were performed at the actual irradiation temperature and at room temperature. Room temperature tests were performed in air. Specimens tested at elevated temperature required about 90 minutes for heatup and stabilization prior to testing in slowly flowing argon. One test was performed for each alloy/irradiation condition.

Small pieces of several tested TEM specimens were also analyzed for helium and hydrogen content to determine whether there was any effect of gas generation from the irradiation. The helium analyses were conducted using the high-sensitivity isotope dilution analysis system at PNNL. Details of the system have been presented elsewhere. [11] Hydrogen analyses were conducted using a new facility recently developed at PNNL for measurement of hydrogen in irradiated materials. [12]

Results

Tensile data

The tensile results are given in Table 2, and are shown in Figures 1-4 along with other vanadium alloy tensile data that were generated in this same experiment by researchers at ANL and ORNL. [13,14] Significant strengthening was observed in the V33, V44, and V55 alloys following irradiation at both temperatures (recall that tensile specimens of the V63 alloy were not irradiated). Yield strength typically increased by at least a factor of 3-4, and uniform elongation (UE) decreased typically to less than 1%. No significant differences were observed between alloys. As shown in the figures, these results are very consistent with the vanadium tensile data generated by the ANL and ORNL researchers [13, 14].

Reduction of area measurements were obtained since uniform elongation values from the tensile tests were so low. Figure 5 shows that irradiation caused significant changes in RA as well as in UE. RA dropped from over 90% in the unirradiated condition to about 60-70% for most tests after irradiation at ~200°C and to 5-30% for most tests after irradiation at ~300°C. Figures 6a – 6r give the photographs from which the reduction of area measurements were taken. It is clear that the amount of deformation at the fracture has decreased with irradiation; fractures shifted from a chisel line in the unirradiated condition to a surface with some ductility following irradiation at ~200°C and to almost a flat surface following irradiation at ~300°C.

Shear punch data

Effective shear strength data are shown in Figures 7 and 8. The trends exhibited by these data are almost identical to those observed in the tensile data, i.e., significant strengthening occurred at all temperatures for all alloys. The shear punch data also showed the same test temperature-dependent strength changes that are apparent in the tensile data. The effective shear stress data indicate that the V63 alloy behaved similarly to the other three alloys.

Gas analysis data

Helium and hydrogen concentrations were measured in six of the irradiated and tested shear

punch specimens and in selected control specimens. The results are shown in Figure 9.

Table 2. Tensile data on vanadium alloy specimens irradiated in ATR-A1.

Alloy	Specimen ID	Dose	Irr. Temp. (C)	Test Temp. (C)	YS (MPa)	UTS (MPa)	UE (%)	TE (%)	RA (%)
V33	P145	0	-	205	126	289	10.8	24.0	97
	P142	0	-	295	102	179	13.5	19.7	97
	P141	3	205	22	987	998	0.5	5.1	68
	P140	3	205	205	813	862	0.4	2.0	27
	P144	3	295	22	989	1007	0.4	2.4	35
	P143	3	295	295	931	931	0.2	1.5	5
V44	P848	0	-	22	349	414	5.9	10.6	91
	P851	0	-	22	327	457	14.5	31.1	93
	P850	0	-	164	271	388	12.9	23.7	95
	P853	3.5	229	22	1062	1101	0.4	5.4	61
	P845	3.5	229	229	888	901	0.1	5.7	64
	P842	4.7	293	22	992	1120	1.2	2.4	18
	P841	4.7	293	293	976	982	0.3	2.0	9
V55	P740	0	-	22	282	448	17.6	31.6	90
	P742	0	-	229	205	322	11.8	21.8	95
	P743	0	-	293	226	369	13.3	22.6	88
	P747	3.5	229	22	1130	1132	0.2	6.1	62
	P753	3.5	229	229	992	994	0.2	6.1	66
	P752	4.7	293	22	1053	1072	0.9	3.1	19
	P751	4.7	293	293	935	943	0.3	5.3	27

In the irradiated samples, measured helium levels ranged from 1.2 to 3.0 appm. Reproducibility between duplicate helium analyses averaged ~2%, somewhat higher than the analysis system reproducibility of ~0.5%, but consistent with previous results that have shown higher levels of helium heterogeneity in materials that have a boron impurity as suggested below. [15]

Measured hydrogen levels in the same irradiated samples ranged from 237 to 480 appm . Reproducibility between the duplicate analyses averaged ~20% and is consistent with the reproducibility observed in standard hydrogen-containing steels. Measured hydrogen levels in the unirradiated alloys showed a higher average variability of ~60%. The reason for the higher variability in the unirradiated specimens is not clear.

Discussion

Gas analyses

Measured helium contents in the irradiated alloys were about a factor of 10 higher than calculated, suggesting the presence of boron at impurity levels. In spite of the large variance from the expected helium level, the few appm He present are not likely to have affected the mechanical properties of the alloys.

Measured hydrogen levels are about two orders of magnitude higher than calculated. The reason for this is not clear, but since approximately the same hydrogen levels were measured in both the unirradiated and irradiated alloys, it appears that much of the hydrogen was present prior to irradiation thus suggesting either that no additional hydrogen was generated during the irradiation, or that any hydrogen generated diffused out of the samples during the irradiation. It is unlikely that the hydrogen present in the materials prior to irradiation would have affected the changes in mechanical properties due to irradiation.

Tensile and shear punch data

The tensile traces on the unirradiated material exhibited both a yield plateau (or evidence of a yield plateau for those tests where the phenomenon was less distinct) and serrated yielding at all test temperatures. The corresponding shear punch traces exhibited neither of these phenomena. However, in tests of other materials such as low carbon steels and aluminum alloys, the fine detail observed in tensile tests, such as a Luders plateau or serrated yielding, has been observed in corresponding shear punch tests. Both tensile and shear punch traces from unirradiated specimens exhibited a large amount of plastic deformation as well. The UTS was typically 40-60% higher than the YS in both types of tests for the unirradiated condition.

The tensile test traces obtained on irradiated specimens exhibited none of the features observed in the traces from the unirradiated specimens. Load increased rapidly to the maximum value with very little work hardening; the UTS was generally within a few percent of the YS. The test traces from irradiated specimens typically exhibited relatively sharp 'peaks' at maximum load and since no serrations or yield plateaus were observed, it appears that the irradiation-induced defects were much more effective than interstitial atmospheres at pinning dislocations. These features suggest that dislocation channeling is the prevalent deformation mechanism in the irradiated alloys, as has indeed been recently confirmed. [16]

While UE was consistently very low, and exhibited no variation with irradiation temperature, reduction of area exhibited a significant difference with irradiation temperature, being consistently much lower after irradiation at about ~300°C. This suggests that although neither YS nor UE varied significantly with irradiation temperature, one might expect that the fracture toughness of these alloys after irradiation at ~300°C would be much lower than following irradiation at ~200°C.

Tensile-shear punch correlation

While the irradiation temperature and dose received by the TEM specimens was often significantly different than that for the corresponding tensile specimens, it was judged worthwhile to construct a correlation between uniaxial and effective shear yield and maximum strengths. The uniaxial yield and the effective shear yield strength data are compared in Figure 10. Two linear regression lines are shown for the yield strength correlation in Figure 10. One is fit to all the data, while the other is fit to just the room temperature data. Both correlations have nearly the same slope, and the slope is in good agreement with previous correlations on other unirradiated and irradiated materials [4, 6-9]. However, as is evident in Figure 10, the tensile and shear punch data obtained from elevated temperature tests do not fall on the same line as the data obtained from room temperature tests. An examination of the both the tensile and the shear punch test traces revealed that the shear punch traces obtained from elevated temperature tests exhibited a very smooth transition from linear elastic to plastic behavior making it difficult to exactly define the yield point. In keeping with the standard method of choosing the yield point as the

deviation from linearity, the yield point was taken as the earliest discernable deviation from linearity, which resulted in low values for the effective shear yield stress.

The reason for the smooth transition from linear elastic to plastic behavior is not understood at this time. It has been suggested that an offset effective shear yield stress be used in a manner analogous to the 0.2% offset yield strength. This was investigated, and due to the geometry of the deformation zone of the shear punch test, a 0.2% offset shear strain is equivalent to only a fraction of the width of the trace line. Thus, such an offset would have no significant effect on the measurement of the effective shear yield strength value.

The correlation for maximum strength, as shown in Fig. 11, is in excellent agreement with previous maximum strength correlations obtained from unirradiated and irradiated materials, and as with previous correlation studies, the maximum strength correlation clearly exhibits less scatter than the yield strength correlation [4, 6-9]. Unlike the yield strength correlation, there is no stratification of the values obtained at room temperature and at elevated temperature.

Summary And Conclusions

Tensile and shear punch tests on vanadium alloys irradiated in ATR at ~200-300°C to 3-5 dpa indicate that significant strengthening and loss of ductility are observed after a small amount of low temperature irradiation and that strength at the irradiation temperature is slightly lower than at room temperature. RA is significantly lower following irradiation at ~300°C than at ~200°C. No significant difference was observed between V33, V44, V55 and V63. The tensile-shear punch relationship was as expected for both the yield and the maximum load conditions, but some variability that is not well understood was observed for the yield condition.

REFERENCES

[1] B. A. Loomis, H. M. Chung, L. J. Nowicki, and D. L. Smith, J. Nucl. Mater., 212-215 (1994), pp. 799-803.

[2] S. J. Zinkle, D. J. Alexander, J. P. Robinson, L. L. Snead, A. F. Rowcliffe, L. T. Gibson, W. S. Eatherly and H. Tsai, DOE/ER-0313/21, p. 73.

[3] G.E. Lucas, G.R. Odette, and J.W. Sheckard, "Shear Punch and Microhardness Tests for Strength and Ductility Measurements", The Use of Small-Scale Specimens for Testing of Irradiated Material, ASTM STP 888, W.R. Corwin and G.E. Lucas, eds., American Society for Testing and Materials, PA, 1986, pp. 112-140.

[4] M.L. Hamilton, M.B. Toloczko, and G.E. Lucas, "Recent Progress in Shear Punch Testing", Miniaturized Specimens for Testing of Irradiated Materials, IEA International Symposium, P. Jung and H. Ullmaier, eds., Forschungszentrum Jülich GmbH, 1995, pp. 46-58.

[5] M.B. Toloczko, M.L. Hamilton, and G.E. Lucas, "Ductility Correlations Between Shear Punch and Uniaxial Tensile Test Data", these proceedings.

[6] M.L. Hamilton, M.B. Toloczko, D.J. Edwards, W.F. Sommer, M.J. Borden, J.A. Dunlap, J.F. Stubbins, and G.E. Lucas, "Correlation Between Shear Punch and

Tensile Data for Neutron-Irradiated Aluminum Alloys", Effects of Radiation on Materials: 17th International Symposium, ASTM STP 1270, 1996, 1057-1067.

[7] Hankin, G.L. Hamilton, M.L., Garner, F.A. and Faulkner, R.G., "Shear Punch Testing of 59Ni Isotopically Doped Model Austenitic Alloys after Irradiation in FFTF at Different He/dpa," Journal of Nuclear Materials, Vols. 258-263, 1998, pp. 1657-1663.

[8] Hankin, G.L., Toloczko, M.B., Hamilton, M.L. and Faulkner, R.G., "Validation of the Shear Punch-Tensile Correlation Technique using Irradiated Materials," Journal of Nuclear Materials, Vols. 258-263, 1998, pp. 1651-1656.

[9] Hamilton, M. L., Garner, F. A., Hankin, G. L., Faulkner, R. G., and Toloczko, M. B., "Neutron-Induced Evolution of Mechanical Properties of 20% Cold Worked 316 as Observed in Both Miniature Tensile and TEM Shear Punch Specimens", Effects of Radiation on Materials: 19th International Symposium, ASTM STP 1366, M. L. Hamilton, A. S. Kumar, S. T. Rosinski and M. L. Grossbeck, Eds., American Society for Testing and Materials, 1999, in press.

[10] H. Tsai, L. J. Nowicki, M. C. Billone, H. M. Chung, and D. L. Smith, DOE/ER-0313/23, pp. 70 – 76.

[11] H. Farrar IV and B. M. Oliver, "A Mass Spectrometer System to Determine Very Low Levels of Helium in Small Solid and Liquid Samples," J. Vac. Sci. Technol. A4, 1740 (1986).

[12] B. M. Oliver, F. A. Garner, and L. R. Greenwood, "Quadrupole Mass Spectrometer System for the Determination of Low to High Levels of Hydrogen in Irradiated Materials," presented at the 9th International Conference on Fusion Reactor Materials, Colorado Springs, CO, October 10-15, 1999 (J. Nucl. Mater., in press).

[13] S. J. Zinkle, L. L. Snead, A. F. Rowcliffe, D. J. Alexander, and L. T. Gibson, DOE/ER-0313/24, pp. 33-40.

[14] H. Tsai, H. Matsui, M. C. Billone, R. V. Strain, and D. L. Smith, J. Nucl. Mater., 258-263 (1998), pp. 1471-1475.

[15] B. M. Oliver, W. N. McElroy, L. S. Kellogg, and H. Farrar IV, "Boron Determinations in Pressure Vessel Steels," Reactor Dosimetry, ASTM STP 1228, ASTM, Philadelphia, 1994, pp. 167-176.

[16] P. M. Rice and S. J. Zinkle, "Temperature Dependence of the Radiation Damage Microstructure in V-4Cr-4Ti Neutron Irradiated to Low Dose," J. Nucl. Mater. 258-263 (1998) 1414-1419.

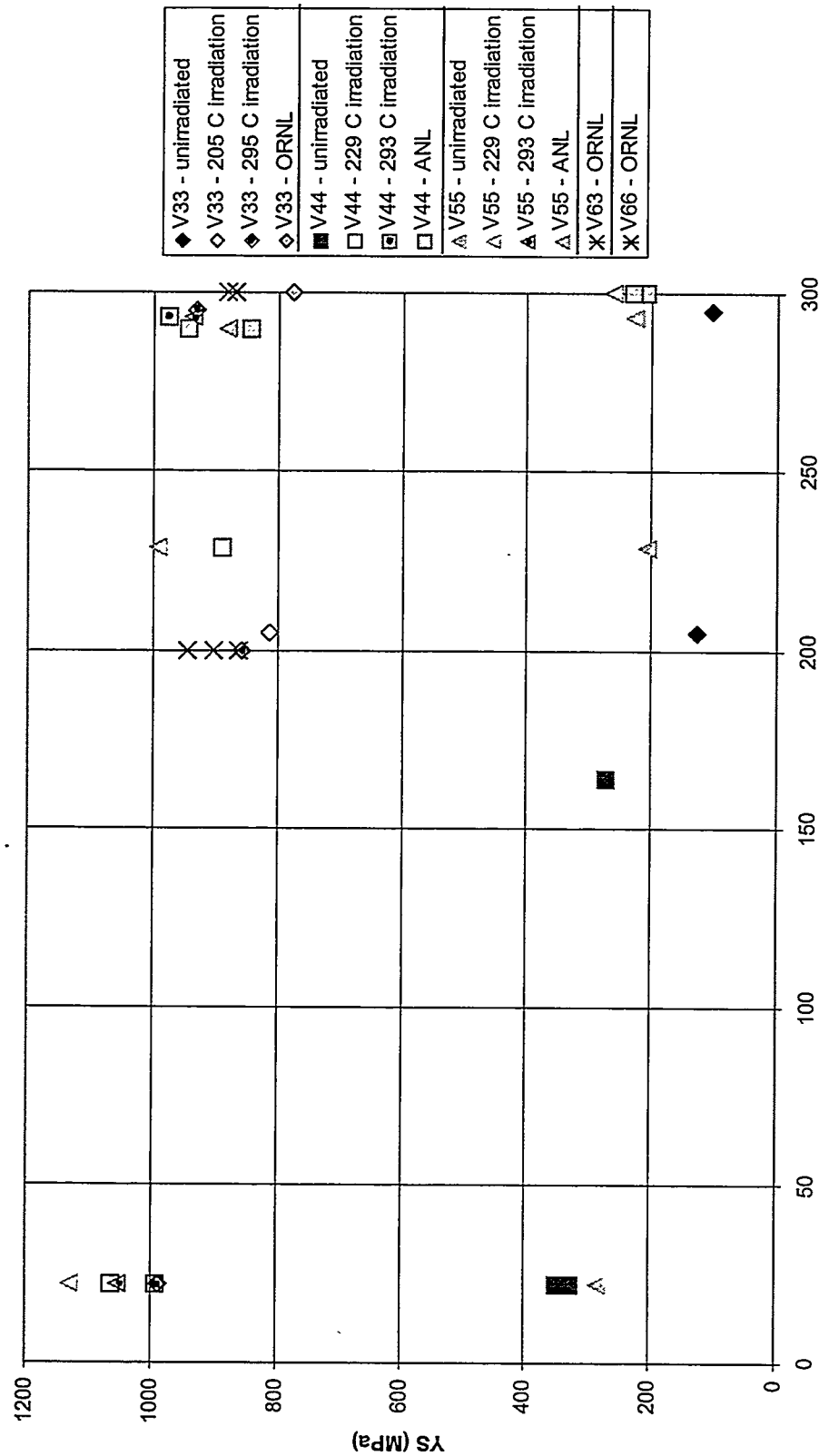

Figure 1 . Yield strength of vanadium alloys irradiated in ATR.

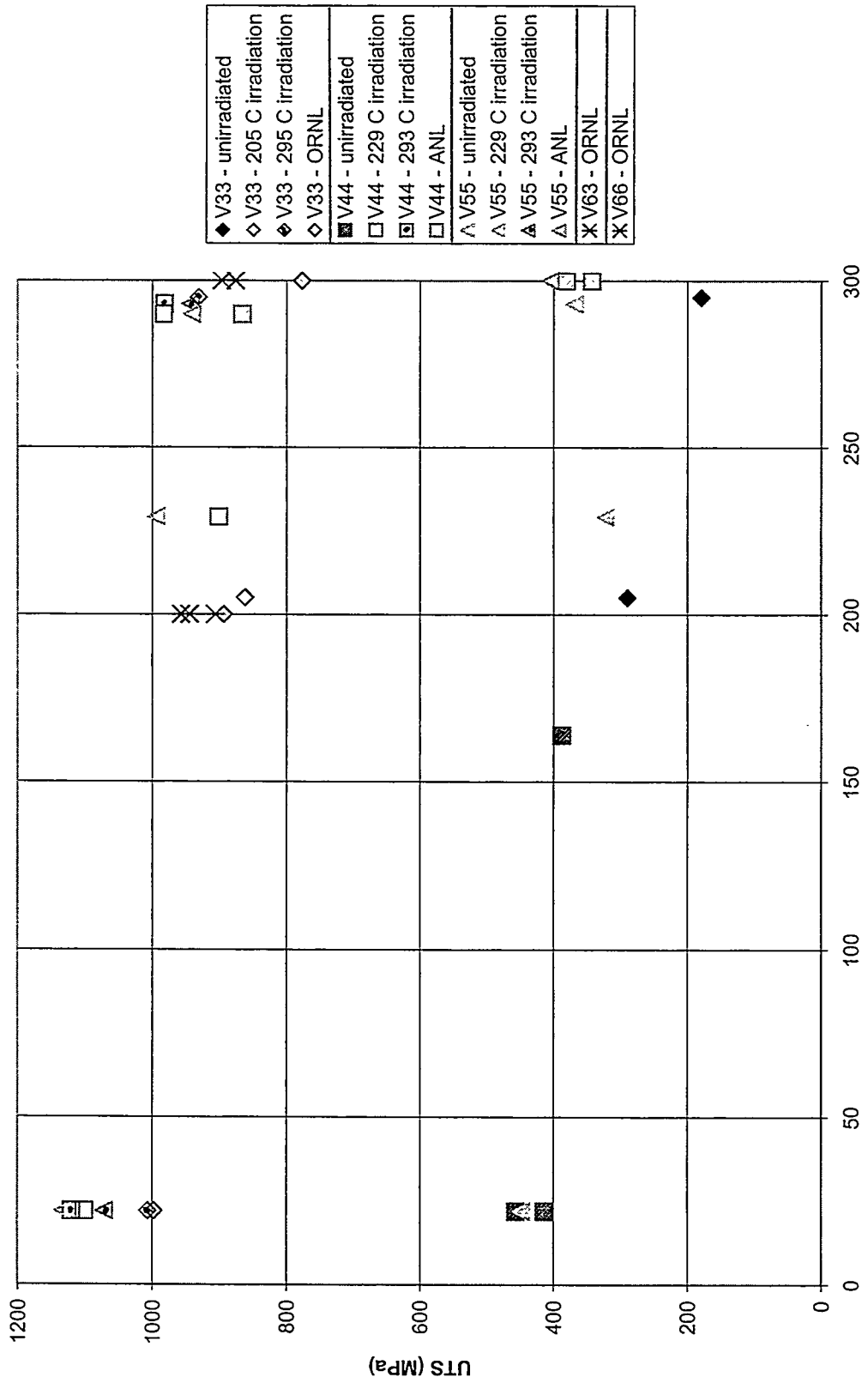

Figure 2. Ultimate strength of vanadium alloys irradiated in ATR.

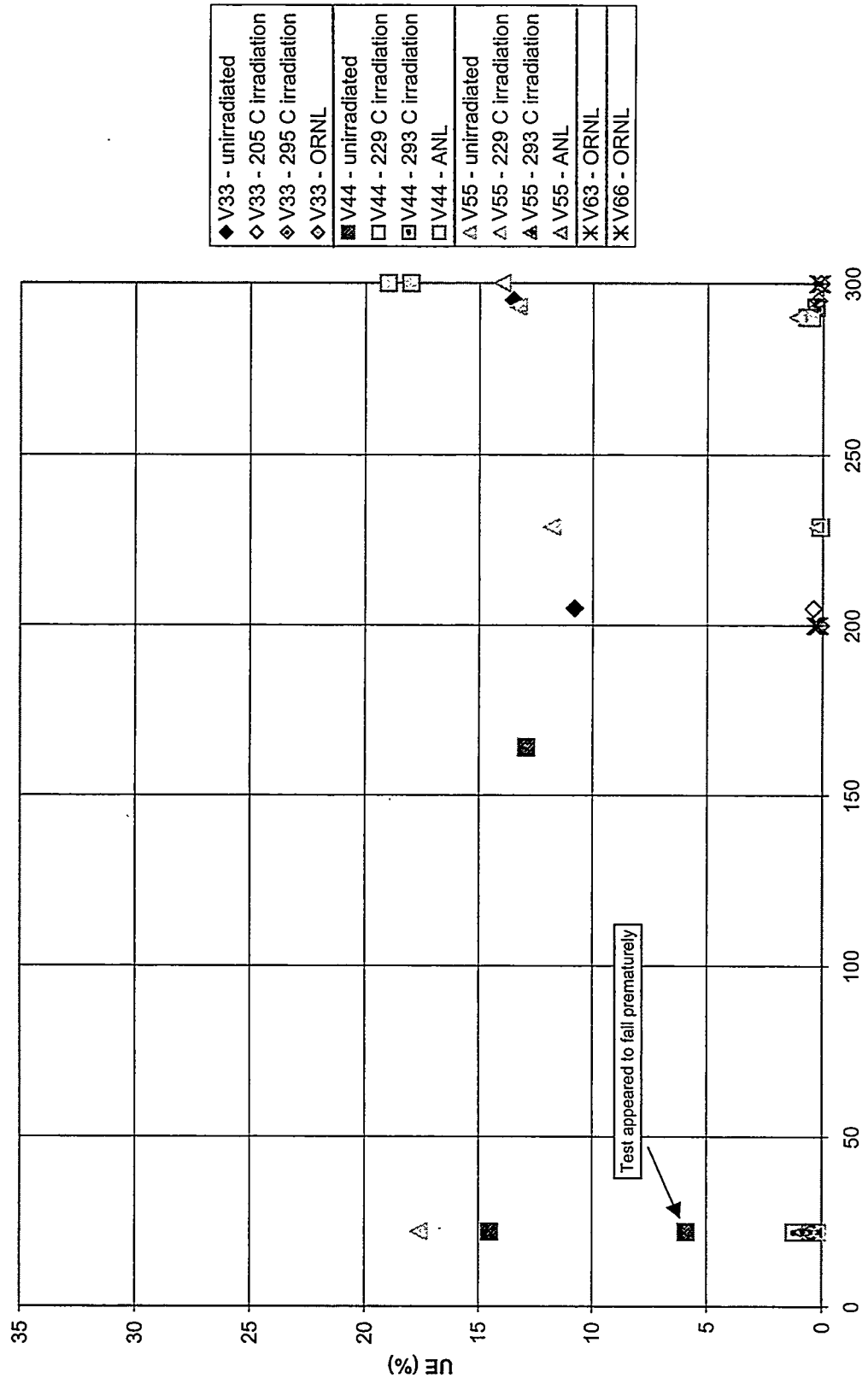

Figure 3. Uniform elongation of vanadium alloys irradiated in ATR.

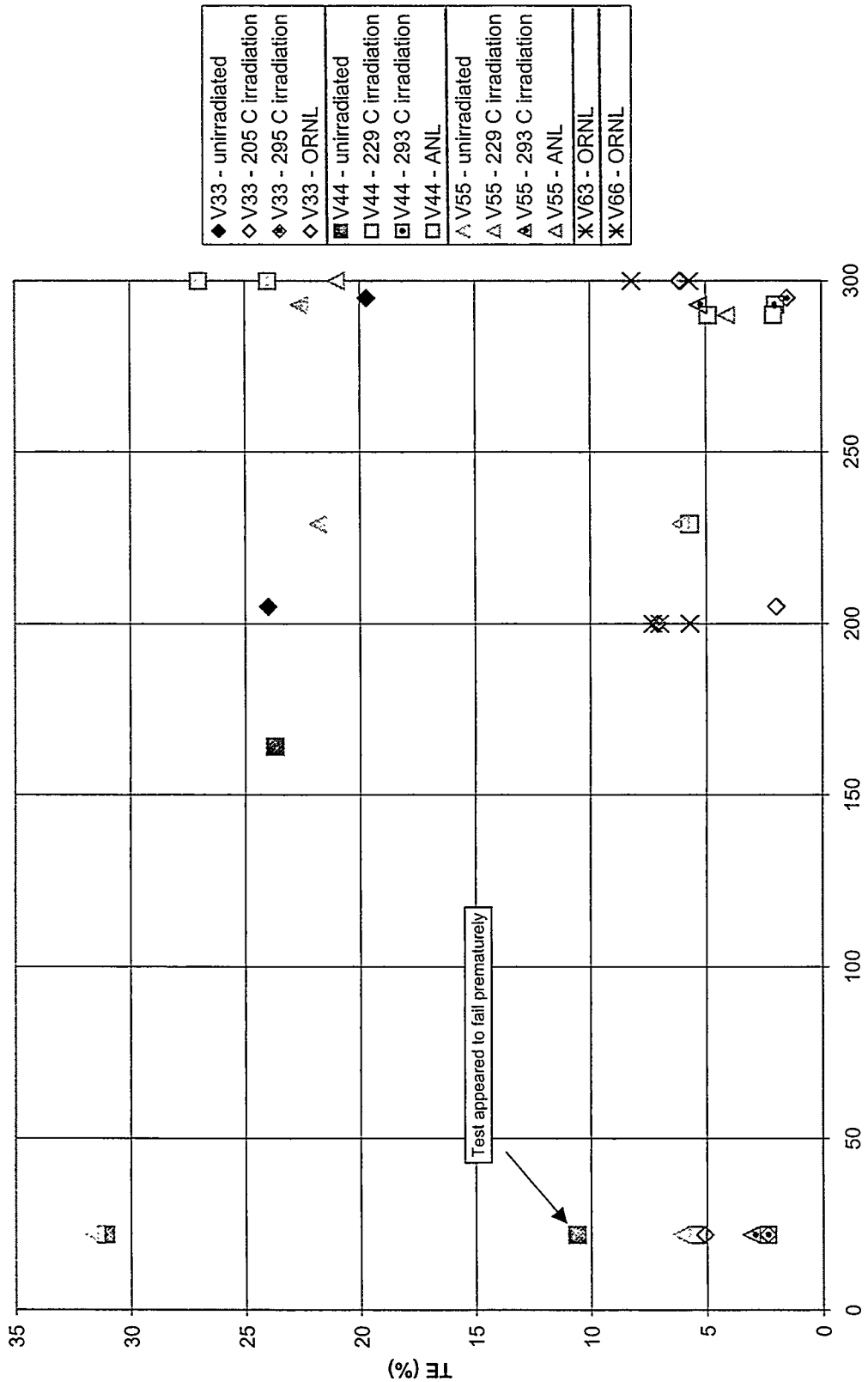

Figure 4. Total elongation of vanadium alloys irradiated in ATR.

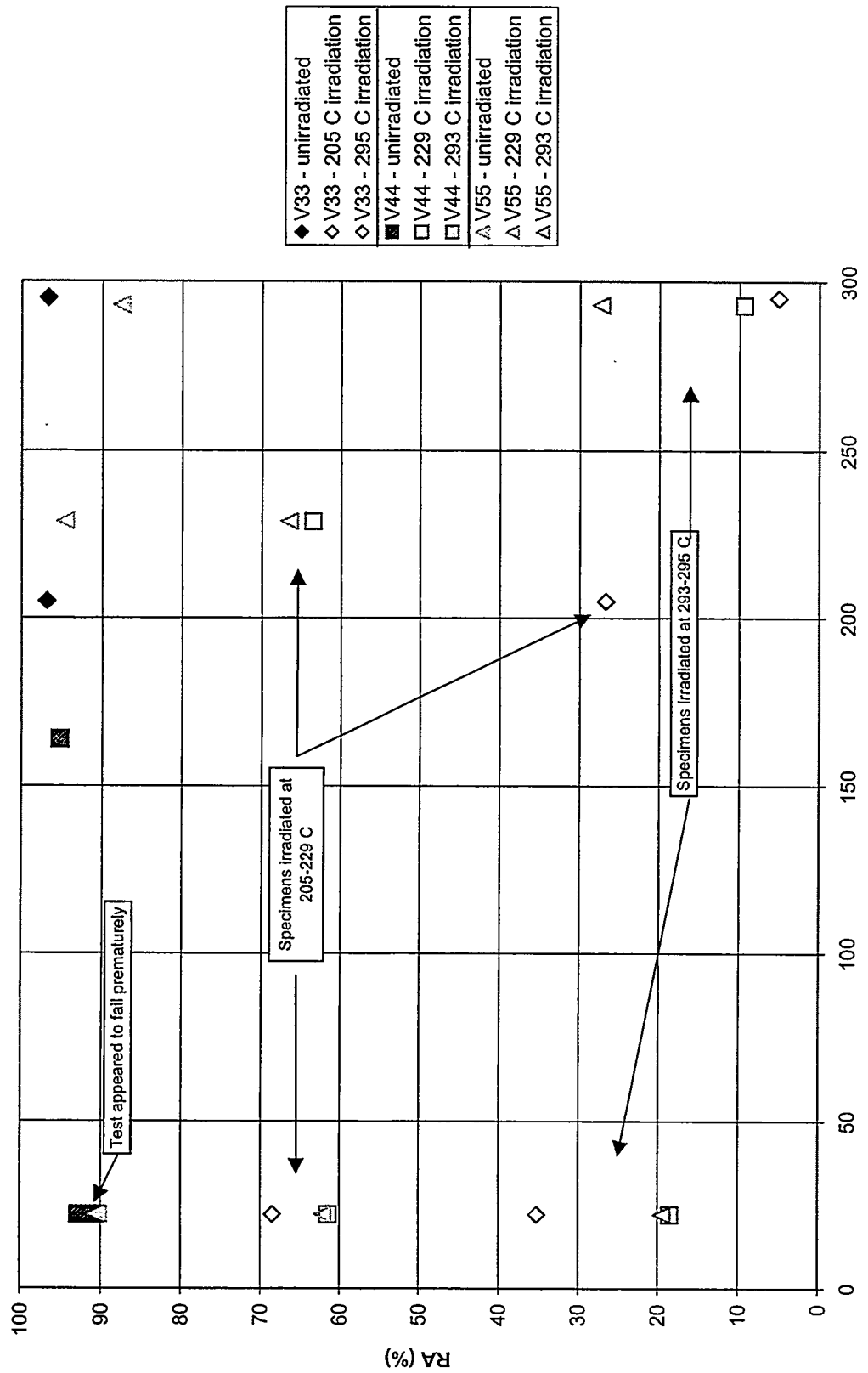

Figure 5. Reduction of area in vanadium alloys irradiated in ATR.

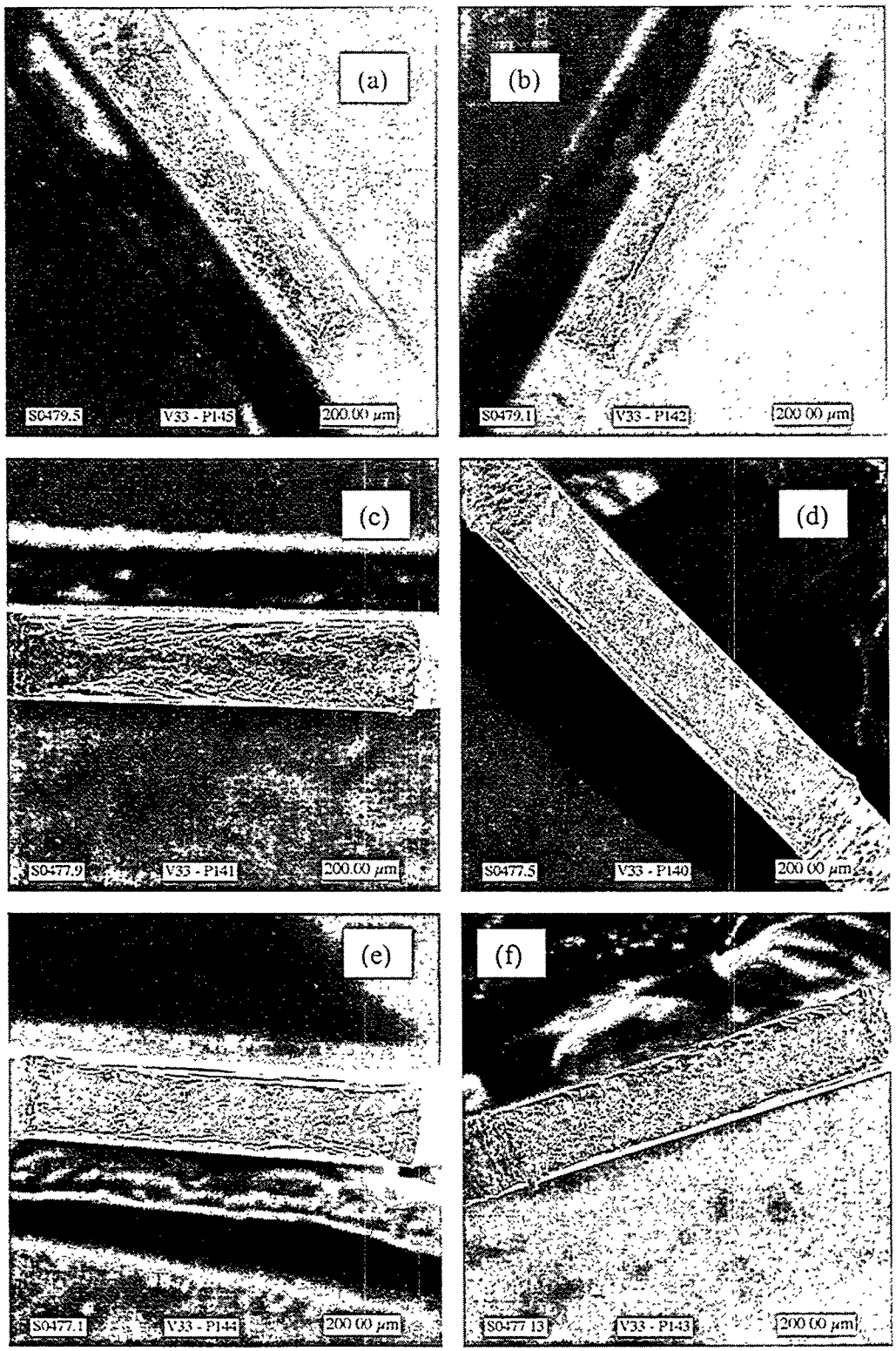

Figure 6a-f. Fractographs of alloy V33 specimens a)P145, b)P142, c)P141, d)P140, e)P144, and f)P143.

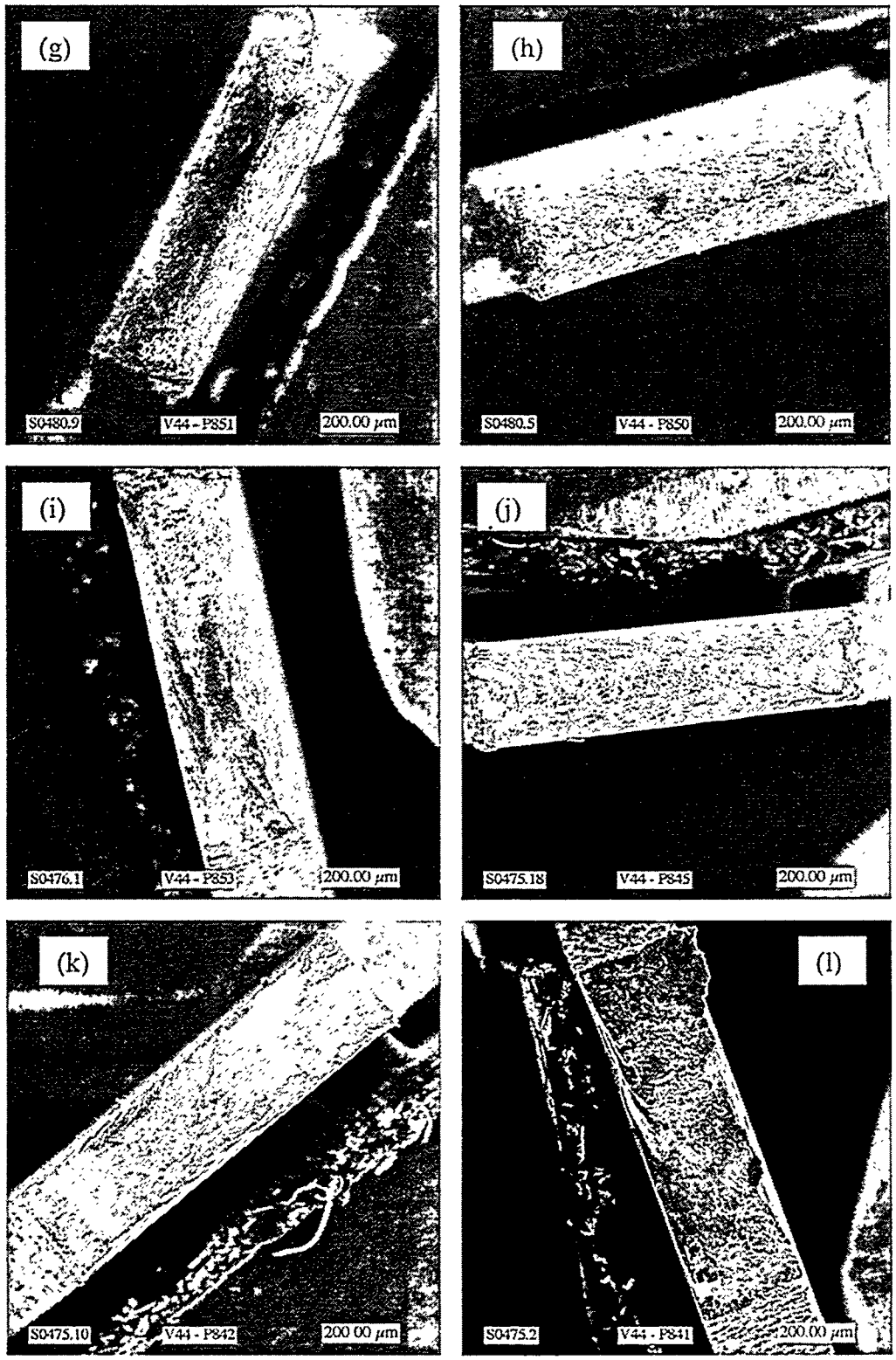

Figure 6g-l. Fractographs of V44 alloy specimens g)P851, h)P850, i)P853, j)P845, k)P842, and l)P841.

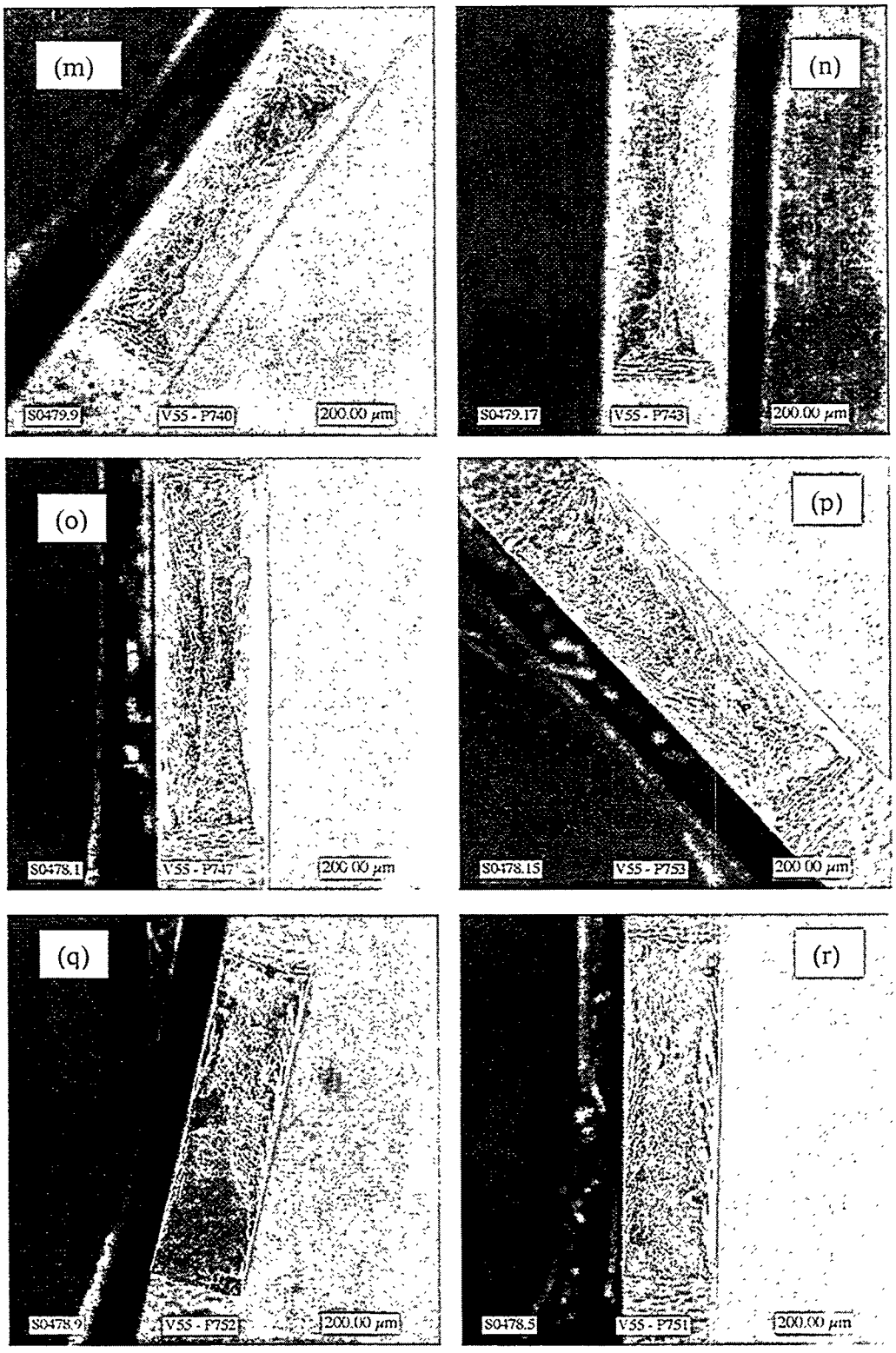

Figure 6m-r. Fractographs of V55 alloy specimens m)P740, n)P743, o)P747, p)P753, q)P752, and r)P751.

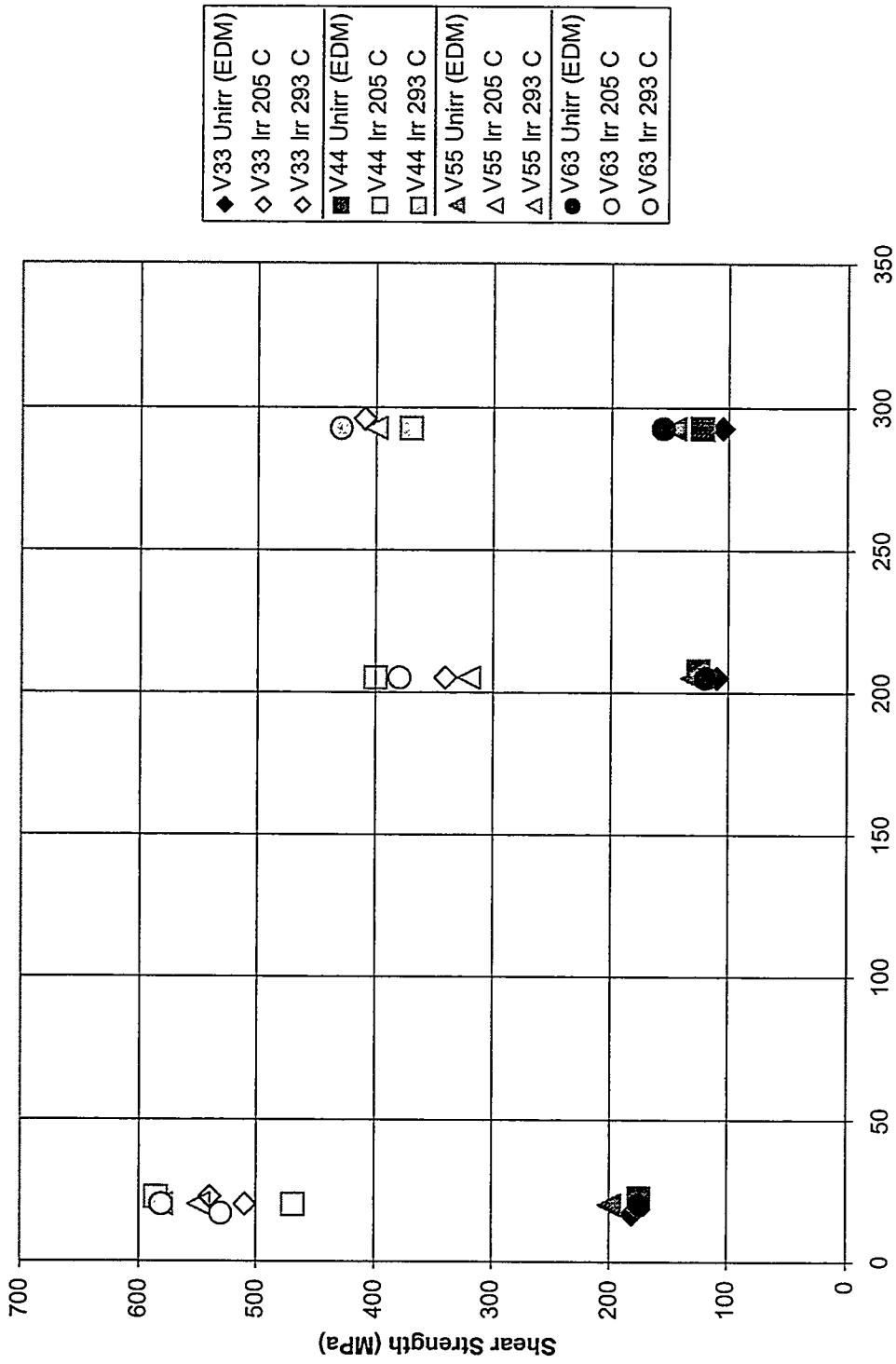

Figure 7. Effective shear yield strength in vanadium alloys irradiated in ATR.

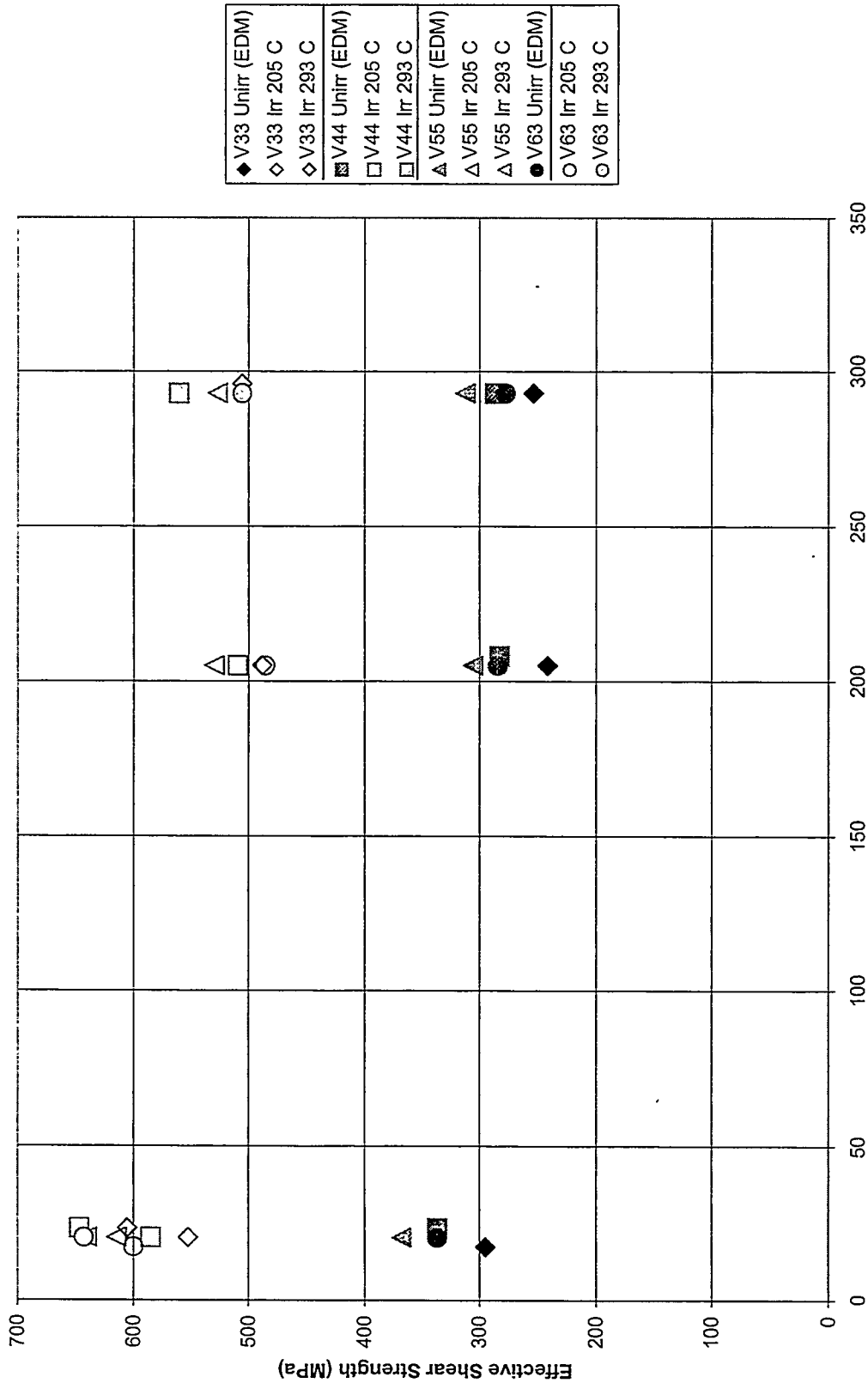

Figure 8. Effective maximum shear strength in vanadium alloys irradiated in ATR.

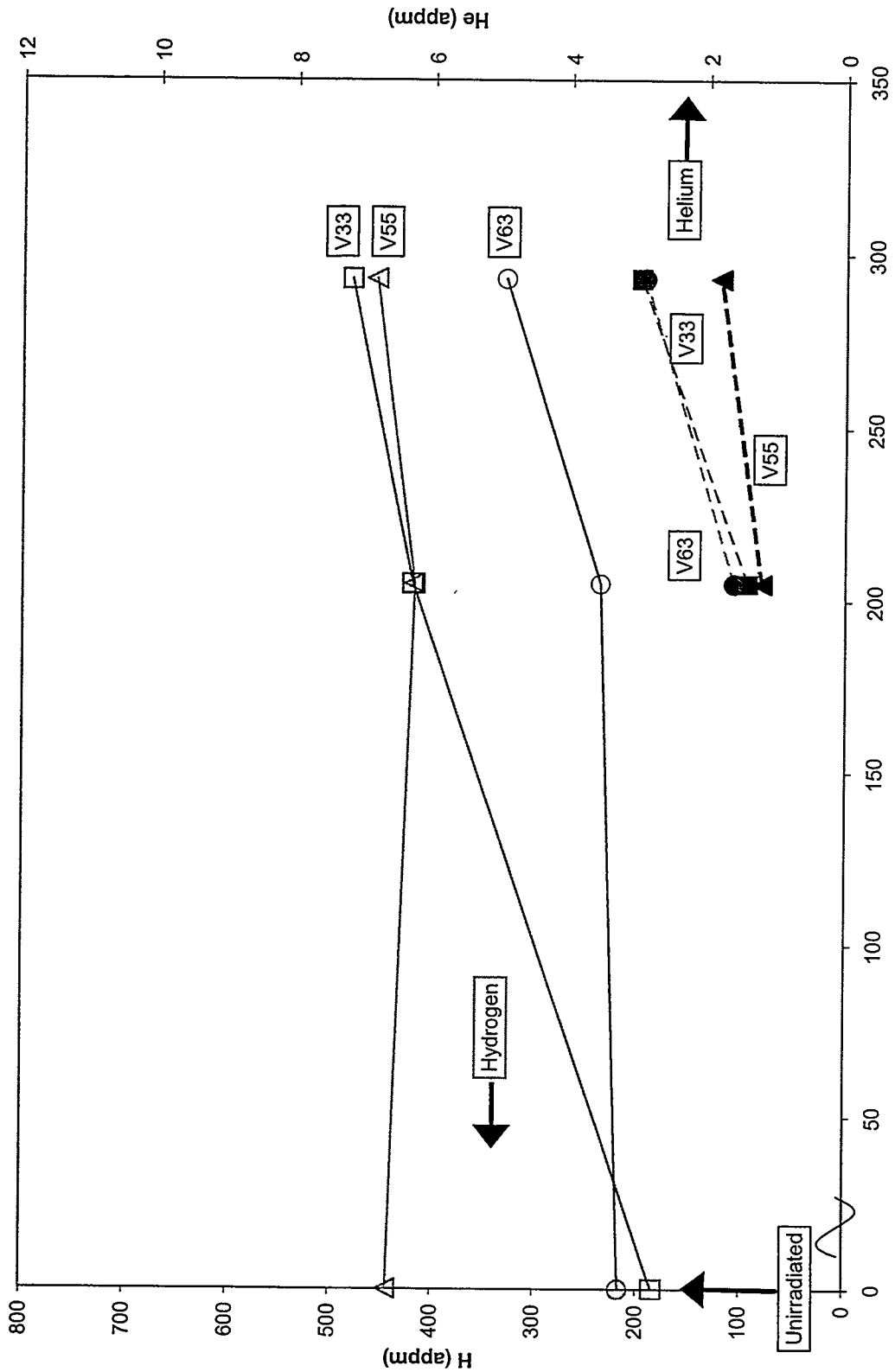

Figure 9. Gas content of selected vanadium alloy specimens irradiated in ATR.

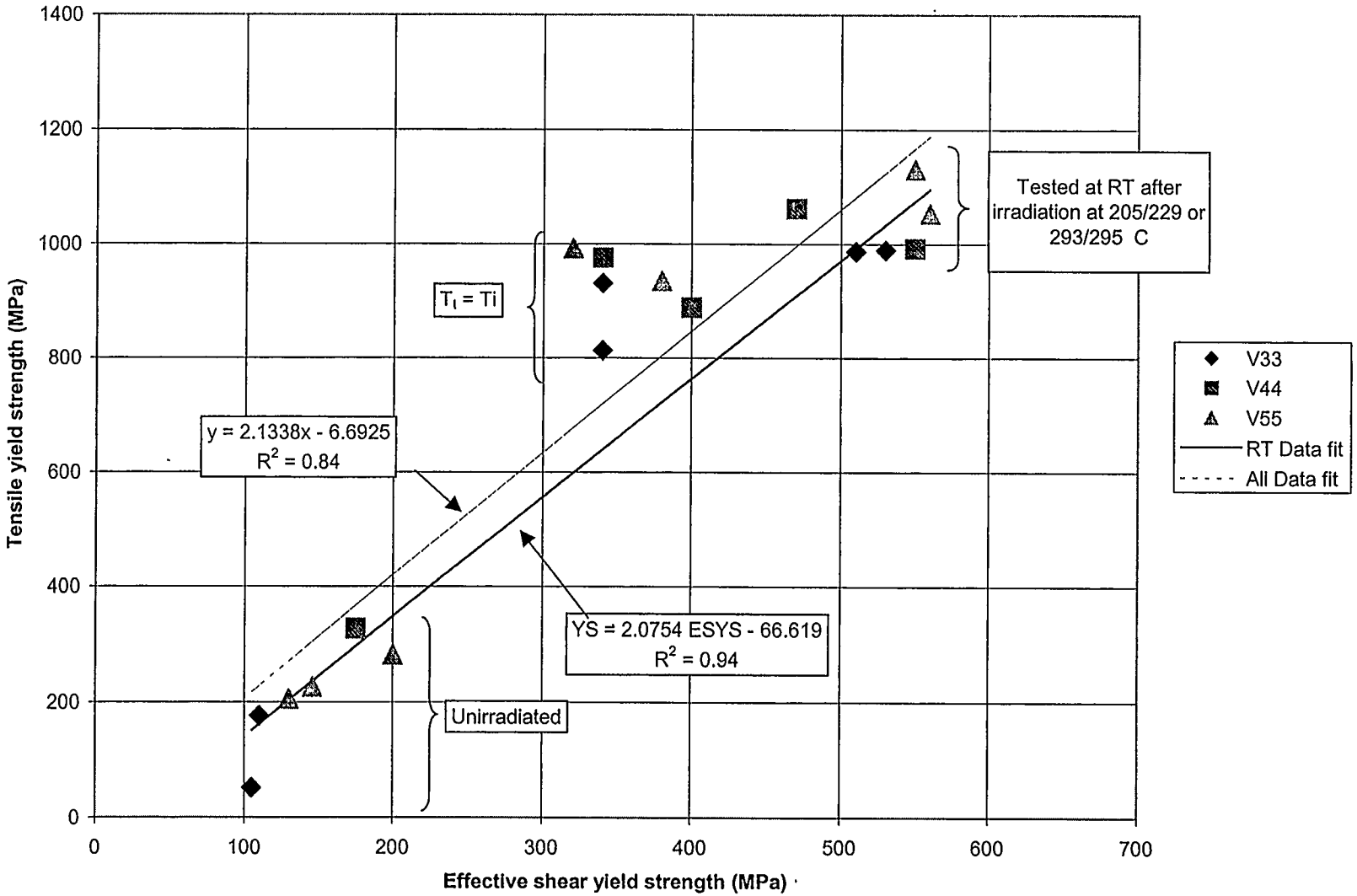

Figure 10. Correlation between tensile yield and effective shear yield strength for vanadium alloys irradiated in ATR.

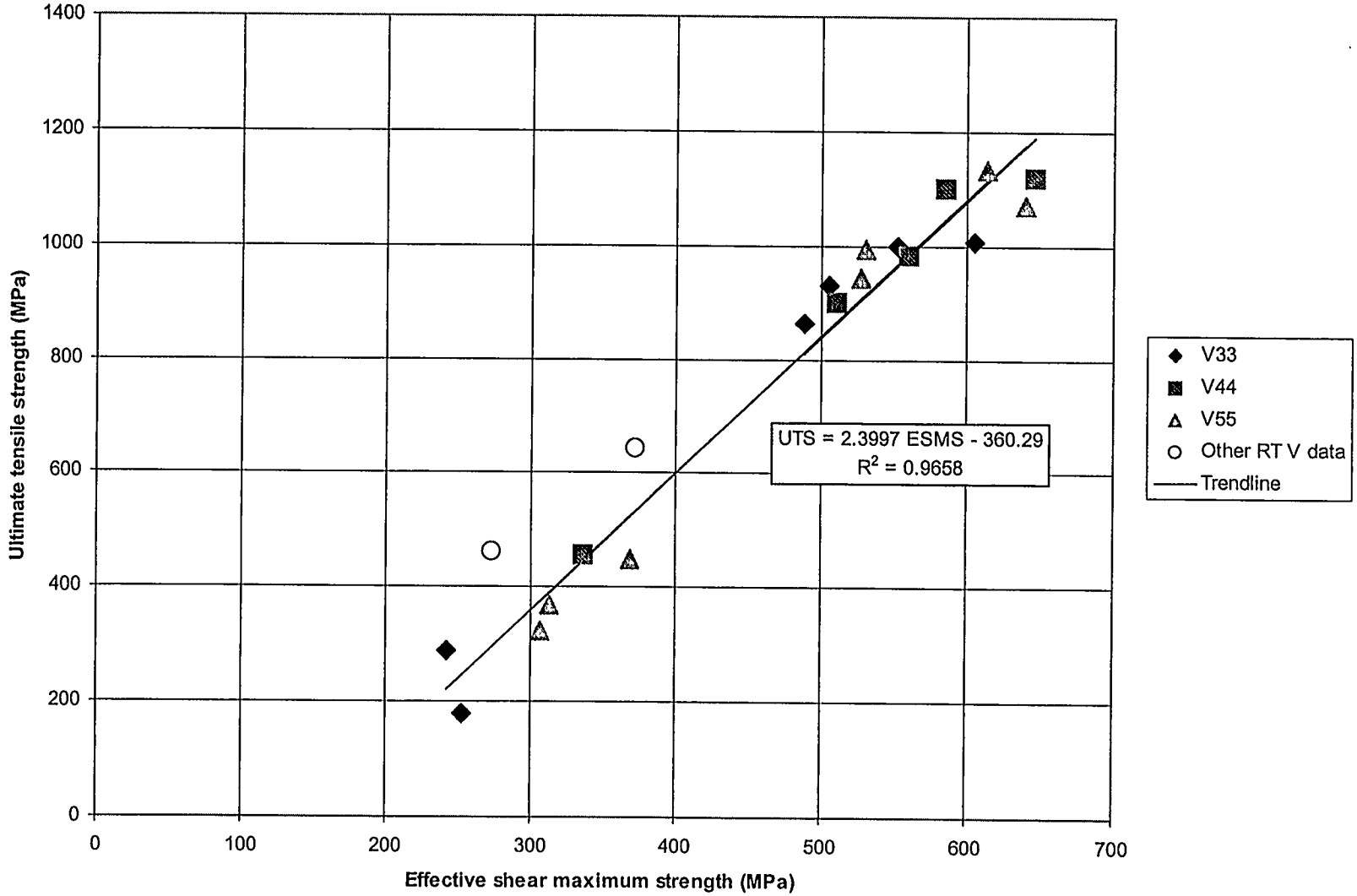

Figure 11. Correlation between maximum tensile and effective shear maximum strength for vanadium alloys irradiated in ATR.

Effect of Strain Rate on the Tensile Properties of Unirradiated and Irradiated V-4Cr-4Ti,
A.F. Rowcliffe, S.J. Zinkle, and D.T. Hoelzer (Oak Ridge National Laborartory).

To be published in Journal of Nuclear Materials as Proceedings of the 9th International Conference on Fusion Materials October 10-15, 1999, Colorado Springs.

Extended Abstract

Tensile tests were carried out on an annealed, unirradiated V-4Cr-4Ti alloy from RT to 850°C at strain rates ranging from 10^{-1} to 10^{-5} s^{-1}. Below 300°C, where interstitial solutes are relatively immobile, deformation is homogeneous, and the strain rate sensitivity (SRS) of the yield and flow stress is positive. Between 300 and 700°C, the formation of solute atmospheres at locked dislocations results in dynamic strain-aging (DSA), deformation becomes heterogeneous, and the SRS of the flow stress is negative; in this regime the lower yield stress is independent of strain rate. Above 700°C, substitutional solutes are also mobile, DSA declines, and the material enters a power law creep regime in which the SRS becomes positive again. Following neutron irradiation to 0.5 dpa at temperatures ≤400°C, severe flow localization occurs due to the high number density of <110> and <111> loops. However, above 400°C, strain hardening capacity returns but without the Lüders extension. At 500°C, after several percent plastic deformation, DSA occurs as interstitial solutes are released from the defect structure.

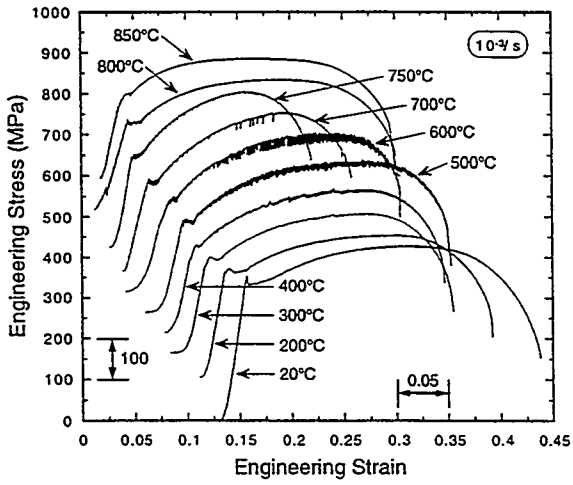

Figure 1. Load-elongation curves for annealed V-4Cr-4Ti at a strain-rate of 10^{-3} s^{-1} illustrating DSA regime; curves offset on stress and strain axes for clarity.

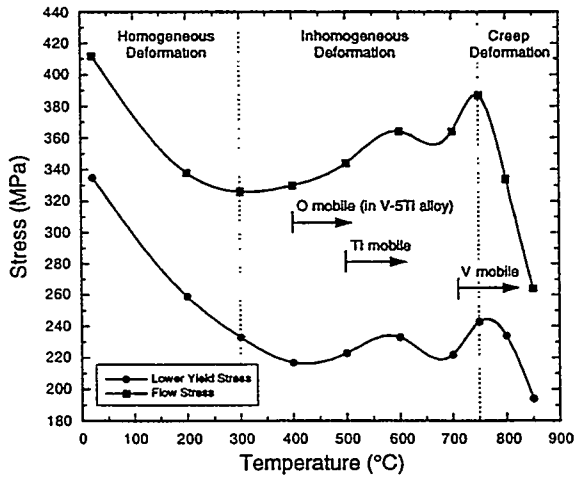

Figure 2. Temperature dependence of σ_y and σ_f illustrating three deformation regimes.

Solute Interactions in Pure Vanadium and V-4Cr-4Ti Alloy* - D.T. Hoelzer, S.J. Zinkle, and A.F. Rowcliffe (Oak Ridge National Laboratory) and M.K. West (University of Tennessee)

To be published in Journal of Nuclear Materials as Proceedings of the 9th International Conference on Fusion Reactor Materials, October 10-15, 1999, Colorado Springs.

Extended Abstract

Room temperature electrical resistivity and microhardness measurements were performed on cold-worked (CW) pure vanadium; solution annealed and CW V-4Cr-4Ti (alloy), and fusion welded alloy over the isochronal annealing temperature range from 200°C to 1200°C. The four-point probe technique was used for measuring electrical resistivity and a Vickers pyramidal indenter with a 1 kg load was used for measuring microhardness on type SS-3 sheet tensile specimens.

The results suggested that differences in property behavior observed for the specimens from 200°C to 400°C were related to interactions between interstitial O, C, and N solutes and Ti solutes in the alloy. In the cold-worked vanadium specimen, the formation of interstitial solute atmospheres around dislocations in the substructure was attributed to the observed increase in hardness and decrease in electrical resistivity. Calculations showed that the interstitial solutes possessed sufficient mobility at the lower temperatures to account for this type of thermally activated process. No significant increase in hardness was observed in the different alloy specimen conditions over this temperature range. However, differences in electrical resistivity were observed for these specimens. The resistivity and hardness data was interpreted as showing a cumulative effect that was balanced between processes involving the clustering of interstitial solutes around immobile Ti solute atoms (annealed alloy condition) and formation of atmospheres around dislocations (cold-worked and welded alloy conditions).

The measured property data for isochronal annealing temperatures above 400°C showed three distinct trends that were observed to depend on the composition and condition (i.e. deformed, annealed, or welded) of the specimens. The analysis of the three trends suggested that; (1) recovery of dislocation structures began in the CW vanadium, CW alloy, and welded alloy specimens at temperatures above 400°C, (2) a precipitation reaction occurred in the CW alloy and welded alloy specimens between ~600°C and 800°C, and (3) recrystallization and grain growth processes occurred in all the specimens above ~900°C. The results that supported the precipitation reaction consisted of decreasing electrical resistivity from 600°C to ~800°C and of corresponding maxima in hardness near 700°C for the CW alloy and welded alloy specimens. The property measurements for the CW vanadium and annealed alloy specimens showed no evidence of the precipitation reaction.

EFFECTS OF OXYGEN AND HYDROGEN AT LOW PRESSURE ON THE MECHANICAL PROPERTIES OF V-Cr-Ti ALLOYS – J. R. DiStefano, B. A. Pint, J. H. DeVan (Oak Ridge National Laboratory), H. D. Röhrig (Projektleitung Kernfusion, Forschungszentrum Karlsruhe), and L. D. Chitwood (Oak Ridge National Laboratory)

Extended Abstract (the full paper will be published in the Journal of Nuclear Materials as Proceedings of the Ninth International Conference on Fusion Reactor Materials, October 10-15, 1999, Colorado Springs, Colorado).

The interest in vanadium alloys as a first-wall material in fusion reactors led to a study of the effects of oxygen and hydrogen on the mechanical properties of two V-Cr-Ti alloys. At temperatures of interest, reaction with small amounts of hydrogen or oxygen in the environment can lead to deleterious effects on the mechanical properties.

Hydrogen in V-Cr-Ti alloy affects its room temperature tensile properties. In the absence of an increase in oxygen concentration, matrix hardening, and a slight effect on total elongation were noted up to ~400 ppm (~2.2 at. %) hydrogen in the alloys. At higher concentrations, brittle behavior rapidly occurred.

In air at 0.1 MPa (1 atm), oxygen uptake was logarithmically dependent on exposure time at 400°C and parabolically dependent at 500°C. At lower oxygen partial pressures ($\leq 100^{-2}$ Pa), oxygen uptake at 400°C was below measurable limits after the first 10-25 h. At the lower pressures, the rate of uptake at 500°C was also parabolic, but the rate was much lower than in air and did not vary over the pressure range 10^{-2} to 10^{-4} Pa. The primary effect of oxidation at 500°C on room temperature tensile properties was to reduce ductility. There was little or no effect on yield strength or ultimate tensile strength.

Exposure of V-Cr-Ti alloys to low partial pressures of oxygen at high temperature resulted in oxygen absorption and internal oxidation. Characterization of a V-4Cr-4Ti alloy after oxidation and homogenization at 500°C revealed a microstructure with ultrafine oxide precipitates throughout the matrix and along the grain boundaries. However, bordering the grain boundaries was a zone denuded inn precipitates. Heat treatment at 950°C following oxidation resulted in large TiO_x precipitates in the matrix and grain boundaries. However, the denuded zone adjacent to the boundaries was retained. Tensile ductility of the V-Cr-Ti alloys was reduced by exposure to low pressure oxygen under the test temperature and pressure conditions. However, heat treatment at 950°C following oxidation was generally effective in recovering ductility irrespective of the initial annealing treatment or grain size.

THE EFFECT OF LASER WELDING PROCESS PARAMETERS ON THE MECHANICAL AND MICROSTRUCTURAL PROPERTIES OF V-4CR-4TI STRUCTURAL MATERIALS[§]

C. B. Reed, K. Natesan, Z. Xu, and D. L. Smith

Fusion Power Program, Argonne National Laboratory
9700 S. Cass Ave., Argonne, IL 60439, USA
Telephone: ++1 630 252-5970, FAX: ++1 630 252 5287, E-mail: cbreed@anl.gov

EXTENDED ABSTRACT for Reference [1]

V-Cr-Ti alloys are among the leading candidate materials for the first wall and other structural materials applications in fusion power reactors because of several important advantages including inherently low irradiation-induced activity, good mechanical properties, good compatibility with lithium, high thermal conductivity and good resistance to irradiation-induced swelling and damage. However, weldability of these alloys in general must be demonstrated, and specifically laser welding has high potential but must be developed. Laser welding is considered to be an attractive process for construction of a reactor due to its high penetrating power and potential flexibility.

This abstract summarizes the most recent results obtained in a systematic study conducted to examine the use of a pulsed Nd:YAG laser to weld sheet materials of V-Cr-Ti alloys and to characterize the microstructural and mechanical properties of the resulting joints. Deep penetration and defect-free welds were previously achieved[2] under an optimal combination of laser parameters including focal length of lens, pulse energy, pulse repetition rate, beam travel speed, and shielding gas arrangement. The key for defect-free welds was found to be stabilization of the keyhole and providing an escape path for the gas trapped in the weld. An innovative method was also developed to obtain deep penetration and oxygen contamination free welds. Oxygen and nitrogen uptake were reduced to levels only a few ppm higher than the base metal by design and development of an environmental control box. An effort directed at developing an acceptable postweld heat treatment showed that five passes of a diffuse laser beam over the welded region softened the weld material, especially in the root region of the weld.

Using Vanadium alloy, V-4 wt% Cr-4 wt% Ti, bead-on-plate (BOP) welds were produced on 4 mm thick sheets of the alloy using a 1.6 kW pulsed Nd:YAG laser with optical fiber beam delivery. Effects of laser parameters on depth of penetration, oxygen and nitrogen uptake, and microhardness, were determined experimentally. Three main tasks were studied:

(a) Determine the optimal parameters for full penetration, defect-free, laser welding of 4mm thick sheets of V-Cr-Ti alloys, and examine the microstructural characteristics of the welded sections, including base metal, heat-affected-region, and core of the weld.

(b) Evaluate the influence of different postweld heat treatments on microstructural characteristics and local hardness profiles.

(c) Determine the extent of oxygen uptake from the welding process, its influence on weld joint hardness, and minimize it.

Topics (a) and (b) have been reported previously[2]; a summary of the results for topic (c) is given here.

The most recent work focused on weld purity issues, starting with oxygen, carbon, and nitrogen uptake during weld processing[1]. Uptake of oxygen can lead to embrittlement of the alloy and therefore must be avoided. With laser schedule, beam travel speed, lens, and shielding gas flow identical to those which produced full penetration welds previously[2], two weld specimens, 990223B (23B) and 990223C (23C), were produced and the core of each weld was machined into chips and analyzed for O, C, and N. Oxygen, nitrogen, and carbon concentrations in laser-welded samples were analyzed by the Inert Gas Fusion (IGF) method. Results of those analyses, along with analyses of the base material adjacent to the welds (specimen 23A), are shown in Figure 1. Also shown in Figure 1 for comparison purposes, are reference analyses of O, C, and N from the original Heat 823665, from which the 4mm sheets were produced. It can be seen that specimens 23A and 23B obviously exhibit unacceptably large amounts of oxygen and nitrogen.

A custom-designed environmental control box (ECB) capable of purging with high-purity argon (99.995%) was integrated with the Nd:YAG laser to improve the quality of the welding atmosphere by minimizing oxygen and nitrogen uptake. Specimens were placed in the ECB with fixtures. High-purity argon was purged into the box from both sides and the flow rate was well controlled such that a slow flow of argon out from the slit on the top of the box could be formed This provided a good welding atmosphere to minimize the impurity uptake during welding. A shielding disk just above the slit enhanced the shielding effect and also provided a guiding surface for the lens protection gas[1].

Figure 1 shows that the welds produced in the ECB with nearly optimal shielding gas (12B and 12C) have the lowest oxygen content. Welds using the ECB but with a less than optimal gas shielding arrangement (09A and 09B) have higher oxygen content compared to those with nearly optimal shielding. The welds obtained without using the ECB have the highest oxygen content. The specimens were wiped with acetone before and after welding except specimen 09B, which was cleaned in a pickling solution after welding. The O, N, and C contents of welds produced using the ECB with near-optimal shielding gas are essentially the same as the values reported as the reference analysis for the starting material. Oxygen analyses obtained from the chip samples (23B & 23C) apparently include additional contamination. Subsequent specimens were not milled into chips prior to chemical analysis, but rather submitted as small bars. By design and development of this environmental control box method, oxygen and nitrogen uptake were reduced to levels only a few ppm higher than the base metal.

A microhardness profile across the width of weldment 12D showed only a slight increase in hardness in the weld metal, in comparison to that of the adjacent base metal[1].

In summary, a systematic study was conducted to examine the use of a pulsed Nd:YAG laser to weld sheet materials of V-Cr-Ti alloys and to characterize the microstructural and mechanical properties of the resulting joints. Deep penetration and defect-free welds were achieved under an optimal combination of laser parameters including focal length of lens, pulse energy, pulse repetition rate, beam travel speed, and shielding gas arrangement. The key for defect-free welds was found to be the stabilization of the keyhole and providing an escape path for the gas trapped in the weld. An innovative method was developed to obtain deep penetration and contamination-free welds. Oxygen and nitrogen uptakes in weldments were reduced to levels only a few ppm higher than the base metal, by design and development of an environmental control box. The effort directed at developing an acceptable postweld heat treatment showed that five passes of diffuse laser beam energy over the welded region softened the weld material, especially in the root region of the weld.

REFERENCES

1. "The Effect Of Laser Welding Process Parameters On The Mechanical And Microstructural Properties Of V-4Cr-4Ti Structural Materials", C. B. Reed, K. Natesan, Z. Xu, and D.L. Smith, presented at the 9th International Conference on Fusion Reactor Materials, Colorado Springs, Colorado, October 10-15, 1999.

2. Z. Xu, C. B. Reed, K. Natesan, and D. L. Smith, "Improvement of Laser Weld Quality of V-Cr-Ti Alloys," Fusion Reactor Materials Progress Report for the Period Ending June 30, 1999, Argonne National Laboratory, DOE/ER-0313/26, p. 49, September,.1999.

---

§The submitted manuscript has been created by the University of Chicago as Operator of Argonne National Laboratory ("Argonne") under contract No. W-31-109-ENG-38 with the U.S. Department of Energy. The U.S. Government retains for itself, and others acting on its behalf, a paid-up, nonexclusive, irrevocable worldwide license in said article to reproduce, prepare derivative works, distribute copies to the public, and perform publicly and display publicly, by or on behalf of the Government.

Work supported by the Office of Fusion Energy Sciences, U.S. Department of Energy, under Contract No. W-31-109-ENG-38.

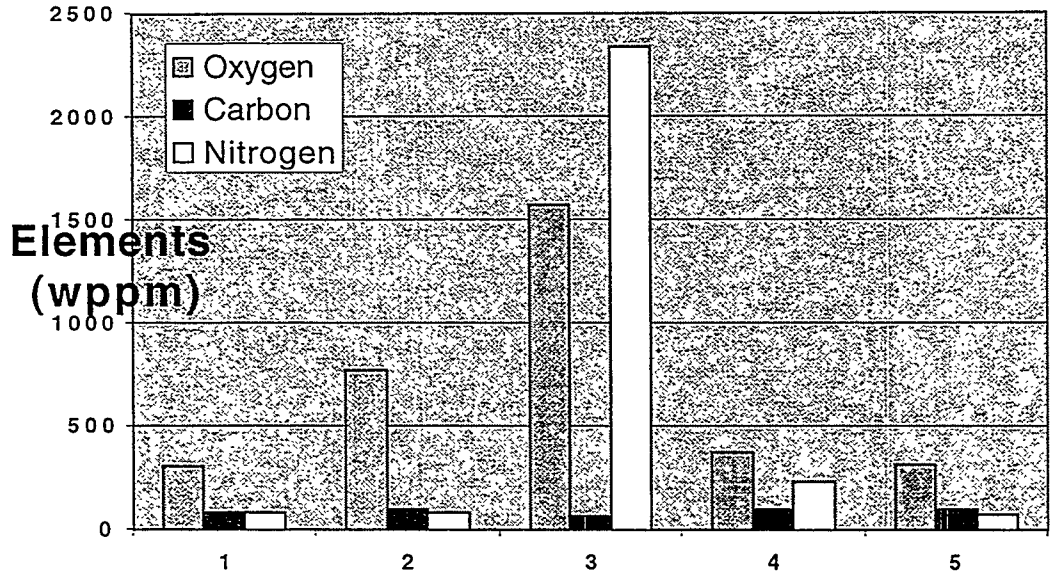

Analysis #	Specimen #	Welding Conditions	Lens	Beam travel speed (cm/s)	Sample form
1	Heat 832665	Reference Heat Analysis	-	-	-
2	23A	Base material	-	-	Chips
3	23B&23C	No ECB	76mm	1	Chips
4	09A&09B	ECB, Non-optimal gas flow	127mm	0.6, 0.5	Bar
5	12B&12C	ECB+ Optimal gas flow	127mm	0.4, 0.25	Bar

Figure 1. Chemical analysis results of laser welded V-Cr-Ti alloy samples from Group V welds.

PERFORMANCE OF V-Cr-Ti ALLOYS IN A HYDROGEN ENVIRONMENT*

K. Natesan and W. K. Soppet (Argonne National Laboratory)

OBJECTIVE

The objectives of this task are to (a) determine the hydrogen uptake of several heats of V-Cr-Ti alloys as a function of temperature and partial pressure of hydrogen (pH_2) in the exposure environment, (b) examine the microstructural characteristics of surfaces and cross sections of the alloys after exposure, (c) evaluate the influence of hydrogen uptake in low-pH_2 environments on the tensile properties and cracking propensity of the alloys at room and elevated temperatures, and (d) determine the effects of oxygen/hydrogen interactions on the tensile properties of the alloys.

EXTENDED ABSTRACT

A paper on this subject was presented at the 9th International Conference on Fusion Reactor Materials in Colorado Springs, Oct. 10-15, 1999. An extended abstract of that paper is given below.

A systematic study is being conducted to evaluate the performance of several V-Cr-Ti alloys after exposure to environments containing hydrogen at various partial pressures. The goal is to correlate the chemistry of the exposure environment with hydrogen uptake by the samples and the resulting influence on the microstructures and tensile properties of the alloys. Other variables of interest are the effect of initial grain size on hydrogen uptake and tensile properties, and the synergistic effects, if any, of oxygen and hydrogen on the tensile behavior of the alloys.

Experiments were conducted on specimens of various V-Cr-Ti alloys exposed to pH_2 levels of 0.05 and 3×10^{-6} torr at temperatures between 200 and 500°C. Negligible effect of H_2 was observed on either maximum engineering stress or uniform and total elongation. The uniform and total elongation values for the alloy ranged between 0.14-0.20 and 0.18-0.31, respectively, at temperatures between 200 and 500°C and in a pH_2 of<0.05 torr. However, uniform and total elongation decreased to 0.002 when the alloys were exposed at 500°C to 1.0 torr H_2 pressure. This corresponded to an H concentration of 358 wppm in the alloy.

Preliminary data from sequential exposures of the materials to low-pO_2 and several low-pH_2 environments were obtained in a subsequent study. The preexposure of the specimens to a low-pO_2 environment, followed by exposure to a pH_2 environment, resulted in O concentrations in a range of 550-2230 wppm and H concentrations in a range of 6-16 wppm. For example, a V-4Cr-4Ti specimen that was pretreated for 100 h in 3×10^{-6} torr pO_2 at 500°C and subsequently exposed for 100 h in a pH_2 of 3×10^{-6} torr at 500°C contained O, N, and H concentrations of 1030, 100, and 7 wppm,

* This work has been supported by the U.S. Department of Energy, Office of Fusion Science, under Contract W-31-109-Eng-38.

respectively. The specimen exhibited uniform and total elongation values of 0.15 and 0.23, respectively. TEM examination of the specimen showed precipitates measuring 100-200 Å in size, predominantly along the grain boundaries; these can be attributed to the pretreatment in low-pressure O_2 environment. Similarly, a V-4Cr-4Ti specimen that was pretreated for 100 h in 1×10^{-4} torr pO_2 at 500°C and subsequently exposed for 100 h in pH_2 of 3×10^{-6} torr at 500°C contained O, N, and H concentrations of 2000, 110, and 12 wppm, respectively. That specimen exhibited uniform and total elongation values of 0.14 and 0.18, respectively. Based on these results, we concluded that such a pretreatment had no significant effect on the tensile properties of the alloy, indicating no synergistic effect of O and H on the properties in the range of our investigation.

DEVELOPMENT OF ELECTRICALLY INSULATING COATINGS FOR SERVICE IN A LITHIUM ENVIRONMENT*

K. Natesan, M. Uz, and S. Wieder (Argonne National Laboratory)

OBJECTIVE

The objectives of this task are to (a) develop electrically insulating coatings, with emphasis on the basic understanding of the thermodynamic conditions and kinetics of coating development needed to achieve stable coatings of CaO that are compatible in an Li/Li-Ca environment; (b) perform detailed postexposure analysis of the surface layers by several electron/optical techniques to characterize the elemental and phase compositions, quantify stratification in the layers, and establish the role of compositional changes in the coating defects and microstructure; (c) measure the electrical resistance of the coatings, before and after exposure external to Li; and (d) establish optimal procedures from the standpoint of sample preparation procedures, exposure time and temperature, and sequence of operations in order to obtain reliable and reproducible coatings with adequate electrical resistance for use in an Li environment.

EXTENDED ABSTRACT

A paper on this subject was presented at the 9th International Conference on Fusion Reactor Materials in Colorado Springs, Oct. 10-15, 1999. An extended abstract of that paper is given below.

Several experiments were conducted to develop electrically insulating CaO coatings on a V-4Cr-4Ti alloy for application in an Li environment. Coatings were developed by a vapor phase transport process external to Li and in-situ in an Li-Ca environment at elevated temperature. In the vapor phase study, several geometrical arrangements were examined to obtain a uniform coating of Ca on the specimens, which were typically coupons measuring 5 to 10 x 5 x 1 mm. After Ca deposition from the vapor phase, the specimens were oxidized in a high-purity argon environment at 600°C to convert the deposited metal into oxide. The specimens exhibited insulating characteristics after this oxidation step. Several promising coated specimens were exposed to high-purity Li at 500°C for 48-68 h to examine coating integrity. Microstructural characteristics of the coatings were evaluated by scanning electron microscopy and energy-dispersive X-ray analysis. Electrical resistance of the coatings was measured between room temperature and 700°C before and after exposure to Li by a two-probe method.

Results showed that thick adherent coatings can be fabricated by thermal/chemical vapor deposition process, especially if a double Ca treatment is applied. Coatings developed in-situ in an Li-Ca environment had thicknesses much less than desired. Furthermore, the coating composition was nonuniform, with significant presence of V in several locations on the coated surface. Microstructural analysis of the coatings developed by the thermal/chemical process showed almost 100% CaO over a coating thickness of 20-30 μm; electrical resistance of such coatings was at least two orders of

* This work has been supported by the U.S. Department of Energy, Office of Fusion Science, under Contract W-31-109-Eng-38.

magnitude higher than the minimum required for blanket application. Electrical resistance of in-situ-developed coatings was adequate at temperatures up to ≈350°C, but decreased substantially at higher temperatures. The results obtained in this study indicate that CaO is a viable coating for a V-Li advanced blanket, but needs significant additional effort, especially from the standpoint of structure/composition relationship to its electrical resistance. Furthermore, in-situ measurement of resistance in Li is required in order to simultaneously evaluate the coating integrity, its resistance, and Li compatibility.

BIAXIAL THERMAL CREEP OF V-4Cr-4Ti AT 700°C AND 800°C – R. J. Kurtz and M. L. Hamilton (Pacific Northwest National Laboratory)*

Extended abstract of a paper submitted to the Journal of Nuclear Materials as part of the proceedings of the 9th International Conference on Fusion Reactor Materials, Colorado Springs, Colorado, USA, October 10-15, 1999.

EXTENDED ABSTRACT

A study of the biaxial thermal creep properties of V-4Cr-4Ti (Heat No. 832665) is being performed using pressurized tube specimens. The specimen geometry, stress levels and test temperatures are designed to compliment ongoing efforts to characterize the irradiation creep performance of the same alloy [1-4]. The current study is a companion to another research effort underway at Argonne National Laboratory [5] to evaluate the uniaxial creep behavior of V-Cr-Ti alloys.

Sections of V-4Cr-4Ti tubing with a nominal 4.572 mm OD by 0.254 mm wall thickness and ~45% cold-work level were obtained from Argonne National Laboratory for fabricating creep specimens. Details of the tubing fabrication process have been reported previously [2]. Specimens were pressurized with high-purity helium gas to mid-wall effective stress levels below the uniaxial yield strength. The specimens were loosely wrapped with Ti foil and then placed in an ultra-high vacuum furnace and heated to 700 or 800°C. Periodically the specimens were removed from the furnace to measure the change in OD with a high-precision laser profilometer. Effective (von Mises) mid-wall creep strains were computed from the diameter change data.

The stress dependence of the effective secondary creep rate is presented in Figure 1 along with uniaxial data obtained by Chung et al., at 600°C and higher stresses [6]. All of the data in Figure 1 were fitted to

$$\dot{\varepsilon}_e = A\sigma_e^n \qquad (1)$$

where $\dot{\varepsilon}_e$ is the effective secondary creep rate, σ_e is the effective stress, A and n are constants. Note the stress exponent, n, is 9.9 for the 600°C data gathered at stress levels greater than 300 MPa. For the higher temperature data generated at stress levels less than 160 MPa n is between 2.7 and 3.7. This difference in stress exponent is not due to biaxial versus uniaxial specimen geometries, but is characteristic of creep in vanadium and vanadium alloys [3-8]. Values of $n \sim 3$ suggest that dislocation creep is the predominant deformation mechanism for the thermal and stress conditions employed here [7]. Microstructural studies of several failed creep specimens lend additional support for this conclusion [8].

The activation energy for creep in V-4Cr-4Ti was estimated at effective stress levels of approximately 70, 90 and 120 MPa. Equation (2) was used to compute the activation energy, Q, as

---

*Pacific Northwest National Laboratory (PNNL) is operated for the U.S. Department of Energy by Battelle Memorial Institute under contract DE-AC06-76RLO-1830.

$$Q = \frac{R\ln(\dot{\varepsilon}_1/\dot{\varepsilon}_2)}{1/T_1 - 1/T_2} \qquad (2)$$

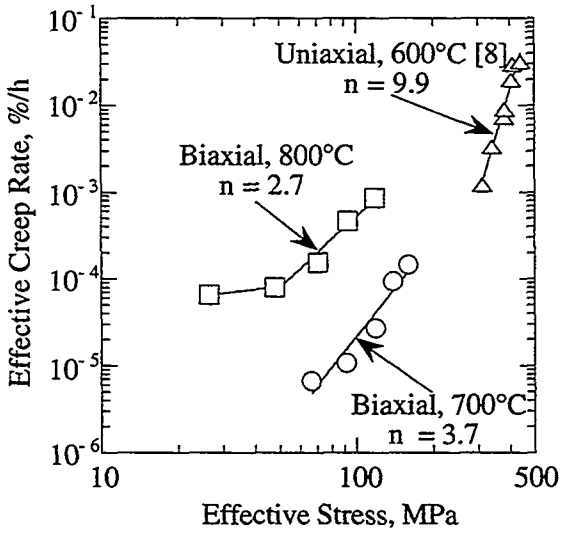

Figure 1. Stress dependence of the minimum creep rate of unirradiated V-4Cr-4Ti (Heat 832665) between 600-800°C.

where R is the universal gas constant, and $\dot{\varepsilon}_1$ and $\dot{\varepsilon}_2$ are the effective creep rates at temperatures T_1 and T_2. Activation energies ranging from 272 to 326 kJ/mole were obtained, with an average value of 299 kJ/mole. The activation energy did not vary inversely with stress as has been observed for pure vanadium [9]. These values are somewhat greater than the activation energy for self-diffusion in pure vanadium, which is about 270 kJ/mole in the 700 to 800°C temperature range [10]. This result lends additional support to the observation that the predominant creep mechanism in V-4Cr-4Ti at the temperatures and stresses investigated in this study is climb-assisted glide of dislocations. It also suggests that solute-drag may limit the rate at which dislocations can climb past obstacles in the microstructure, leading to a higher activation energy for creep. A recent study of the high-temperature deformation behavior of V-4Cr-4Ti shows that dynamic strain aging occurs in this material at temperatures up to 750°C [11]. This indicates that solutes are mobile at the test temperatures investigated in this study and could impede dislocation climb.

A comparison of the creep-rupture behavior of specimens tested here to data gathered on V-Cr-Ti alloys [3,5,6,12] and other fusion relevant materials [13] is presented in Figure 2. Both uniaxial and biaxial data are plotted in Figure 2. The data sets are correlated using the Larsen-Miller parameter (LMP), that is

$$P = T(20 + \log t_r)/1000 \qquad (3)$$

where T is the test temperature in K and t_r is the time-to-rupture in hours. Since failure strains for the vanadium alloys were generally large, a good correlation between uniaxial

(constant load tests) and biaxial (constant stress tests) data might not be expected, but this is obviously not the case here. The trend line for V-4Cr-4Ti is quite reasonable, but the data are too sparse to firmly establish an LMP creep-rupture correlation for this alloy. Comparison with V-(10-15)Cr-5Ti data [3,12] indicates that an additional 6 to 9% Cr

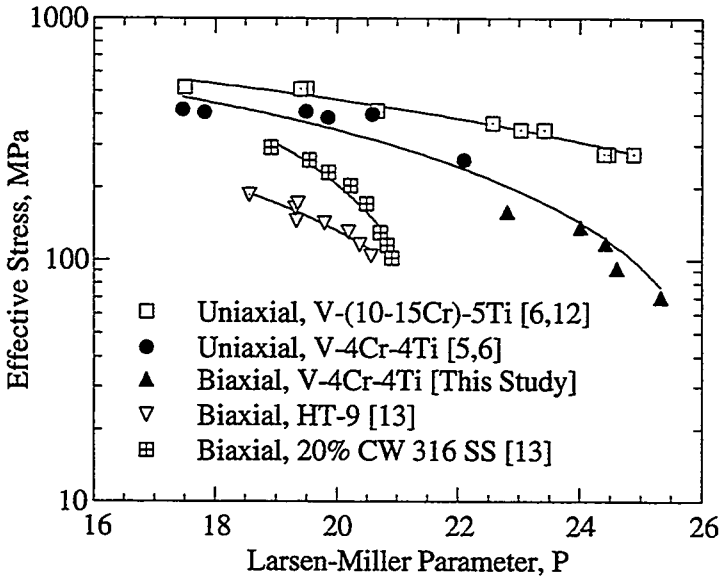

Figure 2. Larsen-Miller Parameter correlation for creep-rupture of unirradiated V-4Cr-4Ti (Heat 832665).

improved the creep-rupture properties of this alloy system considerably. Comparing the performance of V-4Cr-4Ti with HT-9 [13] and 20% cold-worked 316 stainless steel [13] shows that V-Cr-Ti alloys exhibit much better creep-rupture resistance and therefore could tolerate higher average wall temperatures.

An on-going study of the thermal creep properties of V-4Cr-4Ti is being performed using pressurized tube specimens. The secondary creep rate was found to be power-law dependent on the applied stress with a stress exponent of 3.7 at 700°C and 2.7 at 800°C. The average activation energy for creep of V-4Cr-4Ti was 299 kJ/mole, which is quite close to the activation energy for self-diffusion in pure vanadium in this temperature regime. The predominant mechanism of creep deformation for the conditions employed in this study is most likely climb-assisted dislocation motion. Creep-rupture data from uniaxial and biaxial tests of V-4Cr-4Ti specimens yields a reasonable LMP correlation. On this basis the creep-rupture properties of V-4Cr-4Ti were shown to be slightly worse than V-(10-15)Cr-5Ti and significantly better than other candidate fusion structural materials such as HT-9 and 20% cold-worked 316 stainless steel.

REFERENCES

[1] J. M. Vitek, D. N. Braski and J. A. Horak, J. of Nucl. Mater. 141-143 (1986) pp. 982-986.

[2] V. M. Troyanov, et al., J. of Nucl. Mater. 233-237 (1996) pp. 381-384.

[3] H. Tsai, M. C. Billone, R. V. Strain, D. L. Smith and H. Matsui, J. of Nucl. Mater. 258-263 (1998) pp. 1471-1475.

[4] H. Tsai, R. V. Strain, M. C. Billone, T. S. Bray and D. L. Smith, in: Fusion Materials: Semiannual Progress Report for Period Ending June 30, 1999, DOE/ER-0313/26, pp. 36-37.

[5] K. Natesan, W. K. Soppet and D. L. Rink, in: Fusion Materials: Semiannual Progress Report for Period Ending June 30, 1999, DOE/ER-0313/26, pp. 20-24.

[6] H. M. Chung, B. A. Loomis and D. L. Smith, J. of Nucl. Mater. 212-215 (1994) pp. 772-777.

[7] G. E. Dieter, "Mechanical Metallurgy," McGraw-Hill, New York, (1986) p. 447.

[8] D. S. Gelles, M. L. Hamilton and R. J. Kurtz, in: Fusion Materials: Semiannual Progress Report for Period Ending June 30, 1999, DOE/ER-0313/26, pp. 11-19.

[9] K. R. Wheeler, E. R. Gilbert, F. L. Yaggee and S. A. Duran, Acta Metall. Vol. 19 (1971) pp. 21-26.

[10] D. L. Harrod and R. E. Gold, Int. Metals Rev. 4 (1980) pp. 163-221.

[11] A. F. Rowcliffe, D. T. Hoelzer and S. J. Zinkle, in: Fusion Materials: Semiannual Progress Report for Period Ending June 30, 1999, DOE/ER-0313/26, pp. 25-32.

[12] R. E. Gold and R. Bajaj, J. of Nucl. Mater. 122-123 (1984) pp. 759-766.

[13] B. A. Chin, in: Proceedings of Topical Conference on Ferritic Alloys for use in Nuclear Energy Technologies (1983) pp. 593-599.

2.0 SILICON CARBIDE COMPOSITE MATERIALS

THERMAL CONDUCTIVITY OF SIC AND C FIBERS - I - G. E. Youngblood and D. J. Senor (Pacific Northwest National Laboratory)*, W. Kowbel and J. Webb (MER Corporation), and Akira Kohyama (Kyoto University, Japan).

OBJECTIVE

The objective of this task is to examine SiC fibers and SiC/SiC composites fabricated by various processing methods designed to improve the composite thermal conductivity. Specifically, it is desired to increase the thermal conductivity of these composites to meet expected thermal transport requirements for advanced fusion energy systems.

SUMMARY

Several rod-shaped specimens with uniaxially packed fibers (Hi-Nicalon, Hi-Nicalon Type S, Tyranno SA and Amoco K1100 types) and a pre-ceramic polymer matrix have been fabricated. By using appropriate analytic models, the bare fiber thermal conductivity (K_f) and the interface thermal conductance (h) will be determined as a function of temperature up to 1000°C before and after irradiation for samples cut from these rods. Initial results are: (1) for unirradiated Hi-Nicalon SiC fiber, K_f varied from 4.3 up to 5.9 W/mK for the 27-1000°C range, (2) for unirradiated K1100 graphite fiber, K_f varied from 576 down to 242 W/mK for the 27-1000°C range, and (3) h = 43 W/cm^{2}K at 27°C as a typical fiber/matrix interface conductance.

PROGRESS AND STATUS

Currently available fiber-reinforced (Hi-Nicalon) SiC/SiC composites with a chemical vapor infiltrated (CVI) SiC matrix have a transverse thermal conductivity (K_t) of about 13 and 8 W/mK at 300K and 1273K, respectively. Neutron irradiation tends to degrade the K_t-values of this type of SiC/SiC by about 25% and 50% for 300K and 1273K, respectively (i.e., to 4 W/mK or below) [1]. A K_t-value of 4 W/mK for SiC/SiC is at most about 25% of that desired for anticipated fusion power system applications [2]. By comparison, thermal conductivity values of unirradiated, high-purity and dense monolithic CVD-SiC, whose values represent an upper limit attainable for SiC, can exceed 300 and 60 W/mK at 300K and 1273K, respectively [3]. These high K-values indicate that there is room for substantial improvement of the thermal transport properties in SiC/SiC. Nevertheless, attaining a K_t-value of 30 W/mK at 1273K for unirradiated SiC/SiC, one-half that of monolithic CVD-SiC at this temperature and the approximate K_t-value needed to provide a desired 15 W/mK material during irradiation, will present a serious challenge.

The cause of low K_t-values for SiC/SiC has been attributed to the approximately 10-15% porosity in the matrix, and particularly to the presence of numerous, fairly large interlaminar voids [4]. The relatively low K-values of the fiber reinforcement, which makes up about another 40% of a typical composite volume, also contribute to low overall K_t-values. Furthermore, thermal conductance across the various interfaces (fiber/matrix or matrix/matrix) or thin interphases (purposely applied at the fiber/matrix interface to provide composite toughness) is a very important factor affecting K_t [5]. Better control of the porosity geometry and amount (especially the reduction of the interlaminar void content) can help improve the K_t-values somewhat. However, to achieve significant improvement in the SiC/SiC K_t-values, both the fiber thermal conductivity and the interface thermal conductances must be improved.

---

* Pacific Northwest National Laboratory (PNNL) is operated for the U.S. Department of Energy by Battelle Memorial Institute under contract DE-AC06-76RLO-1830.

Fortunately, new near-stoichiometric SiC fibers have recently become available that claim to have K-values of about 50 W/mK (e.g., Tyranno™ SA and Dow™ Sylramic), a value significantly greater than the K-values of widely used Nicalon™ or Hi-Nicalon™ fibers (≈2 and 5 W/mK, respectively) [6,7]. Furthermore, the new SiC fibers promise to be more radiation resistant, in which case the rather large differential swelling/shrinking observed between the fiber and matrix components in composites made with first generation Nicalon SiC fibers should be considerably alleviated [8]. Improved dimensional stability of the fibers, in turn, should lead to improved fiber/matrix interface conductances in SiC/SiC composites. By using such new fibers and by careful design of the fiber/matrix interface, the opportunity to make significant improvements in the thermal transport of SiC/SiC composites now exists.

The use of 3D SiC fiber architectures has shown some promise to improve K_t-values [9]. Another method to improve K_t-values, now being investigated by MER Corp. (Tucson, AZ) under an SBIR program with the DOE Office of Fusion Energy Sciences, consists of "spiking" conventional 2D-SiC/SiC composite with high thermal conductivity, graphite fiber bundles in the transverse or Z-direction. The thermal conductivity of high modulus graphite fibers is very anisotropic, but can exceed 1000 W/mK along the fiber length [10].

In common, all strategies to improve K_t-values of SiC/SiC will require the use of fibers with correspondingly high K-values. This work describes a method to evaluate fiber K-values before and after irradiation up to 1000°C, which covers the relevant temperature range 600-1000°C for potential SiC/SiC fusion applications.

In this method, rod-shaped composites (20 mm long x 6.0 mm dia) with uniaxial fiber alignment were fabricated. The rods were sliced into several discs (about 2.0 mm thick) appropriate for thermal diffusivity measurements [11]. The composite matrix was made from Ceraset™, a pre-ceramic liquid polymer at RT that is converted to SiC by pyrolyzing in an argon atmosphere. The Ceraset matrix was purposely made amorphous so that the fiber contribution would dominate the overall composite K-values. To do this, a final heat treatment was given at 1100°C, a temperature high enough to exsolve most of the gaseous components but well below the 1600°C temperature required for SiC crystallization in Ceraset. Also, to further improve the accuracy of the fiber K-value determinations a high fiber packing density (>60%) was used.

The thermal diffusivity also will be measured for SiC/SiC samples with normal 2D- or 3D- fiber architectures. Knowing the K-values of the bare fiber and matrix components and by using appropriate constituent thermal conductivity models that represent the particular SiC/SiC composite architecture, the interface thermal conductance values can then be investigated.

Analysis

First, the overall thermal diffusivity $\alpha(T)$ of a uniaxial composite with the fibers aligned parallel to the heat transport direction (assumed to be one-dimensional and effectively homogeneous) was measured using the laser flash diffusivity technique [11]. The effective composite thermal conductivity (K_{eff}) was calculated from:

$$K_{eff}(T) = \alpha_{meas}(T)C_{eff}(T)\rho_{bulk}(T) \qquad (1)$$

where the composite specific heat $C_{eff}(T)$ was calculated from:

$$C_{eff}(T) = F_f C_f(T) + F_m C_m(T) \qquad (2)$$

with F_i = weight fractions and $C_i(T)$ = component specific heats. In the above equations, several terms were determined as functions of temperature (T) and the subscript i = f or m stands for fiber and matrix, respectively. The bulk density, $\rho_{bulk}(T)$, was determined from the sample weight and geometrical volume corrected for volume change due to thermal expansion.

Second, the bare fiber thermal conductivity, $K_f(T)$, was extracted from a simple series model expression for the parallel fiber alignment case given by:

$$K_{eff}(T) \approx f_f K_f(T) + f_m K_m(T) \qquad (3)$$

with f_i = volume fractions and K_i = component K-values. Note that the sum of f_f and f_m, estimated by image analysis from several micrographic views of polished rod cross-sections, may not necessarily be equal to one since the rods also contained a void fraction. The matrix contribution (K_m) was determined separately by measuring $\alpha(T)$ of a sample formed only from matrix material (monolithic Ceraset™ heat-treated at 1100°C).

The use of Eqns (1) and (3) assumes 1D heat flow or equilibrium conditions perpendicular to the heat flow direction. Then Eqn (3) can be used to calculate $K_f(T)$, and Eqn (1) is used again to calculate the fiber thermal diffusivity, $\alpha_f(T)$, from values of fiber specific heat, density and $K_f(T)$.

Third, $\alpha(T)$ was measured for a SiC/SiC sample with transverse fiber alignments. For the simple case of uniaxial fibers perpendicular to the heat transport direction, according to Hasselman and Johnson [12], $K_{eff}(T)$ is approximately given by:

$$K_{eff} \approx K_m[(K_f/K_m - 1 - K_f/ah)f_f + (1 + K_f/K_m + K_f/ah)] \times [(1 - K_f/K_m + K_f/ah)f_f + (1 + K_f/K_m + K_f/ah)]^{-1} \qquad (4)$$

with K_i = component conductivity, a = fiber radius, f_f = fiber volume fraction, and h = the interfacial thermal conductance in W/m^2K. From the measured value of $K_{eff}(T)$ for the transverse configuration of the composite, and the already determined values of a, f_f, K_m and K_f, h(T) was backed out of Eqn (4).

The approximation given by Eqn (4) is fairly good for the range $0.1 < K_f/K_m < 10$ and when $f_f <$ 30% [13]. In this expression, the product "ah" is equivalent to the thermal conductivity of an interphase layer making perfect thermal contact with both the fiber and matrix. For the limiting case (ah) >> K_f (perfect fiber/matrix thermal contact), Eqn (4) reduces to the Releigh-Maxwell conductivity expression for a dilute distribution of conducting cylinders in a matrix. When ah -> 0 (perfectly insulated fibers), K_{eff} approaches the limiting value $K_m(1-f_f)/(1+f_f)$.

For this analysis, h(T) includes the combined effect of transverse conduction through a thin interphase coating and across any porosity or other mismatch thermal barriers that might occur at the fiber/matrix interface. For temperatures less than about 1200K, h(T) will be dominated by the asperities of the interface contacts and the conduction through any gaseous medium contained within intervening porosity. A separation of the relative conductance contributions through actual contacts and a gaseous medium can be obtained by performing the thermal diffusivity measurements in vacuum and in a controlled atmosphere [14]. Furthermore, K_m itself may be an effective conductivity when the matrix contains porosity or filler particles.

Results

In this section, some preliminary results are presented for the Hi-Nicalon™ and K1100™ fibers. Hi-Nicalon™ is a SiC-based fiber type made by Nippon Carbon Co. while K1100™ is a high

modulus graphite fiber with high thermal conductivity made by Amoco. Preliminary values of $C_{eff}(T)$, $k_f(T)$ and $\alpha_f(T)$ determined for the Hi-Nicalon fiber and $k_f(T)$ for the K1100 graphite fiber are given in Table 1.

Table 1. Thermal transport properties of Hi-Nicalon SiC and K1100 graphite fibers.

Temperature (K)	Hi-Nic $C_{eff}(T)$ (J/gK)	Hi-Nic $k_f(T)$ (W/mK)	Hi-Nic $\alpha_f(T)$ (cm^2/s)	K1100 $k_f(T)$ (W/mK)
300	0.689	4.29	0.0232	576
400	0.904	5.41	0.0223	495
500	1.016	5.68	0.0208	430
600	1.088	5.75	0.0197	380
700	1.140	5.72	0.0187	342
800	1.183	5.65	0.0178	313
900	1.219	5.61	0.0172	293
1000	1.252	5.59	0.0167	278
1100	1.283	5.67	0.0166	266
1200	1.312	5.78	0.0165	255
1300	1.339	5.91	0.0166	242

The bulk density of the particular batch of Hi-Nicalon fiber examined, measured by the liquid gradient technique, was 2.69 g/cc. The average Hi-Nicalon fiber diameter, determined by image analysis, was 13.8 ± 1.8 μm [8]. The manufacturer (Nippon Carbon Co.) lists the chemical composition (in wt. %): Si (62.4), C (37.1), O (0.5) and C/Si (atomic) = 1.39. From these values, the weight and volume fractions of the components SiC, C and SiO_2 in Hi-Nicalon fiber were calculated to be: 0.882, 0.107 and 0.011 (weight) and 0.819, 0.168 and 0.013 (volume), respectively.

The free C-content in Hi-Nicalon fiber is relatively high and consists of turbostratic aggregates. According to Hochet, et al, in Hi-Nicalon the C-aggregates are approximately 8-10 atomic layers thick by 2-5 nm in length [15]. These C-aggregates probably have a marked influence on the thermal (and electrical) conductivity of Hi-Nicalon fiber and likely are responsible for the peculiar temperature dependence of $K_f(T)$ exhibited by Hi-Nicalon. Furthermore, the presence of these C-aggregates probably affects the dimensional stability of Hi-Nicalon during irradiation.

Although there is considerable uncertainty when using Eqn (4) to calculate h(T), the 300K value of h(T) was ≈43 W/cm^2K, which agrees fairly well with literature values determined for similar composites: 40 W/cm^2K and 29 W/cm^2K (by S. Graham [13] and H. Bhatt, et al [5], respectively). Obviously, a radiation induced swelling/shrinking mismatch between fiber and matrix components could also affect h(T). Such an effect on the transverse thermal conductivity in irradiated SiC/SiC has been neglected in previous studies, and needs to be analyzed. As previously discussed, high values of both K_f and h are necessary to ensure high transverse thermal conduction in a SiC/SiC composite. Also, high values of K_f and h are desired to provide effective thermal conduction paths around micro-cracked regions in the matrix for conduction parallel to the fibers in a SiC/SiC composite. The behavior of h(T) during and after irradiation should be of keen interest and importance.

Finally, the extremely high K_f-values determined for the K1100 graphite fiber (40-100 times that of Hi-Nicalon) confirm that the strategy of spiking 2D-SiC/SiC in the Z-direction with these fibers to improve K_t has merit. The effect of irradiation on $K_f(T)$ for the K1100 fiber also will be of keen interest and importance.

FUTURE WORK

The thermal diffusivity data for the uniaxial rod samples made from the Hi-Nicalon, Hi-Nicalon Type S and Tyranno SA SiC fibers and the K1100 graphite fibers will be analyzed before and after irradiation. Twenty-eight (28) fiber and four (4) CVD-SiC thermal diffusivity disc samples will be irradiated in the ATR reactor at 300°C to a dose of 1.5 dpa commencing in June, 2000. The samples should be available for final analysis by the end of year 2000.

ACKNOWLEDGMENTS

This work is a joint effort funded by the US DOE Fusion Energy and the Japan Monbusho programs. Also, part of this work is being supported by a DOE-SBIR, Phase I (Contract DE-FG03-99ER82823) with the MER Corporation, Tucson, AZ.

REFERENCES

[1] D.J. Senor, G.E. Youngblood, C.E. Moore, D.J. Trimble, G.A. Newsome and J.J. Woods, "Effects of Neutron Irradiation on Thermal Conductivity of SiC-Based Composites and Monolithic Ceramics," Fusion Technology 30(3), 943-955 (1996).

[2] R.H. Jones, "IEA Agreement – Performance Requirements for Structural Applications of SiC/SiC," p. 196 in the Proceedings of the IEA International Workshop on SiC/SiC Ceramic Composites for Fusion Structural Applications, 28-29 October 1996, Ispra (Va), Italy.

[3] Jitendra S. Goela and Michael A. Pickering, "Chemical Vapor Deposited SiC for High Thermal Conductivity Applications," paper S1-006-99 presented at the 51st Pacific Coast Regional Meeting of the American Ceramic Society, Oct 27-29, 1999, Bellevue, WA.

[4] G.W. Hollenberg, C.H. Henager, Jr., G.E. Youngblood, D.J. Trimble, S.A. Simonson, G.A. Newsome and E. Lewis," The Effect of Irradiation on the Stability and Properties of Monolithic and SiC_f/SiC Composites up to 25 dpa," J. Nucl. Mater. 219, 70-86 (1995).

[5] Hemanshu Bhatt, Kimberly Y. Donaldson, D.P.H. Hasselman and Ramakrishna T. Bhatt, "Role of Interfacial Carbon Layer in the Thermal Diffusivity/Conductivity of SiC Fiber-Reinforced Reaction-Bonded Si_3N_4 Matrix Composites," J. Amer. Ceram. Soc. 75(2), 334-340 (1992).

[6] K. Kumagawa, H. Yamaoka, M. Shibuya and T. Yamamura, "Fabrication and Mechanical Properties of New Improved Si-M-C-(O) Tyranno Fibers," p. 65 in Ceram. Eng. and Sci. Proc. 19(3), 1998.

[7] Jon Lipowitz, "Sylramic™ Silicon Cabide Fiber," p. 147 in Ceram. Eng. and Sci. Proc. 18(3), 1997.

[8] G.E. Youngblood, R.H. Jones, Akira Kohyama and L.L. Snead, "Radiation response of SiC-based fibers," J. Nucl. Mater. 258-263 (1998) 1551-56.

[9] L. Giancarli, J.P. Bonal, G. Le Marois and J.F. Salavy," SiC/SiC Composites as Structural Material for Self-Cooled Pb-17Li Blankets," p.35 in the Proceedings of the IEA International

Workshop on SiC/SiC Ceramic Composites for Fusion Structural Applications, 28-29 October 1996, Ispra (Va), Italy.

[10] Jean-Babtiste Donnet and Roop Chand Bansal, p. 362 in Carbon Fibers, 2nd edition, Marcel Dekker, Inc., New York (1990).

[11] D.J. Senor, G.E. Youngblood, D.V. Archer and C.E. Chamberlin, "Recent Progress in Thermal Conductivity Testing of SiC-based Materials for Fusion Reactor Applications," p. 102 in the Proceedings of the Third IEA Workshop on SiC/SiC Ceramic Composites for Fusion Structural Applications, January 29-30, 1999, Cocoa Beach, FL.

[12] D.P.H. Hasselman and Lloyd F. Johnson, "Effective Thermal Conductivity of Composites with Interfacial Thermal Barrier Resistance," J. Comp. Mater. 21, 508-515 (1987).

[13] Samuel Graham, "Random geometry influences on effective thermal conductivity," Chapter V in PhD thesis, Georgia Institute of Technology, Atlanta, GA, 1999.

[14] Kimberly Y. Donaldson, Barbara D. Trandell, Yangsheng Lu and D.P.H. Hasselman, "Effect of Delamination on the Transverse Thermal Conductivity of a SiC Fiber-Reinforced SiC-Matrix Composite," J. Amer. Ceram. Soc. 81(6), 1583-88 (1998).

[15] N. Hochet, M.H. Berger and A.R. Bunsell, "Microstructural evolution of the latest generation of small-diameter SiC-based fibers tested at high temperatures," J. of Microscopy 185(2), 243-258 (1997).

REACTION-BASED SIC MATERIALS FOR JOINING SILICON CARBIDE COMPOSITES FOR FUSION ENERGY - C. A. Lewinsohn and R. H. Jones (Pacific Northwest National Laboratory)*, M. Singh (NASA Glenn Research Center, Ohio), H. Serizawa (Osaka University, Japan), and Y. Katoh and A. Kohyama (Kyoto University, Japan).

OBJECTIVE

Reliable and practical joining techniques are required to enable the use of silicon carbide composites in fusion energy systems. Based on criteria relevant to fusion applications, silicon carbide has been selected as a promising joint material. The objective of this work is to evaluate the thermal stability and mechanical properties of silicon carbide joints fabricated via reaction-based methods.

SUMMARY

The fabrication of large or complex silicon carbide-fiber-reinforced silicon carbide (SiC/SiC) components for fusion energy systems requires a method to assemble smaller components that are limited in size by manufacturing constraints. Previous analysis indicates that silicon carbide should be considered as candidate joint materials. Two methods to obtain SiC joints rely on a reaction between silicon and carbon to produce silicon carbide. This report summarizes preliminary mechanical properties of joints formed by these two methods. The methods appear to provide similar mechanical properties. Both the test methods and materials are preliminary in design and require further optimization. In an effort to determine how the mechanical test data is influenced by the test methodology and specimen size, plans for detailed finite element modeling (FEM) are presented.

PROGRESS AND STATUS

Introduction

A limitation of SiC/SiC composite materials is that they can only be produced in limited sizes and shapes. Therefore, to fabricate a complete fusion energy system a method of joining SiC/SiC components is required. In fusion energy systems utilizing silicon carbide first-wall materials it would be undesirable to use a joining technique that introduces dissimilar materials at the inner face of the first wall. In addition, to avoid poisoning the plasma the first wall must be hermetic. Therefore, two attractive methods of joining silicon carbide with other forms of silicon carbide have been developed: reaction bonding [1-4], and preceramic polymer adhesives [5-11]. In this paper, preliminary results obtained from joints formed by two reaction-based methods will be presented. Reaction bonding consists of adding molten silicon to a mixture of carbon and silicon carbide powders, which subsequently react to form silicon carbide with small amounts of residual silicon or porosity. Reaction forming consists of adding molten silicon metal to a porous carbon network, which subsequently converts to silicon carbide with minor amounts of residual silicon metal or porosity. Although design criteria for SiC/SiC and joints have not been determined there are several practical test methods for measuring the failure conditions under a variety of stress states. To obtain a better correlation between anticipated service stresses and test methods a study utilizing FEM has been initiated and will be described.

---

* Pacific Northwest National Laboratory (PNNL) is operated for the U.S. Department of Energy by Battelle Memorial Institute under contract DE-AC06-76RLO-1830.

EXPERIMENTAL TECHNIQUE

To evaluate the suitability of joints formed by the reaction-based forming approach, plates of monolithic silicon carbide (Hexoloy SA, Carborundum Co., Niagara, NY) were joined using the ARCjoinT technique at NASA Glenn Research Center [2-4]. Two plates of monolithic silicon carbide, approximately 4 mm thick, were cut into 25 mm-long by 30 mm-wide pieces. A carbonaceous mixture was applied to the ends of the plates that were to be joined and this was cured at 110-120°C for 10 to 20 minutes. Subsequently, a slurry of pure silicon powder was applied to the surface of the joint region and heated up to 1425°C for 5-10 minutes. Capillary forces drew the molten silicon into the joint region where it reacted with the carbon to form silicon carbide. The resulting joint material consisted of silicon carbide with controllable amounts of silicon and other phases as determined by the composition of the raw materials and infiltrant.

A limited number of joints between pieces of silicon carbide composite material were also fabricated. This composite was reinforced with Hi-Nicalon fibers (Nippon Carbon Co., Yokohama, Japan) that had been coated with a 1 μm-thick layer of carbon prior to matrix infiltration via chemical vapor infiltration. In addition, an approximately 2 μm-thick layer of silicon carbide was deposited on the outside of the composite to inhibit oxidation at high-temperatures.

Plates of monolithic silicon carbide (Hexoloy SA, Carborundum Co., Niagara, NY) were also joined using a reaction bonding technique. One or two layers of SiC and C powders held in tape form by organic binding agents were placed between two plates of monolithic silicon carbide that was cut into 25 mm-long by 30 mm-wide pieces. The plates were held in a proprietary fixturing and heating apparatus capable of rapid heating and cooling (Busek Co. Inc., Natick, MA). The specimens were heated to 1425°C for 10 to 30 minutes, under applied pressure ranging from $6.90 - 9.65 \times 10^5$ Pa.

The plates that were joined using the methods described above were cut into bars that were 44 x 4 x 4 mm. The bars were cut so that the joint was at the middle of the bar and the plane of joining was aligned so that it was parallel to the applied load. Several of the bars were annealed for 100 h, at 1100°C, in a vacuum furnace or in flowing, gettered argon. Mechanical tests were performed by applying flexural loading by 1/4, four-point bending (Figure 1a) to the bars described above. This configuration subjects the specimens to a constant bending moment in the region between the two inner load points. This test, therefore, is a measure of the flexural strength of the joint. The other test uses asymmetrical four-point loading (Figure 1b). This test, as described by Unal [12], subjects the specimens to a constant, through-thickness shear stress in the middle of the specimen. This test, therefore, is a measure of the shear properties of the joint material. Flexural loading was obtained by applying a compressive force on the fixtures using a rigid, mechanical test frame.

Results

At room temperature, the maximum tensile stress obtained in flexural loading of composites and unreinforced SiC (monolithic) joined using the reaction forming method were similar (Figure 2). The room temperature strength of reaction-formed silicon carbide joints between Hexoloy SA silicon carbide has been reported as 255 $\pm$ 3.2 MPa, by researchers at the NASA Glen Research Center [2]. In this study a value of 53 MPa with a standard deviation of 6 MPa (3 specimens) was measured. Two specimens, from the same batch as used to obtain the data in Figure 2, were provided to an independent investigator

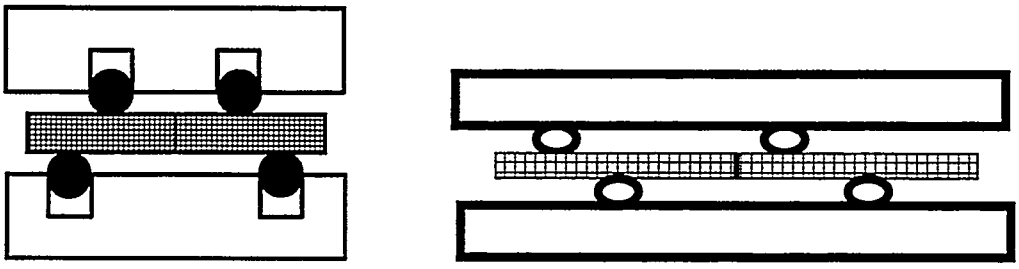

(a) (b)

Figure 1. Schematic drawings of mechanical test configurations: (a) 1/4, four-point bending, and (b) assymetric, four-point bending.

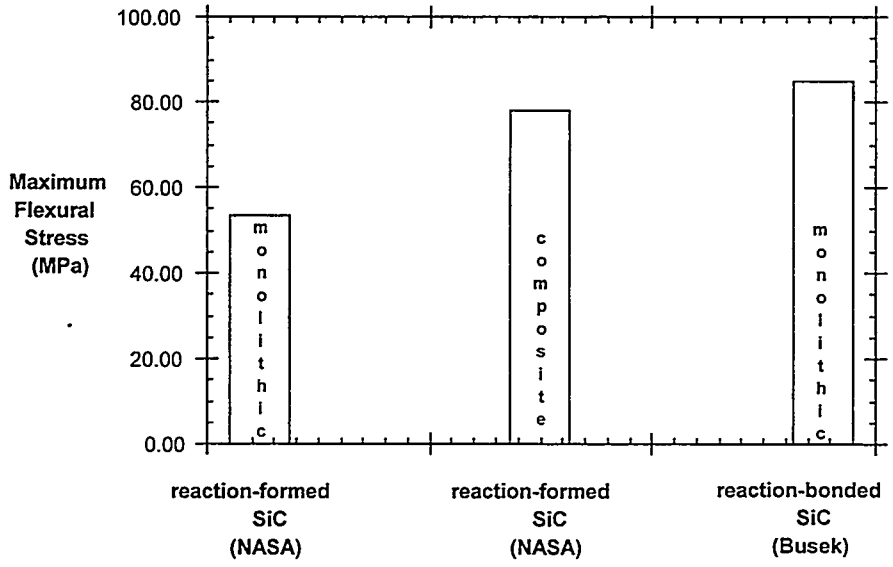

Figure 2. Comparison of room-temperature flexural strength

(Dr. O. Unal, Ames Laboratory, Ames, IA) who had earlier measured values similar to those that had been reported by investigators at NASA Glenn Research Center. These specimens exhibited 1/4, four-point flexural loading of 72 MPa and 122 MPa. These results indicate that although there may be some experimental error in the measurements made at PNNL, the material provided by NASA Glenn Research Center had a lower than average strength. The reasons for the lower than anticipated flexural stress values are not fully understood. The initial microstructural investigation [13], however, revealed that the untreated joints contained excess carbon and silicon that is indicative of an incomplete reaction. Therefore, it is likely that the joints were weaker than expected because the reaction to silicon carbide had not been completed.

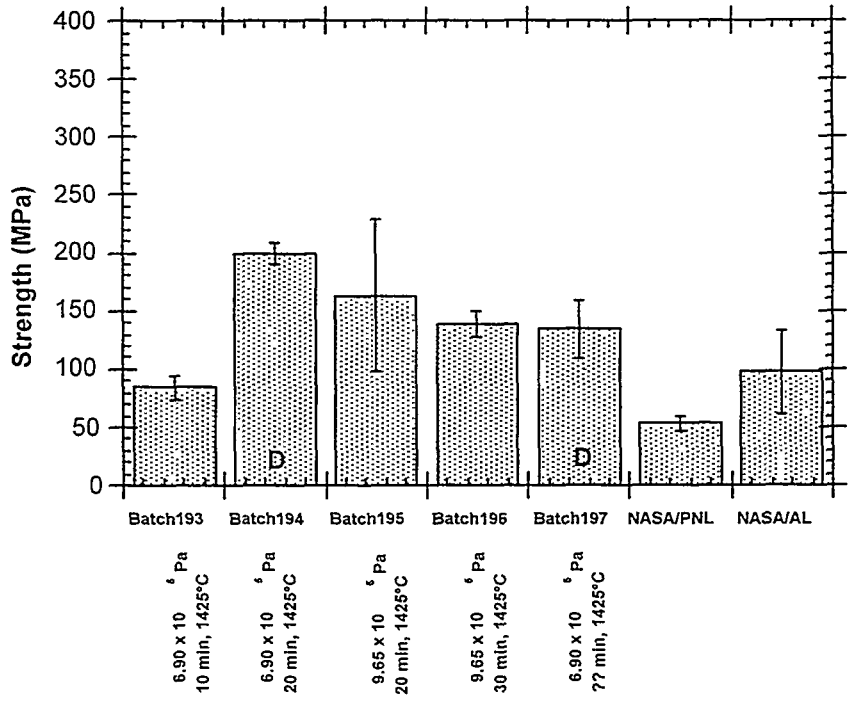

Figure 3. Room-temperature flexural strength of reaction bonded and reaction formed joints

Several batches of joints consisting of reaction bonded SiC were also tested in 1/4, four-point bending (Fig. 3). The processing temperature and applied pressure are indicated underneath the graph abcissa. Data for joints consisting of reaction formed SiC, labeled as "NASA", are also shown in Figure 3. The results obtained at PNNL and by Dr. Ozer Unal, at Ames Laboratory, are further identified by the designation "PNL" or "AL", respectively. There was no clear trend in the value of the joint strength and the processing conditions, although the joints that were formed by using a double layer of precursor tape (indicated by the symbol "D" in Figure 3) showed a slightly higher strength than those processed under identical conditions using only a single layer. The strength of the reaction bonded joints was slightly higher than that of the reaction formed joints, but it has already been mentioned that the reaction formed joints were from a batch with lower than average strength values.

To evaluate the effect of high temperature exposure on the properties of joints consisting of reaction bonded silicon carbide, the strength of specimens was measured at 1100°C (Figure 4). The specimen was held at 1100°C for 15-30 minutes, prior to testing, to allow the temperature to equilibrate. The strength of specimens measured at 1100°C was higher, 247 $\pm$ 85 MPa, than that measured at room temperature, 134 $\pm$ 25 MPa. In addition, specimens that were annealed at 1100°C for 100 h, in flowing gettered argon (<20 ppm O_2) had a strength of 212 $\pm$ 108 MPa. These results suggest that high temperature annealing improves the strength of the joints. Additional microscopy will be conducted to determine if microstructural changes are responsible for the improved strength after heat treating. It was assumed earlier that the strength of reaction formed joints improved after heat treatment due

to additional reaction between free silicon and carbon. Due to the rapid processing times of the reaction

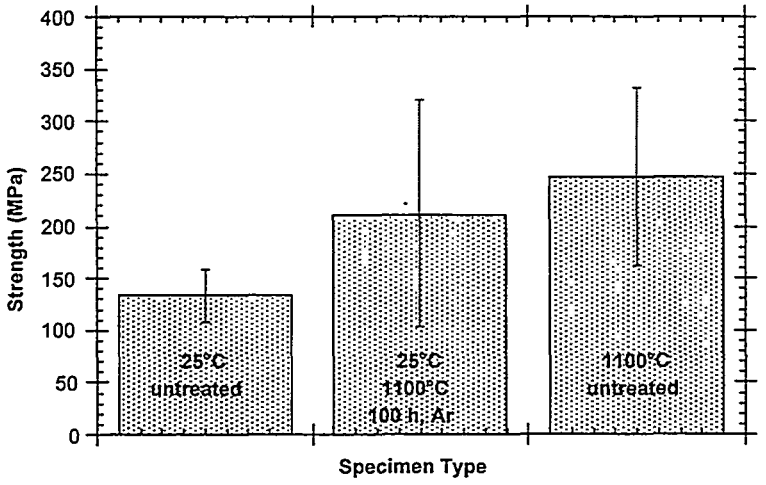

Figure 4. 1/4, four-point flexural strength of monolihtic SiC joined by reaction bonded SiC, before and after heat treatment.

bonded joints a similar effect may have occurred. It is possible that deleterious residual stresses, remaining after processing, may be relieved during heat treatment, thus explaining the improved strength after heat treatment. Without further testing, it cannot be determined if there was also an increase in strength of the joints measured at 1100°C due to the temperature dependence of the material properties.

All of the strength results described above were obtained by using 1/4, four-point flexural loading. This test methodology subjects the test specimens to a constant bending moment between the inner loading points. The stress state of a joint within a reactor, however, will experience a generalized stress state. In addition, the stress state in the joint will be influenced by its geometry. To analyze the implications of these two issues, and to evaluate test methods for determine likely failure modes within realistic joints a plan to conduct analysis by the finite element method (FEM) of several joint geometries and test methods was made. The test configurations that will be evaluated are shown in Figure 5. The dimensions of the specimens that will be analyzed are given in Table I, and relevant material property values are given in Table II.

Butt-joined flexural test specimen

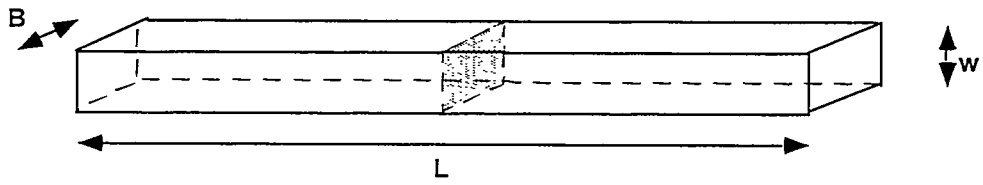

45° Butt-joined flexural test specimen

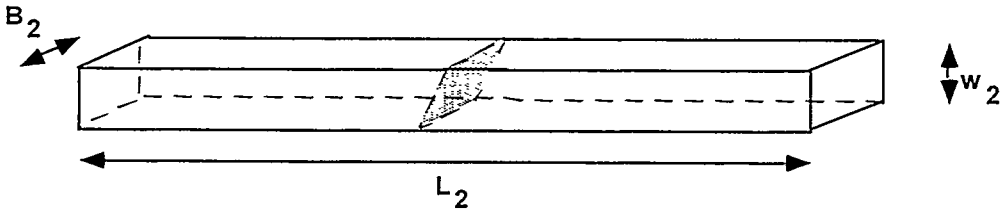

Double-notch-shear specimen

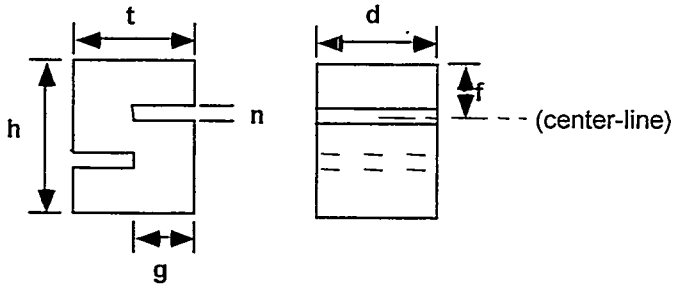

Offset sandwich specimen

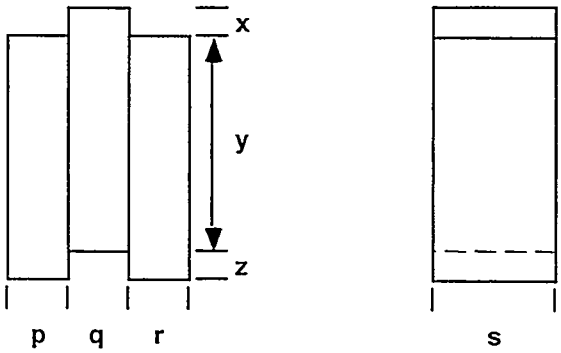

not drawn to scale.

Figure 5. Test specimen geometries to be analyzed by FEM.

Table I
Physical Dimensions (in mm) of Specimens to be Analyzed by FEM

Butt-joined flexural test specimen	Size 1	Size 2
B	4.00	2
w	3.00	1.5
L	50.00	30.00
45° Butt-joined flexural test specimen		
B_2	4.00	2
w_2	3.00	1.55
L_2	50.00	25.00
Double-notch shear specimen		
t	8.00	4.00
d	15.00	7.5
h	30.00	15.00
f	11.5	5.75
n	0.50	0.25
g	4.00	2.00
Offset sandwich specimen		
p	3.00	1.50
q	3.00	1.50
r	3.00	1.50
s	10.8	5.0
x	4.00	2.00
y	12.4	6.00
z	4.00	2.00

TABLE II
Material Property Values for FEM Modeling

	Monolithic SiC (SA)	SiC_f/SiC_m	Joint (RB SiC)
Young's Modulus (GPa)	408[M]	300[H]	393[C]
Poisson's Ratio	0.14[M]	0.3[H]	0.19[C]
Coefficient of Thermal Expansion (10^{-6} °C^{-1})	5.8 (25 – 1 000°C)[K]	3.0[H]	4.3 (25 – 1 000°C)[C]
Thermal Conductivity (W/m·K)	125.6[S]	10[Y]	125[C]

M= McHenry & Tressler, J. Am. Ceram. Soc., vol. 63[3-4], pp.152-156 (1980).
K = Kern et al., Mat. Res. Bull., vol. 4, pp. S25 – S32 (1969).
C = "Materials Properties Standard 2000, Coors Ceramics Company, Golden, Colorado, 1999.
H = K. Kageyama, and I. Kimpara, Key Engineering Materials, vols. 164-165, pp. 127-132 (1999).
Y = Youngblood et al. Fusion Materials semiannual report.

S = "Physical Properties of Hexoloy® SA Silicon Carbide"
(http://www.carbo.com/hexoloy/properties/index.html), Carborundum Corporation, Niagara Falls, NY.

CONCLUSIONS

Preliminary studies have shown that joints between silicon carbide and silicon carbide composites can be fabricated by both reaction forming and reaction bonding methods. Both methods result in similar flexural strength values measured by 1/4, four-point bending. The specimens joined by reaction formed silicon carbide had lower than average strength values, probably due to insufficient reaction time during processing. Efforts to analyze the stress state in practical joints and joint test methodologies via finite element analysis have begun.

REFERENCES

[1] B.H. Rabin, and G.A. Moore, "Joining of SiC-Based Ceramics by Reaction Bonding Methods," J. Mat. Synth. & Proc., **1** [3], 195-201 (1993).

[2] M. Singh, "A Reaction Forming Method for Joining of Silicon Carbide-Based Ceramics," Scripta Mater., **37** [8], 1151-1154 (1997).

[3] M. Singh, S.C. Farmer, and J.D. Kiser, "Joining of Silicon Carbide-Based Ceramics by Reaction Forming Approach," Cer. Eng. Sci. Proc. 18 [3], 161-166 (1997).

[4] M. Singh, "Joining of Sintered Silicon Carbide Ceramics For High Temperature Applications," J. Mat. Sci. Lett, in press.

[5] S. Yajima, K. Okamura, T. Shishido, Y. Hasegawa, and T. Matsuzawa, "Joining of SiC to SiC Using Polyborosiloxane," Am. Ceram. Soc. Bull., **60**, 253, (1981).

[6] A. Donato, P. Colombo, and M.O. Abadirashid, "Joining of SiC to SiC using a preceramic Polymer," pp. 471-476 in High-Temperature Ceramic -Matrix Composites I, A.G. Evans and R. Naslain (eds.), Ceram. Trans., **57**, The American Ceramic Society, Westerville, Ohio, USA, 1995.

[7] W.J. Sherwood, C.K. Whitmarsh, J.M Jacobs, and L.V. Interrante, "Joining Ceramic Composites Using Active Metal/HCPS Preceramic Polymer Slurries," Cer. Eng. Sci. Proc., **18**, 177-184 (1997).

[8] O. Unal, I.E. Anderson, M. Nostrati, S. Ijadi-Maghsoodi, T.J. Barton, and F.C. Laabs, "Mechanical Properties and Microstructure of a Novel SiC/SiC Joint," pp. 185-194 in Ceramic Joining, I.E. Reimanis, C.H. Henager, Jr., and A.P. Tomsia (Eds.), Ceramic Transactions, vol. 77, The American Ceramic Society, Westerville, Ohio, USA, 1997.

[9] P. Colombo, "Joining Ceramics Using Preceramic Polymers," in Interfacial Science in Ceramic Joining, NATO Advanced Research Workshop, Bled, Slovenia, November 12-15, 1997.

[10 P. Colombo, V. Sglavo, E. Pippel, and J. Woltersdorf, "Joining of Reaction-Bonded Silicon Carbide Using a Preceramic Polymer," J. Mat. Sci., **33**, 2409-2416 (1998).

[11] E. Pippel, J. Woltersdorf, P. Colombo, and A. Donato, "Structure and Composition of Interlayers in Joints Between SiC Bodies," J. Eur. Ceram. Soc., **17**, 1259-1265 (1997).

[12] O. Unal, I.E. Anderson, and S.I. Maghsoodi, "A Test Method to Measure Shear Strength of Ceramic Joints at High Temperatures," J. Am. Ceram. Soc., **80** [5], 1281-1284 (1997)

[13] C.A. Lewinsohn, R.H. Jones, M. Singh, T. Shibayama, T. Hinoki, M. Ando, Y. Katoh, and A. Kohyama, "Methods for Joining Silicon Carbide Composites for High Temperature Structural Applications," Fusion Materials Semiannual Progress Report for the Period Ending December 31, 1998, DOE/ER.

EVALUATION OF NEUTRON IRRADIATED NEAR-STOICHIOMETRIC SILICON CARBIDE FIBER COMPOSITES – L. L. Snead (Oak Ridge National Laboratory), Y. Katoh and A. Kohyama (Kyoto University), and J. L. Bailey, N. L. Vaughn, and R. A. Lowden (ORNL)

Extended Abstract (the full paper will be published in the Journal of Nuclear Materials as Proceedings of the Ninth International Conference on Fusion Reactor Materials, October 10-15, 1999, Colorado Springs, Colorado).

Composites have been fabricated by either isothermal or forced flow chemical vapor infiltration of silicon carbide (SiC) into SiC-based fiber preforms. Fibers were Ceramic Grade Nicalon™, High-Nicalon™, and High-Nicalon™ Type-S. These fibers cover a wide range in oxygen and excess carbon content, with the Ceramic Grade Nicalon™ being the furthest from purity and the Type-S fiber being >99% stoichiometric SiC. Results are presented for two parallel studies on the effects of neutron irradiation on these materials. In the first study, neutron irradiation-induced changes in mechanical properties, as measured by bend testing, for High-Nicalon™ fiber materials of varied interphase structures are measured. The three interphases chosen were pyrolytic carbon, pseudo porous SiC, and multilayer SiC. In the second study, the mechanical properties of composites fabricated from all three fiber types are measured. For these composites, a pyrolytic carbon interphase was selected. Results indicate that both the Ceramic Grade Nicalon™ and High Nicalon™ materials degrade substantially under irradiation, though the higher oxygen content Ceramic Grade fiber degrades more rapidly and more substantially. Of the three interfaces studied in the High Nicalon™ system, the multilayer SiC is the most radiation resistant. At a dose of ~1 dpa, the mechanical property degradation of the High Nicalon™ composite is consistent with a fiber densification-induced debonding. At a dose of 10 dpa, the properties continue to degrade, raiding the question of degradation in the CVD SiC matrix as well. Low dose results on the High Nicalon™ Type-S fabricated materials are encouraging, as they appear to not lose, and perhaps slightly increase, in ultimate bend strength. This result is consistent with the supposition that as the oxygen content in SiC-based fibers is reduced, the irradiation stability, and hence, composite performance under irradiation will improve.

3.0 FERRITIC/MARTENSITIC STEELS

A UNIFIED MODEL FOR CLEAVAGE TOUGHNESS IN THE TRANSITION – G. R. Odette
(University of California Santa Barbara)

OBJECTIVE

The objective of this research is to develop advanced methods for defect tolerant integrity assessments that will enable the use of small specimens in generating an irradiated fracture toughness data base and for fusion applications atypical of traditional heavy section structures based on fundamental understanding of fracture micro-mechanisms, mechanics and irradiation embrittlement.

SUMMARY

A Master Curves-Shifts (MC-ΔT) method has been previously proposed as an engineering expedient to enable the use of small specimens to predict the effects of geometry, irradiation, loading rates on fracture conditions for large fusion structures. However, in addition to other unresolved issues, the MC-ΔT requires a better basic understanding, including the universality of the MC shape. Thus a new unified micromechanics model of fracture toughness in the cleavage transition regime is proposed. The model combines analytical representations of finite element method simulations of crack tip stress fields with a local critical stress-critical stressed area (σ^*-A*) fracture criteria. The model, and simpler alternatives, have been very successful in predicting geometry and loading rate effects, as well as irradiation hardening induced Charpy shifts. However, the standard models do not predict a constant MC $K_{Jc}(T)$ shape following irradiation. This apparent inconsistency with experiment is now resolved by incorporating a modest temperature dependence in σ^* that appears to be consistent with an independent body of data. Several experiments suggest high helium levels may increase irradiation induced toughness temperature shifts above levels associated with hardening alone. However, these experiments are all confounded, and must be interpreted with great caution. If real, helium effects may be relatively modest. Single variable experiments and complementary data which will allow a mechanism-based interpretation of the mechanical test data are needed to characterize the influence of helium on fast fracture.

PROGRESS AND STATUS

Backround

A master curves (MC)-shifts (ΔT) method has been previously proposed as a possible practical approach to dealing with the enormous amount of information that is needed to characterize and apply fracture toughness [1]. Following the approach for heavy section applications [2], the MC-ΔT method assumes a master toughness $K_{Jc}(T')$ curve shape can be placed (indexed) on an absolute temperature (T) scale by a reference temperature ($T' = T - T_{or}$) at a reference toughness (e.g., 100 MPa$\sqrt{m}$). An illustration of the MC-ΔT method is shown in Figure 1. The static MC deep crack shape is shown as the dashed line plotted on a $T - T_{or}$ scale. The solid line is the

corresponding reference (unirradiated) MC placed on an absolute temperature scale, at T_{or} = -50°C, by six tests shown as filled circles. A net shift of 200°C, arising from irradiation ($\Delta T_{\sigma t}$ = 150°C), dynamic loading ($\Delta T_{P'}$ = 50°C), a thin-walled, shallow crack geometry (ΔT_g = -40) and a margin (ΔT_m = 40°C), places the absolute MC, used for in-service structural evaluations, at T_o = 150°C, shown as the dotted line. Ideally, there would be only a single MC shape applicable to all conditions. While, in practice this is not the case, a small family of MC shapes may be sufficient for most practical purposes. The key advantage is the $K_{Jc}(T)$ curves can be established with a relatively small number of tests on small relatively small specimens; and b) effects of other key variables would be accounted for by direct measurement or independently established shifts and a small set of MC shapes.

Open questions about MC–ΔT method include: a) Is there a constant of the MC shape, or small set of shapes, and if so why? b) How should effects of size and geometry, in both testing and applications, be treated? c) How can T_{or} and the ΔTs be modeled to characterize effects of irradiation; d) What are the effects of high helium?

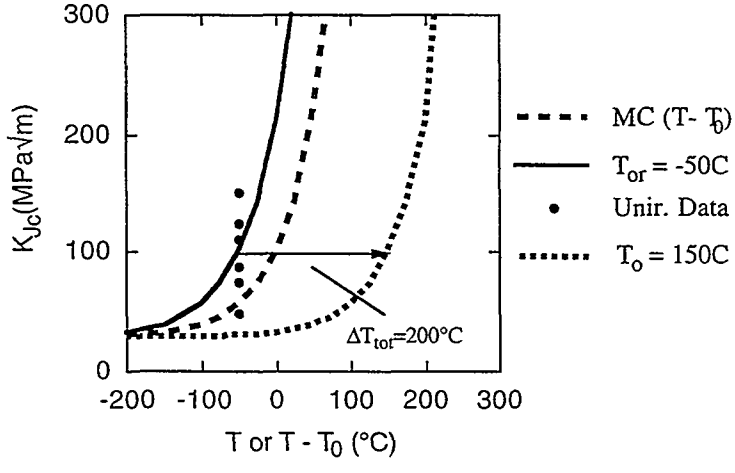

Figure 1. Illustration of the MC-ΔT method.

Macro-Micromechanics of the MC and Cleavage Intitiation Toughness in the Transition – A Unified Model.

It is generally accepted that cleavage fracture involves stress controlled fracture of brittle 'trigger' particles (e.g., grain boundary carbides) and subsequent dynamic micro-cleavage crack propagation into the tougher metal matrix []. Models of cleavage toughness require combining simulations of the crack tip stress fields with local micromechanical models of the field conditions required to initiate cleavage. A useful local fracture criteria is a critical stress (σ^*) acting over a critical area in front of the blunting crack (A^*). Based primarily on blunt notch tests, and the coarse (μm) scale of the microstructures involved, a typical assumption has been that σ^*-A^* are independent of temperature, strain rate and, in many cases, irradiation exposure [1,3-7].

For deep cracks in sufficiently large cracked bodies or small scale yielding (SSY) conditions K_{Jc} can be analytically represented in terms of A* and $R = \sigma^*/\sigma_y$, where σ_y is the yield stress as [8,9]

$$K_{Jc} = \sigma_y[A^*10^{P^*}]^{1/4} \quad (1)$$

where $P = C_o + C_1R + C_2R^2$; and the C_i are determined from fits to the FEM results for a given constitutive law.

For cases with shallow cracks or large scale plastic deformation outside the SSY regime, the effective toughness (K_e) is larger than K_{Jc} due to the loss of constraint [8,9]. The K_e/K_{Jc} ratio is a function of R, the constitutive law, the cracked body geometry and the deformation level $D = K_e^2/bE\sigma_y$, where the characteristic dimension is usually taken as the uncracked ligament length, b. For a specified geometry and constitutive law, K_e/K_{Jc} can be analytically fit to results of FEM simulations with simple polynomial expressions in the form [].

$$K_e/K_{Jc} = [C_{co} + C_{c1}R^* + C_{c2}R^{*2}]^{1/2} \quad (2a)$$

where the C_{ci} coefficients depend on D as

$$C_{ci} = C_{ri0} + C_{ri1}D + C_{ri2}D^2 \quad (2b)$$

Equations 1 and 2 represent a unified model of effective fracture toughness in the transition region.

Application of the model is illustrated in Figure 2, where the predicted $K_{Jc}(T)$ shape (solid line) is compared to the MC for pressure vessel steels with T_{or} = - 50°C (dashed line). The model parameters are $A^* = 10^{-8}$ m^2, σ^* = 2080 MPa and a power law strain hardening exponent of n = 0.1 and $\sigma_y(T)$ fit to RPV steel data. The dotted line shows the corresponding $K_e(T)$ curve for a small 3.3x3.3x16.6 mm (1/3 sized Charpy) specimen tested well beyond the SSY limit.

The broad success of the simple constant σ^*/A^* model have been discussed previously []. However, one key limitation of this model is that significant reductions in the slope of the $K_{Jc}(T)$ curves in the transition are predicted at high T_o, associated with severe irradiation hardening. Such shape changes have generally not been observed. This is illustrated by the dashed line in Figure 3 for $\Delta\sigma_y$ = 200 MPa. Thus we must seek a fundamental explanation for the constant MC shape. The standard assumption is that σ^*-A* are independent of temperature. However, we challenge assumption by using Equation 1 to estimate the $\sigma^*(T)$ that is consistent with experimental observations for RPV steels: a) a MC-type shape over a wide range of T_o; and b) the observed ΔT as a function of $\Delta\sigma_y$.

The results of this exercise are shown as the heavy solid lines in Figure 4 for $A^* = 10^{-8}$ m^2 and $\Delta\sigma_y$ of 0, 100, 200 and 300 MPa. The thinner, dashed lines are RPV steel MCs indexed at the same 100 MPa$\sqrt{m}$-temperature as the model predictions. Figure 5 compares the corresponding

predicted temperature-shifts at 100 MPa$\sqrt{m}$ as a function of $\Delta\sigma_y$ (solid line) with experimental data (filled circles) compiled by Sokalov [10] and the least squares fit to this data (dashed line). As discussed in more detail elsewhere, as well as a body of independent data and theoretical considerations are qualitatively the empirical $\sigma^*(T)$ derived in this work [11].

Implications to Irradiation Embrittlement

Figure 6 shows MC fits to for F82H data before and following irradiation to 2.5 dpa at 300°C [12]. Charpy and fracture toughness temperature shifts have also been treated previously using a simple equivalent yield stress model (EYSM) [1,13]. An example of the model predictions for several F82H Charpy and a single ΔT are shown in Figure 7. There results confirm that irradiation hardening results in toughness shifts in both RPV and martensitic steels, with a typical ration of $\Delta T/\Delta\sigma_y$ of about 0.7±0.2 °C/MPa.

The potential effect of transmutation helium on fast fracture is a complex and contentious issue, that cannot be effectively resolved at this time since all existing experiments that have been interpreted to show a effect of helium may be confounded by uncontrolled or unaccounted for variables. However, several available data sets do seem to consistently show that higher helium levels increase $\Delta T_{\phi t}$ [14-20]. For irradiation at around 300°C, the maximum $\Delta T_{\phi t}$ attributable to helium differences appears to be about 70°C for 300 appm helium. The corresponding normalized $\Delta T_{\phi t}$/He mean and median values for these studies are about 0.15 and 0.11 °C/appm. However, even if these crude estimates are accurate, there is no logical basis or physical justification to linearly extrapolate possible enhanced shifts to very high helium levels. Indeed, at worst, effect of helium on shifts should be of order, or less than, that produced by displacement damage. There is some indication that helium effects may be more significant at higher irradiation temperatures, but this may be mitigated by reduction is the corresponding contributions due to irradiation hardening.

The models described in this work provide a useful framework for considering the existing data, and designing new experimental approaches to evaluate helium effects on fracture. For example, it is clear that to the extent that higher levels of helium lead to larger $\Delta\sigma_y$, corresponding increases in $\Delta T_{\phi t}$ are anticipated. In general, however, the limited database indicates that increases in $\Delta\sigma_y$ at higher helium levels are modest. Thus the implication is that helium effectively reduces σ^*. Shifts that increase with helium, and that are much larger than can be attributed to $\Delta\sigma_y$ alone, would support this hypothesis. However, such data is lacking. Helium effects on fast fracture, if any, must be better characterized by well-designed experiments. Ideally, single variable experiments would involve only controlled differences in helium levels, with all other variables held constant. In practice, this is very hard to achieve; thus the effects of potentially confounding factors must always be carefully considered. Nickel and iron isotope tailoring experiments probably come the closest to achieving this ideal, but to date have provided limited opportunity for fracture testing. However, an equally important objective of such experiments should be to obtain the body of the complementary data (constitutive properties, fractography, microstructure,...) so that the test results can be interpreted and linked to the models, such as those described in this report.

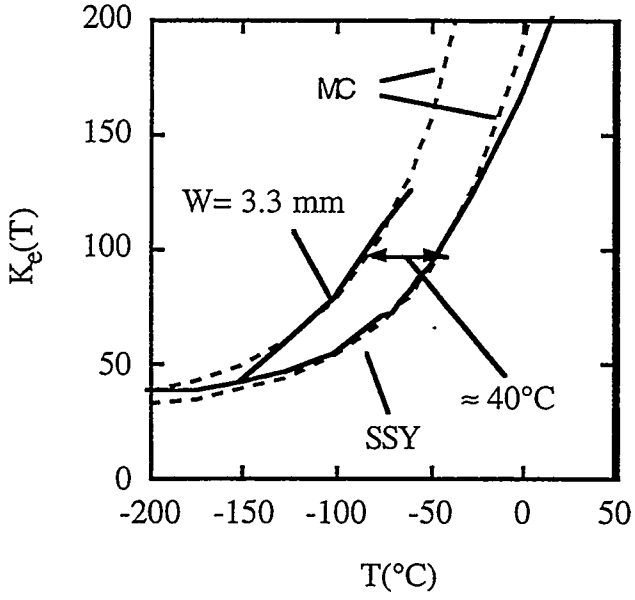

Figure 2. $K_{Jc/e}(T)$ curves from Equations 1 and 2 for SSY and a subsized specimen.

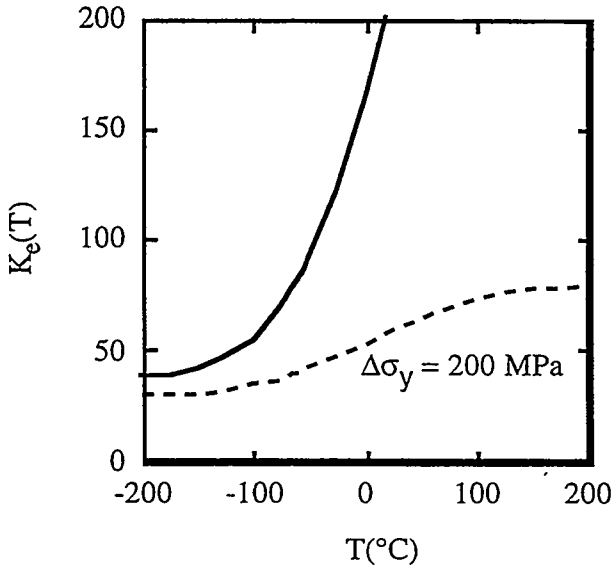

Figure 3. The corresponding predicted $K_{Jc}(T)$ for $\Delta\sigma_y$ = 200 MPa.

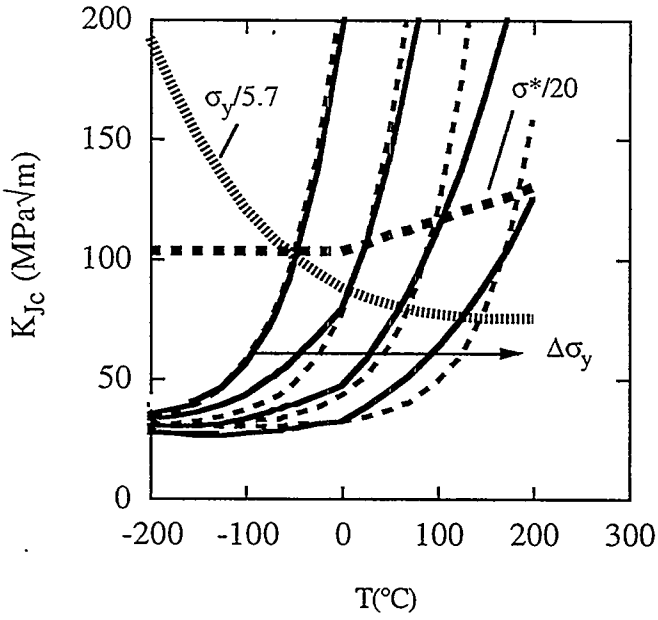

Figure 4. Predicted vs. MC shapes for fitted σ*(T)/A*.

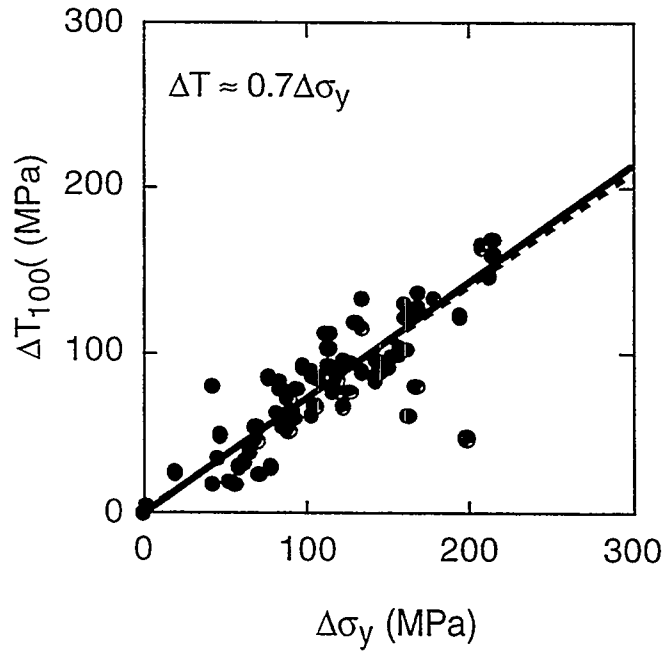

Figure 5. Predicted and measured ΔT_{K100} versus $\Delta\sigma_y$ for RPV steels.

Summary and Conclusions

A Master Curves-Shifts (MC-ΔT) method has been proposed as an engineering expedient to enable the use of small specimens consistent with predicting the effects of geometry, irradiation and loading rates on the fracture of fusion structures. In support of the MC-ΔT method a new unified model of fracture toughness in the cleavage transition regime is proposed which is consistent with a constant $K_{Jc}(T)$ MC shape and ΔT versus $\Delta\sigma_y$ data for both RPV and martensitic steels. While there are no unambiguous results regarding the potential role of helium on fast fracture, several experimental data sets do suggest that high helium levels increase $\Delta T_{\phi t}$ above levels associated with irradiation hardening alone. However, if real, helium effects on fast fracture may be modest. Resolution of the *'helium question'* will require carefully designed single variable experiments and assembling the range of complementary data (tensile, fractrographic, microstructal) needed for mechanism based interpretations of the mechanical test data.

REFERENCES

1. Odette, G.R., Edsinger, K., Lucas, G.E., and Donahue, E, *Small Specimen Test Techniques*, ASTM STP-1329, (1998) 298
2. ASTM E 1921-97, *Standard Test Method for Determination of Reference Temperature, T_o, for Ferritic Steels in the Transition Range* (1998)
3. Ritchie, R.O., Knott, J.F., and Rice, J.R., *J. Mech. & Phys. Solids*, 21 (1973) 395
4. Ritchie, R.O., Server, W.L., and Wullaert, R.A., *Met. Trans. A*, 15A (1979) 1557
5. Edsinger, K., Odette, G.R., Lucas, G.E. and Wirth, B., *Effects of Irradiation on Materials 17*, ASTM STP 1270 (1996) 670,
6. Odette, G.R., *J. Nuc. Mat.*, 212-215, (1994) 45
7. Fabry, A., *Small Specimen Test Techniques*, ASTM STP-1329, (1998) 274
8. Nevalainen, M., and Dodds, R.H., Jr., *Int. Jour. of Fract*, 74 (1995) 131
9. He, M.Y. and Odette, G.R., "Three Dimensional FEM Assessment of Constraint Loss Effects on Cleavage Initiation Fracture," in preparation
10. Sokolov, M.A., and Nanstad, R.K., *Effects of Radiation on Materials* 18, ASTM STP1325, (1999) 167
11. Odette, G.R., "A Unified Model for Cleavage Toughness in the Transition", *J. Nucl. Mat.* (submitted ICFRM 9)
12. van Osh, E. V., Horsten, M. G., Odette, G. R., and Lucas, G.E., "Mechanical Properties of Reduced Activation Martensitic Steel IEA Heat F82H Base Metal After 2.5 dpa, 300°C Irradiation", *Effects of Irradiation on Materials 19*, ASTM 1336 (in press)
13. Odette, G. R., Lombrozo, P. M. and Wullaert, R. A., *Effects of Irradiation on Materials 11*, ASTM STP 870 (1985) 841
14. Klueh, R. L. and Alexander, D. J., *J. Nuc. Mat.*, 218 (1995) 151
15. Gelles, D.S., *J. Nuc. Mat.*, 230 (1996) 187

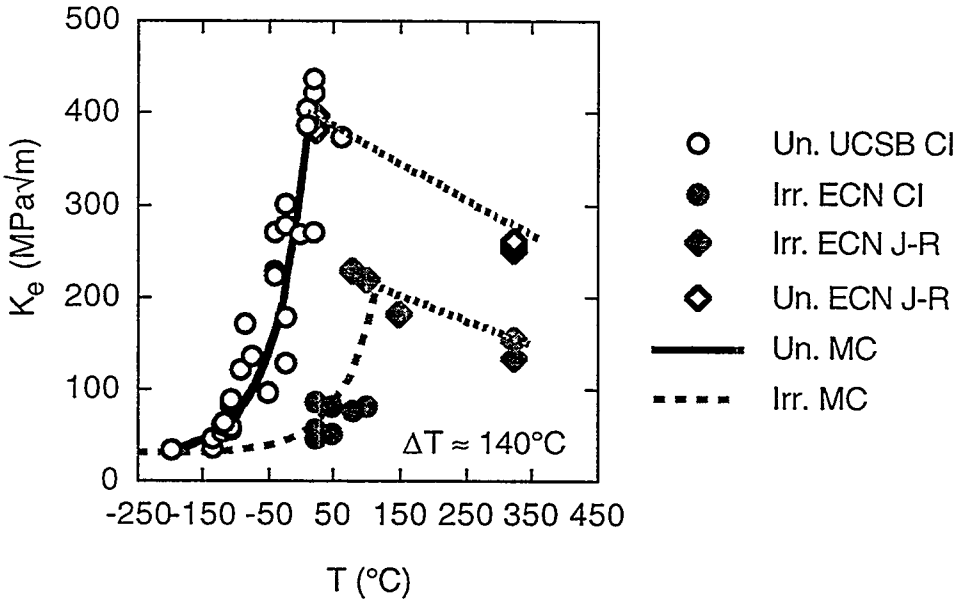

Figure 6. MC fits to F82H data before and after irradiation to 2.5 dpa at 300°C.

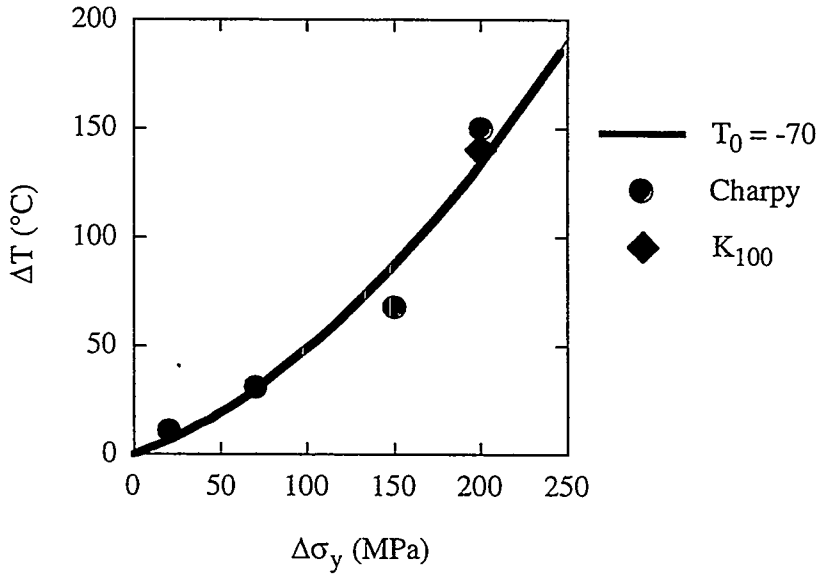

Figure 7. Predicted versus measured F82H Charpy and the toughness shifts from due to $\Delta\sigma_y$ based on the EYSM.

16. Klueh, R. L. and Alexander, D., J., *J. Nuc. Mat.,* 230 (1996) 191
17. Hamilton, M. L., Hankin, G. . and Gelles, D. S., *Small Specimen Test Techniques*, ASTM STP-1329 (1998) 614
18. Shiba, K., "Tensile and Charpy Properties of B-Doped F82H After Irradiation", *Proceedings of the IEA Workshop/Working Group Meeting on Ferritic/Martensitic Steels*
Petten, Netherlands (1998)
19.Kimura, A. "Further Assessment of Helium Induced Embrittlement in RAMS", ibid
20. Ohnuki, S., Kohno, Y., Koyama, A., Shiba, K., and Hishinuma, A., "Ferritic Isotope Tailoring (FIST) Experiment" ibid 18

A POTENTIAL FERRITIC/MARTENSITIC STEEL FOR FUSION APPLICATIONS

—R. L. Klueh, N. Hashimoto (Oak Ridge National Laboratory), R. F. Buck (Advanced Steel Technology, and M. A. Sokolov (Oak Ridge National Laboratory)

OBJECTIVE

This work was conducted as part of the effort to develop a ferritic/martensitic steel for fusion applications at higher temperatures than the conventional or reduced-activation steels are capable of operating at.

SUMMARY

The A-21 steel is an Fe-Cr-Co-Ni-Mo-Ti-C steel that is strengthened by a fine distribution of small titanium carbide (TiC) precipitates formed by thermo-mechanical treatment. After a high-temperature austenitization treatment, the steel is cooled to an intermediate temperature and hot worked in the austenitic condition. During hot working, small TiC precipitates form on the dislocations generated by the working. When cooled to ambient temperature, martensite forms; finally, the steel is tempered. Transmission electron microscopy of the A-21 reveals a high number density of small TiC particles uniformly distributed in the matrix. The strength of the A-21 is less than the average value for modified 9Cr-1Mo below 600°C, but is greater above 600°C. In a Charpy impact test, the transition temperature of A-21 is similar to that of modified 9Cr-1Mo, but the upper-shelf energy is higher. Because of the fine TiC particles in the matrix, the creep-rupture properties of A-21 are superior to those of conventional Cr-Mo or reduced-activation Cr-W steels. Although the composition of the A-21 is not applicable for fusion because of the cobalt, the innovative production process may offer a route to an improved steel for fusion.

PROGRESS AND STATUS

Introduction

High-chromium ferritic/martensitic steels, such as the conventional Cr-Mo steels (modified 9Cr-1Mo and Sandvik HT9) or the reduced-activation Cr-W steels (F82H, ORNL 9Cr-2WVTa, and JLF-1), that are being considered for a fusion power plant first wall and blanket structure would limit the upper operating temperature to 550-600°C. One way suggested to increase this limit to 650°C or higher and still maintain the advantages inherent in ferritic/martensitic steels (e.g. high thermal conductivity and low swelling) is to use oxide dispersion-strengthened (ODS) steels. Elevated temperature strength of these steels is obtained through microstructures that contain a high density of small Y_2O_3 or TiO_2 particles dispersed in a ferrite matrix.

Production of ODS steels involves complicated and expensive powder metallurgy and mechanical alloying procedures that usually involve extrusion. The directionality that derives from these processing procedures generally results in anisotropic mechanical properties.

Numerous attempts have been made to extend the upper operating temperature for the conventional ferritic/martensitic steels. Early modifications of the Cr-Mo steels led to modified 9Cr-1Mo or Sandvik HT9, which have been considered for fusion applications. In recent years, the conventional Cr-Mo steels have been further modified by replacing some or all of the molybdenum in the composition by tungsten [1]. With these efforts, operating temperatures have been pushed to a maximum of ≈620°C.

Dispersion strengthening is the most likely mechanism available to provide the creep strength required for higher operating temperatures for ferritic/martensitic steels. The low number density of relatively large precipitates in conventional or reduced-activation ferritic/ martensitic steels is not

capable of providing the strength required for temperatures beyond ≈600°C. This has led to the proposal to use ODS steels.

Obviously, a ferritic or martensitic steel that could be used at temperatures to 650°C and above that could be formed by more conventional steel processing techniques would result in a cheaper product than ODS steels produced by powder metallurgy/mechanical alloying procedures. Furthermore, with such a processing technique, it should be easier to produce a non-directional microstructure, which has been a problem for the ODS steels. Such an experimental steel, called A-21, has been developed [2]. Although this steel might not be directly applicable for fusion, the technique used to develop this steel may be applicable to produce an acceptable steel.

In this paper, tensile and impact properties have been determined for a heat of A-21 steel, and the results have been compared with properties for modified 9Cr-1Mo (9Cr-1MoVNb) and Sandvik HT9 (12Cr-1MoVW).

Experimental Procedure

The A-21 steel is an Fe-9.5Cr-3Co-1Ni-0.6Mo-0.3Ti-0.07C steel (all compositions are in wt. %) [2]. The 181-kg heat of steel used for this study was produced as a 17.5-mm thick plate that was austenitized at >1100°C to dissolve the carbides and put all elements into solution. Austenitization was followed by cooling to an intermediate temperature (700-1000°C), where the steel was hot worked in the austenitic condition. After the hot-working procedure was complete, the steel was cooled to ambient temperature to transform the matrix to martensite. Finally, the steel was tempered in the range 650-750°C for 1 h. Miniature tensile and Charpy specimens were machined from the tempered steel plate.

Tensile specimens 44.5-mm long with a reduced gage section of 20.3 x 1.52 x 0.76 mm were machined from the tempered plate with gage lengths parallel to the rolling direction. Tensile tests were conducted over the range room temperature to 700°C in vacuum on a 44-kN Instron universal testing machine at a nominal strain rate of $\approx 4 \times 10^{-4}$ s^{-1}.

One-third-size Charpy specimens 3.3 x 3.3 x 25.4 mm with a 0.51-mm-deep 30° V-notch and a 0.05- to 0.08-mm-root radius were machined from the plate along the rolling direction with the notch transverse to the rolling direction. Charpy tests were carried out in a pendulum-type impact machine specially modified to accommodate subsize specimens [3]. The absorbed energy values were fitted with a hyperbolic tangent function to permit the upper-shelf energy (USE) and ductile-brittle transition temperature (DBTT) to be evaluated. The DBTT was determined at the energy midway between the upper- and lower-shelf energies. Note that for these miniature specimens different DBTT and USE values are obtained than for full-size specimens. However, it has been shown that a low transition temperature for miniature specimens translates to a low value for full-size specimens [4-6]. A correlation likewise exists for the USE [4-6].

Properties of A-21 were compared against those of modified 9Cr-1Mo (9Cr-1MoVNb—T91) steel, a conventional Fe-9Cr-1Mo-0.2V-0.07Nb-0.03N-0.1C steel and Sandvik HT9 (12Cr-1MoVW), a conventional Fe-12Cr-1Mo-0.5W-0.5Ni-0.25V-0.2C steel [7]. Both of these steels were once considered for fusion applications. These steels were tested in their standard heat treated conditions. For the 9Cr-1MoVNb, austenitization was at 1040°C with tempering 1 h at 760°C, and for the HT9 austenitization was at 1040°C followed by a 2.5 h temper at 780°C.

The A-21 steel was examined by optical and transmission electron microscopy (TEM). Standard 3-mm diameter TEM disks were machined from the center of the 17.5-mm plate. Disks were thinned using an automatic tenupole electropolishing unit and were examined using a JEM-2000FX (LaB_6) microscope. Foil thicknesses were measured by thickness fringes in order to quantitatively determine the number density of the precipitates.

Results

Microstructure

Observation by optical microscopy indicated the steel had a 100% tempered martensite structure with a prior austenite grain size of 5-15μm [Fig. 1(a)]. The TEM examination at low magnification revealed a subgrain structure typical of tempered martensite [Fig. 1(b)].

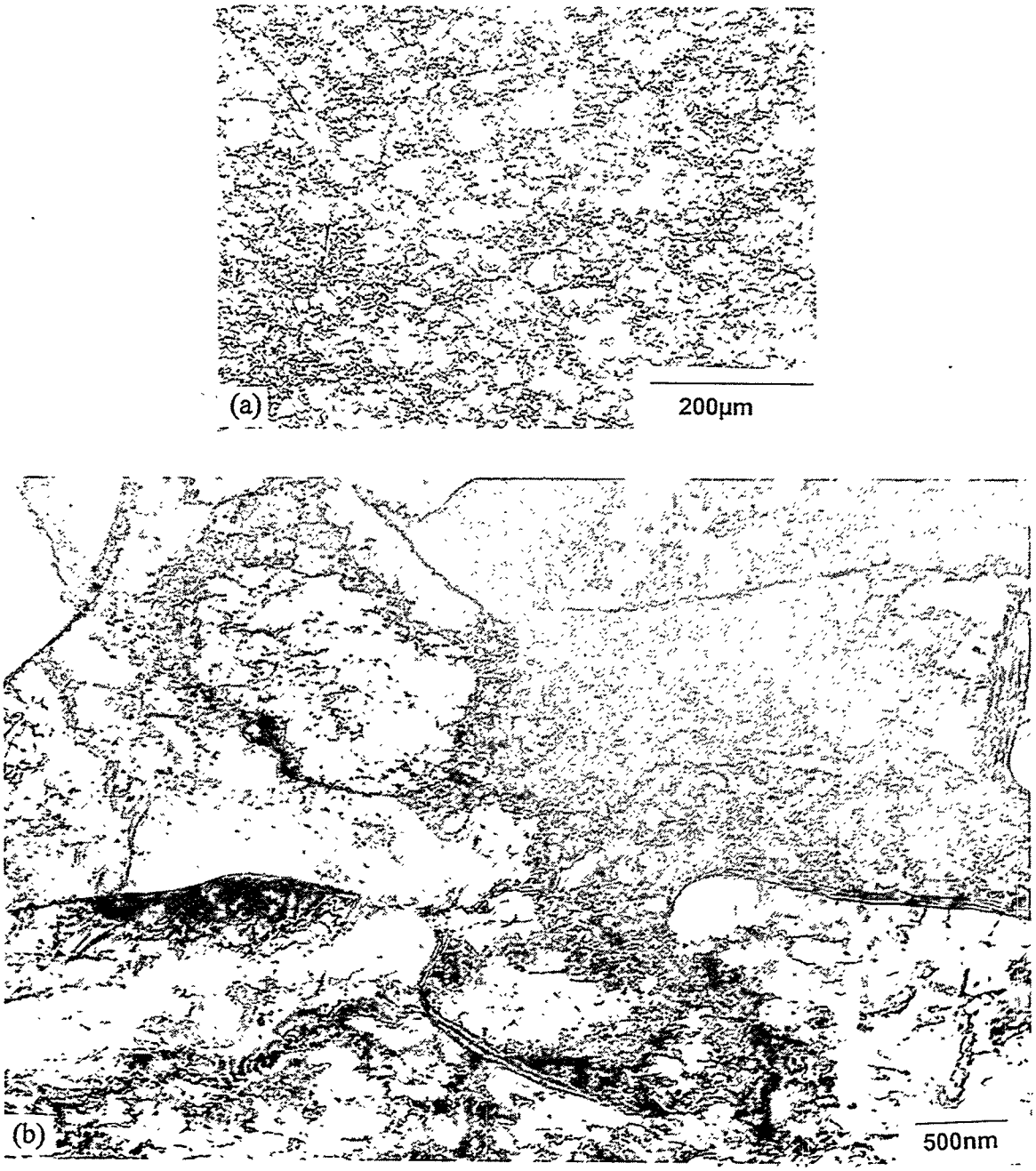

Figure 1. The (a) optical and (b) transmission electron microscopy views of the tempered martensite microstructure of A-21 steel.

The subgrains contain a high number density of precipitates [Figs. 2(a) and 2(b)] uniformly distributed with no indication of denuded zones near boundaries. Although some precipitates formed on boundaries, the number density and size of precipitates on the boundaries were not substantially different from those in the matrix. Essentially all the precipitates in the matrix formed on dislocation lines [Figs. 2(c) and 2(d)].

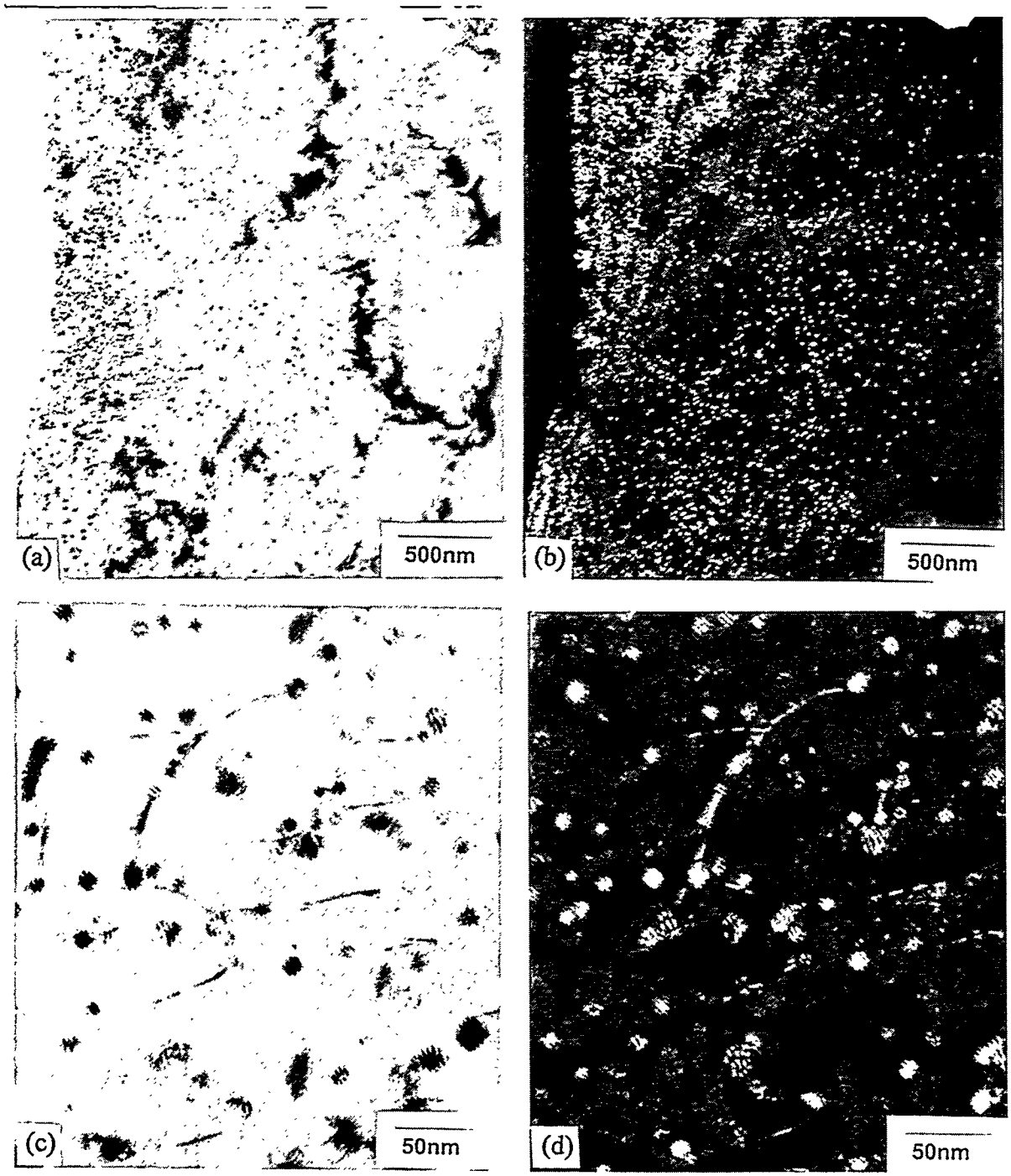

Figure 2. Transmission electron micrograph showing high number density of TiC precipitates in (a) bright field and (b) dark field and showing precipitates on dislocations in (c) bright field and (d) dark field.

Diffraction measurements and Moiré fringe measurements indicated the precipitates were titanium carbide (TiC). No other precipitates were observed. There were no indications of strain fields around the precipitates. The TiC particle size varied from about 5 to 20 nm (Fig. 3), with the average size about 9.3 nm. The total number density was estimated to be 4.7×10^{21} m^{-3}.

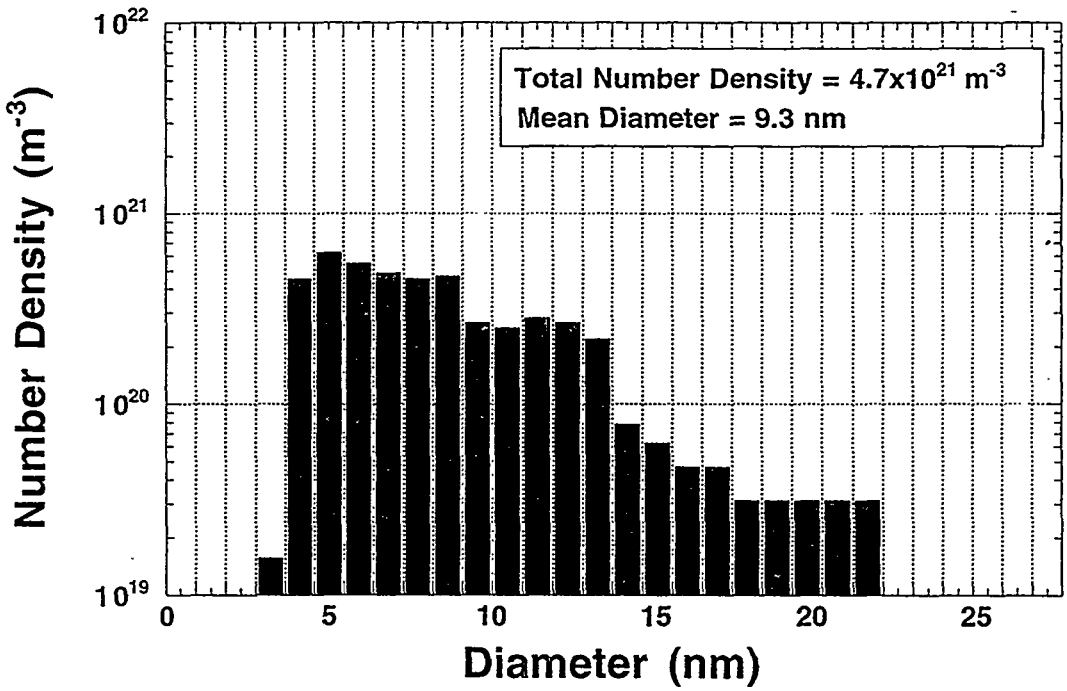

Figure 3. Size distribution of precipitates in A-21 steel.

Tensile Properties

Figure 4 shows the yield stress of A-21 compared with average properties of modified 9Cr-1Mo steel [8]. The 9Cr-1MoVNb steel is stronger than A-21 at the lowest test temperatures, but above ≈600°C the A-21 becomes stronger than the 9Cr-1MoVNb steel. Similar results were observed for the ultimate tensile strength. The ductilities are also similar, with the values for the A-21 being somewhat higher than for the average value for 9Cr-1MoVNb steel [8].

Charpy Impact Properties

The Charpy impact curve for the A-21 steel is shown in Fig. 5 compared to the curve for a heat of modified 9Cr-1Mo steel [7]. The ductile-brittle transition temperature (DBTT) for A-21 at half the upper-shelf temperature was similar to that of modified 9Cr-1Mo steel and the Sandvik HT9, while the upper-shelf energy for A-21 is significantly higher than that of both modified 9Cr-1Mo and HT9 (Table 1).

Discussion

Since A-21 steel contains 3% cobalt, it would not be an acceptable structural material for a neutron environment, such as a fusion power plant, because transmutation of cobalt would produce a highly radioactive structure. The objective of these studies was to determine if the A-21 steel possessed the properties required for the higher operating temperatures of a fusion

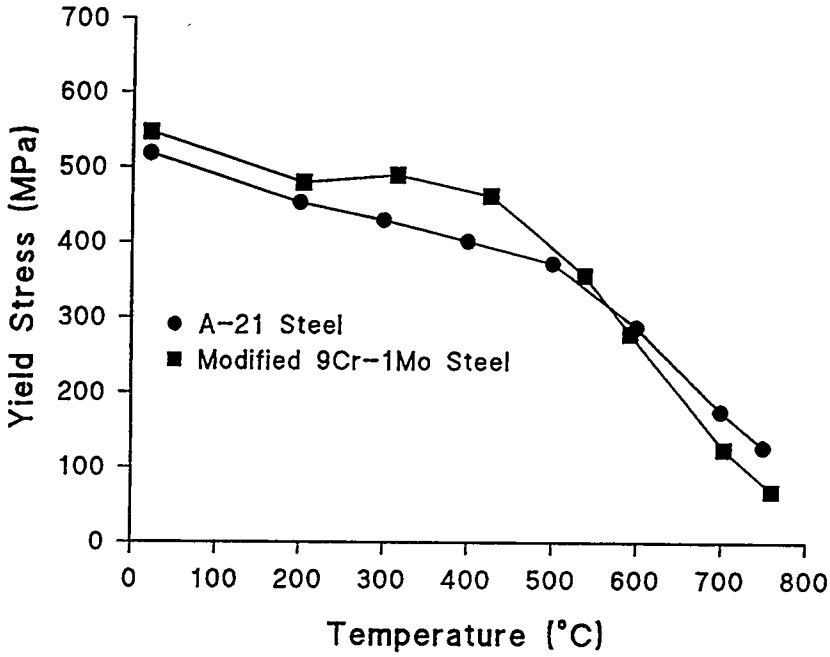

Figure 4. Tensile properties of A-21 steel compared to modified 9Cr-1Mo steel.

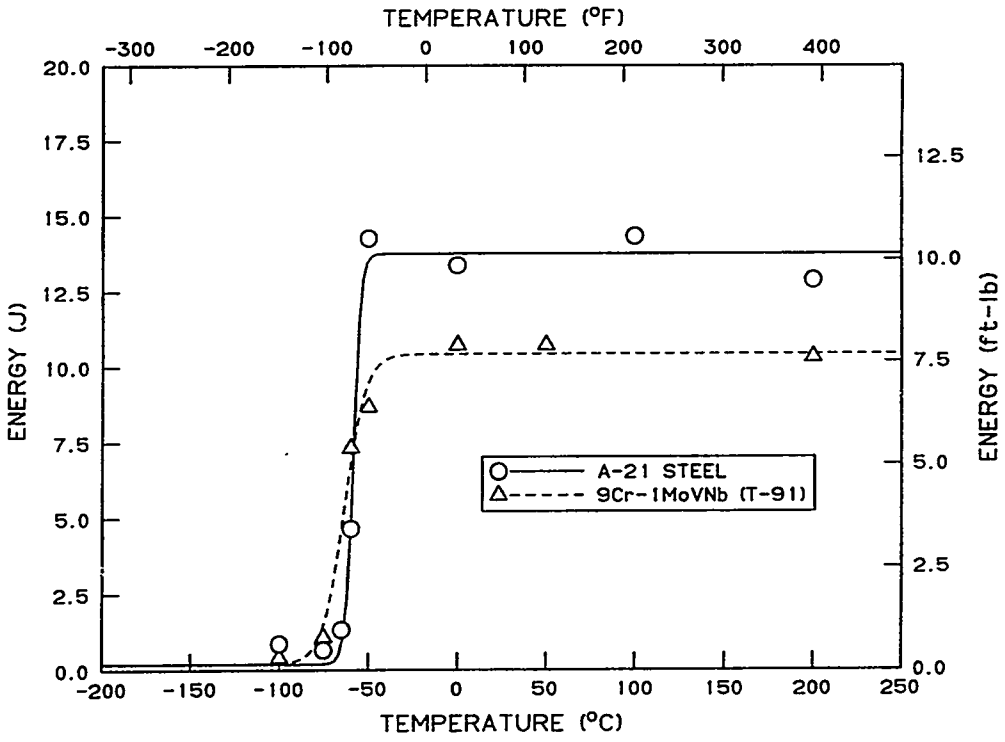

Figure 5. Charpy curves for A-21 and modified 9Cr-1Mo steels.

Table 1. Charpy Properties of Steels

Steel	Transition Temperature (°C)	Upper-Shelf Energy (J)
A-21	-59	13.7
9Cr-1MoVNb (T91)[a]	-64	10.5
12Cr-1MoVW (HT9)[b]	-35	7.6

[a] Heat treatment for 9Cr-1MoVNb: austenitized 1 h at 1040°C, AC; tempered 1 h at 760°C.
[b] Heat treatment for 12Cr-1MoVW: austenitized 1 h at 1040°C, AC; tempered 2.5 h at 780°C.

plant than are possible with conventional Cr-Mo steels or reduced-activation Cr-W steels. If higher operating temperatures are possible for A-21, then it would appear reasonable to seek the development of an acceptable composition with the process used to produce A-21.

At present, the best candidate ferritic/martensitic steels available to raise the operating temperature over that possible with the conventional and reduced-activation steels appear to be the ODS steels. Although ODS steels have been produced for some time, they still have problems with anisotropic properties that originate from the production techniques. Mechanical alloying and powder metallurgy production techniques are expensive, and given the more conventional processing used for the A-21 steel, an A-21-type steel would have significant advantages for fusion applications, as well as many other applications.

The mechanical properties of A-21 steel indicate that, it has the kind of properties required for a candidate for fusion applications. Irradiation embrittlement, which results in reduced toughness and is observed as an increase in DBTT and a decrease in USE in a Charpy impact test, causes the most concern for ferritic/martensitic steels for fusion applications. Generally, steels with a low DBTT before irradiation have a low value after irradiation. The modified 9Cr-1Mo steel showed a relatively small increase in DBTT when irradiated in the absence of the formation of significant amounts of helium [7]. Since the shift in DBTT is caused by irradiation hardening due to the irradiation-induced formation of dislocation loops and precipitates, A-21 steel might have an advantage. The high density of precipitate particles and dislocations associated with the precipitates could act as dominant recombination sites for the vacancies and interstitials formed during irradiation, thus retarding the irradiation hardening that causes embrittlement. The particles could also trap helium, thus ameliorating any effect it might have on embrittlement. This needs to be verified by irradiation experiments.

Crack initiation in steels generally occurs at precipitate particles, and in the 9Cr-1MoVNb and 12Cr-1MoVW steels, initiation probably occurs at the large $M_{23}C_6$ particles, which are the dominant precipitates in these steels. If these large precipitates could be avoided, the impact toughness should be improved. In the thermo-mechanical treatment of the A-21 used to produce the TiC, the objective is to use up all the carbon to form TiC, thus avoiding the formation of the $M_{23}C_6$. Based on the TEM, this has occurred. Because of the smaller precipitates in A-21, crack initiation must occur at a higher stress than in the 9Cr-1MoVNb. Another advantage of the A-21 for the impact tests is that it has a smaller prior-austenite grain size than the 9Cr-1MoVNb (estimated prior-austenite grain sizes were 5-15μm for the A-21 vs. 16-22 for the 9Cr-1MoVNb [7]).

If the operating temperature of a fusion system with a ferritic/martensitic steel is to be increased, the creep strength of the steel must be improved over that of conventional or reduced-activation steels. Although no creep tests were conducted in this work, such tests have been conducted previously [9]. In Fig. 6, a comparison of Larson-Miller curves shows the creep-rupture behavior of A-21 to be superior to that of the modified 9Cr-1Mo steel. This is expected, given the

microstructure. Most of the points on the Larson-Miller curve for the A-21 steel were obtained for steel that had been tempered at 700°C, the same heat treatment used in the present work. However, four of the points on the curve were for specimens without the temper. As indicated in Fig. 6, it appears that results for all of the specimens—tempered or untempered— fall on the same smooth curve. If the steel could be used without a temper, that would be a further advantage for the steel. Use without tempering appears possible, since essentially all carbon is incorporated in the TiC precipitate, which means a low-carbon, and thus, softer martensite results.

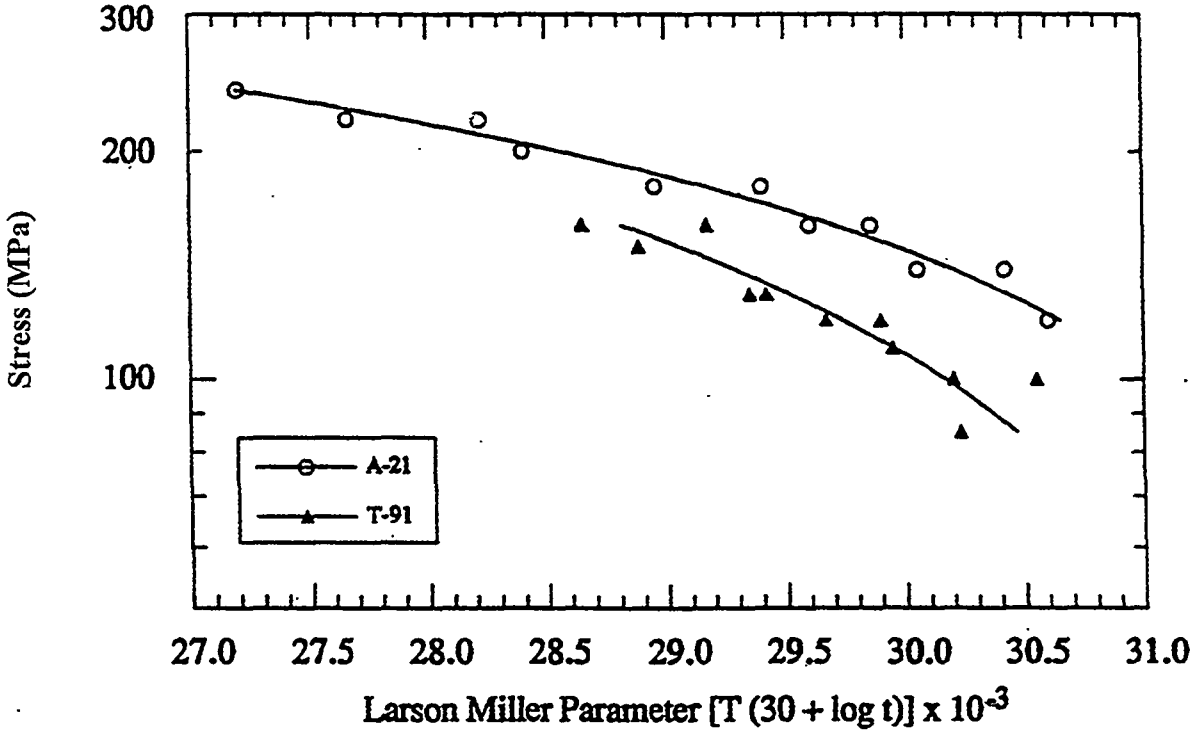

Figure 6. A comparison of the Larson-Miller curves of A-21 and modified 9Cr-1Mo steel.

The A-21 offers another advantage. If no $M_{23}C_6$ forms, essentially all the chromium remains in solution, thus enhancing the elevated-temperature oxidation and corrosion resistance. Over 1.5% of the 9% Cr in a conventional steel can be lost from the matrix by precipitation [10].

SUMMARY AND CONCLUSION

Tensile and Charpy impact properties were determined for A-21 steel, an Fe-9.5Cr-3Co-1Ni-0.6Mo-0.3Ti-0.07C ferritic/martensitic steel. Microstructure was also examined. By hot working the steel in the austenitic condition following austenitization to put all elements in solution, a high number density of fine TiC particles are produced on dislocations generated during the hot working. No large grain boundary and matrix $M_{23}C_6$ precipitates of the type found in the conventional Cr-Mo and reduced-activation Cr-W steels were observed. The strength of the A-21 steel is lower than that of modified 9Cr-1Mo steel at ≤600°C, but it becomes stronger at higher

temperatures. The transition temperature in a Charpy impact test for A-21 was similar to that of the modified 9Cr-1Mo steel, but the upper-shelf energy was higher.

Because of the presence of the high number density of fine TiC particles, the A-21 steel has superior creep properties to the modified 9Cr-1Mo and other conventional or reduced-activation ferritic/martensitic steels. All indications are that the properties of the A-21 steel should allow for a significantly higher operating temperature of a fusion power plant if the first wall were constructed of A-21 instead of a conventional Cr-Mo or a reduced-activation Cr-W steel.

REFERENCES

[1] J. Orr and L. Woollard, in Microstructural Development and Stability in High Chromium Ferritic Power Plant Steels, eds. A. Strang and D. J. Gooch (Institute of Materials, London, 1997) p. 53.
[2] R. F. Buck, Advanced Materials and Processes, 150(8) (1996) 27.
[3] D. J. Alexander, R. K. Nanstad, W. R. Corwin, and J. T. Hutton, in Automation Technology to Fatigue and Fracture Testing, ASTM STP 1092, eds. A. A. Braun, N. E. Ashbaugh, and F. M. Smith (American Society for Testing and Materials, Philadelphia, 1990) p. 83.
[4] W. R. Corwin and A. M. Hougland, in The Use of Small-Scale Specimens for Testing Irradiated Material, ASTM STP 888, eds. W. R. Corwin and G. E. Lucas (American Society for Testing and Materials, Philadelphia, 1986) p. 325.
[5] D. J. Alexander and R. L. Klueh, in Charpy Impact Test: Factors and Variables, ASTM STP 1072, ed. J. M. Molt (American Society for Testing and Materials, Philadelphia, 1990) p. 179.
[6] M. A. Sokolov and R. K. Nanstad, in Effects of Radiation on Materials: 17th International Symposium, ASTM STP 1270, eds. D. S. Gelles, R. K. Nanstad, A. S. Kumar, and E. A. Little (American Society for Testing and Materials, Philadelphia, 1996) p. 384.
[7] R. L. Klueh and D. J. Alexander, in Effects of Irradiation on Materials: 16th International Symposium, ASTM STP 1175, eds. A. S. Kumer, D. S. Gelles, R. K. Nanstad, and E. A. Little (American Society for Testing and Materials, Philadelphia, 1993) p. 591.
[8] J. R. DiStefano and V. K. Sikka, Summary of Modified 9Cr-1Mo Steel Development Program: 1975-1985, ORNL-6303, Oak Ridge National Laboratory, October 1986.
[9] R. F. Buck, Unpublished Research, 1996.
[10] R. Jayaram and R. L. Klueh, Met. & Mat. Trans. A, 29A (1998) 1551.

ON HYDROGEN AND HELIUM EMBRITTLEMENT IN ISOTOPIC TAILORING EXPERIMENTS - D. S. Gelles, M. L. Hamilton, B. M. Oliver and L. R. Greenwood (Pacific Northwest National Laboratory)*

OBJECTIVE

The objective of this effort is to quantify irradiation hardening response in isotopically tailored ferritic alloys following irradiation at 300°C in order to better understand behavior in this alloy class at low irradiation temperatures.

SUMMARY

The results of shear punch testing performed on irradiated isotopically tailored alloys are considered in terms of hydrogen and helium embrittlement in order to quantify the observed behavior. The results indicate that hydrogen embrittlement may be more significant than helium embrittlement.

PROGRESS AND STATUS

Introduction

Post-irradiation deformation response using shear punch testing has been reported for two series of alloys based on isotopic tailoring in order to study hydrogen and helium embrittlement in single variable experiments. Helium embrittlement using this approach was first studied in a series of Fe-12%Cr steels with intentional additions of 1.5% Ni either as natural Ni, ^{60}Ni or ^{59}Ni.[1,2] Following irradiation in HFIR at 300°C to 6.5 dpa, helium levels were estimated at 2.1 appm for both Fe-12Cr and Fe-12Cr-1.5^{60}Ni, at 41 appm for Fe-12Cr-1.5^{Nat}Ni and 70 appm for Fe-12Cr-1.5^{59}Ni, whereas hydrogen production was expected to be low. In the second experiment known as FIST, isotopic tailoring based on ^{54}Fe addition to the F82H composition was used.[3] In that case, following irradiation in HFIR at 300°C to 34 dpa, helium and hydrogen levels for the ^{54}Fe-containing alloy were measured at 65 appm and 400 appm, respectively and following irradiation at 250°C to 2.3 dpa they were 4.5 appm and 185 appm, respectively.[3] This data base provides an opportunity to separate behavior due to hydrogen and helium embrittlement. However, first, hydrogen and helium levels for the Ni doping experiment are reexamined and then the data are plotted and quantified (with the limitations of such an analysis well understood).

Results and Discussion

Helium concentrations have been measured for the Ni doped specimens irradiated at 300□C and hydrogen concentrations have been estimated for those irradiation conditions, assuming that all hydrogen is retained. The results are provided in Table 1 along with results obtained previously for FIST specimens but including both a revised prediction of the He levels for FIST and a revised measurement of H in FN51-2. The origin of higher H levels in specimen

---

*Pacific Northwest National Laboratory (PNNL) is operated for the U.S. Department of Energy by Battelle Memorial Institute under contract DE-AC06-76RLO-1830.

FN51-2 is not yet understood. From Table 1, it can be shown that the estimates for He in Ni doped specimens given above and in Reference 2 are very close to the measured values. The H levels anticipated in the Ni doped specimens are low and not very different as a function of composition. Most of the hydrogen in these specimens arises from the Fe-12Cr base composition because the Ni content is low, and at these doses, the ^{59}Ni effects are small relative to the fast neutron reactions. Therefore, the results of the Ni doped alloy series can be straightforwardly considered as an effect of He, and the consequences of an effect of H initially ignored. It should be noted that H levels measured for FIST irradiated specimens are closer than expected based on calculation.[3] This has been explained as a difference in behavior due to temperature, 250°C being low enough to retain H and include absorption from other causes and 300°C being high enough to allow release of most of the H produced.[3]

Table 1. Revision of measured (Exp.) and calculated helium and hydrogen concentrations for JP23 alloys irradiated at 300°C and FIST alloys irradiated at 250 and 300°C

Specimen	Material	Condition	He Conc. (appm)		H Conc. (appm)	
			Exp.	Calc.	Exp.	Calc.
6A5M-A	Fe-12Cr	300°C, 6.5 dpa	2.4	2.0	-	32
715M-A	Fe-12Cr-1.5^{60}Ni	300°C, 6.4 dpa	3.0	2.2	-	32
735M-A	Fe-12Cr-1.5^{59}Ni	300°C, 6.6 dpa	64.7	63	-	48
745M-A	Fe-12Cr-1.5^{Nat}Ni	300°C, 6.5 dpa	36.4	37	-	43
FN91-3	F82H ^{54}Fe	unirradiated	-	0	44±7	0
FN51-1&2	F82H ^{54}Fe	250°C, 2.3 dpa	4.5	4.6	340±199	182
C603	F82H ^{54}Fe	300°C, 34 dpa	65	65	396±21	2119

The shear punch results are provided both as test traces in Figure 1 and in tabulated form in Table 2. From Table 2, changes in shear strength values due to irradiation can be determined by comparison of unirradiated and irradiated response, and the results are plotted in Figure 2 as a function of He for the Ni doped specimen series and as a function of H for the FIST specimens. This choice for abscissa values is considered reasonable because the Ni doped alloys show greater variation in He production and the FIST specimens show greater variation in H production. From Figure 2, it can be shown that a trend appears evident in the FIST data as a linear function of H production but with large uncertainties in He level shown using labels in the plot. (Note that this is not likely to be a dose effect because hardening generally saturates quickly.) However, for the Ni doped alloys, the scatter is too large to demonstrate trends clearly. It is possible that there is no effect of He content on yield response whereas a linear response can be identified for the maximum strength response. But in both cases the scatter in the low He data is as large as the trends indicated.

It is well understood that quantitative definition of He and H embrittlement based on very limited data may be questioned; more data is needed. Nonetheless, this analysis indicates that H may play a larger role in embrittlement than He, depending on circumstances such as hydrogen release at higher temperatures. At 10 MWY/m^2 or approximately goal dose, He production is expected to be on the order of 1000 appm and H production on the order of

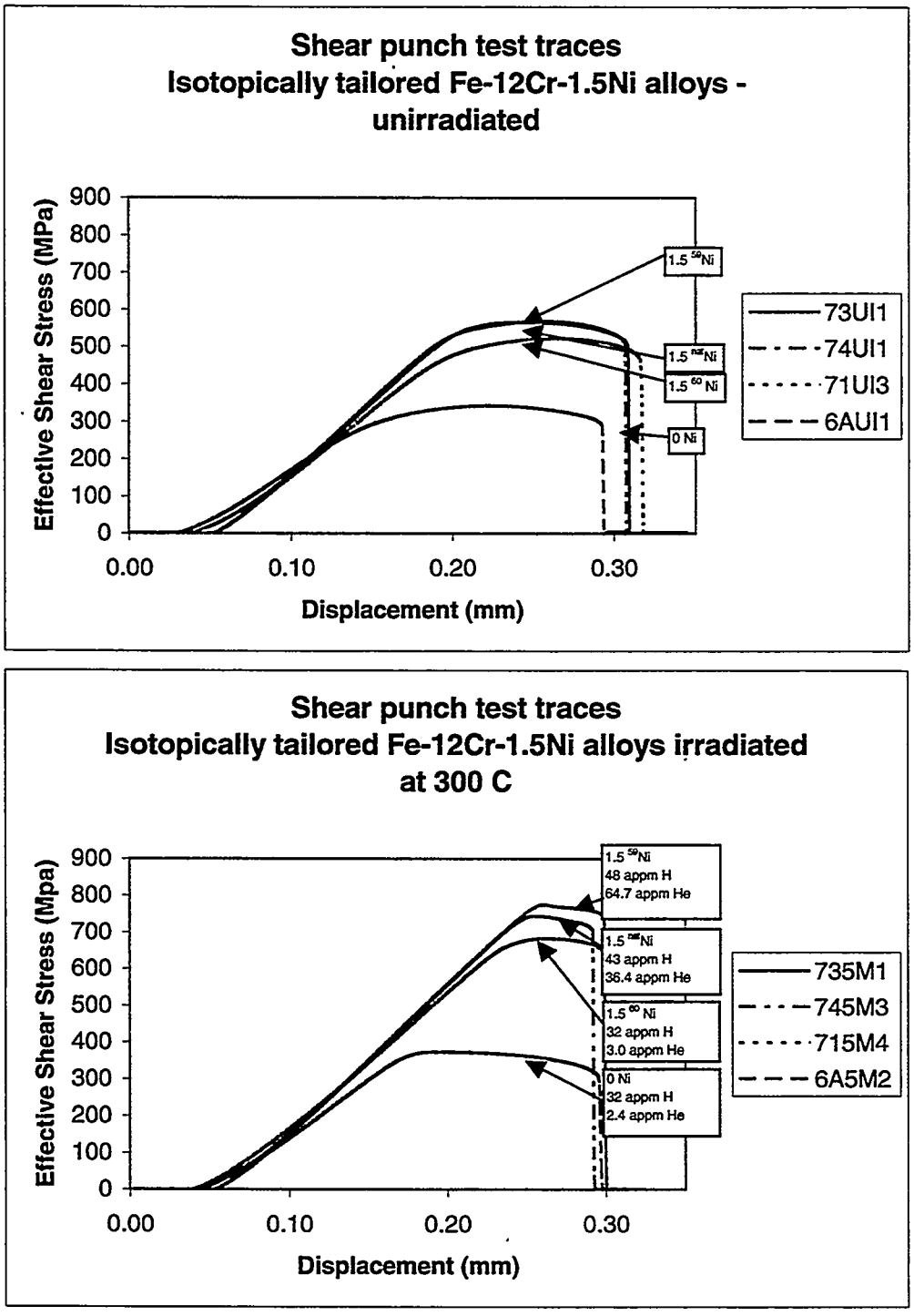

Figure 1 Shear punch test traces for isotopically tailored Fe-12Cr-1.5Ni a) unirradiated and b) irradiated at 300°C and c) for Fe F82H irradiated at 250 and 300°C.

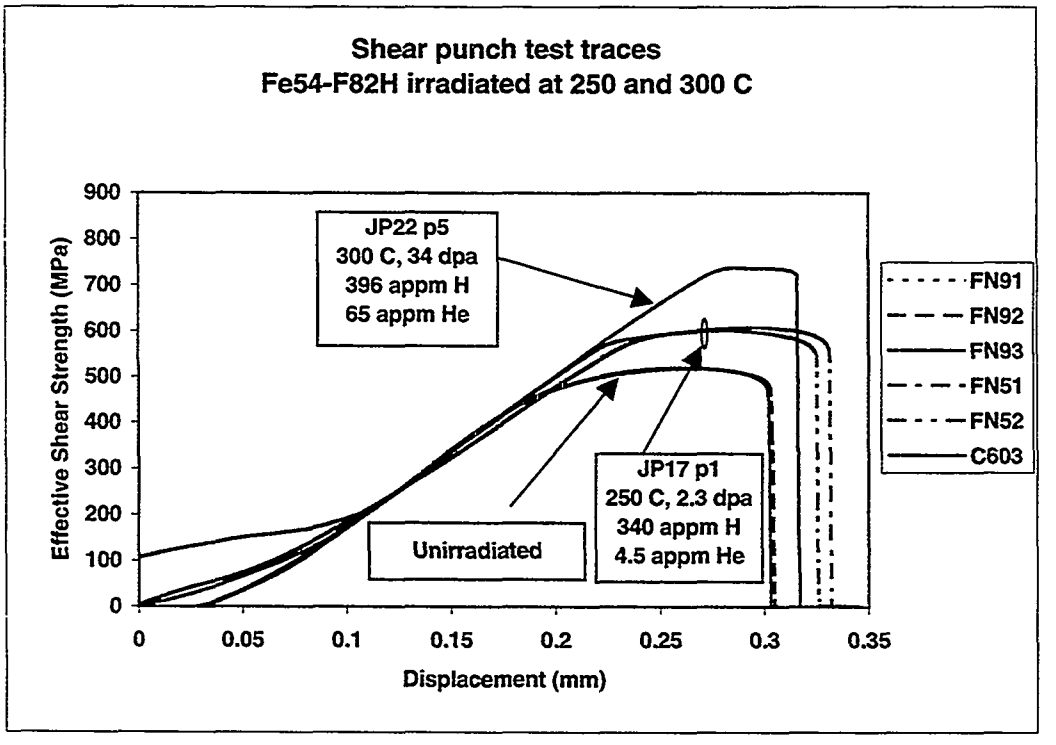

Figure 1 cont. **Shear punch test traces for isotopically tailored Fe-12Cr-1.5Ni a) unirradiated and b) irradiated at 300°C and c) for Fe F82H irradiated at 250 and 300°C.**

Table 2. Results of shear punch testing for Ni doped and FIST specimens.

	ID	Material	Condition	τ_{ys} (MPa)	τ_{ms} (MPa)
Ni doped	6A	Fe-12Cr	unirradiated	160	310
	71	Fe-12Cr-1.5^{60}Ni	unirradiated	360	530
	73	Fe-12Cr-1.5^{59}Ni	unirradiated	440	550
	74	Fe-12Cr-1.5^{Nat}Ni	unirradiated	410	580
	6A5M-A	Fe-12Cr	300°C, 6.5 dpa	300	400
	715M-A	Fe-12Cr-1.5^{60}Ni	300°C, 6.4 dpa	560	680
	735M-A	Fe-12Cr-1.5^{59}Ni	300°C, 6.6 dpa	610	780
	745M-A	Fe-12Cr-1.5^{Nat}Ni	300°C, 6.5 dpa	600	760
FIST	FN91-3	F82H ^{54}Fe	unirradiated	400	520
	FN51-2	F82H ^{54}Fe	250°C, 2.3 dpa	510	605
	C603	F82H ^{54}Fe	300°C, 34 dpa	600	738

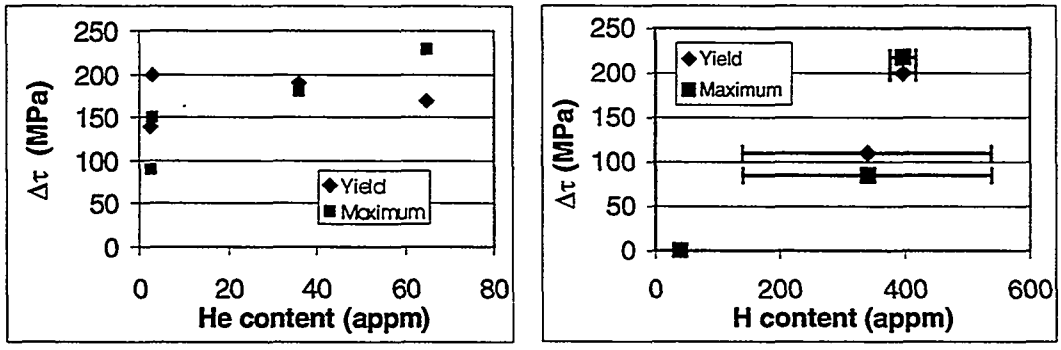

Figure 2 Change in τ_{ys} and τ_{ms} due to irradiation as a function of a) He content for Ni doped alloys and b) H content for FIST alloys.

10,000 appm. If our interpretation of H measurements in FIST specimens is correct, irradiation at temperatures above 250°C mitigates the problem because the H is not retained. The same is not expected for He. Also, synergistic effects can be anticipated at higher doses such that He bubbles may trap H at higher operating temperatures.

CONCLUSIONS

He levels obtained in Ni doped isotopically tailored alloys have been measured and the measurements agree with predictions.

H levels obtained in Ni doped isotopically tailored alloys have been estimated and it is found that a significant fraction of the H is obtained from transmutation of the base alloy for these low doses.

Analysis of limited shear punch data indicates a well-defined increase in strength with increasing H content whereas the data scatter as a function of He is as large as any trend indicated. However, more data is needed.

FUTURE WORK

This work will be continued when more specimens are available for testing.

REFERENCES

1. G. L. Hankin, M. L. Hamilton, D. S. Gelles and M. B. Toloczko, DOE/ER-0313/21 (1997) 156.
2. D. S. Gelles, G. L. Hankin, and M. L. Hamilton, J. Nucl. Mater. 258-63 (1998) 1216.
3. M. L. Hamilton, D. S. Gelles, S. Ohnuki, K. Shiba, Y. Kohno, and A. Kohyama, DOE/ER-0313/25 (1999) 136.
4. L. R. Greenwood, B. M. Oliver, S. Ohnuki, K. Shiba, Y. Kohno, A. Kohyama, J. P. Robertson, J. W. Meadows and D. S. Gelles, submitted for publication in the proceedings of ICFRM-9 to be published in J. Nucl. Mater.

EMBRITTLEMENT OF REDUCED-ACTIVATION FERRITIC/MARTENSITIC STEELS IRRADIATED IN HFIR AT 300 AND 400°C—R. L. Klueh, M. A. Sokolov (Oak Ridge National Laboratory), K. Shiba, and Y. Miwa (Japan Atomic Research Institute)

Extended Abstract*

Miniature Charpy and tensile specimens of the following reduced-activation ferritic/martensitic steels and one modified (nickel-doped) steel were irradiated in the High Flux Isotope Reactor (HFIR) to a maximum dose of ≈11 dpa: a 5-ton heat of standard F82H (F82H-Std), nominally Fe-7.5Cr-2W-0.2V-0.04Ta-0.0034B-0.1C (compositions in wt. %); a 5-ton heat of the IEA modified F82H (F82H-Mod), nominally Fe-7.5Cr-2W-0.15V-0.02Ta-0.1C; an experimental 400-g heat of ORNL 9Cr-2WVTa, nominally 9Cr-2W-0.25V-0.07Ta-0.1C; and an experimental 400-g heat of the 9Cr-2WVTa modified by the addition of 2% Ni (9Cr-2WVTa-2Ni). The two F82H steels were irradiated at 300 and 400°C, and the 9Cr-2WVTa and 9Cr-2WVTa-2Ni steels were irradiated at 400°C.

An objective of these tests was to determine if there is a helium effect on impact behavior over and above that due to irradiation hardening. Nickel was added to the 9Cr-2WVTa to produce helium from (n,α) reactions of ^{58}Ni with thermal neutrons in the HFIR spectrum. For the maximum dose of ≈11 dpa, ≈115 appm He formed in the 9Cr-2WVTa-2Ni. The F82H-Std contained ≈40 appm He after ≈11 dpa. For this steel, helium was produced from (n,α) reactions of thermal neutrons with the 34 wppm B in this steel. The F82H-Mod and the 9Cr-2WVTa steels contained ≈5 appm He after irradiation to 11 dpa.

All of the steels hardened during irradiation at 300 and 400°C, as determined by the increase in strength. The F82H-Mod showed a slightly larger increase than the F82H-Std, although the F82H-Std was somewhat stronger than the F82H-Mod at 300°C before irradiation. Before irradiation, the strength at 400°C of the 9Cr-2WVTa and 9Cr-2WVTa-2Ni were similar. Irradiation caused a similar increase in the yield stress of 9Cr-2WVTa-2Ni and 9Cr-2WVTa steels. Ductilities of the two steels before and after irradiation were also similar.

Irradiation embrittlement was observed for all of the steels as a shift in ductile-brittle transition temperature (DBTT) and a decrease in upper shelf energy (USE) in the Charpy tests. The largest shift in DBTT (ΔDBTT) occurred for the two F82H steels irradiated at 300°C, but there was little difference in ΔDBTT of the two steels. At 400°C where all four steels were irradiated, the 9Cr-2WVTa had the smallest shift (79°C), and the F82H-Mod had the largest shift (146°C), with intermediate values for the F82H-Std (117°C) and the 9Cr-2WVTa-2Ni (133°C).

Whether helium affects the Charpy behavior of the F82H-Std relative to the F82H-Mod is unclear. If helium concentration was the only difference between the two steels, then the results indicated no helium effect. However, there are differences in composition and in grain sizes of the two steels, so the effect of helium, if any, was not discernable. The 9Cr-2WVTa-2Ni steel was irradiated to determine if there was an effect of ≈115 appm He produced from the ^{58}Ni in the steel. The ΔDBTT of the 9Cr-2WVTa-2Ni (133°C) was 68% greater than for 9Cr-2WVTa (79°C). Irradiation hardening of the steels was similar. The results were tentatively taken to be a helium effect. However, in previous work on nickel-doped modified 9Cr-1Mo and Sandvik HT9, there were indications of possible intergranular fracture on specimens tested on the lower shelf, and this led to the proposal that helium affected the fracture behavior of the steels by causing a change in fracture mode. No indication of intergranular fracture was observed on the 9Cr-2WVTa-2Ni steel.

* Extended abstract of paper submitted for publication in the *Journal of Nuclear Materials* (Proceedings of the Ninth International Conference on Fusion Reactor Materials).

A Microstructural Study of the Oxide Scale Formation on ODS Fe-13Cr Steel, D.T. Hoelzer, B.A. Pint, I.G. Wright (Oak Ridge National Laboratory)

To be published in Journal of Nuclear Materials as Proceedings of the 9th International Conference on Fusion Reactor Materials, October 10-15, 1999, Colorado Springs.

Extended Abstract

The high-temperature oxidation behavior of an Y_2O_3-oxide dispersion strengthened (ODS) Fe-13Cr steel was investigated in air at temperatures of 700°, 800°, and 900°C for 10,000 h. The specimen-only mass gains shown in Figure 1 indicated that the oxidation closely followed a parabolic rate law at each temperature and that the oxidation rate was lower than other studies based on shorter test times. Oxidation at 700°C and 800°C resulted in very low mass gains and intermediate mass gains at 900°C due to CrO_3 evaporation. Parabolic rate constants were derived from the kinetic data for the ODS Fe-13Cr steel.

The microstructural analysis of the oxide scales formed at 700° and 800°C was conducted using cross-section light microscopy and analytical electron microscopy (AEM) using cross-sectional thin foils; at the time of reporting, the 900°C specimen was not ready for characterization. The surface scales that formed on the ODS Fe-13Cr steel during oxidation at 700°C and 800°C were relatively uniform in thickness and adherent to the steel. In general, the scale thickness was <1μm at 700°C and <5μm at 800°C. The AEM analysis showed that the main scale was a continuous Cr-oxide and that an underlying amorphous silica layer formed at both temperatures, despite the low Si content (0.05wt.%) in the alloy. The surface scales consisted of $(Fe,Cr)_3O_4$ at 700°C and Cr_2O_3 (chromia) at 800°C. The underlying silica layer was nearly continuous but showed that areas of contact still existed between the Cr-oxide scale and steel. The silica layer was non-uniform in thickness and the thickness depended on the oxidation temperature; the layers were ~0.3μm at 700°C and ~0.9μm at 800°C.

The excellent oxidation behavior of the ODS Fe-13Cr steel could not be attributed solely to the formation of a continuous Cr-oxide surface scale at all temperatures, since the oxidation rates were found to be significantly slower than expected for rate control by a chromia scale. Two possible factors could have influenced the scale formation and kinetics of oxidation at 700°C and 800°C; the Y-oxide dispersion and the silica layer. The dispersion of small stable Y-oxide particles resulted in a fine grain microstructure which allowed rapid diffusion of Cr by grain boundary diffusion to the surface where it could react with O to form the Cr-oxide scale. The formation of the silica layer acted as a diffusion barrier to inward migrating O and outward migrating metallic elements such as Fe and Cr.

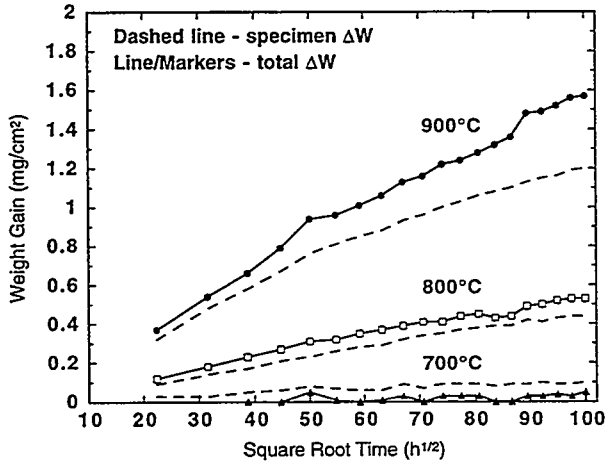

Figure 1. Parabolic plot of weight grain against the square root of time at each temperature.

IMPURITY CONTENT OF REDUCED-ACTIVATION FERRITIC STEELS AND THE EFFECT ON THE REDUCED-ACTIVATION CHARACTERISTICS—R. L. Klueh (Oak Ridge National Laboratory), E. T. Cheng (TSI Research, Inc.), M. L. Grossbeck, and E. E. Bloom (Oak Ridge National Laboratory)

Extended Abstract*

Development of low- or reduced-activation materials for fusion has focused on the issue of radioactive waste disposal or recycling of materials from fusion power plant components after they have reached the end of their service lifetime. The objective has been to eliminate or minimize those elements from an alloy that would produce long-lived radioactive isotopes during irradiation in a fusion neutron spectrum. Emphasis in the development process has generally centered on eliminating Nb, Cu, Ni, Mo, and N, widely used alloying elements, with niobium usually receiving the most attention, because of the very low levels (<1 wppm) that niobium cannot exceed if the steel is to meet low-activation criteria.

Besides the elements listed above, various other elements that could appear in the materials as tramp impurities must be restricted to extremely low levels. These elements include Ag, Ho, Bi, Co, Sm, Lu, Dy, Gd, and Cd. To determine the levels of these elements in steels, three heats of reduced-activation martensitic steel were analyzed by inductively coupled plasma mass spectrometry, which is capable of detecting very small levels of impurities. The steels analyzed were: a 5-ton heat of modified F82H for which an effort was made during production to reduce detrimental impurities, a 1-ton heat of JLF-1, and an 18-kg heat of ORNL 9Cr-2WVTa. Specimens from commercial heats of modified 9Cr-1Mo and Sandvik HT9 were also analyzed. The objective was to determine the difference in the impurity levels in the F82H and steels for which less effort was used to insure purity.

The results for the steels indicated that progress has been made in reducing the level of detrimental impurities for the two large heats of reduced-activation steel. The F82H produced with present technology had the lowest levels of the restricted elements, but in some cases the levels were not much different from the other heats. Silver, niobium, and molybdenum proved to be the most important of the restricted elements, and the steels that have been made up to now do not meet the criteria for low activation for shallow land burial of nuclear waste made up of these steels after an integrated wall loading of 20 MW y/m^2 after a 100 y cooling off period. However, it appears that reduced-activation steels could be produced with these detrimental impurity elements at levels low enough to meet the present criteria for shallow land burial. If instead of shallow land burial, it is desired to recycle the steel, with a "hands-on" dose rate limit of 25 $\mu Sv h^{-1}$ after a 100 y cooling time, then considerable research and expense will be required to develop processes that will allow the production of steel that will meet these criteria.

There has probably never been a requirement for a structural material to be processed to have specified impurity levels as low as those required to meet the reduced-activation criteria. Even though the materials will not be needed for some time, it would appear that an effort should be mounted to determine the means to achieve the desired purity levels, especially if recycling is to be pursued. Such an effort should enlist support from industrial materials processors to examine techniques used in the past to produce high-purity materials and determine ways that these techniques might be combined with the latest technology for future application. The effort should not be delayed if reduced-activation materials are to be available when fusion power production is ready to begin operation.

* Extended abstract of paper submitted for publication in the *Journal of Nuclear Materials* (Proceedings of the Ninth International Conference on Fusion Reactor Materials).

EFFECT OF HELIUM PRODUCTION ON SWELLING OF F82H IRRADIATED IN HFIR – E. Wakai (Japan Atomic Energy Research Institute), N. Hashimoto (Oak Ridge National Laboratory), J. P. Robertson and R. L. Klueh (ORNL), and S. Jitsukawa (JAERI)

Extended Abstract (the full paper will be published in the Journal of Nuclear Materials as Proceedings of the Ninth International Conference on Fusion Reactor Materials, October 10-15, 1999, Colorado Springs, Colorado).

Swelling of tempered F82H-std, F82H steels doped with natural boron (309 appm), isotope ^{10}B (305 appm) and non-tempered F82H steels doped with 1.31 at% ^{58}Ni, and 1.27 at5% ^{60}Ni irradiated at 300 and 400°C to 51 dpa in the HFIR have been examined by TEM. The swelling of F82H-std irradiated at 400°C to 51 dpa was about 0.45% and the natural B and ^{10}B doped F82H steels was 0.9 and 1.1%, respectively. In the ^{58}Ni and ^{60}Ni doped F82H steels, the swelling was 0.02 and 0%, respectively, even though the ^{58}Ni-doped specimen had the highest helium production. Large cavities in the F82H-std were observed in the matrix but not observed near many lath boundaries, while in the ^{10}B doped specimens, cavities were formed even near lath boundaries. While the cavities formed at 300°C to 51 dpa were observed in only the F82H+ ^{10}B and F82H+ ^{58}Ni steels, the swelling value was insignificant. The number densities of dislocation loops formed in these steels at 300°C to 51 dpa were very high (i.e., on the order of 10^{22} m^{-3}), and at 400°C to 51 dpa the number densities were very low (i.e., on the order of 10^{22} m^{-3}). In the F82H+Ni, high-density carbides were formed in the matrix at these temperatures. The production of helium atoms enhanced the swelling of the F82H steel. However, the non-tempered treatment for the F82H+Ni suppressed remarkably the swelling. The cause of low swelling in the F82H+Ni may be due to the occurrence of high density carbides acting as sink or the decrease of mobility of vacancies interacted with carbon atoms in matrix.

SWELLING OF F82H IRRADIATED AT 673 K UP TO 51 DPA IN HFIR – Y. Miwa, E. Wakai, K. Shiba (Japan Atomic Energy Research Institute), J. P. Robertson, A. F. Rowcliffe (Oak Ridge National Laboratory), and A. Hishinuma (JAERI)

Extended Abstract (the full paper will be published in the Journal of Nuclear Materials as Proceedings of the Ninth International Conference on Fusion Reactor Materials, October 10-15, 1999, Colorado Springs, Colorado).

Reduced-activation ferritic/martensitic steel, F82H (8Cr-2W-0.2V-0.04Ta-0.1C), and the same alloy doped with isotopically tailored boron were irradiated at 673 K up to 51 dpa in the High Flux Isotope Reactor (HFIR). The concentrations of ^{10}B in these alloys were 4, 62, and 325 appm, during HFIR irradiation, which resulted in the production of 4, 62, and 325 appm He, respectively. After irradiation, transmission electron microscopy was carried out, and the following conclusions were made.

(1) Swelling of F82H-std and the two alloys doped with ^{10}B increased linearly with increasing displacement damage. The root mean cube of voids increased and the number density of voids decreased with increasing displacement damage.

(2) With the addition of ^{10}B, number density of cavities increased. Larger swelling was observed in alloys that contained higher concentrations of ^{10}B.

(3) Voids were observed in the matrices, but rarely on the lath boundaries or the precipitate/matrix interfaces.

DAMAGE STRUCTURE OF ISOTOPICALLY TAILORED HT9 STEELS IRRADIATED AT 400°C IN THE HFIR – N. Hashimoto, J. P. Robertson (Oak Ridge National Laboratory), and S. Jitsukawa (Japan Atomic Energy Research Institute)

Extended Abstract (the full paper will be published in the Journal of Nuclear Materials as Proceedings of the Ninth International Conference on Fusion Reactor Materials, October 10-15, 1999, Colorado Springs, Colorado).

The microstructures of reduced-activation martensitic steel, HT9-std. (12Cr-1MoVW), and HT9 doped with ^{58}Ni and ^{60}Ni, irradiated at 400°C to 16.3 dpa in the High Flux Isotope Reactor (HFIR) were investigated by transmission electron microscopy. Cavities were observed in HT9-std. And HT9 doped with ^{58}Ni irradiated to 16.3 dpa, while cavities were not observed in HT9 doped with ^{60}Ni. Swelling of HT9-std. And HT9-1.4wt% ^{58}Ni was estimated to be 0.002 and 0.004% respectively; these values correlate with the helium concentrations in each alloy. Irradiation-induced a_0<100> and $a_0/2$)<111> type dislocation loops were observed in all alloys; the number density and the mean diameter of a_0<100> type loops were higher and larger than those of ($a_0/2$)<111> Type loops, respectively. The loop density was highest in the HT-91.4 wt. of ^{58}Ni, which contained the highest concentration of helium. Irradiation-induced precipitates, which were identified as M_6C (η) carbide, α'-phase and M_2X phase, were observed in all alloys. The M_6C (η) and α' were formed along dislocation loops, suggesting that dislocation loops are sites of Cr-rich precipitates during irradiation.

4.0 COPPER ALLOYS AND HIGH HEAT FLUX MATERIALS

ELECTRICAL CONDUCTIVITY AND TENSILE PROPERTIES OF COPPER AND OXIDE DISPERSION STRENGTHENED COPPER ALLOYS FOLLOWING HFIR IRRADIATION TO 13 DPA AT 200 AND 400°C – S. J. Zinkle and L. T. Gibson (Oak Ridge National Laboratory)

OBJECTIVE

The objective of this report is to summarize recent tensile and electrical resistivity measurements on pure copper and oxide dispersion strengthened copper alloys following HFIR irradiation to ~13 dpa at 200 and 400°C

SUMMARY

The tensile properties and room temperature electrical resistivity have been measured for pure copper and MAGT 0.2, GlidCop AL15 and GlidCop AL25 oxide dispersion strengthened copper alloys following irradiation in the spectrally tailored HFIR-MFE-200J and –400J irradiation capsules. The tensile measurements were performed at the irradiation temperature and at room temperature, at strain rates between $2x10^{-5}$ s^{-1} and 0.01 s^{-1}. Significant increases in the tensile strength were observed following irradiation at 200°C, accompanied by a reduction in uniform elongation. The irradiation at 400°C had only a moderate effect on the tensile properties. A large increase in the electrical resistivity (mainly attributable to solid solution transmutation products) was observed for both irradiation temperatures. The tensile strength increased with increasing strain rate, particularly for the GlidCop Al25 alloys irradiated and tested at 400°C. The effect of test temperature on the yield and ultimate strengths was much more pronounced in the irradiated GlidCop specimens compared to the unirradiated specimens.

PROGRESS AND STATUS

Introduction

High-strength, high-conductivity copper alloys are being considered for first wall heat sink and divertor structural applications in fusion energy systems such as the proposed International Thermonuclear Experimental Reactor (ITER) [1-3]. Copper alloys have also been proposed for the centerpost magnet in spherical tokamaks. Although a considerable amount of high fluence microstructural and room temperature tensile data exist for copper alloys irradiated at temperatures above ~380°C [1,4-6], there are only a few high dose (>1 dpa) studies on copper irradiated at lower temperatures. The main radiation effects which occur in copper alloys at 200-400°C are radiation hardening (with accompanying embrittlement) and void swelling. Low dose (<1 dpa) studies of copper irradiated at temperatures $\leq$200°C suggest that the amount of radiation hardening approaches saturation for damage levels above ~0.1 dpa. One of the objectives of the present study was to determine whether this apparent hardening saturation is maintained up to damage levels in excess of 10 dpa.

Experimental Procedure

A limited amount of space was allocated to copper alloy specimens in the HFIR-MFE-200J and –400J irradiation capsules. Based on the promising radiation resistance obtained in prior high-dose irradiation studies in FFTF [1,4-6], the HFIR matrix placed a heavy emphasis on dispersion strengthened copper alloys (GlidCop and MAGT alloys). Several of the specimen heats were identical to those used in prior irradiation experiments in order to facilitate comparisons. Pure

copper was also included as a reference material. The GlidCop Al15 and Al25 alloys contained 0.15 wt.% and 0.25 wt.% Al, respectively, in the form of small aluminum oxide particles. The B-deoxidized GlidCop alloys contained ~0.01 wt.%B. The MAGT 0.2 alloys had a chemical composition of Cu-0.2%Al-0.05%Hf-0.05%Ti-0.2%O, and consisted of a pure copper matrix with small oxide particles [7]. GlidCop Al15 induction brazed sheet tensile specimens were machined from a brazed bar such that the braze joint was located in the center of the gage region (butt joint configuration). These specimens were brazed with a Cu-6%P-5%Ag alloy at 810°C for 81 s in a Gleeble resistance-heating machine. Both type SS1 and SS3 miniature sheet tensile specimens were included in the irradiation capsules (nominal gage dimensions of 1.52x0.76x20.3 mm and 1.52x0.76x7.6 mm, respectively). The 80% cold-rolled GlidCop Al25 +B tensile specimens had a nominal thickness of 0.51 mm. The gage dimensions of all of the individual specimens were measured prior to irradiation. All of the specimens were electroplated with a 5-10 μm layer of Ni prior to irradiation in order to minimize diffusion bonding of the copper specimens during the irradiation.

The specimens were loaded in the Hf spectrally shielded HFIR-MFE-200J and –400J capsules, which operated for 440.6 effective full power days in the Removable Beryllium irradiation positions of HFIR [8,9]. The detailed specimen matrix (including TEM disks) for the irradiation capsules is described elsewhere [10]. Most of the Cu alloy tensile specimens were located in the top half of the two irradiation capsules. The fast neutron fluence in the capsules ranged from 1.36 to 1.94×10^{26} n/m^2-s, which corresponds to 10.4 to 14.9 dpa in copper [9]. The 4.2 mm hafnium shielding reduced the horizontal midplane thermal neutron flux to 9.2×10^{18} n/m^2-s, which is ~20% of its normal value. The calculated dominant solute transmutations in copper were 1.4% Ni and 0.5% Zn. The irradiation produced a calculated He concentration of 2 appm in pure copper. Higher levels of helium (up to ~100 appm) should have been produced in the boron-deoxidized GlidCop specimens. The average irradiation temperatures of the 200J and 200J capsules were maintained at 200 and 400°C, respectively. The detailed operating temperature history is given in ref. [8].

Four-point probe electrical resistivity measurements were performed at room temperature on the irradiated SS-1 and SS-3 sheet tensile specimens, using procedures summarized elsewhere [11]. The temperature was recorded for each measurement and the resistivity data were corrected to a reference temperature of 20°C using the copper resistivity temperature coefficient of $d\rho/dT = 6.7 \times 10^{-11}$ Ω-m/K. Nonuniformities in the width and thickness in the specimen gage region caused the typical experimental uncertainty of individual resistivity measurements to be ±0.5%. The resistivity data were corrected for the influence of the Ni plating, which amounted to an ~2% change compared to the raw data.

All of the tensile specimens were tested in a hot cell using a 200 pound load cell mounted on a screw-driven Instron machine. Table 1 summarizes the tensile specimen experimental matrix. Several specimens were broken (specimens C2, F3 and X1 from HFIR-200J and A11 from HFIR-400J) or bent during capsule disassembly (cf. Table 1). The induction brazed specimen F4 (HFIR-400J) broke during mounting for tensile testing in the hot cells. Specimen L8 from HFIR-400J was severely bent and was not tested. Specimens W3, T1 and X3 from HFIR-200J and H5, L7 from HFIR-400J were also significantly deformed during capsule disassembly such that valid tensile data could not be obtained. Strain rate variation tests were performed on some specimens, including several of the bent specimens in order to measure the strain rate sensitivity of the radiation hardened samples. The crosshead speed was varied from 0.001 to 0.5 inch per minute, which resulted in strain rates of 2×10^{-5} to 0.01 s^{-1}. The room temperature tests were performed in air, and the elevated temperature tests were performed in vacuum (<10^{-5} torr). The samples were held at the test temperature for 15 minutes prior to testing.

Table 1. Specimen matrix and tensile test conditions for the pure copper and GlidCop dispersion strengthened copper alloys irradiated in the HFIR-200J and –400J capsules. The specimens with ID code in parentheses were bent during capsule disassembly.

SS-1 and SS-3 specimens from HFIR-MFE-RB*-200J-1 capsule

Alloy	Geometry	ID code	Test temperature & crosshead speed
99.999% copper, as wrought (MRC Marz grade rod)	SS-1	A6 A8 (A7)	200°C, 0.02"/min 29°C, 0.02"/min 200°C, 0.001"/min through 0.2% yield, then increase to 0.02"/min
GlidCop AL15+B, as wrought (ORNL plate)	SS-1	L1 L2 L3	200°C, 0.5"/min 200°C, 0.001"/min 200°C, 0.02"/min
GlidCop AL25, as wrought (Risø rod, no boron)	SS-1	H2 H3 (H1)	200°C, 0.02"/min 29°C, 0.02"/min 200°C, 0.001"/min through 0.2% yield, then increase to 0.02"/min
GlidCop AL25, 50%CW (PNL "R4" 40 mil sheet)	SS-3	X2 (X3)	200°C, 0.02"/min 200°C, 0.001"/min through 0.2% yield, then increase to 0.02"/min
GlidCop AL25+B (Risø), 80% CW, 0.02" thick (626AAF, lot #4005m09)	SS-3	C1 C3	200°C, 0.02"/min 200°C, 0.001"/min
GlidCop AL25+B (Risø), as-wrought (616 AAE, lot #4005806 rod)	SS-3	W1 W2 (W3)	200°C, 0.02"/min 20°C, 0.02"/min 200°C, 0.001"/min through 0.2% yield, then increase to 0.02"/min
MAGT 0.2, 50%CW (Technology 1)	SS-3	T2 T3 (T1)	200°C, 0.02"/min 200°C, 0.02"/min 200°C, 0.001"/min through 0.2% yield, then increase to 0.02"/min
GlidCop AL15+B, Auburn U. induction brazed (ORNL as-wrought plate)	SS-3	F1 F2	200°C, 0.02"/min 29°C, 0.02"/min

Table 1, continued: SS-1 and SS-3 specimens from HFIR-MFE-RB*-400J-1 capsule.

Alloy	Geometry	ID code	Test temperature & crosshead speed
99.999% copper, as wrought (MRC Marz grade rod)	SS-1	(A09) (A10)	400°C, 0.02"/min 29°C, 0.02"/min
GlidCop AL15+B, as wrought (ORNL plate)	SS-1	L06 (L07)	400°C, 0.02"/min 400°C, 0.02"/min
GlidCop AL25, as wrought (Risø rod, no boron)	SS-1	H04 H06 (H05)	400°C, 0.02"/min 30°C, 0.02"/min 400°C, 0.001"/min through 0.2% yield, then increase to 0.02"/min
GlidCop AL25, 50%CW (PNL "R4" 40 mil sheet)	SS-3	X4 X5 X6	400°C, 0.02"/min; 30°C, 0.02"/min; 400°C, 0.001"/min through 0.2% yield, then increase to 0.02"/min
GlidCop AL25+B (Risø), 80% CW, 0.02" thick (626AAF, lot #4005m09)	SS-3	C6 C7 C8	400°C, 0.02"/min; 400°C, 0.001"/min; 30°C, 0.02"/min
GlidCop AL25+B (Risø), as-wrought (616 AAE, lot #4005806 rod)	SS-3	W4 W5 W6	400°C, 0.02"/min; 400°C, 0.02"/min; 30°C, 0.02"/min
MAGT 0.2, 50%CW (Technology 1)	SS-3	T4 T5 T6	400°C, 0.02"/min; 30°C, 0.02"/min; 400°C, 0.001"/min through 0.2% yield, then increase to 0.02"/min
GlidCop AL15+B, Auburn U. induction brazed (ORNL as-wrought plate)	SS-3	F5 F6	400°C, 0.02"/min; 30°C, 0.02"/min

Results and Discussion

The electrical resistivity measurements on the unirradiated and irradiated specimens are summarized in Table 2. A large variability was obtained for the resistivity of the unirradiated induction-brazed GlidCop Al15 specimens, presumably due to variations in the thickness of the braze layer. The resistivity of the unirradiated pure copper and dispersion-strengthened copper alloys were in agreement with data obtained on other heats of these materials [12-16]. The increase in resistivity for most of the copper alloys in both the 200J and 400J capsules was ~6 to 8 nΩ-m. Previous work has found that the resistivity increase associated with defect cluster (stacking fault tetrahedra, small dislocation loops) formation in copper saturates at ~1.2 nΩ-m [13]. The remaining 5-7 nΩ-m resistivity increase for the HFIR-200J specimens can be attributed to Ni, Zn, Co solid transmutation products, since transmission electron microscopy (TEM) did not find evidence for void formation in Cu and Cu alloy specimens in this capsule [17]. The resistivity of the as-wrought GlidCop Al25+B specimens irradiated in the HFIR-400J capsule were anomalously high for unknown reasons. The resistivity of the specimens in the HFIR-400J capsule was generally higher than that of the HFIR-200J capsule. TEM investigation did not detect void formation in GlidCop Al25, whereas a moderate density of large cavities was observed in pure copper irradiated in the HFIR-400J capsule [17].

Table 2. Summary of electrical resistivity measurements on the pure copper and GlidCop dispersion strengthened copper alloy specimens from HFIR-MFE-200J and –400J capsules.

Alloy, ID number	Unirrad. resistivity (nΩ-m)	Resistivity of specimens irrad. at 200°C (nΩ-m)	Resistivity of specimens irrad. at 400°C (nΩ-m)
pure copper, as wrought (SS1)	17.18±0.11	23.40±0.16	23.61 (1 spec.)
GlidCop AL15+B, as wr't (SS1)	18.79±0.12	27.36±0.32	25.38±0.22
GlidCop AL25, as wrought (SS1)	19.26±0.08	26.38±0.18	29.59±1.4
GlidCop AL25, 50%CW (SS3)	19.40±0.16	26.52±0.70	27.75±1.28
GlidCop AL25+B, 80% CW (SS3)	19.35±0.07	26.20±0.07	28.56±1.61
GlidCop AL25+B, as-wr't (SS3)	19.42±0.15	25.93±0.25	35.32±0.35
MAGT 0.2, 50%CW (SS3)	21.91±0.08	27.47±0.05	29.28±0.24
GlidCop AL15+B, induction brazed (SS3)	25.5±3.1	27.06±0.50	27.02±0.78

Tables 3 and 4 summarize the tensile data obtained on the specimens from the HFIR-200J and –400J capsules, respectively. The strain hardening capacity of the irradiated specimens was low in all specimens tested at the irradiation temperature, with typical uniform elongation values of ~1%. Irradiation at 200°C produced a 100-150 MPa increase in the room temperature yield strength of the GlidCop dispersion strengthened copper alloys, and a ~200 MPa increase in the room temperature yield strength of pure copper. Figure 1 plots the room temperature yield strength of copper (specimen A8) along with previous low temperature (20-150°C) results on pure copper [18-24]. The results suggest that saturation in the radiation hardening occurs for doses above ~0.1 dpa, although the influence of the higher irradiation temperature of the HFIR-200J experiment (200°C) compared to the other experiments summarized in Fig. 1 (20-150°C) needs further investigation.

Table 3. Tensile test results on copper alloy specimens from HFIR-MFE-200J capsule. The tensile data in parentheses are considered unreliable due to bent or brittle tensile specimens.

Alloy, ID number	Temper-ature (°C)	Strain rate (s^{-1})	Yield Strength (MPa)	Ultimate Strength (MPa)	Uniform Elong. (%)	Total Elong. (%)
Marz copper, as wrought						
A6 (SS1)	200	$4.2x10^{-4}$	239	242	1.1	7.7
A8 (SS1)	29	$4.2x10^{-4}$	306	308	2.2 (stn)[a]	7.1
A7 (SS1)-sharp bend	200	$0.21->4.2x10^{-4}$	($\Delta\sigma$~3.5)	–	–	–
GlidCop AL25, as wrought						
H2 (SS1)	200	$4.2x10^{-4}$	430	445	0.5	7.2
H3 (SS1)	30	$4.2x10^{-4}$	529	560	0.7	3.8
H1 (SS1)-bent/twisted	200	$0.21->4.2x10^{-4}$	($\Delta\sigma$~7)	–	–	–
GlidCop AL15+B, as wr't						
L1 (SS1)	200	0.010	461	475	0.6	2.2
L2 (SS1)	200	$2.1x10^{-5}$	402	406	0.4	1.7
L3 (SS1)	200	$4.2x10^{-4}$	431	433	0.3	1.2
GlidCop AL25, 50%CW						
X2 (SS3)	200	$1.1x10^{-3}$	490	524	0.8	2.8
X3 (SS3)-bent	200	$0.56->11x10^{-4}$	$\Delta\sigma$~11	–	–	–
GlidCop AL25+B, 80% CW						
C1 (SS3)	200	$1.1x10^{-3}$	575	580	0.4	1.9
C3 (SS3)	200	$5.6x10^{-5}$	530	549	0.5	2.2
GlidCop AL25+B, as-wr't						
W1 (SS3)	200	$1.1x10^{-3}$	471	490	0.5	8.3
W2 (SS3)	29	$1.1x10^{-3}$	569	601	0.5	6.7
W3 (SS3)-bent sample	200	$0.56->11x10^{-4}$	$\Delta\sigma$=17		–	–
MAGT 0.2, 50%CW						
T2 (SS3)	200	$1.1x10^{-3}$	497	523	0.7	4.8
T3 (SS3)	200	$1.1x10^{-3}$	477	499	0.7	4.7
T1 (SS3)-bent	200	$0.56->11x10^{-4}$	$\Delta\sigma$=16.5	(495/512)	–	–
GlidCop AL15+B, ind. braze						
F1 (SS3)	200	$1.1x10^{-3}$	(363)	(363)	0.0	<0.05
F2 (SS3)	29	$1.1x10^{-3}$	531	533	0.07	0.07

[a] Strain to necking (uniform elongation measured after occurrence of yield drop)

Table 4. Tensile test results on copper alloy specimens from HFIR-MFE-400J capsule. The tensile data in parentheses are considered unreliable due to bent or brittle tensile specimens.

Alloy, ID Number	Temper-ature (°C)	Strain Rate (s^{-1})	Yield Strength (MPa)	Ultimate Strength (MPa)	Uniform Elong. (%)	Total Elong. (%)
pure copper, as wrought						
A9 (SS1)—bent/twisted	400	$0.21->4.2x10^{-4}$	($\Delta\sigma$~10)	–	–	–
A10 (SS1)-badly bent	400	$4.2x10^{-4}$	(75)	(113)	(4.7)	(6.1)
GlidCop AL25, as wrought						
H4 (SS1)	400	$4.2x10^{-4}$	172	190	0.8	9.9
H6 (SS1)	30	$4.2x10^{-4}$	408	447	5.9	9.1
H5 (SS1)-badly bent	400	$0.21->4.2x10^{-4}$	($\Delta\sigma$~7.3)	–	–	–
GlidCop AL15+B, as wr't						
L6 (SS1)	400	$4.2x10^{-4}$	196	211	1.2	2.5
L7 (SS1)-bent	400	$4.2x10^{-4}$	(205)	(245)	(2.5)	(5.1)
GlidCop AL25, 50%CW						
X4 (SS3)	400	$1.1x10^{-3}$	237	273	1.5	10.5
X5 (SS3)	30	$1.1x10^{-3}$	427	469	8.8	16.2
X6 (SS3)	400	$0.56->11x10^{-4}$	$\Delta\sigma$=25.5	219/245	–	–

Table 4 (cont'd). Tensile test results on copper alloy specimens from HFIR-MFE-400J capsule. The tensile data in parentheses are considered unreliable due to bent or brittle tensile specimens.

Alloy, ID Number	Temper-ature (°C)	Strain Rate (s^{-1})	Yield Strength (MPa)	Ultimate Strength (MPa)	Uniform Elong. (%)	Total Elong. (%)
GlidCop AL25+B, 80% CW						
C6 (SS3)	400	$1.1x10^{-3}$	300	325	1.0	4.0
C7 (SS3)	400	$5.6x10^{-5}$	256	280	1.3	1.8
C8 (SS3)	30	$1.1x10^{-3}$	476	527	7.2	11.5
GlidCop AL25+B, as-wr't						
W4 (SS3)	400	$1.1x10^{-3}$	201	216	1.0	12.8
W5 (SS3)	400	$1.1x10^{-3}$	201	225	1.2	11.5
W6 (SS3)	30	$1.1x10^{-3}$	392	454	8.8	17.2
MAGT 0.2, 50%CW						
T4 (SS3)	400	$1.1x10^{-3}$	314	328	0.8	5.8
T5 (SS3)	30	$1.1x10^{-3}$	474	521	8.8	16.2
T6 (SS3)	400	$0.56->11x10^{-4}$	$\Delta\sigma$=16.2	310/326	–	–
GlidCop AL15+B, ind. braze						
F5 (SS3)	400	$1.1x10^{-3}$	(149)	(149)	0.0	<0.05
F6 (SS3)	29	$1.1x10^{-3}$	(214)	(214)	0.0	<0.05

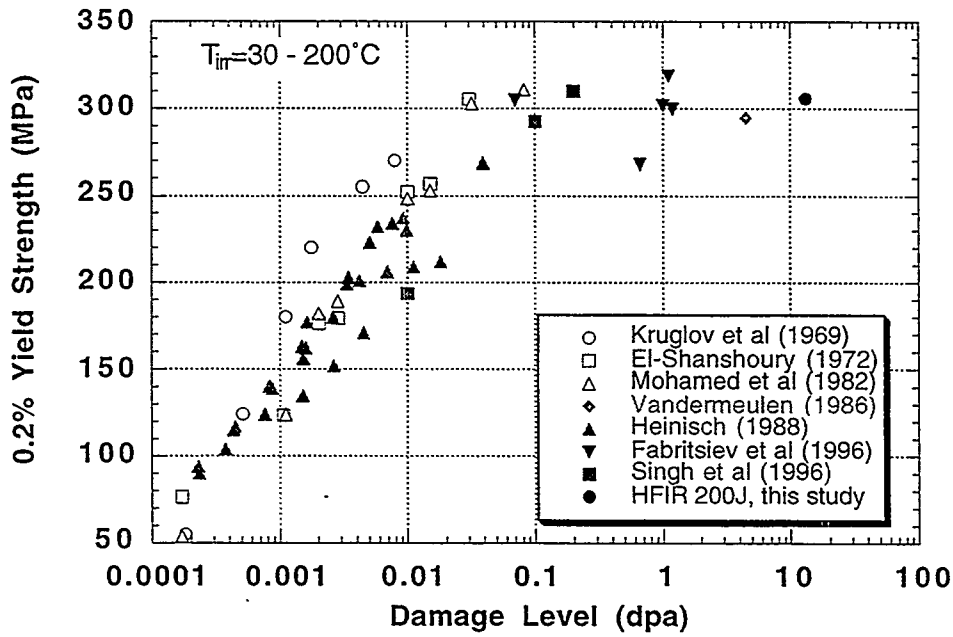

Fig. 1. Dose dependence of radiation hardening in copper irradiated with neutrons at 20-200°C and tested near room temperature [18-24].

An estimate of the barrier strength to dislocation motion can be obtained from a comparison of the radiation-induced defect microstructures [17] and tensile property changes. Figure 2 shows the engineering load-elongation tensile curves for pure copper irradiated at 200°C and tested at room temperature and 200°C (specimens A6 and A8). Using the well-known dispersed barrier hardening equation [25,26] with a Taylor factor of M=3.06 (valid for uniaxial tensile tests on FCC metals [26,27]), the dislocation barrier strength of the defect clusters is estimated to be α=0.15 at

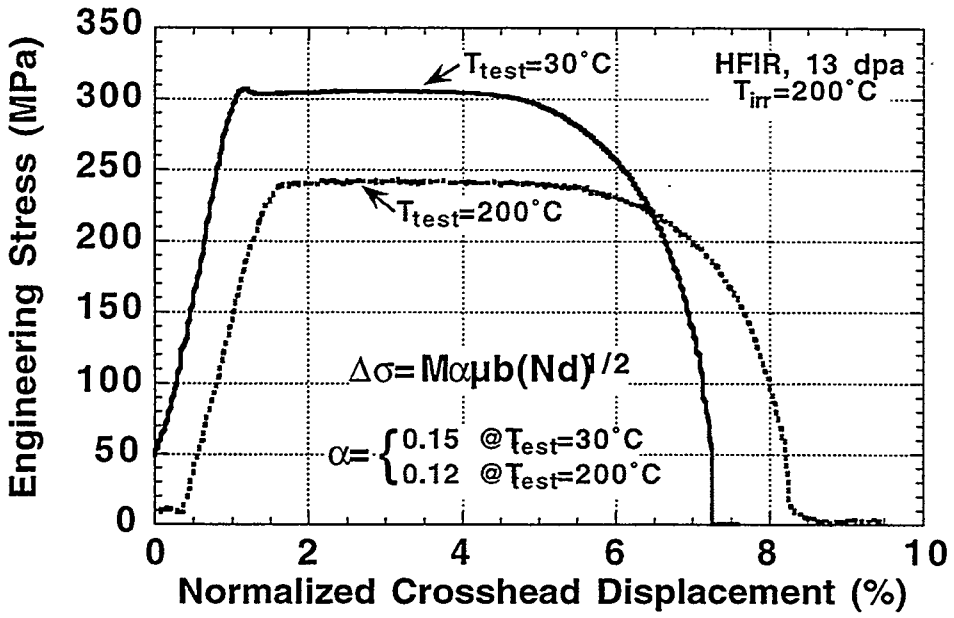

Fig. 2. Uniaxial load-elongation curves for pure copper irradiated to ~13 dpa at 200°C and tested at 30 and 200°C (specimens A6 and A8).

room temperature and 0.12 at 200°C. This result is in agreement with previous estimates obtained on copper irradiated at room temperature to significantly lower doses [26,28]. It is worth noting that a small yield drop was observed in the 200J copper specimen tested at room temperature, whereas a yield drop was not observed in the specimen tested at 200°C.

Figure 3 shows the effect of test temperature on the load-elongation curves of as-wrought GlidCop Al25+B irradiated at 200°C (specimens W1 and W2). There was no clear evidence for a yield drop at either test temperature. From a comparison of Figs. 2 and 3, it is apparent that the irradiated GlidCop Al25 specimens in the HFIR-200J capsule exhibited a steeper test temperature dependence of the yield and ultimate strengths compared to pure copper. The room temperature yield strength of as-wrought GlidCop Al25 was ~550 MPa, which is about 230 MPa higher than the unirradiated value. The corresponding radiation-induced increase in the yield strength at a test temperature of 200°C was ~170 MPa. Therefore, the temperature dependence of the yield strength was more pronounced in irradiated GlidCop Al25 compared to unirradiated specimens.

Figure 4 compares the load-elongation curves of GlidCop Al15 irradiated in the HFIR-200J capsule and tested at 200°C at three different strain rates. The yield strength increased by ~60 MPa and the ultimate tensile strength increased by ~70 MPa as the strain rate was increased by a factor of 500. The initial ("elastic modulus") slope of the stress-strain curves increased with increasing strain rate, which implies that the specimen grip load train system has visco-elastic behavior. There was no significant effect of strain rate on the tensile elongations.

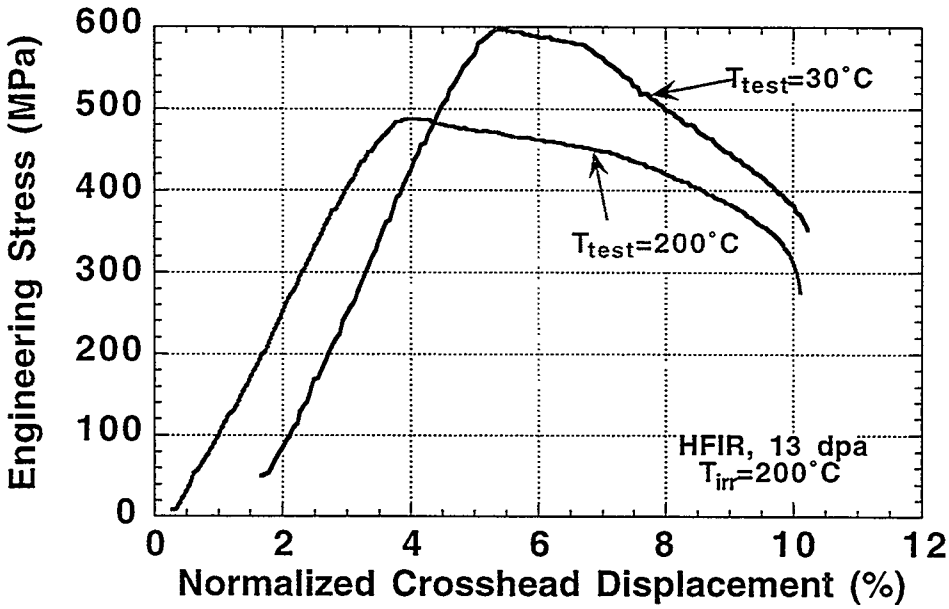

Fig. 3. Uniaxial load-elongation curves for GlidCop Al25+B irradiated to ~13 dpa at 200°C and tested at 30 and 200°C (specimens W1 and W2).

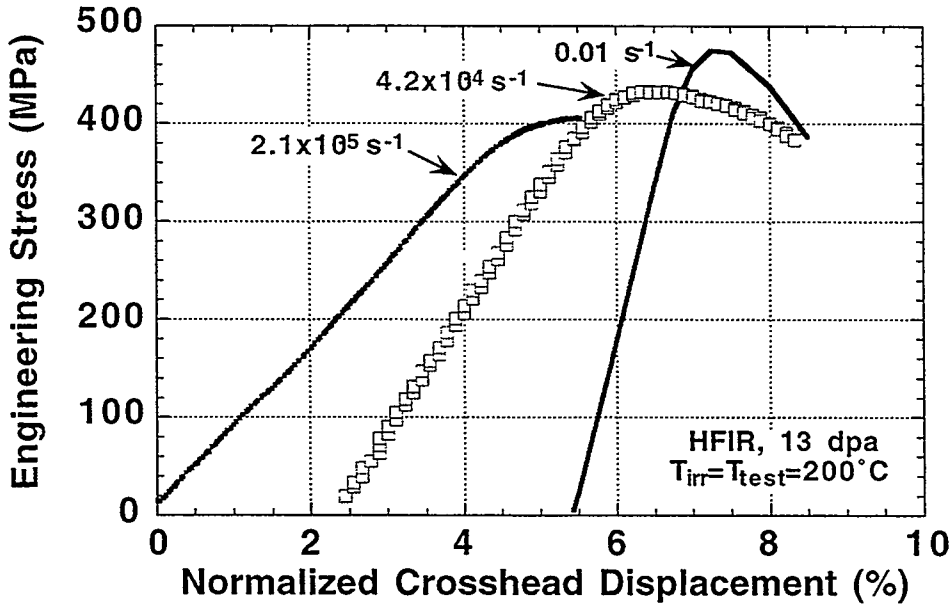

Fig. 4. Uniaxial load-elongation curves for GlidCop Al15+B irradiated to ~13 dpa at 200°C and tested at 200°C at three different strain rates (specimens L1, L2 and L3).

Figure 5 shows the results of a prompt change in strain rate on the load-elongation curve for MAGT 0.2 dispersion strengthened copper irradiated in the HFIR 200J capsule and tested at 200°C (specimen T1). Increasing the strain rate by a factor of twenty produced a small (~16 MPa) increase in tensile strength. The test was performed on a specimen that was bent during capsule disassembly. The bent specimens from the HFIR-200J and –400J capsules were used only for strain rate jump tests, since the deformation produced during capsule disassembly would produce an anomalous and uncontrollable increase in strength. The ~1 to 2% straining prior to the change in strain rate should enable qualitative trends on strain rate sensitivity to be examined in these bent samples. The quantitative accuracy of the strain rate results obtained on the bent samples is uncertain. The ultimate strength measured after the strain rate jump was in good agreement with the value obtained on specimens tested at a constant strain rate of 1.1×10^{-3} s^{-1} (specimens T2 and T2, cf. Table 3).

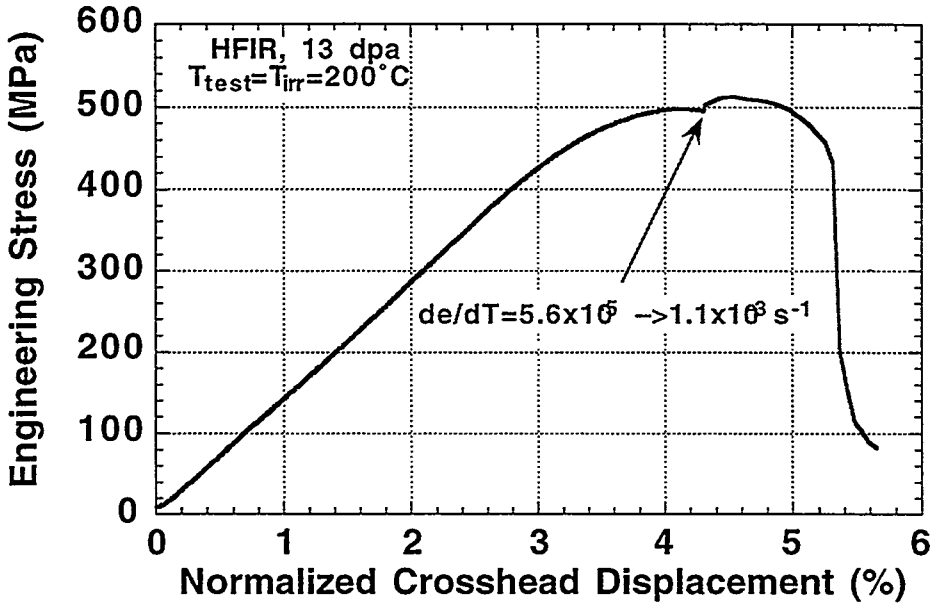

Fig. 5. Effect of increase in strain rate on the uniaxial load-elongation curve for MAGT 0.2 irradiated to ~13 dpa at 200°C and tested at 200°C (specimen T1).

The magnitude of radiation hardening was less pronounced for specimens irradiated at 400°C compared to the 200°C irradiations. For example, the room temperature ultimate strength of wrought GlidCop Al25 was ~580 MPa for the HFIR-200J capsule and ~450 MPa for the HFIR-400J capsule. Figure 6 shows the effect of test temperature on the tensile behavior of GlidCop Al25 irradiated at 400°C (specimens W5, W6). The yield and ultimate strengths varied by a factor of two for the two test temperatures. The radiation-induced increase in yield strength was ~25 MPa at 400°C and ~80 MPa at room temperature. Therefore, both the 200°C and 400°C irradiations resulted in a steeper dependence of yield strength on test temperature compared to unirradiated GlidCop Al25.

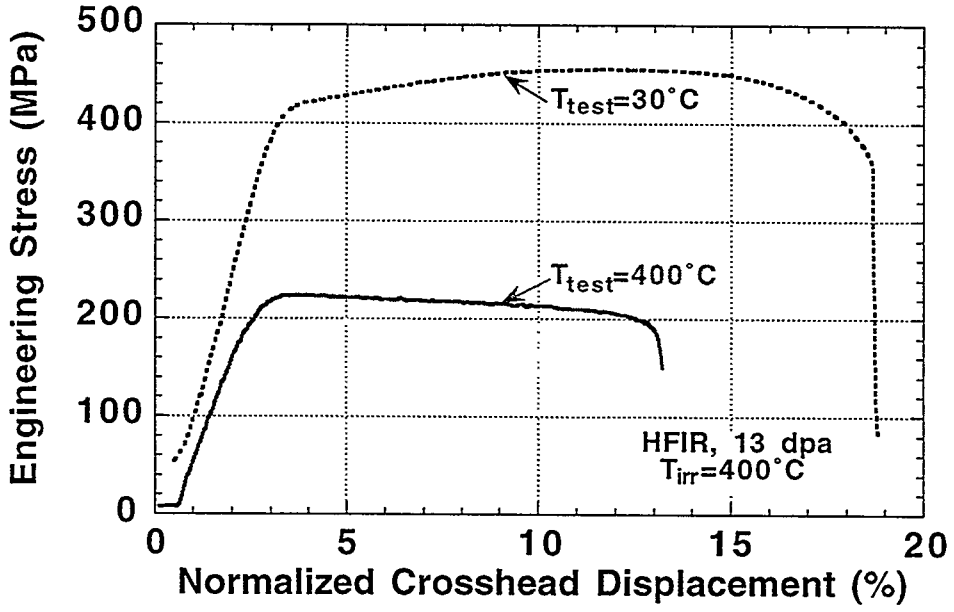

Fig. 6. Uniaxial load-elongation curves for GlidCop Al25+B irradiated to ~13 dpa at 400°C and tested at 30 and 400°C (specimens W5 and W6).

Figure 7 shows the effect of a change in strain rate on the load-elongation curve for 50% cold-worked GlidCop Al25 that was irradiated and tested at 400°C (specimen X6). The factor of 20 increase in strain rate produced an ~25 MPa increase in strength. It is interesting to note that the ultimate tensile strength after the change in strain rate was lower than that of a companion 50% cold-worked GlidCop Al25 specimen tested at a constant strain rate of 1.1×10^{-3} s^{-1} (specimen X4, cf. Table 4). Additional work is needed to determine whether testing of GlidCop Al25 at a slow strain rte at 400°C occurs by a different deformation mode (e.g., grain boundary sliding) compared to faster strain rates, and whether this deformation mode continues to operate if the strain rate is changed during tensile testing (are the results of the strain rate jump test affected by the deformation processes occurring prior to the change in strain rate?).

Figure 8 shows the effect of a factor of twenty increase in strain rate on the load-elongation curve of MAGT 0.2 irradiated and tested at 400°C (specimen T6). The magnitude of the strength increase associated with the change in strain rate (16 MPa) was less than observed for GlidCop Al25 irradiated and tested at the same conditions (Fig. 7). The ultimate strength following the change in strain rate was similar to that obtained from a companion specimen tested at a constant strain rate of 1.1×10^{-3} s^{-1} (specimen T4, cf. Table 4).

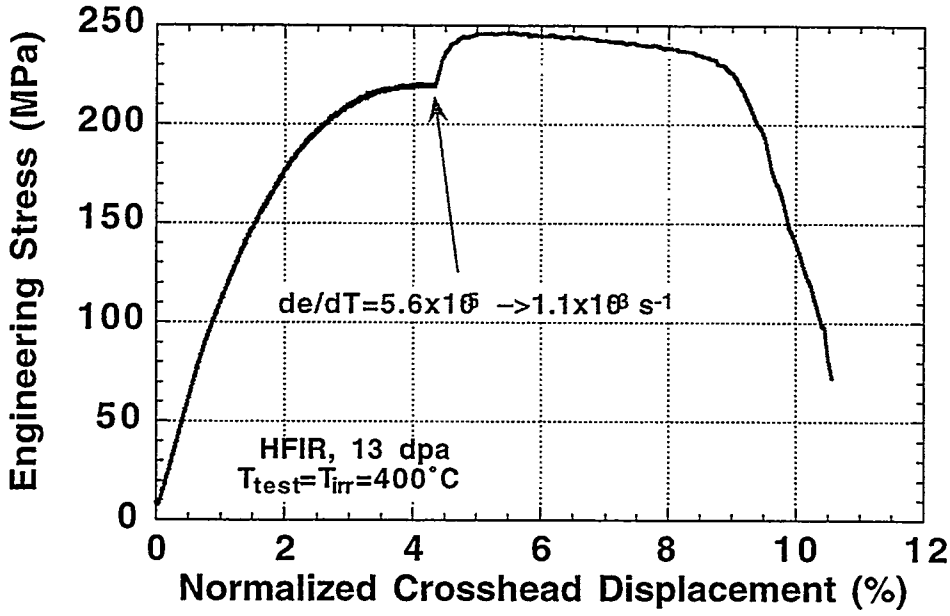

Fig. 7. Effect of increase in strain rate on the uniaxial load-elongation curve for 50% cold-worked GlidCop Al25 irradiated to ~13 dpa at 400°C and tested at 400°C (specimen X6).

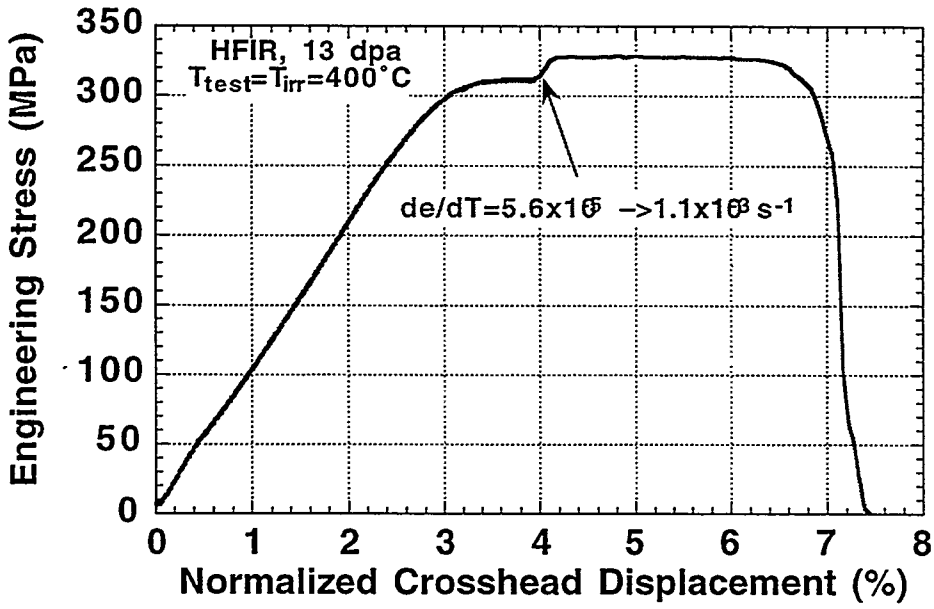

Fig. 8. Effect of increase in strain rate on the uniaxial load-elongation curve for MAGT 0.2 irradiated to ~13 dpa at 400°C and tested at 400°C (specimen T6).

Acknowledgements

The 50% cold-worked sheet of GlidCop Al25 was supplied by F.A. Garner (PNNL), and the remaining GlidCop Al25 (with and without boron) were supplied in rod form by B.N. Singh (Risø). The wrought GlidCop Al25 rod was provided by Bachu Singh via Frank Garner. The MAGT 0.2 sheet was supplied by V.R. Barabash (Efremov Inst.). Auburn University (B.A. Chin) performed the induction brazing of the GlidCop Al15 specimens. The authors thank J.E. Pawel-Robertson for coordinating the specimen insertion and recovery from the HFIR MFE-200J and -400J capsules.

REFERENCES

1. S.J. Zinkle and S.A. Fabritsiev, Atomic and Plasma-Material Interaction Data for Fusion (supplement to Nuclear Fusion) 5 (1994) 163.
2. S.A. Fabritsiev, S.J. Zinkle and B.N. Singh, J. Nucl. Mater. 233-237 (1996) 127.
3. G.M. Kalinin and R. Matera, J. Nucl. Mater. 258-263 (1998) 345.
4. F.A. Garner et al., J. Nucl. Mater. 191-194 (1992) 386.
5. D.J. Edwards et al., J. Nucl. Mater. 191-194 (1992) 416.
6. D.J. Edwards, F.A. Garner, J.W. Newkirk and A. Nadkarni, J. Nucl. Mater. 212-215 (1994) 1313.
7. S.J. Zinkle et al., J. Nucl. Mater. 208 (1994) 119.
8. A.W. Longest et al., in Fusion Materials Semiannual Progress Report for Period ending Sept. 30, 1993, DOE/ER-0313/15 (Oak Ridge National Lab, 1993) p. 23.
9. L.R. Greenwood and C.A. Baldwin, in Fusion Materials Semiann. Prog Rep. for period ending Dec. 31 1997, DOE/ER-0313/23 (Oak Ridge National Lab, 1997) p. 329.
10. A.W. Longest et al., in Fusion Materials Semiannual Progress Report for Period ending March 31, 1993, DOE/ER-0313/14 (Oak Ridge National Lab, 1993) p. 14.
11. S.J. Zinkle and W.S. Eatherly, in Fusion Materials Semiannual Progress Report for Period ending June 30, 1996, DOE/ER-0313/20 (Oak Ridge National Lab, 1996) p. 207.
12. S.J. Zinkle and W.S. Eatherly, in Fusion Materials Semiannual Progress Report for Period ending Dec. 31, 1996, DOE/ER-0313/21 (Oak Ridge National Lab, 1996) p. 165.
13. S.A. Fabritsiev et al., J. Nucl. Mater. 233-237 (1996) 526.
14. S.A. Fabritsiev and A.S. Pokrovsky, J. Nucl. Mater. 249 (1997) 250.
15. D.J. Edwards, F.A. Garner and L.R. Greenwood, J. Nucl. Mater. 212-215 (1994) 404.
16. B.N. Singh, D.J. Edwards and P. Toft, J. Nucl. Mater. 249 (1996) 1.
17. S.J. Zinkle and B.N. Singh, Proc. ICFRM-9, to be published in J. Nucl. Mater. (2000).
18. A.S. Kruglov, V.N. Bykov, I. El-Shanshuri and K. Gaber, Sov. Atomic Energy 26 (1969) 582.
19. I.A. El-Shanshoury, J. Nucl. Mater. 45 (1972) 245.
20. H.G. Mohamed, A.M. Hammad and F.H. Hammad, Trans. Indian Inst. Metals 35 (1982) 258.
21. W. Vandermeulen, V. Massaut, J. Van der Velde and W. Hendrix, in 14th Symp. on Fusion Technology (Pergamon Press, New York, 1986) p. 1031.
22. H.L. Heinisch, J. Nucl. Mater. 155-157 (1988) 121.
23. S.A. Fabritsiev, A.S. Pokrovsky, S.J. Zinkle and D.J. Edwards, J. Nucl. Mater. 233-237 (1996) 513.
24. B.N. Singh, D.J. Edwards and P. Toft, J. Nucl. Mater. 238 (1996) 244.
25. A.L. Bement, Jr., in 2nd Int. Conf. on Strength of Metals and Alloys vol. II, ed. W.C. Leslie (Am. Society for Metals, Metals Park, OH, 1970) p. 693.
26. S.J. Zinkle, Radiat. Eff. Def. Solids 148 (1999) 447.
27. U.F. Kocks, Metall. Trans. 1 (1970) 1121.
28. S. Kojima, S.J. Zinkle and H.L. Heinisch, J. Nucl. Mater. 179-181 (1991) 982.

THERMOPHYSICAL AND MECHANICAL PROPERTIES FOR Ta-8%W-2%Hf –

S. J. Zinkle (Oak Ridge National Laboratory)

OBJECTIVE

The objective of this report is to summarize the thermophysical and mechanical properties of Ta-(8-10)%W alloys that are being considered as a possible alternative high temperature structural alloy in the Advanced Power EXtraction (APEX) project.

SUMMARY

The key thermophysical and mechanical properties for Ta-(8-10)%W alloys are summarized, including unirradiated temperature-dependent tensile properties, stress-rupture behavior, elastic constants, thermal conductivity, thermal expansion, specific heat, and ductile-to-brittle transition temperature. The estimated lower and upper temperatures limits for structural applications are 700 and 1000°C due to radiation hardening/embrittlement and thermal creep considerations, respectively, although there are very few fracture properties data for irradiated Ta alloys.

PROGRESS AND STATUS

Introduction

In order to provide a reference design basis for the Advanced Power EXtraction (APEX) project, published data on the thermophysical and mechanical properties for Ta-(8-10)%W alloys have been compiled. Although tantalum alloys have unfavorable decay heat and long term induced activation characteristics, the APEX program is considering a wide range of structural alloys which may have the potential for dramatically improving the thermal efficiency and reliability of fusion reactors (high risk, high payoff). If a more compact, high power density design can be achieved, the reduction in total waste volume may offset the disadvantages associated with undesirable transmutation products.

The key thermophysical and mechanical properties for Ta-8%W-2%Hf (alloy T-111) are summarized in the following. This solid solution alloy was developed in the early 1960s and was commercially produced by several vendors [1]. Most of the development work on refractory metals stopped in the early 1970s due to the suspension of funding for nuclear space power systems and the decision to utilize reusable surface ceramic tiles rather than coated refractory metals for the Space Shuttle [2]. The T-111 alloy is presently not being produced due to lack of demand, and there is some concern that a "relearning" process would be needed before the alloy could once again be reliably produced (based on problems with a recent attempt to produce the tantalum alloy T-222) [1]. The alloy T-222 has a composition of Ta-10%W-2.5%Hf-0.01%C, and has somewhat superior mechanical strength compared to T-111 although the data base is not as comprehensive.

Tantalum alloys are susceptible to hydrogen embrittlement, as are its Group V-A siblings vanadium and niobium [3]. All of the Group V-A refractory alloys are ductile at room temperature, whereas the group VI-A refractory alloys (Mo and W) are generally brittle at room temperature. All refractory metals suffer from well-known oxidation problems at elevated temperatures (>500°C). Therefore, either vacuum or an inert cover gas are required during elevated temperature processing (hot working, welding, etc.). Tantalum has a melting point of 2996°C and a density of 16.7 g/cm^3 at room temperature.

All high-temperature refractory alloys are generally designed to be used in the stress-relieved condition rather than the fully recrystallized condition, in order to take advantage of the higher strength present in the stress-relieved condition. The recrystallization temperature depends on the amount of cold- or warm-work and also on the exposure time. The temperature to fully recrystallize 75% cold-worked alloy T-111 has been reported to be 1650°C for a 1 hour anneal [4]. The enhanced diffusion associated with irradiation would cause a significant decrease in the recrystallization temperature, particularly is the operating stress on the component is significant. For design purposes, the recrystallized strengths should be used in order to provide an adequate safety margin in the event of radiation-enhanced recrystallization.

1. Ultimate tensile strength (unirradiated)

The ultimate tensile strength for Ta-8%W-2%Hf (alloy T-111) has been measured by several researchers. Dynamic strain aging occurs at temperatures between ~500 and 1000°C for typical tensile strain rates of ~10^{-3} s^{-1}, which produces a local maximum in the ultimate strength in this temperature range. Figure 1 summarizes some of the ultimate tensile strength (UTS) data obtained in tensile tests on stress-relieved and recrystallized specimens [1,4-6]. Using the data summarized in the Aerospace Structural Metals Handbook [4] (filled square symbols in Fig. 1), the least squares fitted equation for the ultimate tensile strength of recrystallized T-111 over the temperature range of 20-1500°C is

$$\sigma_{UTS}(MPa)=630 - 1.532*T +0.003388*T^2 -2.807e-06*T^3 +7.338e-10*T^4$$

where the temperature (T) is in °C. The correlation coefficient for this equation is R=0.988.

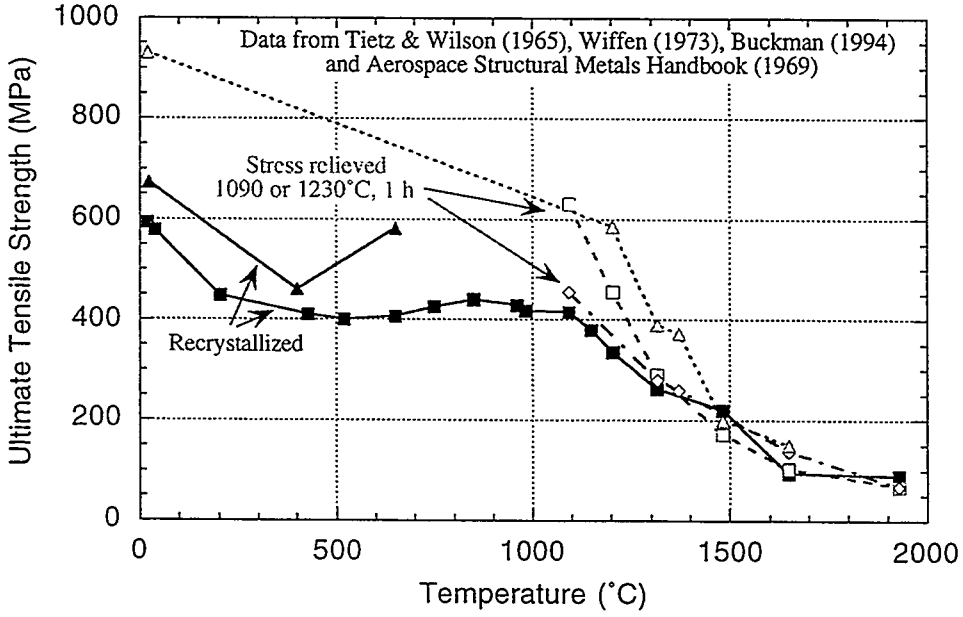

Fig. 1. Ultimate tensile strength of unirradiated Ta-8W-2Hf [1,4-6].

2. Yield strength (unirradiated)

Figure 2 summarizes the yield strength data obtained on stress-relieved and recrystallized specimens of Ta-8%W-2%Hf (alloy T-111) [4-6]. Using the data summarized in the Aerospace Structural Metals Handbook [4] (filled square symbols in Fig. 2), the least squares fitted equation for the yield strength of recrystallized T-111 over the temperature range of 20-1500°C is

$$\sigma_Y(\text{MPa}) = 612 - 1.743*T + 0.003585*T^2 - 3.076e\text{-}06*T^3 + 8.819e\text{-}10*T^4$$

where the temperature (T) is in °C. The correlation coefficient for this equation is R=0.996.

3. Yield and ultimate strength (irradiated)

There have been few studies on irradiated T-111, with no known studies at temperatures above 650°C [7]. Neutron irradiation causes a pronounced increase in the yield and ultimate tensile strength of Ta-8%W-2%Hf (alloy T-111) at temperatures below ~650°C. The yield and ultimate strength increased to ~1250 MPa for a specimen tested at ~400°C following fast reactor irradiation at ~410°C to 1.9×10^{26} n/m^2 (E>0.1 MeV), which corresponds to a dose of ~2.5 dpa [6,7]. The yield and ultimate strength were ~1000 MPa for a corresponding irradiation and test temperature of ~640°C and a similar dose [6]. Only a modest amount of radiation hardening was observed in Ta-10W irradiated at 800°C, whereas severe radiation embrittlement occurred in a similar specimen irradiated at 350°C [8]. The yield strength of solution annealed Ta-10W irradiated at 800°C to a dose of ~2.5 dpa was reported to be 300 MPa compared to an unirradiated value of ~220 MPa, although the sample was apparently embrittled either by radiation or interstitial solute pickup (total elongation ~2%) [8]. This very limited tensile data base is consistent with radiation hardening results obtained on other BCC alloys (in particular vanadium alloys), where significant radiation

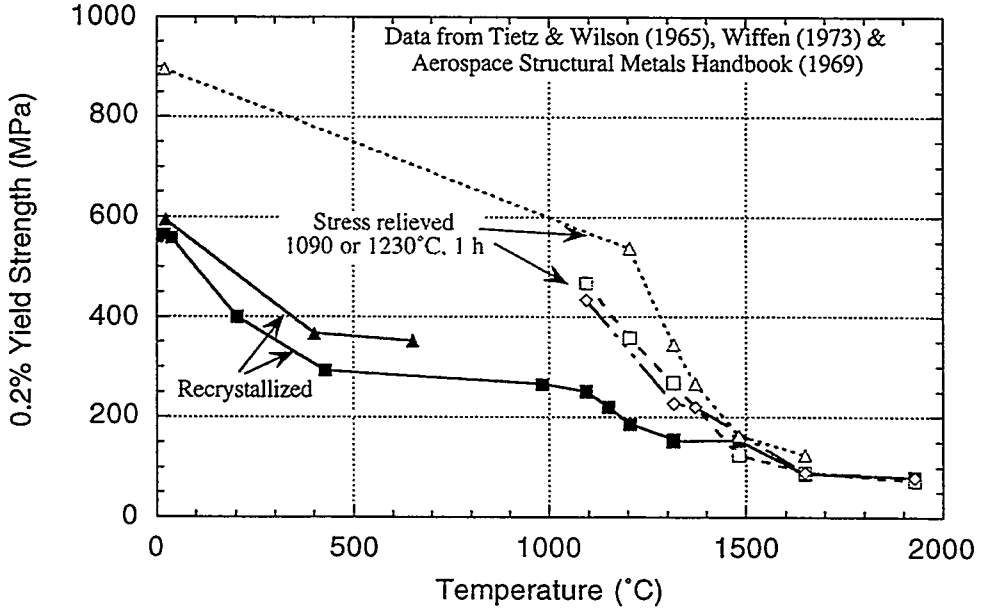

Fig. 2. Yield strength of unirradiated Ta-8W-2Hf [4-6].

hardening occurs at temperatures below 0.3 T_M (~700°C for Ta). There is a clear need for mechanical property data on Ta alloys at temperatures ≥700°C in order to further investigate radiation hardening and embrittlement effects. There are no known Charpy impact or fracture toughness measurements on irradiated Ta alloys.

4. Uniform and Total Elongation, Reduction in Area (unirradiated and irradiated)

There are very few reports of the uniform elongation in unirradiated or irradiated T-111 specimens. Figure 3 summarizes the unirradiated total elongation data obtained on stress-relieved and recrystallized specimens of Ta-8%W-2%Hf (alloy T-111) [4-6]. Wiffen [6] has reported on the uniform and total elongation of recrystallized T-111 following fast reactor irradiation to 1.9×10^{26} n/m^2 (E>0.1 MeV) at 410 and 640°C (corresponding damage level ~2.5 dpa). The unirradiated elongations were 16-22% for test temperatures between 20 and 650°C. The uniform elongation decreased to <0.5% following irradiation at 410°C, and decreased to 1.9% following irradiation at 640°C. The total elongations decreased to 4.5 to 10% following irradiation. The corresponding reduction in area following irradiation ranged from 36% for irradiation and testing at ~410°C to 65% for irradiation and testing at ~640°C. The unirradiated reduction in area ranged from 81 to 99% for testing at 20 to 650°C [6]. The total elongation of Ta-10%W was zero (brittle failure) following irradiation to a dose of 0.1 dpa at 350°C, and ~2% after a dose of ~2.5 dpa at 800°C, where the tensile testing was performed at the irradiation temperature [8].

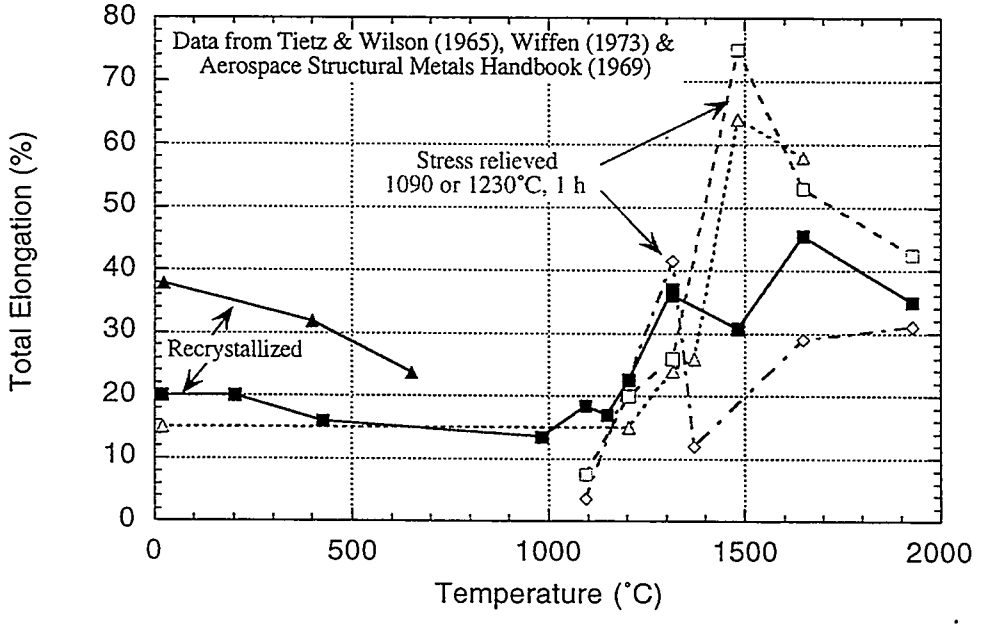

Fig. 3. Total elongation of unirradiated Ta-8W-2Hf [4-6].

5. Elastic constants

Young's modulus has been measured from -100 to 2000°C for T-111 [4,5]. As shown in Fig. 4, the temperature-dependent Young's modulus for T-111 is comparable to that for pure Ta. The shear modulus (G) and Poisson's ratio (ν) of T-111 apparently have not been measured. Based on

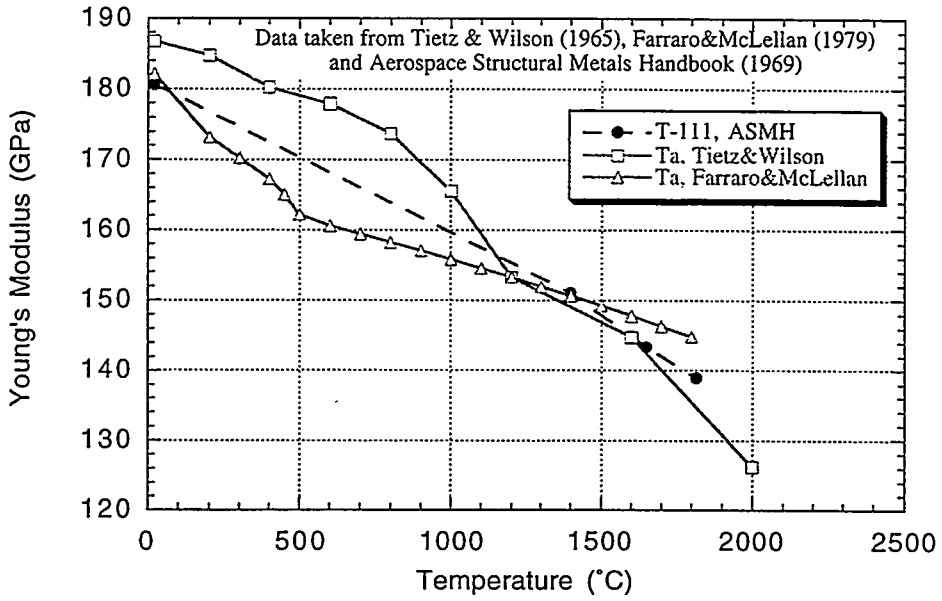

Fig. 4. Comparison of Young's modulus for unirradiated Ta-8W-2Hf and tantalum [4,5,9].

the measurements by Farraro and McLellan, the least-squares fitted polynomial expression for the elastic constants of pure Ta at temperatures above 700 K are [9]

$$E_Y=((1.69 - 8.22\times10^{-5}*T-1.66\times10^{-8}*T^2)\pm0.051)\times10^{11}\ \text{Pa}$$

$$G=((0.774 - 1.73\times10^{-4}*T)\pm0.016)\times10^{11}\ \text{Pa}$$

where the temperature is given in Kelvin. According to the measurements by Farraro and McLellan [9], Poisson's ratio equals 0.273 for pure Ta at room temperature. This value is lower than what is recommended in the ASM Metals Handbook (10th edition, Vol. 2), ν=0.35 at room temperature. Poisson's ratio at elevated temperatures can be obtained using the well-known relation $\nu=(E_Y/2G) - 1$.

6. Stress-rupture and creep

There have been numerous studies of the creep and stress-rupture behavior of unirradiated T-111 at temperatures up to 1600°C (0.57 T_M) [10-12], but there are no known irradiation creep studies. The stress to produce 1% strain in T-111 in 1000 h is ~110 MPa at 1100°C and ~50 MPa at 1250°C [11]. Using a 1000 h creep-rupture stress level of 100 MPa as a guideline, the maximum operating temperature of T-111 is 1150-1200°C [11]. Using the more conservative creep criterion of 1% plastic strain, the maximum operating temperature of T-111 for an applied stress of 100 MPa is 1000°C for long-term (7 year) operation [10].

7. Thermal expansion, specific heat, thermal conductivity and electrical resistivity

Several thermophysical properties for T-111 have been measured from room temperature to ~1300°C. The mean coefficient of thermal expansion (α_{th}) is very similar to that of pure Ta and Ta-10W, and varies from 5.9 ppm/°C at room temperature to 7.6 ppm/°C at 1650°C [4,5,11]. The specific heat at constant pressure (C_P) is ~150 J/kg-K at 20°C [4]. The electrical resistivity of T-111 ranges from 217 nΩ-m at room temperature to 665 nΩ-m at 1180°C [4]. As shown in Fig. 5, the thermal conductivity varies from ~42 W/m-K at room temperature to ~56 W/m-K at 1350°C. Using the Aerospace Structural Metals Handbook data, the thermal conductivity can be described by the following equation:

$$K_{th}\ (W/m\text{-}K) = 41.0 + 0.020\ T - 6.32 \times 10^{-6}\ T^2 \qquad \text{(temperature in °C)}$$

8. Ductile to brittle transition temperature (unirradiated and irradiated)

The measured value of the ductile to brittle transition temperature (DBTT) in body-centered cubic materials depends on numerous experimental parameters, including the specimen geometry, strain rate, and the sharpness of the notch where the crack is initiated (notch acuity). The DBTT in unirradiated T-111 has generally been estimated from reduction in area measurements on un-notched tensile specimens [5,13]. The resultant DBTT value (~-200°C) is a severe underestimate

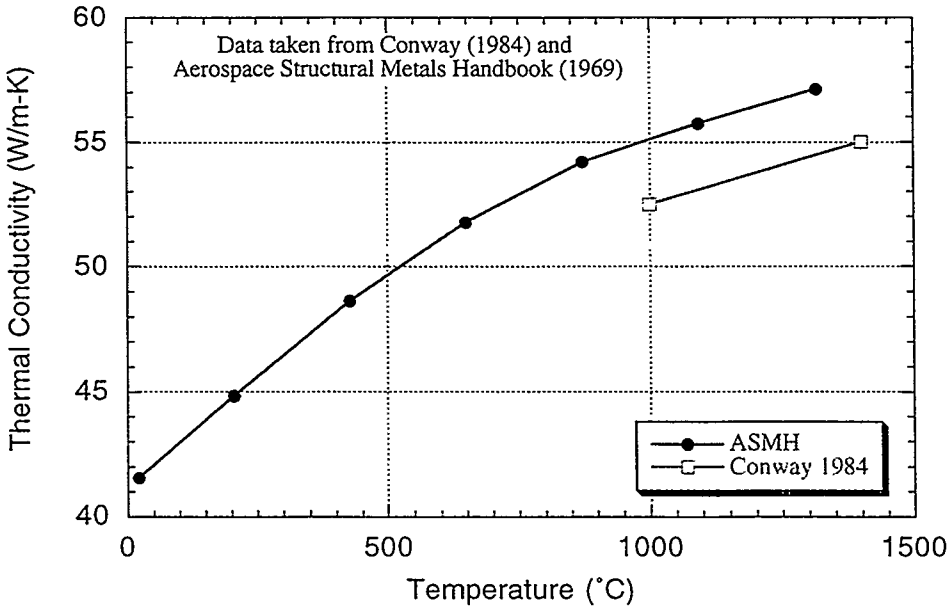

Fig. 5. Thermal conductivity of unirradiated Ta-8W-2Hf [4,11].

of the value which would be obtained on machined or precracked Charpy vee-notch (CVN) specimens or precracked compact tension (fracture toughness) specimens. There are no known DBTT studies on irradiated T-111, although a significant increase in the DBTT would be expected for irradiation at temperatures up to at least 650°C, based on the large increase in hardening [6] associated with these relatively low irradiation temperatures (<0.3 T_M).

9. Recommended reference operating temperature limits

Several forced-flow corrosion and engineering loop studies have demonstrated that T-111 has good compatibility with liquid lithium at least up to temperatures of ~1370°C [14-17]. Ta alloys have also exhibited good compatibility with other liquid metals at elevated temperatures, including Na, K and Pb to ~1200°C [14-17]. Thermal creep becomes high in T-111 at temperatures above ~1200°C (~0.45 T_M), which is near the maximum temperature that corrosion data are available. Using a conservative criterion of 1% plastic strain for long-term (>10,000 h) exposure to an applied stress of 100 MPa, the maximum operating temperature is ~1000°C for Ta-base alloys such as T-111. Additional work on irradiated specimens is needed before the minimum operating temperature limit can be established. The reference minimum operating temperature limit will likely be controlled by radiation hardening, which causes loss of ductility and an increase in the ductile to brittle transition temperature. There are no known DBTT data on irradiated T-111 alloys. For the purposes of the APEX design study, the proposed reference minimum operating temperature for T-111 is 700°C (~0.3 T_M) based on expectations of low-temperature radiation embrittlement.

References

[1] R.W. Buckman, Jr., in: High Temperature Silicides and Refractory Alloys, eds. C.L. Briant et al., MRS Symp. Proc., vol. 322 (Materials Research Society, Pittsburgh, 1994) p. 329.

[2] T.G. Nieh, J. Wadsworth, in: High Temperature Silicides and Refractory Alloys, eds. C.L. Briant et al., MRS Symp. Proc., vol. 322 (Materials Research Society, Pittsburgh, 1994) p. 315.

[3] R.T. Webster, in: Refractory Metals and Their Industrial Applications, ed. R.E. Smallwood, ASTM STP 849 (American Society for Testing and Materials, Philadelphia, 1984) p. 18.

[4] D.C. Goldberg, in: Aerospace Structural Metals Handbook, AFML-TR 68-115, ed. W.F. Brown, Jr. (Metals and Ceramics Information Center, Battelle Columbus Laboratories, 1969.

[5] T.E. Tietz, J.W. Wilson, Behavior and Properties of Refractory Metals, Stanford University Press, Stanford, CA, 1965.

[6] F.W. Wiffen, in: Proc. Int. Conf. on Defects and Defect Clusters in BCC Metals and Their Alloys, Nuclear Metallurgy, Vol. 18, ed. R.J. Arsenault (National Bureau of Standards, Gaithersburg, MD, 1973) p. 176.

[7] F.W. Wiffen, in: Proc. Symp. on Refractory Alloy Technology for Space Nuclear Power Applications, CONF-8308130, eds. R.H. Cooper, Jr., E.E. Hoffman (Oak Ridge National Lab, 1984) p. 252.

[8] I.V. Gorynin et al., J. Nucl. Mater. 191-194 (1992) 421.

[9] R.J. Farraro, R.B. McLellan, Metall. Trans. 10A (1979) 1699.

[10] H.E. McCoy, Oak Ridge National Lab Report ORNL/TM-10127 (1986).

[11] J.B. Conway, in: Proc. Symp. on Refractory Alloy Technology for Space Nuclear Power Applications, CONF-8308130, eds. R.H. Cooper, Jr., E.E. Hoffman (Oak Ridge National Lab, 1984) p. 252.

[12] K.D. Sheffler, J.C. Sawyer, E.A. Steigerwald, Trans. Am. Soc. Metals 62 (1969) 749.

[13] J.R. Hughes, in: High Temperature Silicides and Refractory Alloys, eds. C.L. Briant et al., MRS Symp. Proc., vol. 322 (Materials Research Society, Pittsburgh, 1994) p. 363.
[14] J.H. DeVan, J.R. DiStefano, E.E. Hoffman, in: Proc. Symp. on Refractory Alloy Technology for Space Nuclear Power Applications, CONF-8308130, eds. R.H. Cooper, Jr., E.E. Hoffman (Oak Ridge National Lab, 1984) p. 34.
[15] J.R. DiStefano, J. Mater. Eng. 11 (1989) 215.
[16] E.E. Hoffman, J.H. DeVan, J.R. DiStefano, in: Evolution of Refractory Metals and Alloys, eds. E.N.C. Dalder, T. Grobstein, C.S. Olsen (The Minerals, Metals and Materials Society, Warrendale, PA, 1994) p. 137.
[17] R.H. Burns, F.S. Shuker, Jr., P.E. Manning, in: Refractory Metals and Their Industrial Applications, ed. R.E. Smallwood, ASTM STP 849 (American Society for Testing and Materials, Philadelphia, 1984) p. 50.

NEUTRON IRRADIATION EFFECTS ON PLASMA-FACING MATERIALS – V. Barabash, G. Federici (ITER Joint Central Team), M. Roedig (Forschungszentrum Juelich), L. L. Snead (Oak Ridge National Laboratory), and C. H. Wu (EFDA – Close Support Unit)

Extended Abstract (the full paper will be published in the Journal of Nuclear Materials as Proceedings of the Ninth International Conference on Fusion Reactor Materials, October 10-15, 1999, Colorado Springs, Colorado).

Beryllium, tungsten, and carbon fibre composites are leading candidate armour materials for plasma facing components of the Next Step fusion device. In recent years, the data base on the influence of neutron irradiation on the properties of Be, W, and CFC has been significantly improved.

- Mainly in the frame of ITER R&D program the qualitative data on physical and mechanical properties for the modern Be grades and CFCs have been generated;

- The study of the combined effects of the neutron irradiation and high heat fluxes on the behavior of the armour materials has started; for future activities it is important to define the expected operational conditions.

This paper reviews the effects of neutron irradiation on thermal and mechanical properties and bulk tritium retention of armour materials (beryllium, tungsten, and carbon). For each material, the main properties affected by neutron irradiation are determined and described. For beryllium and tungsten the key issues are the loss of ductility and embrittlement at low irradiation temperature, for carbon based materials neutron irradiation affects mainly the thermal conductivity. The results of a study of the damage of neutron irradiated armour materials under thermal shock and disruption conditions are also summarized. Based on current knowledge and recent experimental observations, the expected thermal and structural performance of neutron irradiated armour materials in the ITER plasma facing components are analyzed.

For ITER application all three armour materials such as Be, W, and CFCs are selected. The expected performance of the armour materials in ITER seems adequate and at least indicative supported by the available experimental results. For each material, the key problem is the mechanical integrity and keeping their function of the wall structure protecting. The issue for Be and W is integrity of brittle material after neutron irradiation and at transient and steady state high heat fluxes. Still more activity is needed to validate the performance of neutron irradiated armour materials.

EFFECT OF HIGH DOSE NEUTRON IRRADIATION ON THE MECHANICAL PROPERTIES AND STRUCTURE OF COPPER ALLOYS AND CU/SS JOINTS FOR ITER APPLICATIONS – S. A. Fabritsiev (D.V. Efremov Scientific Research Institute), A. S. Pokrovsky (Scientific Research Institute of Atomic Reactors), D. J. Edwards (Pacific Northwest National Laboratory), S. J. Zinkle, and A. F. Rowcliffe (Oak Ridge National Laboratory)

Extended Abstract (the full paper will be published in the Journal of Nuclear Materials as Proceedings of the Ninth International Conference on Fusion Reactor Materials, October 10-15, 1999, Colorado Springs, Colorado).

The base copper alloys Cu-Cr-Zr IG and GlidCopAl25 IG and Cu/SS joints manufactured in RF, US, EU, JA with the HIP method were irradiated up to 2 dpa at 200°C in SM-2 reactor. Tensile tests, shear tests, metallography and SEM investigations were performed. In general, the trends in radiation hardening and embrittlement were observed also at higher irradiation doses.

Hardening and embrittlement were found to be essentially the same in copper alloys of different types, i.e. PH - Cu-Cr-Zr and ODS - GlidCopAl25. The joints of GlidCopAl25/316 and Cu-Cr-Zr/316 type had high strength characteristics and satisfactory ductilities after irradiation.

The irradiated joints of GlidCopAl25/316 type demonstrated a high level of strength properties (σ_u ~350 MPa). Still, their σ_u is lower by about 100 MPa than for the irradiated base alloy GlidCopAl25 IG. It was shown that the lower ultimate strength of joints is partly determined by the lower σ_u of GlidCopAl25 alloy in the Z direction.

Cu-Cr-Zr/316 joints demonstrated strength properties at a level of the irradiated Cu-Cr-Zr (HIP) alloy σ_u ~260 MPa and a high ductility δ_{tot}~13%. It is apparently associated, first of all, with a higher capacity of the base alloy Cu-Cr-Zr for local deformation, when irradiated, than in the GlidCopAl25 alloy.

It should be noted that the last generation of joints demonstrated an essentially higher level of strength properties as compared with the first generation despite a ten times higher irradiation dose. The fact that none of the new joints (EU, JA, RF) demonstrated brittle fracture at low ~ 150 to 200 MPa stresses, as happened with the first generation of joints [6] reflects substantial progress in the technology of joint fabrication.

EFFECT OF IRRADIATION TEMPERATURE ON THE MECHANICAL PROPERTIES AND STRUCTURE OF CU/SS JOINTS IRRADIATED TO LOW DOSES –

S. A. Fabritsiev (D.V. Efremov Scientific Research Institute), A. S. Pokrovsky (Scientific Research Institute of Atomic Reactors), D. J. Edwards (Pacific Northwest National Laboratory), S. J. Zinkle, and A. F. Rowcliffe (Oak Ridge National Laboratory)

Extended Abstract (the full paper will be published in the Journal of Nuclear Materials as Proceedings of the Ninth International Conference on Fusion Reactor Materials, October 10-15, 1999, Colorado Springs, Colorado).

A second generation of copper alloy/stainless steel joints manufactured in the RF, EU, and JA by Hot Isostatic Pressing (HIP) has been irradiated to 0.4 dpa at 150 and 300°C. Post-irradiation tensile tests and optical microscopy were performed.

Irradiation up to 0.4 dpa at 150°C increased the strength of GlidCopAl25/316 joints by about 150 MPa. The levels of uniform and total elongation of GlidCopAl25/316 specimens after irradiation up to 0.4 dpa at 150°C were very low.

The Cu-Cr-Zr/316SS joints were characterized by significantly less strengthening and for $T_{irr} = T_{test}$ = 150°C ($\Delta\sigma_y$ was ~50 MPa). The level of uniform and total elongation of Cu-Cr-Zr/316SS specimens after irradiation up to 0.4 dpa at 150°C was in the range 5 to 7%.

Irradiation at 300°C only slightly strengthened the GlidCopAl25/316-type joints, but the uniform and total elongation of the GlidCopAl25/316-type joints was very low.

Irradiation at T_{irr} = 300°C did not affect the strength properties of Cu-Cr-Zr/316SS joints; the uniform elongation of the irradiated joint Cu-Cr-Zr/316SS was in the range of 3 to 8%, and total elongations ranged from 12 to 20%.

In general, the second generation of HIP joints irradiated to a higher dose (0.4 dpa) demonstrated a higher radiation resistance than the first generation of joints irradiated to 0.2 dpa.

EFFECT OF NEUTRON DOSE AND IRRADIATION TEMPERATURE ON THE MECHANICAL PROPERTIES AND STRUCTURE OF DISPERSION STRENGTHENED COPPER ALLOYS –A. S. Pokrovsky (Scientific Research Institute of Atomic Reactors), S. A. Fabritsiev (D.V. Efremov Scientific Research Institute), D. J. Edwards (Pacific Northwest National Laboratory), S. J. Zinkle, and A. F. Rowcliffe (Oak Ridge National Laboratory)

Extended Abstract (the full paper will be published in the Journal of Nuclear Materials as Proceedings of the Ninth International Conference on Fusion Reactor Materials, October 10-15, 1999, Colorado Springs, Colorado).

This report is the first to present data on the effect of neutron irradiation doses of 0.2 and 0.4 dpa at T_{irr} ~150°C and T^{irr} ~300°C, on the mechanical properties of the GlidCop Al25IG alloy in different metallurgical conditions (Cr + annealed, HIP, extruded). It was found that low temperature radiation embrittlement was less pronounced in GlidCop Al25 fabricated to the IGO specification than in earlier versions of the alloy. At $T_{test} = T_{irr} = 150°C$, the increase in yield strength increased with dose to reach a value of $\Delta\sigma_y$ ~100 MPa at 0.4 dpa. Irradiation at 300°C to 0.4 dpa produced only a small ~30 MPa) increase in yield strength.

Although the uniform elongation was reduced significantly under these conditions, total elongations remained in the range 6 to 10%. However, IGO material that was subjected to a HIPping cycle during the manufacture of a GlidCop/316 SS joint exhibited a marked tendency towards intergranular fracture during tensile testing ≥300°C. this tendency was exacerbated by irradiation and brittle failure occurred following irradiation to 0.4 dpa at $T_{irr} = T_{test} = 300°C$.

MICROSTRUCTURES IN Ti-Al INTERMETALLIC COMPOUNDS IRRADIATED AT 673 K IN HFIR – Y. Miwa, T. Sawai, and K. Fukai (Japan Atomic Energy Research Institute), D. T. Hoelzer (Oak Ridge National Laboratory), and A. Hishinuma (JAERI)

Extended Abstract (the full paper will be published in the Journal of Nuclear Materials as Proceedings of the Ninth International Conference on Fusion Reactor Materials, October 10-15, 1999, Colorado Springs, Colorado).

Four kinds of Ti-Al intermetallic compounds were made from powder metallurgical processing using mechanical alloying or plasma rotating electrode processing. One consisted of α_2-Ti_3Al single phase, and the others consisted of α_2-Ti_3Al and γ-TiAl duplex phases. These intermetallic compounds were irradiated at 673 K to the fluence of 5.16×10^{25} n/m^2 (E>1 MeV) in the High Flux Isotope Reactor. After irradiation, transmission electron microscopy was carried out. Cavities were observed in both the α_2-Ti_3Al and γ-TiAl phases. The cavities were observed around pores that existed prior to irradiation and contained Ar gas. But in the γ-TiAl phases, no cavities were observed around the pores. The number density of cavities in α_2-Ti_3Al or γ-TiAl was different among specimens that had different chemical compositions and fabrication processes.

EFFECTS OF HEAT TREATMENTS ON MICROSTRUCTURE CHANGES IN THE INTERFACE OF CU/SS316L JOINT MATERIALS - Q. Xu and T. Yoshiie (Kyoto University, Japan) and D. J. Edwards (Pacific Northwest National Laboratory)*

Extended abstract of a paper submitted to the Journal of Nuclear Materials as part of the proceedings of the 9th International Conference on Fusion Reactor Materials, Colorado Springs, Colorado, USA, October 10-15, 1999.

EXTENDED ABSTRACT

The joining of dissimilar metals will likely be an important fabrication step in the use of copper alloys for advanced reactor designs. One possibility is that precipitation and dispersion strengthened copper alloys will be joined with 316L austenitic stainless steel for heat sink applications in the first wall and divertor structures of fusion power systems. In the present study, the effects of heat treatment on microstructural stability in the interface of CuNiBe/SS316L and CuAl25/SS316L have been investigated.

GlidCop CuAl25/SS316L and CuNiBe/SS316L joints formed by hot isostatic pressing (HIP) of solid plates were examined in this study. The joints were fabricated at a bonding temperature of 1255K for CuAl25/SS316L, and at 1245K for CuNiBe/SS316L. The pressure and the holding time for the HIP process were fixed at 101 MPa and 2 h. For further details on the materials and joining procedures please refer to reference 1.

The joints were thinned to 0.1 mm, and cut into 3 mm discs for transmission electron microscope (TEM) observation. Two kinds of annealing experiments were carried out to investigate the microstructural stability of the joint. Isochronal annealing of thinned CuAl25/SS316L TEM specimens was conducted in-situ using a high temperature heating stage in a JEOL 2000ES TEM. The specimens were annealed over the temperature range of 298-973K at 100K intervals, and the temperature was maintained for 30 minutes. Bulk specimens of the two joints were annealed separately at 573K and 673K for 100 h, respectively, and TEM specimens prepared by ion milling from the cross-section of the joints. The interfaces were examined using TEM and scanning electron microscopy (SEM, JEOL JSM-5800LV) to characterize the interfacial and the overall microstructure.

Figure 1 shows the SEM micrograph of as-received CuAl25/SS316L and CuNiBe/SS316L joints. Energy dispersive x-ray line analyses were conducted for Fe, Ni, Cr and Cu. Typical results of EDX line analyses (Fe and Cu) are also shown in the figure. It was found that there was interdiffusion of the two base materials. The concentration of Fe, Cr and Ni decreased and that of Cu increased in the region of stainless steel adjacent Cu alloy. Many precipitates, mainly composed of Cr and Fe, were found in the Cu alloy side of interfaces. In the CuAl25/SS316L joints, small voids, about 2 μm in diameter, were observed in the Cu alloy side near the interface, whereas in the CuNiBe/SS316L joints, voids, about 5 μm in diameter, were observed in the interface, and small voids, about 1 μm in diameter, were observed in the SS316L near the interface. Figure 2 shows the TEM micrograph of CuAl25/SS316L and CuNiBe/SS316L interfaces. As in the microstructures observed by SEM, the precipitates were not found at the interface of both joints. Also, voids were only found at the interface of CuNiBe/SS316L, and they were not observed in the Cu matrix and stainless steel far from interface.

Typical microstructures in the joints before and after the annealing experiment are shown in Figure 3. Figure 4 shows that the microstructures at the interfaces of the joint materials

---

* Pacific Northwest National Laboratory (PNNL) is operated for the U.S. Department of Energy by Battelle Memorial Institute under contract DE-AC06-76RLO-1830.

were thermally stable even after annealing at 573K or 673K for 100 h. The microstructures in the matrix of both joints and the interdiffusion within joints were also not affected by the annealing.

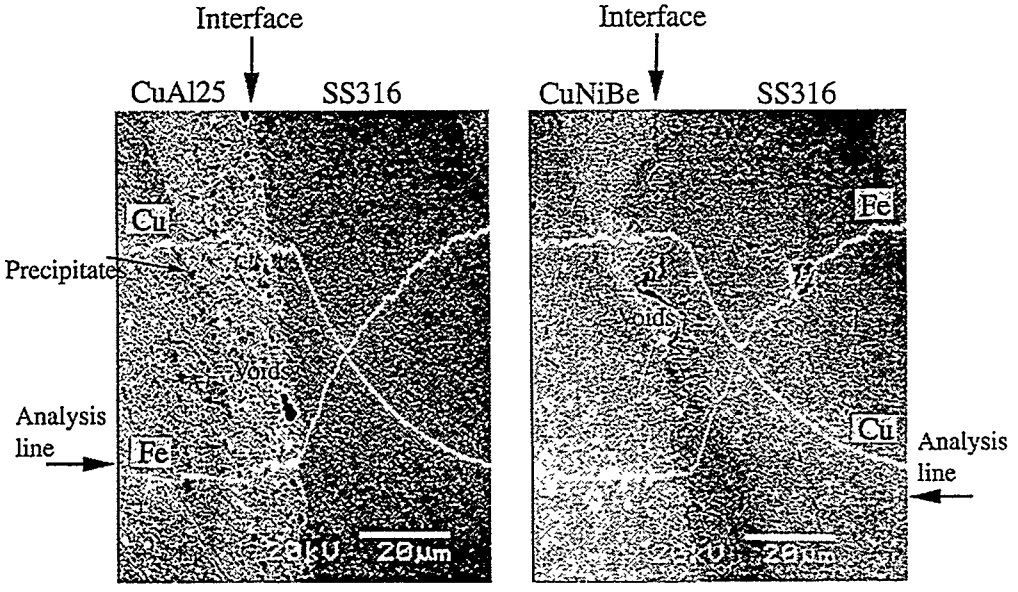

Figure 1. SEM micrograph of joint materials of CuAl25/SS316L and CuNiBe/SS316L, and typical results of EDX line analyses.

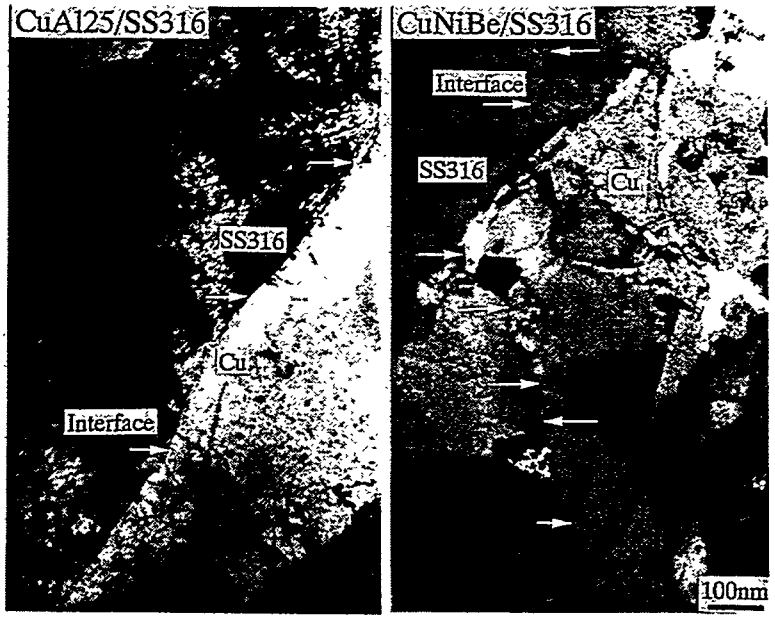

Figure 2. Microstructure in the interface of as-received joint materials.

Figure 3. Typical microstructure in the bonded joint of CuAl25/SS316L before and after isochronal annealing.

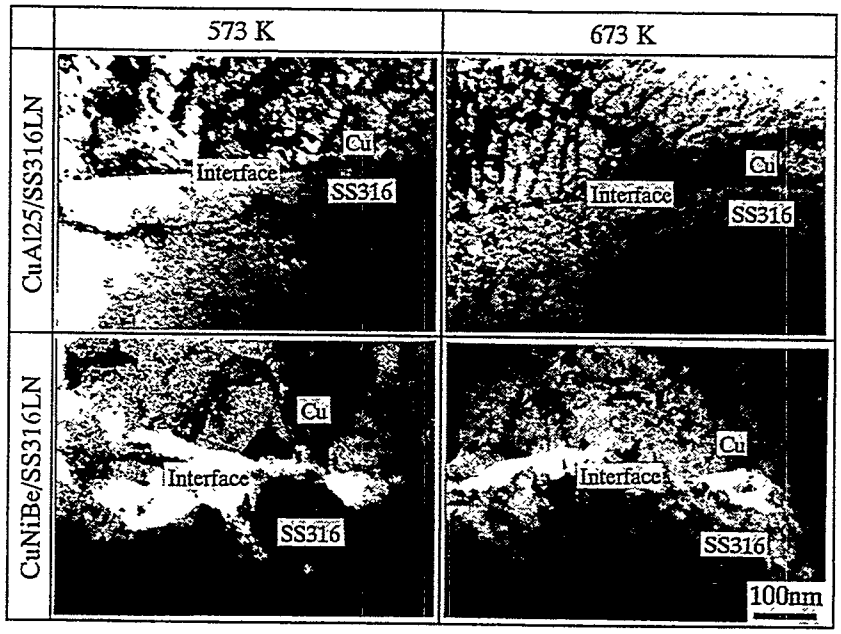

Figure 4. Microstructure in the interface of joint materials annealed at 573K and 673K for 100 h.

The results of annealing experiments showed that temperatures ≤ 673K did not change the initial microstructure or composition of CuAl25/SS316L and CuNiBe/SS316L joints. Although there are no data from annealing experiments longer than 100 hours, it is expected that the microstructure and composition of CuAl25/SS316L and CuNiBe/SS316L are stable at temperatures below 673K . However, irradiation may lead to significant changes because of radiation-enhanced segregation, precipitation or dissolution near and at the interface that could alter the properties. In addition, the preexisting voids near the interface of the joints may coarsen under irradiation and enhance the sensitivity of joints to failure. Given the uncertainties in the response to irradiation, neutron irradiation experiments should be performed at appropriate temperatures to investigate the response of the different materials.

ACKNOWLEDGEMENT

The authors wish to thank Prof. T. Muroga of National Institute for Fusion Science for providing ion milling instrument to make TEM samples, and Prof. N. Yoshida of Kyushu University for providing TEM to observe the samples. This work was supported by Japan-US collaborative JUPITER program on fusion materials research. D.J. Edwards' participation was supported by the U.S. Department of Energy under contract DE-AC06-76RLO-1830 with the Battelle Memorial Institute at the Pacific Northwest National Laboratory.

REFERENCES

[1] J.F. Stubbins, Amanulah, M. James, J, Heuer, P. Kurath, K.D. Leedy, G. Li, G.D. Morgan, K.T. Slattery, B.G. Thomas and G.W. Wille, ITER/US/97/IV-BL-1, Final Report for US ITER Task T212 (CY1996)

5.0 AUSTENITIC STAINLESS STEELS

TENSILE PROPERTIES AND DAMAGE MICROSTRUCTURES IN ORR/HFIR-IRRADIATED AUSTENITIC STAINLESS STEELS – E. Wakai and S. Jitsukawa, (Japan Atomic Energy Research Institute), N. Hashimoto (Oak Ridge National Laboratory), T. Sawai (JAERI), J. P. Robertson (ORNL), and A. Hishinuma (JAERI)

Extended Abstract (the full paper will be published in the Journal of Nuclear Materials as Proceedings of the Ninth International Conference on Fusion Reactor Materials, October 10-15, 1999, Colorado Springs, Colorado).

The synergistic effect of displacement damage and helium generation under neutron irradiation on tensile behavior and microstructures of austenitic stainless steels was investigated. The steels were irradiated at 400°C in the spectrally tailored (ST) ORR/HFIR capsule to 17 dpa with a helium production of about 200 appm and in the HFIR target capsule to 21 and 34 dpa with 1590 and 2500 appm He, respectively. The results may be summarized as follows:

(1) The increase of yield strength in the JPCA-SA irradiated at 400°C to 17 dpa in the spectrally tailored ORR/HFIR capsules was about 390 MPa, and that in the HFIR target one to 21 and 34 dpa were about 630 and 600 MPa, respectively.

(2) The spectrally tailored irradiation-induced Frank-type loops with a number density of 8×10^{21} m^{-3} and the mean size of 19.3 nm, bubbles and voids with 8×10^{21} and 8×10^{19} m^{-3}, respectively, and the mean sizes of 3 and 9.5 nm, respectively, and carbides with 8×10^{21} m^{-3} and 3.4 nm.

(3) The HFIR target irradiation also induced these defect clusters, and the number densities of these clusters were higher than the former case and these mean sizes were smaller than those.

(4) The values of hardening due to these clusters were calculated from the model of dispersed barrier hardening and were 331 and 666 MPa, respectively, and these coincide with the increase of yield strengths.

(5) This analyses wad furthermore suggested that the main factor of hardening in the spectrally tailored ORR/HFIR and the HFIR target irradiation were Frank-type loops and cavities, respectively. The similar results were obtained for the J316-SA steels.

DEFORMATION MECHANISMS IN 316 STAINLESS STEEL IRRADIATED AT 60 AND 330°C – N. Hashimoto, S. J. Zinkle, A. F. Rowcliffe, J. P. Robertson (Oak Ridge National Laboratory) and S. Jitsukawa (Japan Atomic Energy Research Institute)

Extended Abstract (the full paper will be published in the Journal of Nuclear Materials as Proceedings of the Ninth International Conference on Fusion Reactor Materials, October 10-15, 1999, Colorado Springs, Colorado).

Plastically deformed microstructures in neutron-irradiated austenitic stainless steel were investigated by transmission electron microscopy (TEM). Neuron irradiation at 60 and 330°C to about 7 displacement per atom (dpa) induced a higher number density of faulted loops and black dots, which resulted in irradiation-induced hardening. In the specimen irradiated at 60°C and tensile tested at 25°C at a strain rate of 4×10^{-4} s^{-1}, the deformation microsctructure consisted of twins, elongated faulted loops, and lath and twin martensite phase. In the specimens irradiated and tested at 330°C at a strain rate of 4×10^{-4} s^{-1} and 4×10^{-6} s^{-1}, in addition to these features, dislocation channeling was also observed. The TEM examination suggests that lath and twin martensite can form during tensile testing at both of these temperatures. Examination of the specimens irradiated and tensile tested at 330°C indicated that twinning was the predominant deformation mode at slower strain rate and dislocation channeling was favored at higher temperature. From the micrographs taken from the {111} plane streak in a diffraction pattern, it is suggested that faulted loops could be the principal twin initiation site during deformation.

6.0 INSULATING CERAMICS AND OPTICAL MATERIALS

IN-SITU THERMAL CONDUCTIVITY MEASUREMENT OF CERAMICS IN A FAST NEUTRON ENVIRONMENT – L. L. Snead (Oak Ridge National Laboratory), R. Yamada (Japan Atomic Energy Research Institute), K. Noda and Y. Katoh (Kyoto University), S. J. Zinkle, W. S. Eatherly, and A. L. Qualls (Oak Ridge National Laboratory)

Extended Abstract (the full paper will be published in the Journal of Nuclear Materials as Proceedings of the Ninth International Conference on Fusion Reactor Materials, October 10-15, 1999, Colorado Springs, Colorado).

An experimental technique for measuring the in-situ thermal conductivity of ceramic materials in an RB* position of the High Flux Isotope Reactor has been successfully demonstrated. The technique is based on measurement of the temperature drop along the axis of a solid cylinder constrained to one dimensional heat flow. The heat source is the intrinsic gamma heating of the core region of the HFIR. Preliminary results indicated that, as expected, the thermal conductivity of the ceramic materials undergo a rapid reduction in thermal conductivity with irradiation followed by an apparent saturation. Final results will be obtained after a detailed post-irradiation examination of the samples and final analysis of the core gamma heating.

7.0 BREEDING MATERIALS

FABRICATION AND PROPERTIES OF A TIN-LITHIUM ALLOY *

K. Natesan and W. E. Ruther (Argonne National Laboratory)

OBJECTIVE

The objectives of this task are to fabricate an Sn-Li alloy containing 25 at.% Li, which is being considered as a potential coolant in a fusion device, and to evaluate the alloy's physical and chemical properties.

SUMMARY

An Sn-25 at.% Li alloy has been fabricated by starting with pure Sn and Li. The alloy was cast into various shapes and sent to researchers in several organizations in the United States and abroad for property measurements. Melting temperature of the alloy is 334°C and its density is 6.36 g/cm^3.

INTRODUCTION

Tin-lithium alloys seem to have several attractive thermo-physical properties, in particular thermal conductivity and heat capacity, when compared with those for another coolant, Pb-17 at.% Li [1]. Furthermore, Sn-Li coolant exhibits low vapor pressure, a significant benefit in the design of the free-flow first wall and divertor that will handle high heat flux and high neutron wall loading in fusion devices [2,3]. Even though conceptually Sn-Li is a potential coolant/breeding material, several technical issues such as physical and chemical properties, materials compatibility, activation characteristics, and breeding potential, must be addressed. We have therefore fabricated an Sn-Li alloy containing 25 at.% Li which will be used by researchers from several institutions in U.S. and abroad to evaluate various properties of the material.

FABRICATION PROCEDURE

Figure 1 is a schematic illustration of the Sn-Li phase diagram, which shows that the melting temperature of the alloy increases monotonically with an increase (above 5 at.%) in Li concentration in the alloy. For tritium breeding, an Li concentration of at least 20 at.% is suggested; a composition of Sn-25 at.% Li was selected for fabrication. The melting temperature for this alloy will be ≈330°C. The phase diagram also shows several Li-Sn compounds (such as Li_4Sn, Li_7Sn_2, Li_5Sn_2, Li_2Sn, and LiSn) that have melting temperatures of 485 to 783°C. If these high-melting compounds form during alloy fabrication, the mixed alloy must be heated to very high temperatures to melt these phases and to develop an alloy with a homogeneous composition. Therefore, it is essential that none of these high-temperature phases form during mixing of Sn and Li to make the alloy. To avoid this, an apparatus was assembled in which Li is gradually added to Sn so that the Li concentration increased monotonically from 0 to 25 at.%, with an associated increase in melting temperature from 250 to

---

*This work has been supported by the U.S. Department of Energy, Office of Fusion Energy Research, under Contract W-31-109-Eng-38.

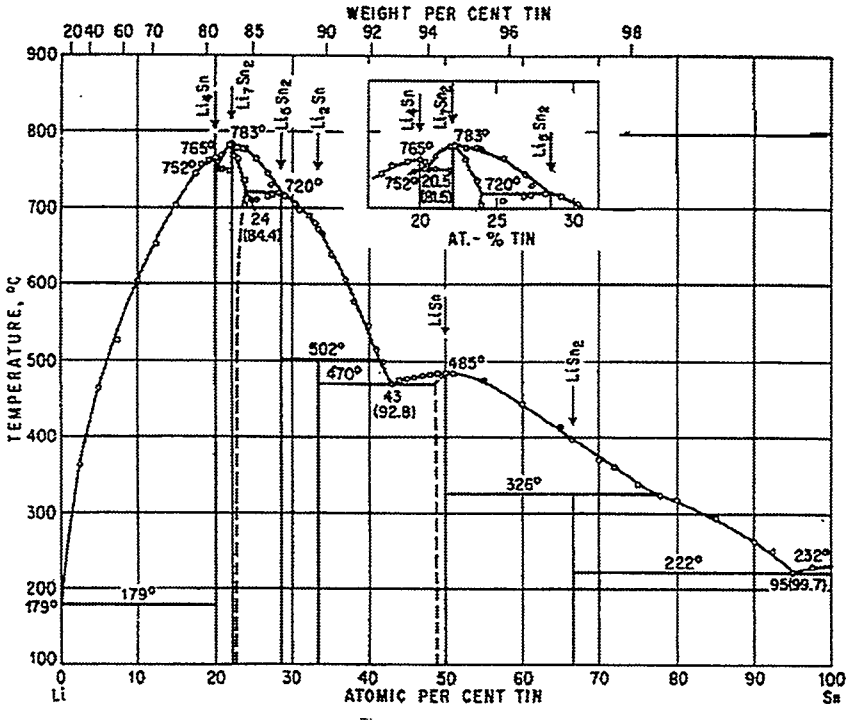

Figure 1. Schematic illustration of Sn-Li phase diagram.

350°C. Furthermore, a stainless steel stirrer was used to stir the liquid while Li was continuously added to Sn to improve the composition homogeneity of the final Sn-Li alloy.

The Sn, obtained from Ames Metal Products, was in the form of 25 x 12.5 x 250 mm castings with a purity of 99.95 wt.% Sn. Lithium was obtained from Cypress Foote Mineral in the form of rods of 12.5 mm dia x 275 mm length. Figure 2 includes a photograph of the Sn ingots and Li contained in an inert environment within a sealed metal can. The equipment used to mix Li into Sn was assembled with components made of austenitic stainless steel. The mixing chamber was a vessel 0.4 m dia. x 0.5 m high and was equipped with a viewing port, thermowell, drain, and two insertion ports at the top. One of these insertion ports was used to assemble a stirrer mechanism and the other was used as a line (12.5-mm-dia. tubing) for transferring Li into Sn vessel. Li was contained in a second vessel (0.15 m dia. X 0.35 m high) above the Sn vessel. Resistance heaters and thermal insulation were applied to both Li and Sn vessels, as well as to the Li transfer line. The gas phase of the two vessels were independently connected to a source of vacuum and purified argon gas. Figure 3 shows photographs of the experimental assembly in different stages of construction.

Calculations on the requirements for Sn and Li were made to produce ≈15 L of the Sn-25 at.% Li alloy. Using the density values of 0.54 and 7.3 g/cm^3 for pure Li and Sn, respectively, we calculated the density of Sn-25 at.% Li alloy as 6.36 g/cm^3. To produce 15 L of the Sn-Li alloy, the initial amounts of Sn and Li needed were 93.5 and 1.81 kg of Sn and Li, respectively.

Figure 2. Photographs of starting materials: Sn (left) and Li (right).

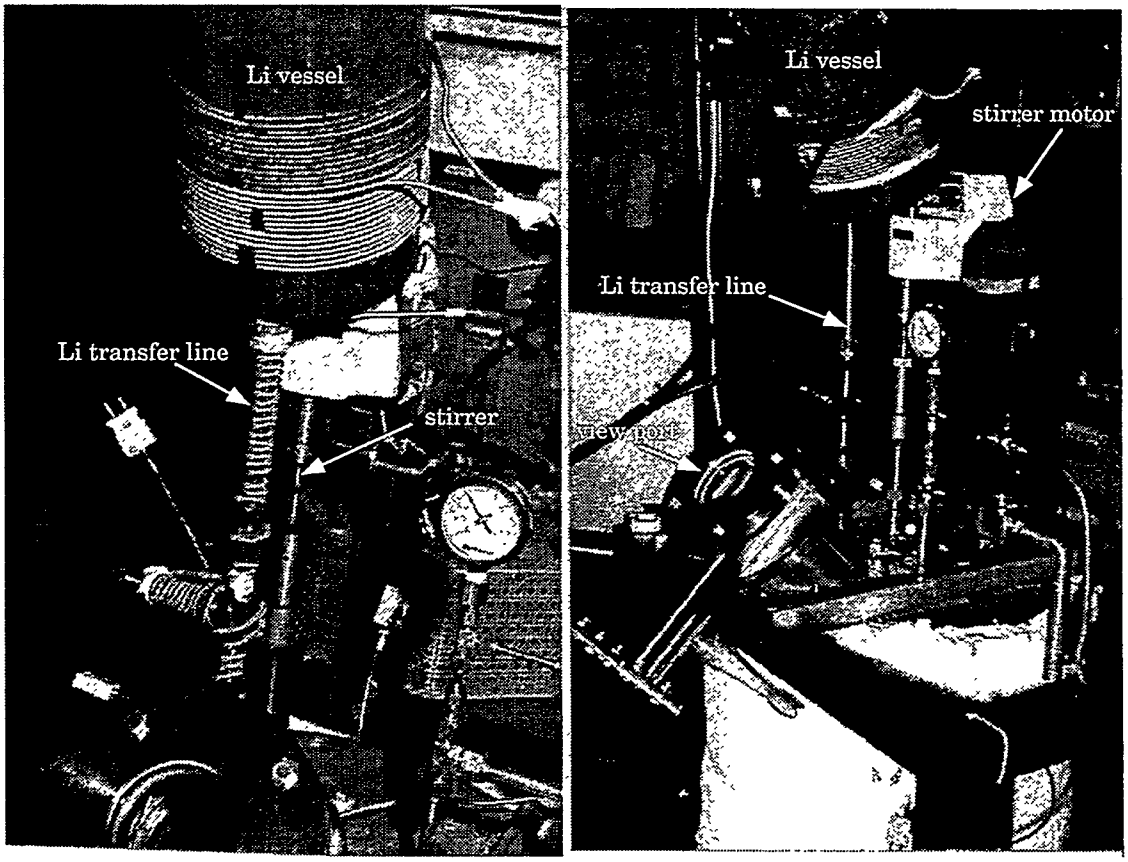

Figure 3. Photographs of experimental set up at different stages of assembly. The key parts of the assembly are Sn vessel (with insulation), Li vessel at the top, Li transfer line, Stirrer with a motor, and a view port.

The initial step was to melt the slender bars of pure Sn in the lower vessel. Since there were a large number of bars, as many as possible were inserted into the vessel through the view port and the system was then closed, evacuated, and back-filled with Ar. The evacuation/refill operations were repeated three times prior to heating the vessel containing Sn. The bars were then melted and cooled. Two loadings of Sn and melting were required to obtain the required 93.5 kg of pure Sn in the vessel. The smaller Li vessel also required two loadings to obtain 1.81 kg of Li. Rods of Li were removed from their secondary protective plastic containment in the vicinity of the Li vessel and inserted in to the Li vessel with minimal exposure to ambient air. In addition, flowing Ar from the vessel mitigated the potential for unwanted oxygen contamination during the transfer. At the end of each loading, the Li was melted and slowly added to the molten Sn in the mixing chamber. An attempt was made to video tape the first addition of Li to Sn, but the viewing window did not allow a clear view of the stream of Li striking the molten Sn, the lighting was poor, and after the initial exothermic reaction, the window became clouded. The results were less than desirable but a VHS tape of the operation does exist.

In the first mixing operation, Sn and Li vessels were maintained at 240 and 200°C, respectively. Upon adding Li to Sn, the temperature of the mixing chamber increased to 419°C. The second batch of Li was added to the mixing chamber maintained at 320°C. The temperature of the mixing chamber rose to 512°C after addition of the second batch of Li. The Sn-Li alloy was maintained at this temperature for 15 min while the stirrer was operating at high speed. A sample of the alloy was taken by casting it under vacuum in a heated stainless steel tube (≈0.5 m long x 12.5 mm dia.) attached to the mixer vessel drain. The initial analysis indicated an Li content of 0.83 wt.%, which was significantly lower than the additions made to the vessel, probably because of the inhomogeneity of the melt. The mixing was held at 400-500°C with vigorous stirring approximately eight times a day for three days to dissolve any high-temperature compounds and to homogenize the melt. A second sample taken in the same manner as before showed an Li content of 1.96 wt.%, based on an analysis of duplicate samples. This value corresponds to an alloy composition of Sn-25 at.% Li. Table 1 lists the concentration of various substitutional and interstitial elements in the alloy.

Figure 4 shows castings of several shapes and sizes made with a copper mold. Material from various product forms have been sent to CEA-CEREM/SCECF in France, the University of Tokyo in Japan, UCSD Fusion Energy Research in San Diego, and the University of Illinois at Urbana-Champaign for measurement of various physical properties. Figure 5 shows scanning electron photomicrographs of the alloys in two magnifications. The two-phase solidified structure consists of Sn and $SnLi_2$ at room temperature. Vickers hardness measurements indicated the average hardness values for the light and dark phases to be ≈20 and 85, respectively. Figure 6 shows the temperature/time cooling curve generated for the alloy. The point where the slope of the line changes (334°C) indicates the melting temperature for the alloy. This agrees well with the temperature depicted in the phase diagram (see Fig. 1) for an alloy with a composition of Sn-25 at.% Li.

Table 1. Chemical composition of Sn-Li alloy fabricated in current project

Element	Concentration (wt.%)	Element	Concentration (wt.%)
Ag	0.017	Na	<0.001
Al	<0.01	Ni	0.02
Ba	0.002	Pb	0.02
Be	<0.001	Si	<0.05
Ca	<0.001	Sr	<0.001
Cd	<0.001	Ti	<0.005
Co	<0.01	V	<0.005
Cr	0.03	Zn	<0.001
Cu	<0.005	Zr	<0.005
Fe	0.08	O	0.091
K	0.011	N	<0.0002
Li	1.96	C	0.085
Mg	<0.001	S	<0.0035
Mn	0.017	Sn	balance

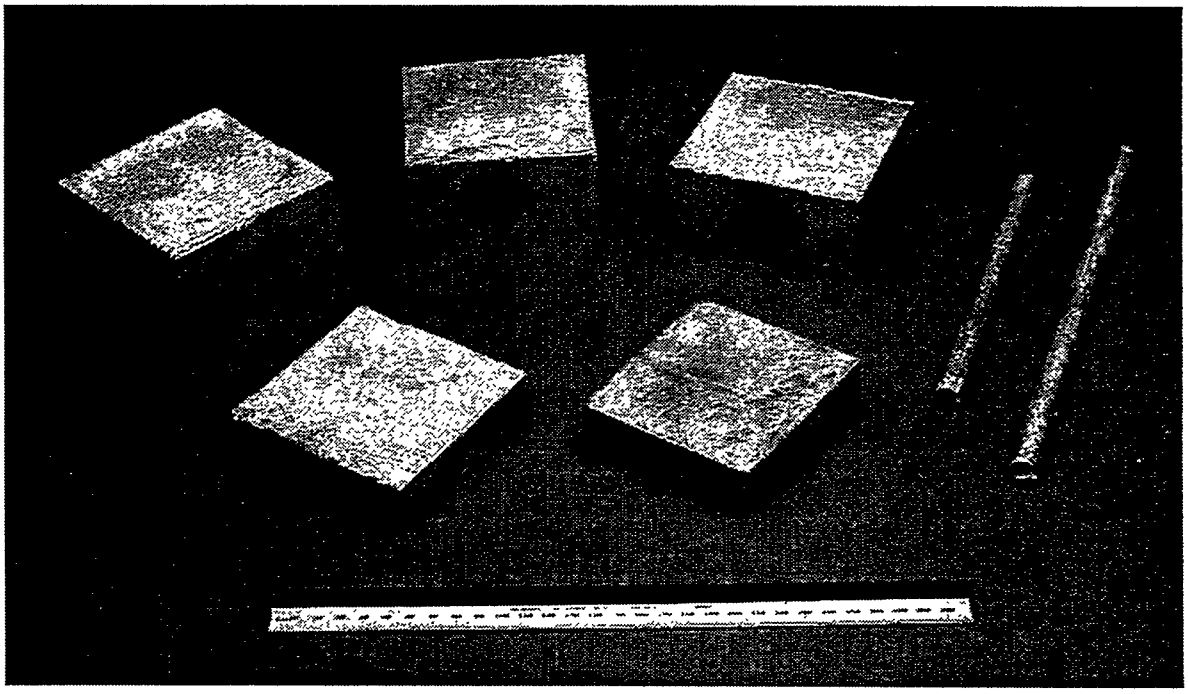

Figure 4. A photograph of different shapes of an Sn-25 at.% Li alloy fabricated in the program

REFERENCES

1. M. A. Futterer, G. Aiello, F. Barbier, L. Giancarli, Y. Poitevin, P. Sardain, A. Li Puma, G. Ruvutuso, and G. Vella, "On the use of tin-lithium alloys as breeder material for blankets of

fusion power plants," presented at 9th Intl. Conf. on Fusion Reactor Materials, Oct. 9-15, 1999, Colorado Springs.

2. D. K. Sze, "The development of Sn-Li coolant/breeding material for APEX/ALPS applications," presented at Intl. Symp. on Fusion Nuclear Technology, Rome, Sept.1999.

3. D. K. Sze, R. F. Mattas, Z. Wang, E. T. Cheng, M. Sawan, S. J. Zinkle, and K. A. McCarthy, "Sn-Li, a new coolant/breeding material for fusion applications," presented at 9th Intl. Conf. on Fusion Reactor Materials, Oct. 9-15, 1999, Colorado Springs.

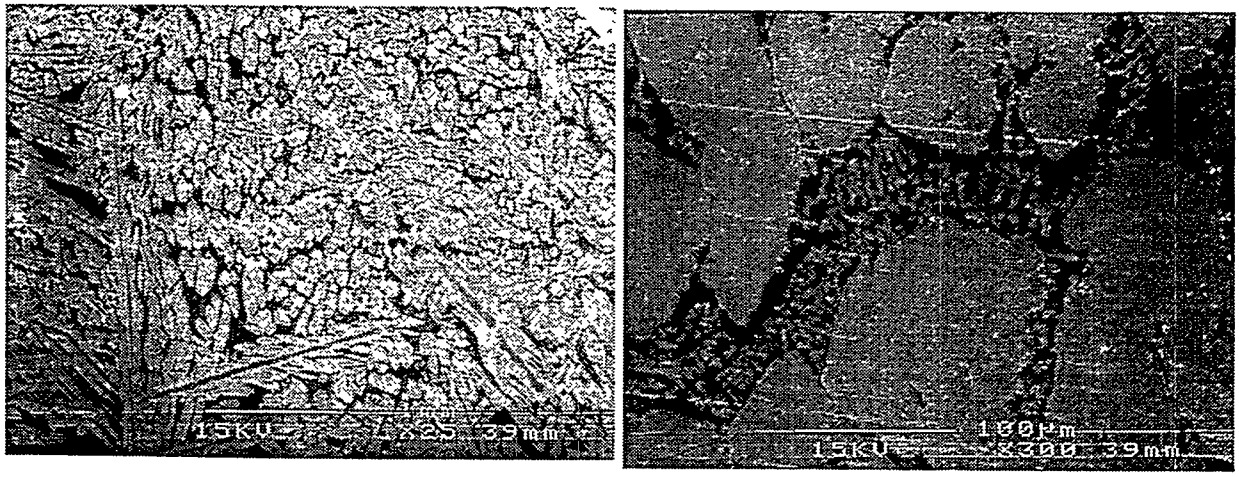

Figure 5. SEM photomicrographs of an Sn-25 at.% Li alloy fabricated at Argonne National Laboratory

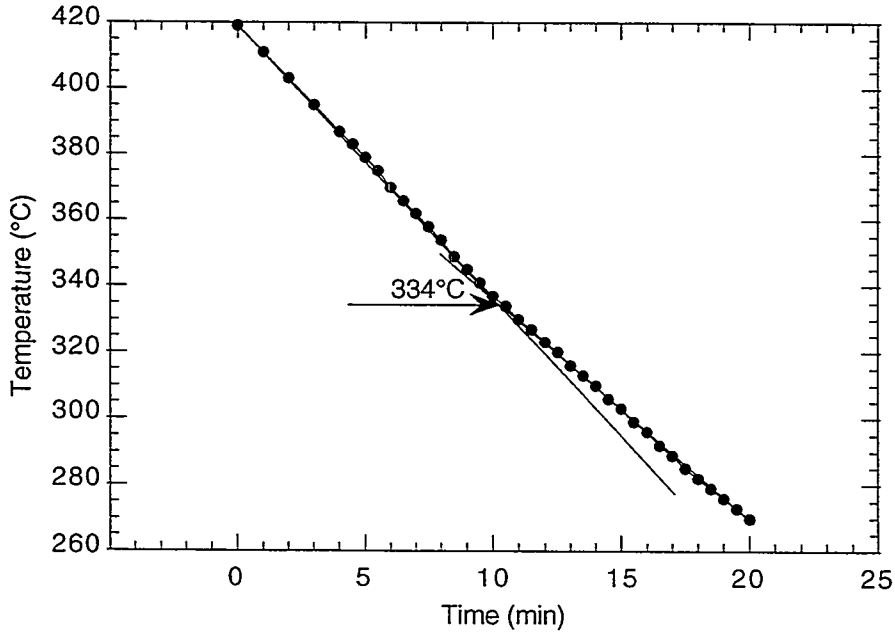

Figure 6. Temperature/time cooling curve for an Sn-25 at.%Li indicating a melting temperature of 334°C.

8.0 RADIATION EFFECTS, MECHANISTIC STUDIES, AND EXPERIMENTAL METHODS

THE EFFECTS OF ONE-DIMENSIONAL GLIDE ON THE REACTION KINETICS OF INTERSTITIAL CLUSTERS - H. L. Heinisch (Pacific Northwest National Laboratory)*, B. N. Singh (Risø National Laboratory, Denmark) and S. I. Golubov (Institute of Physics and Power Engineering, Russia)

Extended abstract of a paper submitted to the Journal of Nuclear Materials as part of the proceedings of the 9th International Conference on Fusion Reactor Materials, Colorado Springs, Colorado, USA, October 10-15, 1999.

EXTENDED ABSTRACT

Collision cascades in metals produce small interstitial clusters and perfect dislocation loops that glide in thermally activated, one-dimensional (1D) random walks. These gliding defects can change their Burgers vectors by thermal activation or by interactions with other defects. Their migration is therefore "mixed 1D/3D migration" along a 3D path consisting of 1D segments. The defect reaction kinetics under mixed 1D/3D diffusion are different from both pure 1D diffusion and pure 3D diffusion, both of which can be formulated within analytical rate theory models of microstructure evolution under irradiation. Atomic-scale kinetic Monte Carlo (kMC) defect migration simulations are being used to investigate the effects of mixed 1D/3D migration on defect reaction kinetics as a guide for implementing mixed 1D/3D migration into the analytical theory. Earlier studies using kMC simulations [1,2] have demonstrated the significant effects of 1D and mixed 1D/3D migration on defect reaction kinetics. The present work seeks to determine the functional dependence of defect reaction kinetics on the variables affecting the defect-sink interactions under mixed 1D/3D migration.

In the kMC simulations, defects migrate one at a time through the crystal by random hopping from one fcc lattice site to an adjacent lattice site in pure 3D or mixed 1D/3D migration, depending on the nature of the defect, until they are absorbed in randomly distributed unsaturable spherical absorbers of equal radius R and number density N. The "sink strength" of defect sinks in 3D is defined as $k^2_{3D} = 6/(a_0^2\langle n\rangle)$, where a_0 is the (fcc) lattice constant and $\langle n\rangle$ is the average number of hops to absorption determined from the simulations. For mixed 1D/3D migration we define the sink strength to be $k^2_M = 4/(a_0^2\langle n\rangle)$ to reflect the 1D nature of the hops. The usual formula used in analytical rate theories to describe the sink strength in terms of the characteristics of the sink population (3D) is

$$k^2 = 4\pi RN, \qquad (1)$$

which is valid for small R, representing volume fractions of absorbers less than a few percent. The simulation results for pure 3D are well-represented by the form of eq (1), modified to take into account the discrete hopping nature of the diffusion process (see the full paper). For pure 1D migration in the analytical theory, the sink strength varies as R^4. Figure 1 is a log-log plot of the sink strength as a function of R for various values of L, the average distance between direction changes for mixed 1D/3D migration. The straight lines are fits of a power law function to the simulation results, with the power m=1 for pure 3D and with values that vary up to about m=2 as L increases.

Thus, the existence of mixed 1D/3D migration introduces a new variable into the reaction kinetics: the average distance between direction changes, L. So, in the analytical theory, the concept of "sink strength" is determined not only by the concentration and properties of

---

* Pacific Northwest National Laboratory (PNNL) is operated for the U.S. Department of Energy by Battelle Memorial Institute under contract DE-AC06-76RLO 1830.

the sinks, but also by the kinetic properties of the migrating defects. Simulation results demonstrate that the dependence of sink strength on the size and concentration of sinks under mixed 1D/3D migration lies between those for pure 1D and pure 3D migration and varies with L.

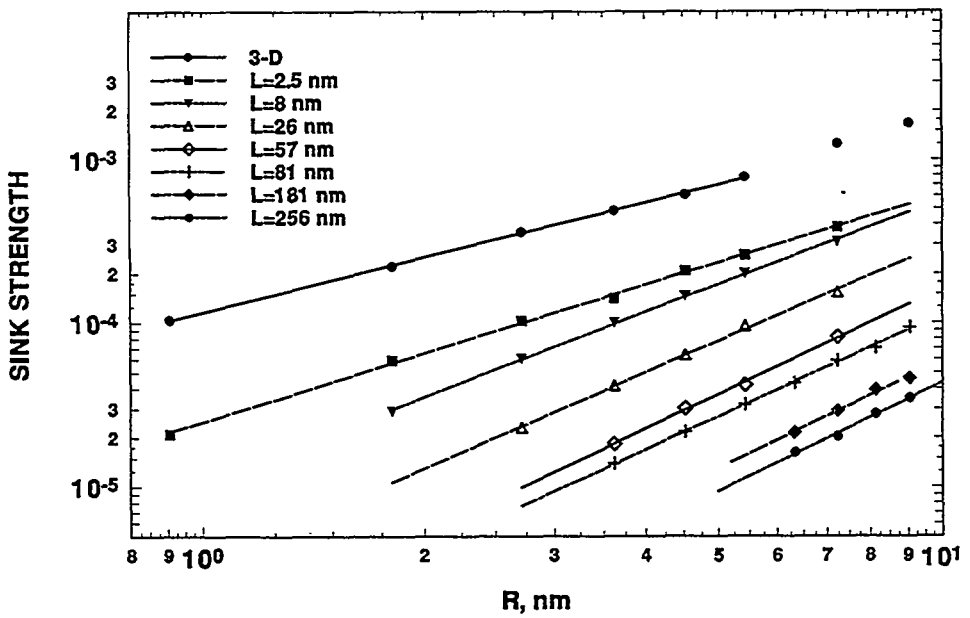

Figure 2. The points are the sink strengths measured in kMC simulations ($k^2 = 4/(a_0^2<n>)$ plotted versus the absorber radius R for various values of L, the distance between direction changes for mixed 1-D/3-D migration. The straight lines are fits of the power law function $k^2_M=\alpha(R-a_0/\sqrt{2})^m$, where α and m are fitting constants that vary with L.

Recent theoretical developments by Barashev, Golubov and Trinkaus [3,4] have, by two different approaches, identified the relationship between the sink strength k^2_M and L and R for mixed 1D/3D reaction kinetics to be

$$k^2_M= 4\pi R^2 N/\sqrt{2}L, \qquad L>>R. \qquad (2)$$

This expression is consistent with the behavior of the exponent m as a function of L in Fig. 1, i.e. that k^2_M varies directly as R^2 (at least approximately), but it is true only for values of L greater than the absorber radii. This is illustrated in Fig. 2, where simulation results are compared with eq. (2). While there is good agreement between the simulations and the analytical theory at values of L larger than the absorber size, the theory still needs to be developed to fully describe the transition between mixed 1D/3D and pure 3D.

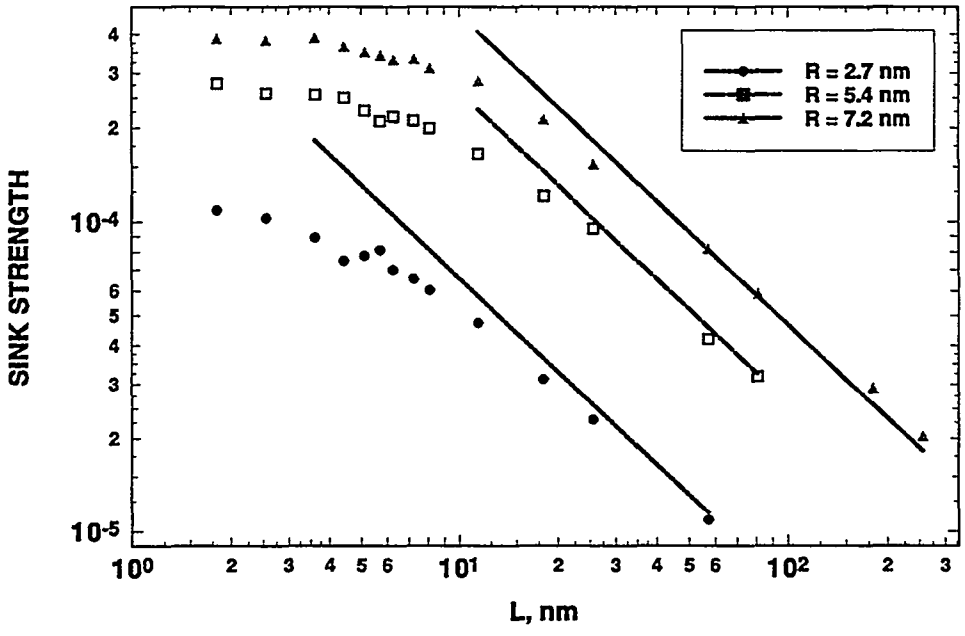

Figure 4. Comparison of kMC simulation results with the analytical expression for the sink strength under mixed 1D/3D migration, eq. (2). The sink strengths are plotted as a function of L, the average distance between direction changes, for several values of R, the absorber radius. All length dimensions are in nm.

Future work will aim at further elucidating the ramifications of mixed 1-D/3-D migration on defect reaction kinetics, especially the transition to pure 3D migration, through additional kinetic Monte Carlo simulations and analytical theory development.

ACKNOWLEDGEMENTS

This work was partly supported by the European Fusion Technology Programme and partly supported by the U.S. Department of Energy under contract DE-AC06-76RLO 1830 with Battelle Memorial Institute at the Pacific Northwest National Laboratory.

REFERENCES

[1] H.L. Heinisch, B.N. Singh and S.I. Golubov, J. Nucl. Mater., 276 (2000) 59.

[2] H.L. Heinisch, B.N. Singh and S.I. Golubov, J. Comp.Aided Mat. Des. (1999) in press.

[3] A.V. Barashev, S.I. Golubov and H. Trinkaus, to be published

[4] H. Trinkaus, A.V. Barashev and S.I. Golubov, to be published.

SIMULATING THE INFLUENCE OF RADIATION TEMPERATURE VARIATIONS ON MICROSTRUCTURAL EVOLUTION – Y. Katoh (Kyoto University), R. E. Stoller Oak Ridge National Laboratory), A. Kohyama (Kyoto University), and T. Muroga (National Institute for Fusion Science)

Extended Abstract (the full paper will be published in the Journal of Nuclear Materials as Proceedings of the Ninth International Conference on Fusion Reactor Materials, October 10-15, 1999, Colorado Springs, Colorado).

The influence of temperature variations on microstructural evolution in austenitic stainless steels is discussed in order to help interpret the response of materials in the HFIR-RB-13J temperature variation experiment. A kinetic microstructural evolution model developed for irradiated austenitic stainless steels was modified to provide a fully dynamic calculation of point defect and point defect cluster concentrations. A dislocation density-dependent interstitial clustering model was introduced so that the calculated dislocation loop evolution might fit the experimental data in a broad temperature range. Using the modified model, microstructural evolution was predicted for simulated HFIR-RB-13J temperature variation experiments and variations in material parameters were evaluated.

Repeated temperature excursion to 573 K from 773 K always resulted in increased dislocation loop density and reduced cumulative defect flux within the calculated material parameter range. Repeated temperature excursions to 473 K from 623 K may increase or decrease the loop density and cumulative defect flux depending on material parameters. The influence of temperature variation could mostly be explained by accumulation and release of matrix defects at the temperatures of interest.

COMPARATIVE STUDY OF DAMAGE ACCUMULATION IN IRON UNDER MAGNETIC AND INERTIAL FUSION CONDITIONS – E. Alonso, M. J. Caturla, and T. Diaz de la Rubia (Lawrence Livermore National Laboratory), N. Soneda (Central Research Institute of Electric Power Industry), J. Marian and J. M. Perlado (Instituto de Fusion Nuclear), and R. E. Stoller (Oak Ridge National Laboratory)

Extended Abstract (the full paper will be published in the Journal of Nuclear Materials as Proceedings of the Ninth International Conference on Fusion Reactor Materials, October 10-15, 1999, Colorado Springs, Colorado).

We present results of kinetic Monte Carlo (KMC) simulations of damage accumulation in Fe under conditions relevant to Inertial (IFE) and Magnetic Fusion Energy (MFE), with input obtained from Molecular Dynamics (MD). MD simulations provide information on the primary state of damage and were carried out for cascades with primary knock-on atom (PKA) energies ranging from 100 eV to 50 keV. These were used as input for a KMC simulation in which pulsed IFE irradiation and continuous MFE irradiation were simulated and compared. The MD collision cascades were introduced into the KMC simulation reproducing a recoil spectrum of 14 MeV neutrons. For pulsed irradiation, we discuss the manner in which damage accumulates depending on temperature and pulse rate. At low temperature, we show that there is no significant difference between pulsed and continuous irradiation when the integrated dose rate is the same.

COMPARISON OF A MICROSTRUCTURE EVOLUTION MODEL WITH EXPERIMENTS ON IRRADIATED VANADIUM – S. Sharafat and N.M. Ghoniem
(University of California at Los Angeles)

Journal: *J. Nucl. Mater*, Paper presented at ICFRM-9, Colorado Springs, Colorado, 1999

Extended Abstract

Interaction of high-energy neutrons with fusion reactor materials will result in simultaneous production of displacement damage and helium atoms. Subsequent reactions between helium and defect clusters determine, to a large extent, most physical and mechanical properties of irradiated materials. Thus, microstructure evolution of neutron-irradiated BCC and FCC metals in the presence of helium has been the focus of research over the past 2 decades. Vanadium and its alloys are now considered as candidate structural materials in fusion reactors, because of their low neutron activation and high-temperature capabilities. Development of a mechanistic understanding for the influence of helium on microstructure evolution of irradiated vanadium can help in tailoring its microstructure by thermomechanical processes for maximum resistance to radiation damage. One of the main themes of current interest is the origin of the asymmetry in the flow of vacancies and interstitials to various microstructures. The asymmetry in vacancy/interstitial flow to microstructural features determines the rate of their evolution. In particular, the growth of voids in irradiated materials was explained in terms of an *"Absorption Bias (AB)"* of dislocations towards interstitials, thus leaving excess vacancies to flow into already nucleated voids. Recently, however, another form of asymmetry has been proposed, in which the fraction of free vacancies produced in collision cascades is higher than that of free interstitials. This type of *"Production Bias (PB)"* can also lead to cavity growth in irradiated materials, and when combined with *AB*, can explain qualitative differences in the swelling behavior of BCC and FCC metals. These arguments, however, are based on the notion that cavities have already nucleated in the material, and that their growth phase dominates subsequent evolution. In the presence of helium production, especially the high levels anticipated under fusion neutron conditions, this scenario might be incomplete. Continuous production of helium in the matrix can result in very long nucleation transients of bubbles. Under these conditions, separation of distinct nucleation and growth phases may not be so clear. During the process of bubble nucleation, helium is trapped in free vacancies to form substitutional sites, from which further agglomeration is possible. If helium production rates are large, the fraction of occupied vacancies, which are tied up with helium-vacancy complexes, can be quite substantial. Thus, the balance between free vacancy and interstitial fluxes arriving at those bubbles to allow their growth can be greatly disturbed by helium trapping. This physical scenario can result in an additional complication to the "bias" idea, in which continuous nucleation of helium bubbles can lead to another type of symmetry breaking for free point defects. We will label this effect as the *"Nucleation Bias (NB).*

A kinetic rate theory model, which includes helium generation and the formation of cascade-induced clusters (CIC), is presented. Comparison of the model to ion irradiation data on vanadium reveals the effects of helium generation and cascade-induced interstitial and vacancy clusters on microstructure evolution. The model includes rate equations for clustering of helium bubbles, immobile vacancy clusters, glissile interstitial clusters, sessile dislocation loops, as well as bubbles on precipitates and in grain boundaries. It is shown that helium transport to dislocations, bubbles and grain boundaries is strongly transient because of coupling between the nucleation and growth modes of bubble evolution. Helium agglomeration in vacancy clusters is shown to reduce the excess vacancy flux for growing matrix and precipitate-affixed bubbles. The direct formation of vacancy and interstitial clusters leads to enhanced nucleation

of matrix bubbles, and a corresponding reduction of their growth rate. In addition to the dislocation and production bias mechanisms, a new mechanism of "helium nucleation bias" is shown to exist under high helium generation rates, and to lead to reasonable agreement with experiments. The present model for the evolution of bubble, dislocation and defect microstructure in irradiated vanadium reveals the delicate balance between rate processes, which control the speed of microstructure evolution. It is clear that bubble nucleation in irradiated vanadium under conditions of high helium generation rates evolves on a long time scale. Strong coupling between the nucleation and growth phases of the microstructure is achieved under these conditions. The presence of helium as additional specie to intrinsic point defects results in a reduction in the concentration of freely migrating vacancies. The growth rate of nucleated bubbles is thus reduced by this form of natural bias dictated by the presence of helium. Comparison with ion irradiation data shows the necessity to include the direct formation of CIC's in rate theory models, and the need to couple both nucleation and growth phenomena.

CLUSTERING THEORY OF ATOMIC DEFECTS – N. M. Ghoniem (University of California at Los Angeles)

Journal: *Radiation Effects and Defects in Solids*, 148: 269-318 (1999)

Extended Abstract

Clustering of atomic defects leads to changes in the microstructure of materials, and hence induces drastic variations in their properties. In many technical fields, the role of defect clustering is very significant, and is sometimes limiting to further progress. We present here a comprehensive review of the theory of atomic defect clustering under non-equilibrium conditions, particularly encountered during irradiation of materials with energetic particles, as well as during material processing by energetic sources. These conditions are met in a wide range of technical applications, ranging from nuclear and fusion energy to microelectronics and surface engineering. We first present a general stochastic framework for the evolution of atomic clusters, and show how this can be described within the context of death-and-birth processes. This leads to the well-known master equation for microscopic atomic clusters. In the limiting case of a Poissonian process for the transition probabilities between cluster sizes, the master equation tends, in the macroscopic limit to the mean field approximation embodied by the theory of rate processes. When atomic clusters grow or shrink by the absorption of single atomic defects, a continuum Fokker-Planck approximation can be derived. Within this approximation, the evolution of interstitial loops, voids, bubbles, and general clusters of complex phases is presented, and in some cases, good agreement with experiments is obtained. It is shown that because of coalescence reactions, the evolution of surface atomic clusters during atom deposition processes is best described by kinetic moment equations, directly derived from rate equations. It is shown that breaking the symmetry of space or time leads to drastic variations in the size and space distributions of defect clusters. Examples are given for pulsed irradiation conditions, where it is shown that non-linear rate processes enhance cluster formation during on time, and could lead to their dissolution during the off time at high temperature. On the other hand, fluctuations are shown to result in instabilities and spatial self-organization of defect clusters. Description of pattern formation during irradiation, such as void and interstitial loop lattices, is very well described by a Ginzburg-Landau type equation, reminiscent of phase transitions under thermodynamic equilibrium conditions.

The theory of defect clustering under non-equilibrium conditions is deeply rooted in statistical physics, and is shown to bear fruitful results for the study of a variety of interesting physical phenomena. Starting from basic understanding of stochastic fluctuations in defect fields, it is shown that one can formulate master equations at the microscopic or atomic level. These equations can be treated in a more macroscopic sense by equivalent rate equations, in the limit of Poisson probability distributions for transitions between states. Under irradiation, diffusion in the bulk of large defect clusters is slow, and the transitions between states are shown to be just between nearest neighbors. A useful approximation is obtained, which is shown to be the Fokker-Planck continuum theory. Several solution methods have been presented for a hybrid scheme that links the rate equations with the continuum F-P equation. The method of moments is particularly useful, because it is relatively simpler than other numerical methods. In addition, the method allows for direct comparison with experiments on the evolution of the size distribution of defect clusters. The theory is shown to be successful in explaining experimental observations on size distributions of interstitial loops under irradiation. The influence of collision cascades is shown to be important, and results in increased dispersion of the size distribution probability function.

The evolution of vacancy and interstitial clusters is shown to proceed on two different time scales. While interstitial clusters form very rapidly, the time scale for the formation of vacancy clusters is many orders of magnitude longer, mainly reflecting the magnitude of the respective time constants of interstitials and vacancies. Good agreement is obtained with experimental data on irradiated materials for the main parameters of the interstitial loop populations. The present theory is also applied to the more complex conditions of void and bubble formation in irradiated materials. It is shown that the deviation of the helium bubbles in neutron irradiated materials form their equilibrium conditions is primarily a result of the ratio of helium-to-displacement damage rates. Under the conditions of a low ratio (i.e. EBR-II), most helium bubbles can be regarded as voids. On the other hand, for higher ratios, helium bubbles are somewhat over-pressurized, particularly for small sizes.

An important feature of defect cluster formation in materials under non-equilibrium conditions is self-organization in regular spatial patterns. When space-time symmetry is broken, non-linear processes play a critical role in altering the microstructure. Under transient or pulsed irradiation conditions, the density of small interstitial clusters is greatly increased, while their size decreases, as compared to steady irradiation. On the other hand, at high enough temperatures, small vacancy clusters may actually dissolve during the off time, and the net result is a much smaller amount of vacancy agglomeration into voids. It has bee shown that pulsed irradiation at sufficiently high temperatures can lead to a smaller amount of swelling, as compared to steady irradiation. Spatial fluctuations in the concentrations of point defects are shown to result in non-linear coupling with the relatively immobile features of the microstructure. Gradients, which develop in the concentrations of mobile point defects, result in self-organization of vacancy and interstitial defect clusters. One important ingredient which seems to be sufficient, even though not necessary, and which leads to spatial self-organization is the preferential production or absorption bias of freely migrating interstitials. The direct production of vacancy clusters in collision cascades, coupled with diffusion-reaction of mobile point defects lead to spatial instabilities. The emerging wavelength of the organized microstructure decreases with increasing the dislocation network density, cascade collapse efficiency, and displacement damage rate. These predictions are in accord with experimental observations. It is also shown that a small degree of diffusion anisotropy of interstitial atoms results in alignment of the organized microstructure along crystallographic directions, as observed experimentally.

FAST SUM METHOD FOR THE ELASTIC FIELD OF 3-D DISLOCATION ENSEMBLES – N. M. Ghoniem and L. Sun (University of California at Los Angeles)

Journal: *Phys. Rev.* B, 60(1): 128-140 (1999)

Extended Abstract

Because the internal geometry of deforming crystals is very complex, a physically based description of plastic deformation can be very challenging. The topological complexity is manifest in the existence of dislocation structures within otherwise perfect atomic arrangements. Dislocation loops delineate regions where large atomic displacements are encountered. As a result, long-range elastic fields are set up in response to such large, localized atomic displacements. As the external load is maintained, the material deforms plastically by generating more dislocations. Thus, macroscopically observed plastic deformation is a consequence of dislocation generation and motion. A closer examination of atomic positions associated with dislocations shows that large displacements are confined only to a small region around the dislocation line (i.e. *the dislocation core*). The majority of the displacement field can be conveniently described as elastic deformation. Even though one utilizes the concept of dislocation distributions to account for large displacements close to dislocation lines, a physically based plasticity theory can paradoxically be based on the theory of elasticity!

Recently, a surge in interest towards understanding the physical nature of plastic deformation has developed. This interest is motivated by the extensive experimental evidence, which shows that the distribution of plastic strain in materials is fundamentally heterogeneous. Because of the complexity of dislocation arrangements in materials during plastic deformation, an approach, which is based on direct numerical simulations for the motion and interactions between dislocations is now being vigorously pursued. The study of dislocation configurations at short-range can be quite complex, because of large deformations and reconfiguration of dislocation lines during their interaction. Thus, adaptive gridding methods and more refined treatments of self-forces have been found to be necessary. In some special cases, however, simpler topological configurations are encountered. For example, long straight dislocation segments are experimentally observed in materials with high Peierel's potential barriers (e.g. covalent materials), or when large mobility differences between screw and edge components exist (e.g. some BCC crystals at low temperature). Under conditions conducive to glide of small prismatic loops on glide cylinders or the uniform expansion of nearly circular loops, changes in the loop *shape* is nearly minimal during its motion. It is therefore advantageous to reduce the number of interacting segments within a given computer simulation, or to develop more efficient approaches to computations of the long range field.

In this work, we aim at enhancing the current computational efforts on 3-D Dislocation Dynamics (DD). We present here a new numerical method for determination of a key ingredient in DD computer simulations; that is the elastic field of topologically complex dislocation ensembles. The main impetus for the present work is the need to describe the complex 3-D topology of dislocation loops in the most flexible way. A wide spectrum of dislocation line deformations, ranging from highly curved to rigid body translations arises within the same computational simulation. Existing methods are based on differential equations of motion for *straight* segments, where the elastic field variables affecting segment motion are computed at its center. When each segment moves under the influence of the stress field, the *connectivity* of the segments must be re-established, resulting in a number of possible complications. Thus, the motivation behind the current work can be stated as follows:

To reduce the computational burden by providing a high degree of flexibility in the selection of both length and shape of a dislocation segment.
To avoid numerical problems arising from singularities at intersecting straight segments.
To calculate the self-force on dislocation segments with a high degree of accuracy.
To provide a flexible tool which sheds more light on the physics of close-range interactions involving in-plane high curvature variations.
To effectively deal with the physics of climb and cross-slip, which require out-of-plane dislocation line curvature.

The fast sum method, which is based on a combination of dislocation loop geometry parameterization, and numerical quadrature integration along parameterized curves, is shown to be computationally feasible and highly accurate. All calculations involve simple algebraic operations, which can be systematically carried out by straightforward computer programming. Although we used FORTRAN-90 to implement the results of calculations, even spreadsheets on personal computers can be effectively utilized. The method is as efficient as analytical solutions, especially because of the index structure associated with tensor notation (i.e. the use of DO loops). However, because analytical solutions are available only for a limited number of special cases, the present approach can be used for calculations involving complex loop geometry. The present method is primarily intended for applications in Dislocation Dynamics computer simulations, where the need for accuracy is critical in close-range dislocation encounters. Moreover, one may consider the present method as an extension of the FEM technique in continuum mechanics. A variety of parameterized elements can thus be chosen (in much the same way as in the FEM approach) to handle special dislocation deformation problems. The method may also be exploited in crack problems, where dislocation distributions can be used to represent complex crack surfaces.

To handle the effects of free crystal surfaces on the redistribution of the elastic field inside the crystal, and hence on computed Peach-Kohler forces, the superposition method of Cleveringa et. al. is extended to 3-D applications. While only 2-D problems have been solved so far by their method, we show that 3-D problems can also be successfully implemented. However, the simple problem shown here required almost 10,000 elements, with an associated large number of degrees of freedom. Other methods (e.g. the Boundary Integral (BI) method) may be more appropriate for 3-D computer simulations, since the stress field should be updated very frequently during Dislocation Dynamics computer simulations.

DISLOCATION DECORATION WITH NANO-SCALE DEFECT CLUSTERS IN IRRADIATED METALS – N.M. Ghoniem, B. N. Singh, L. Z. Sun, and T. Diaz de la Rubia (University of California at Los Angeles)

Journal: *J. Nucl. Mater*, 276 (2000) 166-177

Extended Abstract

Accumulation of nano-size prismatic defect clusters near slip-dislocations results from their mutual elastic interaction. We present here 3-D isotropic elasticity calculations for the interaction energy between radiation-induced nano-size prismatic loops and grown-in dislocation loops. The current treatment extends the work of Trinkaus, Singh and Foreman in two respects. First, a computational method for a full 3-D analysis of interaction energies in BCC Fe and FCC Cu is developed. Second, the theoretical method of Kroupa is computationally implemented for rigorous calculations of force, torque and induced surface energy on defect clusters. It is shown that small clusters are trapped within a zone of ~10 *nm* in BCC Fe, and ~20 *nm* in FCC Cu at room temperature, in rough agreement with experimental observations. Clusters can be absorbed in the core of grown-in dislocations because of unbalanced moments, which provide sufficient energy for rotation of their Burgers vectors in a zone of 2~3 *nm* in Fe. Near the dislocation core (within a few nanometers), sessile defect clusters in Cu are shown to convert to a glissile configuration.

The present study reveals new features of defect cluster interaction with slip dislocations, and is thus complementary to the original work of Trinkaus, Singh and Foreman. The interaction between nano-size defect clusters and slip loops is shown to be highly orientation dependent, unlike the situation with point defects represented as centers of dilatation in calculations of dislocation bias factors. The size of the elastic capture zone is primarily determined by the interaction between the edge components of slip loops, and is not very sensitive to cluster-cluster interaction. Calculated trapping zone sizes are in reasonable agreement with experimental observations. In BCC crystals, unique interaction energy iso-surfaces for only four independent cluster orientations have been identified. These correspond to clusters with Burgers vectors of the type: $<111>$ $<\bar{1}11>$ $<\bar{1}\bar{1}1>$, and $<\bar{1}1\bar{1}>$. Since cluster mobility is constrained by their glide cylinders, the elastic field of slip dislocations can only trap them, if their glide cylinders intersect with energy iso-surfaces whose level is more attractive than cluster thermal energy. Because of this directed motion in BCC crystals, clusters will tend to accumulate just below and above the slip plane, depending on their Burgers vector orientation, and on the character of the adjacent dislocation segment. Maximum cluster trapping is shown to occur near the edge component of a slip loop, while the trapping zone size decreases to zero near purely screw components. It is therefore expected that upon mechanical loading, edge components will be held up by clusters, while screw components will be free to move on the slip plane by glide and out of the plane by cross-slip.

It is also shown that clusters, which are very near dislocation cores (within *~3 nm*) can be absorbed into the core by rotation of their Burgers vector as a result of unbalanced torque exerted on them by slip dislocations. If such clusters change the direction of their Burgers vector, they will move toward the dislocation core, and thus will possibly get absorbed. The dynamics of this final step can be ascertained by Molecular Dynamics (MD) atomistic studies of cluster incorporation into the dislocation core. The distance over which this scenario of cluster incorporation is estimated by the present method to be on the order of *~ 3 nm* for Fe at room temperature. Estimates for the size of the trapping and absorption zones are uncertain, because of the limitations of the model. It is not clear if there are significant effects of elastic anisotropy,

and large deformation close to the dislocation core, on the present results, which are obtained by linear isotropic elasticity. More accurate atomistic simulations may shed light on the inherent limitations of our model. It appears that the initiation of a dislocation channel on the slip plane is associated with the stress required for the dislocation to overcome the collective elastic potential of trapped clusters. This possibility is rather high in BCC crystals, and is a consequence of the high mobility of irradiation defect clusters. It remains to be seen, however, whether the plastic instability is initiated by *"absorption"* of small defect clusters, once they rotate their Burgers vector toward the dislocation core, or is a result of the leading dislocation *"sweeping"* these small clusters. The answer to this question may require dedicated experiments, as well as dynamical computer simulations. Both Molecular Dynamics (e.g. Ref. 20), and Dislocation Dynamics may be required to resolve this question. In either scenario, the type of radiation hardening appears to be of a "Cottrell" nature, similar to hardening by impurity clouds in alloys. This in contrast to hardening by dislocations cutting through dispersed barriers on the glide plane in the normal Orowan mechanism. Several features of cluster-dislocation interactions in FCC crystals are differentiated from the conclusions on BCC crystals. Small prismatic defect clusters in FCC crystals are sessile, because of the low stacking fault energy. They immediately dissociate into Schockley partial dislocations, with out-of-plane Burgers vector, rendering them sessile. However, we have shown that an *"induced surface tension"* is provided if clusters are nucleated near dislocation cores, or even if moving dislocations interact with them, thus altering the energy balance for their dissociation into partials. In either one of these two possibilities, dissociated, sessile clusters in FCC crystals may be converted to a glissile configuration. If these conditions were satisfied, it would potentially lead to the initiation of a plastic instability and the formation of clear channels. These scenarios remain tentative at present and need further analysis.

PARAMETRIC DISLOCATION DYNAMICS: A THERMODYNAMICS-BASED APPROACH TO INVESTIGATIONS OF MESOSCOPIC PLASTIC DEFORMATION

– N.M. Ghoniem, S.- H. Tong, and L. Z. Sun (University of California at Los Angeles)

Journal: *Phys. Rev.* B, 61(2) (2000).913-927

Extended Abstract

A thermodynamics-based variational method is developed and used to establish the equations of motion of three-dimensional (3-D) interacting dislocation loops. A fast sum method for the elastic field of dislocation ensembles is utilized to determine forces acting on generalized coordinates of arbitrarily curved loop segments. Each dislocation segment is represented as a parametric space curve of specified smooth shape functions and *Degrees of Freedom* (DF) associated with beginning and end nodes. Kinetic equations for the generalized coordinates describing dislocation motion are derived for computer simulation of mesoscopic plastic deformation of materials. For general climb/glide 3-D motion of a curved dislocation segment, we show that $N_{DF}\{(j)=3n$, where n=1 for linear; n=2 for cubic; and n=3 for quintic parametric splines, respectively. It is also shown that the position P, tangent T, and normal N vectors at segment nodes are sufficient to describe general 3-D motion. For constrained glide motion, however, we also show that only two degrees of freedom are adequate for determination of dislocation loop profiles, including crystal structure constraints. A number of examples are given to illustrate the following features of the method: (1) adaptive node generation on interacting segments, (2) variable time-step determination for integration of the equations of motion, (3) dislocation generation by the Frank-Read mechanism in fcc, bcc and sc crystals, (4) loop-loop deformation and interaction, (5) formation of dislocation junctions, and (6) dislocation microstructure evolution.

A fundamental description of plastic deformation is now actively pursued, where dislocations play a key role as basic elements of material plasticity. Although continuum plasticity models are extensively used in engineering practice, their validity is limited to the underlying data base. The reliability of continuum plasticity descriptions is dependent on the accuracy of the experimental data. Under complex loading situations, however, the database is often hard to establish. Moreover, the lack of a characteristic length scale in continuum plasticity makes it difficult to predict the occurrence of critical localized deformation zones. Although homogenization methods have played a significant role in determining the elastic properties of new materials from their constituents (e.g. composite materials), the same methods have failed to describe plasticity. It is widely appreciated that plastic strain is fundamentally heterogeneous, displaying high strains concentrated in small material volumes, with virtually undeformed regions in-between. Experimental observations consistently show that plastic deformation is internally heterogeneous at a number of length-scales. Depending on the deformation mode, heterogeneous dislocation structures appear with definitive wavelengths. It is common to observe Persistent Slip Bands (PSB's), shear bands, dislocation pile ups, dislocation cells and sub grains. However, a satisfactory description of realistic dislocation patterning and strain localization has been rather elusive. A relatively recent approach to investigating the fundamental aspects of plastic deformation is based on direct numerical simulation of the interaction and motion of dislocations. This approach, which is commonly known as Dislocation Dynamics (DD), was first introduced for 2-D straight, infinitely long dislocation distributions, and then later for complex 3-D microstructure. Dislocation loops in DD computer simulations are treated as dynamical systems, which can be described by the time dependence of specified coordinates. In this work, we describe the equations of motion for generalized coordinates in much the same way as in Lagrangian mechanics. Regardless of the dislocation loop shape

complexity, we will develop an integral equation of motion for each curved segment within the loop, such that only relationships between global thermodynamic variables are obeyed. For concreteness, we focus the current approach on dislocation line representation by parametric dislocation segments, similar to the Finite Element Method (FEM). Thus, the equations of motion for the transport of atoms within the dislocation core should be consistent with the thermodynamics of irreversibility. A challenging prospect in such a description is the enormous topological complexity of materials containing dislocations. Dislocation lines assume complex shapes, particularly during heavy deformation and at high temperatures where they execute truly 3-D motion as a result of combined glide and climb forces. These dislocations can be highly curved because of their strong mutual interactions, externally applied stress fields, as well as other thermodynamic forces. It is apparent that whenever large curvature variations are expected, the accuracy of computing the dynamic shape of dislocation loops becomes critical. Many applications of the present method are feasible, especially in areas where continuum descriptions of plastic deformation fall short. One such application is the simulation of the onset of plastic instabilities and the formation of dislocation channels in irradiated materials. It is concluded that the present method offers a number of potential advantages:

A natural description of dislocation loop geometry that is not determined by an underlying computational mesh, and which is able to conform to physical constraints imposed by the crystal structure.

Avoidance of numerical divergence problems for very short straight segments, and the loss of accuracy on long segments.

High resolution of short-range reactions in-between curved dislocation segments.
Flexibility in mixing segment types during the same computation, thus leading to a reduction in the overall computational burden.

Compatibility with the standard Finite Element Method, which may lead to direct coupling with the computational methods of continuum mechanics.

INVESTIGATIONS OF RADIATION HARDENING AND PLASTIC INSTABILITY IN FCC METALS – N.M. Ghoniem, L. Z. Sun, B.N. Singh, and S.- H. Tong (University of California at Los Angeles)

Journal: *Phil. Mag.*, submitted, (1999)

Extended Abstract

A sudden transition of state from homogeneous plasticity to a mode of localized deformation is observed in many irradiated and unirradiated materials. This transition is considered to be a consequence of dislocation pinning with nano-scale barriers, such as solute atom atmospheres in unirradiated materials, or defect clusters in irradiated materials. The mechanism of flow localization and post-yield softening is investigated using a computational model of Dislocation Dynamics (DD). Radiation hardening and the onset of plastic instability in FCC metals, irradiated at temperatures below the recovery stage V, are analyzed in terms of three sequential pre-requisites:

trapping of mobile defect clusters during irradiation, leading to dislocation decoration and pinning;
post-irradiation activation of dislocation sources at regions of high stress concentration, such as grain boundaries, surface irregularities or inclusion interfaces;
penetration of activated dislocations through a system of defect barriers, destroying their resistance to subsequent dislocation glide.

A necessary condition for flow localization is a sudden release of large numbers of dislocations, which leads to a *negative* work hardening rate associated with defect cluster destruction. It is shown that irradiation-induced defect clusters in Cu are highly resistive to dislocation motion. At room temperature, stress concentration appears to be required for initiating plastic instability in copper at neutron fluence 10^{-3} dpa. It is also shown that the most likely orientations for dislocation channels are along slip directions of maximum Schmidt factors.

Most experiments on radiation hardening have been fitted to this simple form, showing that the increase in the yield strength scales as $\sqrt{\phi t}$ where ϕt is the fast neutron fluence. In this scaling, the obstacles are all produced from collision cascades, and are approximately of the same size. Fitting to experimental data on irradiated metals has been used to determine the parameter α as an indication of the interaction mechanism (i.e. obstacle strength). It is found that α~0.1 for irradiated Pd, and for irradiated Cu. Unfortunately, there appears to be a *fluence* dependence of α in the case of Cu, irradiated by 14 MeV neutrons, starting from a very low value of α~0.04 at $\varphi t = 10^{20}$ n/m^2 to a higher value of α~0.2 at $\varphi t > 2 \times 10^{21}$ n/m^2. An apparent abrupt change in the value of α occurs around a fluence of φt ~ 6-8 $\times 10^{20}$ n/m^2. Furthermore, a different hardening rate was observed when Cu single crystal measurements were compared with polycrystalline results. Kojima, Zinkle and Heinisch (1991) observed that the low fluence dependence does not scale with $\sqrt{\varphi t}$, and that there appears to be a mechanistic difference between low and high fluence results. Because of the difficulties in ascribing a single hardening mechanism, the experimental data of Mitchell (1978) were re-interpreted by Kojima, Zinkle and Heinisch (1991). The yield stress was linearly fitted with $\sqrt{\phi t}$, and shown to have a negative intercept of ~ (-22 MPa) at the origin. This was attributed to the Hall-Petch effect of grain boundaries in polycrytalline Cu, which is absent in single crystals. The obstacle strength parameter α obtained this way is ~ 0.23, which was concluded to be much smaller than the value proposed by Makin

(1968). If the Pd data of Baluc, Dai and Victoria are fitted in the same manner, without being forced to go through the origin, a positive intercept at the origin of ~ (+20 MPa) is obtained, in contrast with the analysis of Kojima, Zinkle and Heinisch (1991).

The objective of the present study is to assess the mechanisms responsible for the occurrence of plastic instability in irradiated FCC metals. In particular, we apply a new model of 3-D dislocation dynamics to analyze the interaction of slip dislocation loops with {\it both} coplanar and non-coplanar defect clusters in irradiated Cu. The investigation is aimed at explaining the specific mechanisms responsible for hardening in FCC metals and the origin of subsequent softening beyond the upper yield point. The present model extends the concept of CISH by providing detailed and quantitative determination of the increase in the yield stress of Cu under irradiation. We also introduce a new mechanism of post-yield softening, which was not considered in the original CISH model. The results of the present calculations are compared with the experimental data of irradiated copper (Singh, Edwards & Toft 1996), to show that the post-irradiation deformation behavior is controlled by the operation of a small number of dislocation sources that are highly stressed. This view is different from conventional hardening models which assume that {\it all dislocation sources} will operate at the yield point. The physical basis for the onset of plastic instability is discussed next, while we briefly outline our computational method for the simulation of mesoscopic plastic deformation of materials. Since dislocation generation and interaction with other defects dictate the initiation of plastic instability in irradiated materials, we give results of calculations for interaction energetics. Computer simulations for unlocking of slip dislocation loops, opposed by the long-range elastic field of random defect clusters are provided. Slip dislocations also interact with SFT's and sessile dislocation loops on their glide plane.

Under irradiation, dislocation loops in copper attract and trap nano-size glissile interstitial clusters. The size of the elastic capture zone is primarily determined by the interaction between the edge components of slip loops. Calculated trapping zone sizes at room temperature are 18 nm. Clusters which are produced closer than a distance of ~ 3-9 nm from the dislocation core are absorbed, either because of a high torque on their habit plane or by unfaulting of small Frank loops. It is shown that dislocations will be decorated with small defect clusters, which are trapped in their stress field, and are situated at a minimum stand-off distance. Thus, a natural length scale is realized before samples are subjected to a stress state during subsequent post-irradiation mechanical testing. The density of clusters in the immediate vicinity of locked dislocations is thus well above the background random density in the matrix. Our analysis of the required CRSS to unlock dislocations from an atmosphere of cluster density 10^{24} m^{-3} shows that it is on the order of 200 MPa in Cu at RT. This is similar to the value calculated analytically by Singh et al. (1997) and Trinkaus et al. (1997b). It is concluded, therefore, that a higher CRSS is required to unlock dislocations from their cluster atmospheres. Since the measured value of the tensile stress increase because of neutron radiation is 250$ MPa at RT, it is concluded that the initiation of plastic flow within dislocation channels will most likely occur near regions of stress concentrations. Even if a particular slip orientation with a Schmidt factor near 0.5 were selected within the crystal, the operating shear stress would still exceed the applied value. It is also possible that dislocations, which are not heavily decorated, will unlock from their defect atmosphere first without the necessity of a stress concentration. However, if a region in the crystal is near a stress raiser (e.g. precipitate, grain boundary, triple point junction, or surface irregularity), it is most likely that this site will yield first, and will result in flow localization. The directions of slip in localized flow regions are selected along the maximum possible values of the local Schmidt factor. Beyond the upper yield point, dislocation sources will operate by developing segments on the glide plane, which negotiate their way through a field of co-planar obstacles. Nevertheless, it is shown that the required CRSS in this case is less than that for

unlocking the dislocation from its surrounding cluster atmosphere. Once the first loop destroys opposing co-planar obstacles on the glide plane, emission of subsequent F-R loops becomes easy. The stress required for continuing the operation of the F-R source is determined by the normal forest hardening, and/or graining boundary pileup mechanisms, which generally require a smaller value of the CRSS.

3-D DISLOCATION DYNAMICS STUDY OF PLASTIC INSTABILITY IN IRRADIATED COPPER – L. Sun, N.M. Ghoniem, and B.N. Singh (University of California at Los Angeles)

Journal: *J. Nucl. Mater*, Paper presented at ICFRM-9, Colorado Springs, Colorado, 1999

Extended Abstract

Experimental results consistently show that neutron irradiation of metals and alloys at temperatures below recovery stage V causes substantial increase in the upper yield stress and induces yield drop and plastic instability. Commonly, irradiated metals exhibit yield drop (following the upper yield point), do not show any work hardening and in many cases even show work softening. This specific type of plastic flow localization is considered to be one of many possibilities of plastic instabilities treated in the literature. At the upper yield point, plastic deformation is likely to be initiated in a localized fashion at sites acting as dislocation sources in the form of slip bands. These sites could be the locked dislocations themselves, or where the applied stress is intensified (e.g. grain boundaries, inclusions, triple points, etc.). It is important to recognize that when dislocation sources become operative initiating plastic deformation in a localized fashion, the whole specimen is strained at a very high level of applied stress. High velocity dislocations thus generated at sources may cut through soft and incoherent precipitates, or destroy previously built-up dislocation structures, causing softening in the active slip plane. Following neutron irradiation, the yield drop is observed to occur in pure FCC, BCC and HCP metals and alloys, provided that they are irradiated and tested at temperatures below recovery stage V. Recently, it has been proposed that the phenomenon of yield drop is caused by decoration of grown-in dislocations by small clusters or loops of Self-Interstitial Atoms (SIAs) produced in displacement cascades. Consequently, dislocations are immobilized, in a manner similar to that in the case of dislocations with an "atmosphere" of impurities or solute atoms in un-irradiated iron or Cu-30% Zn alloy. It has been shown that the decoration of dislocations by small SIA clusters is likely to occur, but only under cascade damage conditions where small glissile clusters are produced in displacement cascades. Investigations of post-deformation microstructure of irradiated metals and alloys have provided evidence for the formation of "cleared" channels. Virtually, all plastic deformation seems to occur in these channels representing only a small fraction of the specimens' volume. In the volume between these channels no dislocations are created during deformation. Once fresh dislocations are generated, they move very fast on their glide planes and cut, absorb or sweep irradiation-induced defect clusters and loops present on the glide plane. Consequently, cleared channels become almost defect free and thereby soft material for dislocation transport. This reinforces plastic strain localization and induces instability in plastic flow.

The onset of plastic instability in neutron-irradiated copper is investigated. Small prismatic defect clusters produced directly from collision cascades are trapped in the stress field of slip dislocations. Mobile prismatic clusters are absorbed in the dislocation core, when they approach within *~6 nm* as a result of torque-induced changes in their Burgers vector. Sessile vacancy clusters are also absorbed within this *"stand-off"* distance because of an induced surface tension on their stacking fault. The interaction between non-coplanar prismatic defect clusters and slip dislocations is shown to provide significant resistance to plastic deformation in irradiated copper. Coplanar sessile stacking fault tetrahedra and/or interstitial loops can additionally resist dislocation motion by localized forces on the glide plane before they are absorbed by activated dislocation sources. The comparison of the present results with experimentally measured yield stress of neutron-irradiated copper suggests that the plastic instability is most likely to be initiated at sites of stress concentrations.

Under irradiation, dislocation loops in copper are shown to attract small defect clusters. The size of the elastic capture zone is primarily determined by the interaction between the edge components of slip loops. At room temperature, calculated trapping zone sizes are on the order of 18 *nm*. Clusters which are produced closer than a "stand-off" distance of ~ 6 *nm* from the dislocation core are absorbed, either due to a high torque on their habit plane or due to unfaulting of small Frank loops. Recent MD calculations confirm that isotropic elasticity estimates for interaction energies are valid to within a few *nm* from the dislocation core. The flow shear stress required to unlock and push decorated dislocations on the glide plane is estimated to be above ~200-250 MPa for the passage of the first dislocation loop at the saturation level of hardening (i.e. dose > 10^{-3} *dpa*). This value is determined from elastic calculations for the interaction forces between the dislocation and defect clusters, and is somewhat lower than the estimates given in. The basic difference is in using somewhat lower values for average inter-cluster spacing and the standoff distance in. Most of the contributions to the resistive motion of slip dislocations are produced from nearby clusters close to the "stand-off" distance from the dislocation core. Once the dislocation is unlocked from its immediate surrounding clusters, it propagates on the slip plane by interaction and absorption of prismatic loops and SFT's. Beyond the upper yield point, the required shear stress is smaller, on the order of ~185 MPa. Since the experimentally measured tensile hardening value is about 250 MPa (with a maximum CRSS value of 125 MPa), we conclude that the initiation of flow instability is triggered by a stress concentration within the crystal. Even if a particular slip orientation with a Schmidt factor near 0.5 were selected within the crystal, the operating shear stress would still exceed the applied shear stress component by almost a factor of ~2. The current results predict that the orientations of flow localization are determined by the maximum possible value of the Schmidt factor, and that flow localization is most likely to occur in a region of stress concentration, such as an internal interface, inhomogeniety or an external surface. These results clearly demonstrate that while calculating the resistance to dislocation motion, the influence of both coplanar and non-coplanar loops and SFTs must be considered. Consideration of only coplanar obstacles underestimates the magnitude of radiation hardening, and does not account for the occurrence of the plastic instability.

FUTURE DIRECTIONS

Future research efforts will be directed towards computer modeling of various physical mechanisms that control flow localization and plastic instabilities in irradiated materials. We also plan to pursue the development and application of a comprehensive microstructure evolution, rate theory model, which accounts for the effects of helium and alloying elements.

9.0 DOSIMETRY, DAMAGE PARAMETERS, AND ACTIVATION CALCULATIONS

STATISTICAL ANALYSIS OF A LIBRARY OF MOLECULAR DYNAMICS CASCADE SIMULATIONS IN IRON AT 100 K – R. E. Stoller (Oak Ridge National Laboratory) and A. F. Calder (University of Liverpool)

Extended Abstract (the full paper will be published in the Journal of Nuclear Materials as Proceedings of the Ninth International Conference on Fusion Reactor Materials, October 10-15, 1999, Colorado Springs, Colorado).

An extensive database of atomic displacement cascades in iron has been developed using molecular dynamics simulations. Simulations have been carried out at temperatures of 100, 600, and 900K, and at energies between 0.10 and 50 keV. The results presented here focus on the simulations conducted at 100K. A sufficient number of cascades have been completed under each condition of cascade energy and temperature to obtain statistically significant average values for the primary damage production parameters. The cascade database is summarized in Table 1. This statistical analysis has been used to examine the influence of primary knockon direction, simulation cell size, periodic boundary conditions, and lattice heating by the high-energy recoil.

The 100K cascade database can be used to at least partially answer several questions regarding MD cascade simulations. These questions include: what is the effect of PKA direction, how many simulations are required to obtain meaningful average quantities for a given condition, how significant is the effect of periodic boundary conditions, and what is the impact of lattice heating due to the PKA energy input? The first two questions are related, since more simulations are required at energies where the effect of PKA direction is strong. Although the validity of these answers have only been demonstrated for the particular iron potential employed in this work, they should provide useful guidance to investigations of primary damage formation in other materials. A more detailed analysis of these results will be published when a set of 100 keV cascades has been completed and the 600 and 900K simulations have been fully analyzed.

Table 1. Summary of iron cascade database at 100K

Summary of iron cascade database at 100K

MD cascade energy (keV)	NRT displacements	Number of simulations*	multiple of standard error to obtain indicated confidence level:	
			90%	95%
0.1	1	40	1.685	2.023
0.2	2	32	1.696	2.040
0.3	3	104	1.660	1.983
0.5	5	20	1.729	2.093
1.0	10	12	1.796	2.201
2.0	20	10	1.833	2.262
5.0	50	9	1.860	2.306
10.0	100	15	1.761	2.145
20.0	200	10	1.833	2.262
30.0	300	10	1.833	2.262
40.0	400	8	1.895	2.365
50.0	500	9	1.860	2.306
* more simulations have been completed, this is the number used in the average values shown in Figure 1				

The data indicate that some dependence on PKA direction persists up about 1 keV. For the PKA directions used in this work, the maximum difference in defect survival occurred when comparing the [135] and [114] directions. The difference between the [135] and [114] averages are statistically significant at the 95% confidence level for the 0.3 keV simulations, but not at higher energies. For example, although the [114] defect survival was 15% higher than [135] at 2 keV, this difference is not statistically significant at the lower 90% confidence level. These results suggest the necessity of conducting low-energy simulations in a variety of high and low index directions to characterize defect survival before choosing a single direction for high energy simulations. It is interesting to note that the PKA directions that gave higher than average survival were not necessarily directions with a low displacement threshold. Interstitial clustering appears to be somewhat less sensitive to PKA direction than does defect survival.

Using 40 simulations and 12 PKA directions yielded a standard error that was 6% of the average defect survival at 100 eV. A similar value of 8.7% was obtained from the initial 16 simulations and 12 directions at 300 eV. At higher energies, there is a trend supporting the need for fewer simulations, e.g. the ratio of standard error to average value is 6.5% with 12 simulations at 1 keV, less than 5% with 10 simulations at 20 and 30 keV and as small as 2.5% with 9 simulations at 50 keV.

An evaluation of the effect of periodic boundary conditions can be made based on these results. At both 0.5 and 1.0 keV, a set of simulations was carried out in which the PKA was chosen to ensure that the cascade spilled through one face of the simulation cell and reentered the opposing face. The defect survival fraction and the interstitial clustering fraction were not affected. The same result was obtained when 10 keV simulations carried out in 128,000 and 250,000 atom simulation cells were compared. Simulations in the smaller atom block spilled through the periodic boundary in most cases, but the primary damage parameters were not significantly affected. This result holds as long as the recoils that exit and reenter the block do not travel far enough to encounter the cascade region.

A comparison of 0.3 and 10 keV simulations using different atom blocks sizes to reduce heating did not reveal a significant effect. Defect survival is unchanged, while interstitial clustering is slightly greater in the cooler block at 0.3 keV and slightly lower in the cooler block at 10 keV. The change is not statistically significant in either case at the 90% confidence level.

Finally, the results of this analysis confirm an effect of subcascade formation that we have previously reported. The ratio of surviving point defects to the number calculated by the NRT displacement model passes through a minimum value at about 20 keV, and the statistical significance of this minimum seems established. The increase above this value is reflected in the change in slope of the defect survival curve at 20 keV in Figure 1. The reason for the increase is still under investigation but it appears to be related to the spacing between the subcascades at higher energies. Inspection of the cascades indicates that point defects created in regions between subcascades have a higher probability of survival because the defect density in these regions is relatively low, similar to low energy cascades. Such regions of higher defect survival occur with greater frequency at the higher energies, giving rise to the greater-than-linear energy dependence. Initial analysis of a limited number of 100 keV cascades suggests that this effect may be saturating.

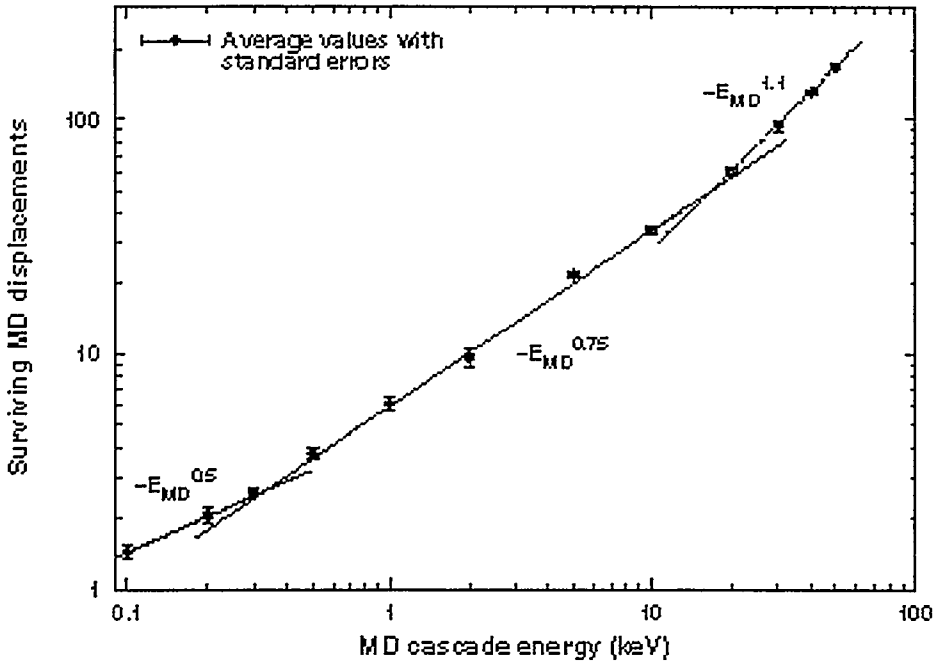

Figure 1. Number of surviving displacements in iron MD cascade simulations at 100K.

ACCELERATED HELIUM AND HYDROGEN PRODUCTION IN ^{54}FE DOPED ALLOYS - MEASUREMENTS AND CALCULATIONS FOR THE FIST EXPERIMENT - L. R. Greenwood and B. M. Oliver (Pacific Northwest National Laboratory)*, S. Ohnuki (Hokkaido University, Japan), K. Shiba (Japan Atomic Energy Research Institute), Y. Kohno (University of Tokyo, Japan), A. Kohyama (Kyoto University, Japan), J. P. Robertson (Oak Ridge National Laboratory), J. W. Meadows (Argonne National Laboratory) and D. S. Gelles (Pacific Northwest National Laboratory)*

Abstract of a paper submitted to the Journal of Nuclear Materials as part of the proceedings of the 9th International Conference on Fusion Reactor Materials, Colorado Springs, Colorado, USA, October 10-15, 1999.

ABSTRACT

Helium analyses of natural iron samples previously irradiated in HFIR indicated a non-linear buildup of helium suggesting accelerated helium production due to isotopic shifts between the iron isotopes. This effect was ascribed to isotopic transmutation since the isotopic gas production cross sections vary significantly. In order to study these isotopic differences in helium and hydrogen production, iron alloys enriched in ^{54}Fe were fabricated in Japan . The F-82H alloy nominally consisted of 8Cr-2WVTa. ^{54}Fe in the alloy comprised 96% of the iron or 86% of the total alloy by weight. For comparison, similar alloys were produced both with natural iron and with natural iron doped with varying amounts of boron.

Helium and hydrogen measurements were performed for samples irradiated in the JP-17 and JP-22 experiments in HFIR. The results are compared to calculations using isotopic helium production cross sections from ENDF/B-VI or the computer code, GNASH, for the radioactive isotope ^{55}Fe. Neutron dosimetry results were used to determine the neutron spectra. Helium measurements demonstrated an accelerated helium (appm)/dpa ratio of 2.3 after a 1.25-year irradiation, an increase of a factor of 4.3 over natural iron. The accelerated helium production is due to higher helium production cross sections for ^{54}Fe and ^{55}Fe. Alloys doped with ^{55}Fe could achieve helium/dpa ratios up to about 20, well above the fusion reactor ratio of 10. Hydrogen measurements were performed using a newly developed quadruple mass spectrometer system at PNNL capable of detecting 5-appm hydrogen in milligram-sized irradiated specimens. Calculations predict that hydrogen production will be accelerated by about a factor of 13 over natural iron. However, measurements show that most of this hydrogen is not retained in the samples.

---

*Pacific Northwest National Laboratory (PNNL) is operated for the U.S. Department of Energy by Battelle Memorial Institute under contract DE-AC06-76RLO-1830.

10.0 MATERIALS ENGINEERING AND DESIGN REQUIREMENTS

IMPACT OF TECHNOLOGY AND RADIATION EFFECTS ON LIFETIME OF THE STRUCTURAL MATERIALS FOR ITER – V. A. Belyakov, S. A. Fabritsiev, and I. V. Mazul (D.V. Efremov Scientific and Research Institute of Electrophysical Apparatus), and A. F. Rowcliffe (Oak Ridge National Laboratory)

Extended Abstract (the full paper will be published in the Journal of Nuclear Materials as Proceedings of the Ninth International Conference on Fusion Reactor Materials, October 10-15, 1999, Colorado Springs, Colorado).

The paper presents an overview of the performance of materials such as refractor metals, beryllium, and copper alloys, for ITER high heat flux structures. High temperature brazing, hot isostatic pressing (HIP), friction welding, explosive bonding, and other methods were explored to join copper alloys to 316 stainless steel for first wall and limiter applications. It is concluded that the main materials problems for the ITER heat high flux components are: (a) degradation of properties after the manufacturing cycle (especially for Be/Cu and Cu/SS joints); (b) helium embrittlement of Be, and Cu, and; (c) radiation-induced loss of fracture toughness for Be, W, and Cu alloys.

Although rapid progress has been achieved in these areas, it is clear that further work is required to improve the unirradiated properties of individual materials and to further substantiate the irradiation-performance of bonded structures for ITER applications.

11.0 IRRADIATION FACILITIES, TEST MATRICES, AND EXPERIMENTAL METHODS

ENGINEERING DEVELOPMENT OF FUSION-2 EXPERIMENT FOR IRRADIATION TESTING OF VANADIUM ALLOYS IN A LITHIUM ENVIRONMENT AT 450-750°C IN THE BOR-60 REACTOR[1] – V. Kazakov, V. Chakin, V. Efimov, A. Tuktabiev, P. Gabiev (Research Institute of Atomic Reactors), H. Tsai, T. S. Bray, D. L. Smith (Argonne National Laboratory); and A. Rowcliffe (Oak Ridge National Laboratory)

OBJECTIVE

BOR-60 is a sodium-cooled fast reactor in Russia with a coolant inlet temperature of 300-330°C. Previous irradiation experiments conducted in the BOR-60, EBR-II, HFIR, ATR, and SM reactors indicate that the threshold for low-temperature embrittlement of vanadium-base alloys is ≈400°C. The purpose of the proposed Fusion-2 experiment in BOR-60 is to study the effects of neutron damage in vanadium-base alloys at temperatures above this threshold, up to ≈700°C. The objective of the present task is to develop the engineering design of the experimental assembly based on the functional requirements of the experiment. Engineering development focuses on construction of the experimental assembly including test volumes and specimens, methods of temperature control and measurement that are especially important for creep tube specimens, and thermal performance of the assembly in the Research Institute of Atomic Reactors (RIAR), where BOR-60 is located.

SUMMARY

The requirements of this task are to complete the engineering designs of irradiation capsules in BOR-60. The specimen matrix will include sheet tensile specimens, Charpy impact specimens, TEM disks, and pressurized creep tubes. This experiment will not include DHCE samples. To better utilize the test volume and provide additional temperature options, it was decided to modify the experiment from a two-capsule to a three-capsule design. All capsules will be liquid-metal-bonded for temperature uniformity. The top two capsules with be fitted with thermocouples for temperature measurement in early stages of the irradiation. Goal temperatures for the three capsules will be 450, 600, and 700-750°C, with an emphasis on 600°C. A key objective of the experiment will be to generate irradiation creep data for vanadium-base alloys, especially at the emphasized temperature of 600°C, where thermal creep may not be dominant. To ensure correct generation of irradiation creep data, knowledge of the temperature profile and minimal temperature fluctuations during irradiation are important.

PROGRESS

The three capsule design for Fusion-2 is shown in Fig. 1. A three-capsule design would permit better utilization of the high-flux space at the core midplane and, because each capsule can operate at a different temperature, a more diverse study of temperature effects on irradiation. By adopting three shorter capsules, there would also be less axial power/temperature variation in each capsule.

The proposed materials of construction for the Fusion-2 experiment are shown in Table 1. The double-wall capsule (Item 3) would be made of austenitic stainless steel or Inconel for compatibility with the bond sodium at elevated temperature. The subcapsules (Items 4 and 5) containing the test specimens would be made of TZM (a Mo-base alloy) for impurity control and compatibility with the specimen lithium bond. There would be two sizes of subcapsules; those of smaller diameter (Item 5) are sized to accommodate pressurized creep tubes.

---

[1] This work has been supported by the U.S. Department of Energy, Office of Fusion Energy Research, under Contract W-31-109-Eng-38.

Thermal analysis has been conducted to determine the construction of capsules for the desired temperatures. For performance assessment of the vanadium-base alloy for fusion applications, we decided that the most important test temperature at this time would be 600°C. Accordingly, the high-flux middle capsule would be allocated for this temperature. Because the lengths of the three capsules need not be the same, the middle capsule would be slightly elongated to provide a ≥40% total test volume. The top and bottom capsules would be designed for 700-750 and 450°C, respectively, and would have a smaller test volume than that of the middle capsule.

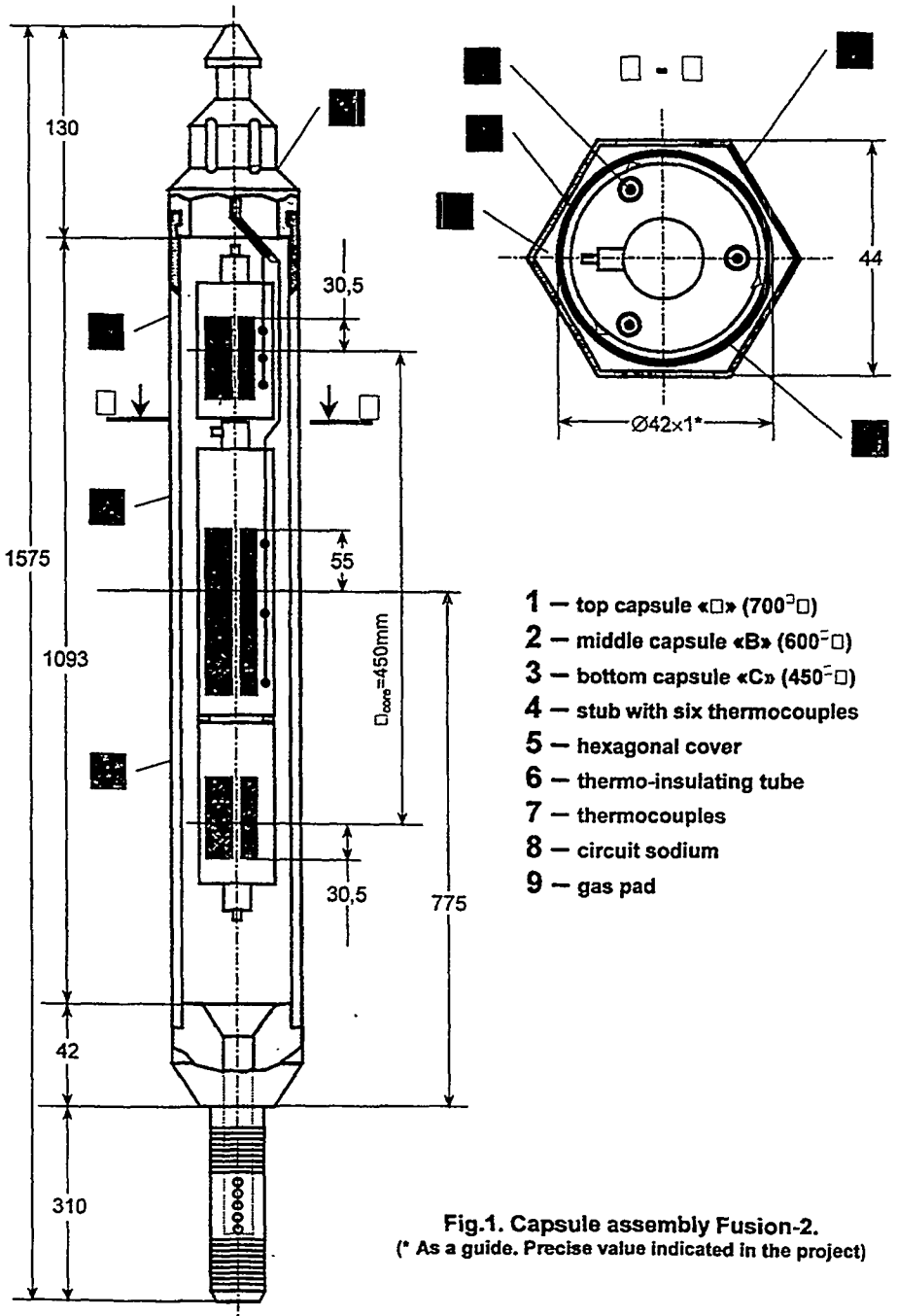

Fig.1. Capsule assembly Fusion-2.
(* As a guide. Precise value indicated in the project)

Table 1. Materials of construction for Fusion-2 test assembly

Item No.	Test Temperature = 450, 550, 600°C	Test Temperature = 700°C	Fill Medium
1	Hex Can	Hex Can	He
2	SS	SS	Na
3	304 SS	Inconel	He (outer) Na(inner)
4	Mo alloy of TZM or VM-1A type	Mo alloy of TZM or VM-1A type	Li-7, specimens
5	Mo alloy of TZM or VM-1A type	Mo alloy of TZM or VM-1A type	Li-7, specimens

To monitor the specimen temperature, thermocouples will be incorporated in the top and middle capsules in the Fusion-2 vehicle. Because only one core location (D-23) in BOR-60 permits deployment of thermocouples, the Fusion-2 experiment would be irradiated at this location for approximately two weeks at the onset of the experiment to establish the thermal baseline.

Steady irradiation temperature is important in testing structural materials samples. For pressurized creep specimens, this is particularly true, because temperature fluctuation affects not only creep properties but also internal gas pressure. Means to ensure steady irradiation temperatures were explored.

Thermal Calculations

Thermal calculations were performed assuming three capsules in the assembly. The thermal calculations were performed in consideration of the reactor power (55 MW), the distribution of radiation heating in the elements, specimens and the coolant at the specimen height, radial and axial heat transfer in the assembly, and convective heat transfer in the capsule. Thermal gas gaps and spatial distribution of temperature were determined using helium as the gap gas.

The calculations show that without extra measures, the axial temperature variation across the capsule can be large. With the addition of mass (tungsten) into the capsule, the temperature deviation can be significantly decreased; however, the temperature variation may still be somewhat unsatisfactory. Various internal wall geometries were evaluated—a multistep-shaped profiling, a conical-multistep-shaped profiling, and a conical-multistep-shaped profiling with additional masses. Figure 2 shows a three step profile for the top (700°C) and bottom (450°C) capsules and a six step profile for the middle (600°C) capsule.

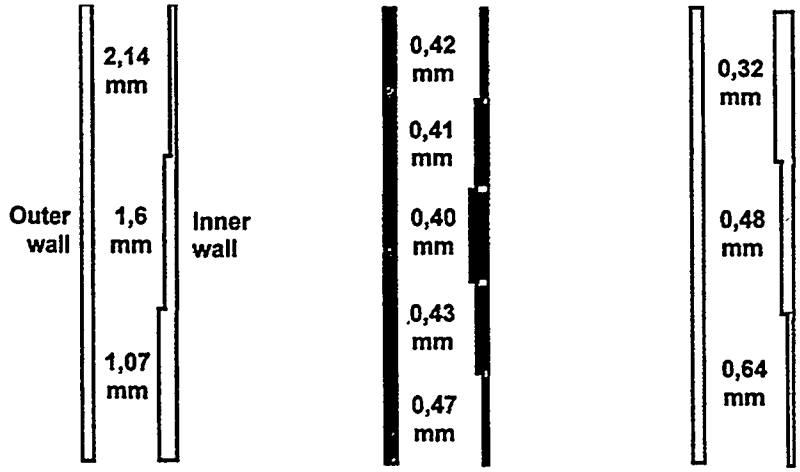

Figure 2. Multi-step Profile for Top (700°C), Middle (600°C), and Bottom (450°C) Capsules. Dimensions only approximate.

Tables 2, 3, and 4 outline the thermal calculations and the impact of the geometry variations on axial temperature variation and uncertainty. The calculations show that a conical-step-shaped profile with additional masses provides the best results in minimizing axial temperature variation and uncertainty.

Table 2: Thermal Calculations for Upper Capsule (700°C)

Variation	Gas Gap (mm)		Additional Mass (g)		Temperature (°C)**	
No Additional Measures	1.45		--		S1* S2* S3*	630±30 705±35 765±25
Gas Gap Plus Additional Masses	1.28		S1* S2* S3*	44.14 16.19 --	S1* S2* S3*	680±30 700±45 725±20
Step-Shaped Gas Gap	S1* S2* S3*	1.78 1.42 1.18	--		S1* S2* S3*	700±40 700±46 700±20
Conical-step-shaped gas gap	S1* S2* S3*	2.02-1.62 1.62-1.26 1.26-1.13	--		S1* S2* S3*	700±7 700±5 700±8
Conical-step-shaped gas gap plus additional masses	S1* S2* S3*	1.40-1.14 1.14-0.92 0.92-0.90	S1* S2* S3*	44.14 44.14 44.14	S1* S2* S3*	700±6 700±5 700±7

*S1 = Top (First) Step of Capsule, M = Middle (Second) Step of Capsule, B = Bottom (Third) Step of Capsule.
**Temperature reported is at the center of the step.

Table 3: Thermal Calculations for Middle Capsule (600°C)

Variation	Gas Gap (mm)		Temperature (°C)**	
No Additional Measures	0.42		S1* S2* S3* S4* S5* S6*	608±5 618±5 625±2 619±3 604±8 585±11
Step-Shaped Gas Gap	S1* S2* S3* S4* S5* S6*	0.41 0.39 0.38 0.39 0.41 0.43	S1* S2* S3* S4* S5* S6*	600±5 600±4 600±2 600±7 600±7 600±12
Conical-step-shaped gas gap	S1* S2* S3* S4* S5* S6*	0.41-0.40 0.40-0.39 0.39-0.38 0.38-0.40 0.40-0.42 0.42-0.46	S1* S2* S3* S4* S5* S6*	600±3 600±4 600±2 600±4 600±4 600±5

*S1= Top (First) Step of Capsule, S2 = Second Step of Capsule, S3 = Third Step of Capsule, S4 = Fourth Step of Capsule, S5 = Fifth Step of Capsule, S6 = Bottom (Sixth) Step of Capsule.
**Temperature reported is at the center of the step.

Table 4: Thermal Calculations for Lower Capsule (450°C)

Variation	Gas Gap (mm)		Additional Mass (g)		Temperature (°C)**	
No Additional Measures	0.38		--		S1* S2* S3*	479±10 452±16 425±11
Gas Gap Plus Additional Masses	0.35		S1* S2* S3*	-- 22.07 44.14	S1* S2* S3*	459±15 450±10 450±8
Step-Shaped Gas Gap	S1* S2* S3*	0.31 0.37 0.48	--		S1* S2* S3*	450±14 450±16 450±8
Conical-step-shaped gas gap	S1* S2* S3*	0.29-0.33 0.33-0.43 0.43-0.54	--		S1* S2* S3*	450±4 450±5 450±6

*S1 = Top (First) Step of Capsule, M = Middle (Second) Step of Capsule, B = Bottom (Third) Step of Capsule.
**Temperature reported is at the center of the step.

Temperature Control

The specimen temperatures cannot be actively controlled in fusion-2. Rather, it will be determined by the preset width of the gas gap. Uncertainties in the radiation heating calculations are ±7% and determination of the reactor power is ±2.5%. There is also some uncertainty in the accuracy of the gas gap and associated with the thermal hydraulic process inside of the capsule. The installed thermocouples will provide information during the first two weeks of irradiation to reduce some of the uncertainties.

The reactor power over the course of a year can be described in two campaigns, winter and summer, divided by 45-day outages between each campaign. In addition, another 10 day refueling outage occurs in the winter campaign. The reactor power typically fluctuates from 35-48 MW in the summer and 45-56 MW in the winter. To attain the required test temperatures during the lower-power summer months, the subassembly will be moved to a more central core location. The typical reactor power fluctuation of ±10-15% during normal operations can be reduced to achieve more steady specimen temperatures; however, this will most likely result in higher experimental costs.

Sample Loading and Test Volume

Table 5 shows the sample loading and test volumes available for the Fusion-2 experiment. Test volume is defined as the space that can be used to load lithium or test specimens, i.e., excluding the plenum. A total of 108 mL of test volume is available for the Fusion-2 experiment. In comparison, the test volumes available in ATR-ITV, RB(10J), and ATR-A1 were 130 mL, 160 mL, and 47 mL, respectively. A total of approximately 95 tensile samples, 77 Charpy V-notch samples, and 69 creep tube samples could be irradiated in the Fusion-2 experiment.

Table 5: Sample Loading and Test Volumes for the Fusion-2 Experiment.

Item	Top Capsule (700°C)	Middle Capsule (600°C)	Bottom Capsule (450°C)
No. of Tensile Specimens	20	45	30
No. of Charpy V-Notch Specimens	20	45	12
No. of Creep Tubes	30	30	9
Small-Diameter Subcapsule Test Volume (mL)	6.6	13.2	6.6
Large Diameter Subcapsule Test Volume (mL)	18.4	36.7	26.5

REFERENCE

1. V. Kazakov et al., "Engineering Development of Fusion-2 Experiment for Radiation Test of Vanadium Alloys in BOR-60 Reactor at 450-700°C in Lithium Environment," Report on Milestone 2 of Subcontract 28X-SZ738V of 06/08/98 with Lockheed Martin Energy Systems, Inc., USA, 1998.

HIGH-SENSITIVITY QUADRUPOLE MASS SPECTOMETER SYSTEM FOR THE DETERMINATION OF HYDROGEN IN IRRADIATED MATERIALS - B. M. Oliver, F. A. Garner, L. R. Greenwood, and J. A. Abrefah (Pacific Northwest National Laboratory)*

Abstract of a paper submitted to the Journal of Nuclear Materials as part of the proceedings of the 9th International Conference on Fusion Reactor Materials, Colorado Springs, Colorado, USA, October 10-15, 1999.

ABSTRACT

Very high levels of helium and hydrogen are generated in metals in fusion, spallation neutron, and high energy charged particle environments. Hydrogen generation is typically an order of magnitude higher than that of helium, but the hydrogen is thought to quickly diffuse out of the metal, although there appears to be some conditions where significant retention can occur. While helium in radioactive materials is routinely measured with high accuracy at PNNL, concurrent measurement of hydrogen is a much more challenging task.

To address this issue, a high-sensitivity analysis system has been developed for the measurement of hydrogen in irradiated solid materials. Measurements can be made in both total release mode or in stepped-anneal or ramped release mode. The system is based on a low-volume extraction furnace in combination with a quadrupole mass spectrometer detector. Very small volumes of radioactive material are required, minimizing safety and waste concerns. Tests conducted using 2 to 5 mg sized specimens cut from a hydrogen-standard steel rod containing approximately 5 wppm indicate a detection limit of ~1 x 10^{14} atoms, or ~2 appm for a 5 mg specimen.

Hydrogen measurements have been conducted on both tungsten and Inconel 718 irradiated with spallation neutrons and 700 to 800 MeV protons, a number of iron-based alloys from the U.S. and U.S.-Japan JUPITER fusion materials programs in HFIR and ATR, vanadium alloys, and stainless steels from light water reactors. Measurements are in progress on SiC and aluminum alloys from a wide variety of radiation spectra. Hydrogen levels measured on irradiated specimens to date have ranged from ~50 to ~7000 appm. Details on the system, and typical hydrogen release curves will be shown.

---

* Pacific Northwest National Laboratory (PNNL) is operated for the U.S. Department of Energy by Battelle Memorial Institute under contract DE-AC06-76RLO-1830.

SCHEDULE AND STATUS OF IRRADIATION EXPERIMENTS – A. F. Rowcliffe (Oak Ridge National Laboratory)

OBJECTIVE

To provide an updated summary of the status of irradiation experiments for the fusion materials program.

SUMMARY

The current status of reactor irradiation experiments is presented in tables summarizing the experimental objectives, conditions, and schedule.

PROGRESS AND STATUS

Currently, there are two experiments in-reactor (RB-14J, and JP-25). Post-irradiation testing is in progress on CTR-62/63 and RB-11J/12J. Experiments TRIST-TC1 and RB-13J have been removed from reactor and are awaiting disassembly. Experiment RB-10J is awaiting shipment to the hot cells for investigation of the source of the gas leak that led to premature removal from the reactor.

Summary of Reactor Irradiation Experiments

Experiment	Lead Lab	Collaborators	Responsible Person	Major Objectives	Materials	Temperature °C	Dose (dpa) or fluence	Irrad. Start	Irrad. Finish	Status
EBR-II, Reactor, ANL, Idaho Falls, ID										
COBRA 1A2	PNL	ORNL, ANL, MONBUSHO	M.L. Hamilton	Tensile and fatigue prop., Charpy impact, fracture toughness, TEM	Austenitic and ferritic steels, Fe-alloys, V, Be, low act. materials, Cu alloys, Ti-Al, SiC, C-C comp.	370, 400, 800	33	Nov-92	Sep-94	
X530	ANL		H. Tsai, H.M. Chung	He-effects, swelling, Charpy impact, fracture toughness, tensile prop.	V alloys	370	5	Aug-94	Sep-94	
High Flux Isotope Reactor, ORNL, Oak Ridge, TN										
HFIR-CTR-60	ORNL		S.J. Zinkle	Flexure bars, TEM, indentation disks	Isotopically tailored ceramics	100-600	2.4E+26 n/m2	Dec-94	Aug-95	
HFIR-CTR-61	ORNL		S.J. Zinkle	Similar to HFIR-CTR-60			7.20E+26	Dec-94	Aug-98	
HFIR-JP-9	ORNL	JAERI	P.J. Maziasz/ J.E. Pawel	He effects by isotopic tailoring, tensile prop., TEM	Austenitic and ferritic steels	300-600	57	Jul-90	Apr-94	
HFIR-JP-12	ORNL	JAERI	P.J. Maziasz/ J.E. Pawel	Similar to HFIR-JP-9			57	Jul-90	Apr-94	
HFIR-JP-15	ORNL	JAERI	P.J. Maziasz/ J.E. Pawel	Similar to HFIR-JP-9			57	Jul-90	Apr-94	
HFIR-JP-20	ORNL	JAERI	J.E. Pawel	Tensile Prop., TEM, He effects by isotopic tailoring	Austenitic and ferritic steels	300-600	8	Dec-93	Jun-94	
HFIR-JP-21	ORNL	JAERI	J.E. Pawel	Similar to HFIR-JP-20			18	Dec-93	Apr-95	
HFIR-JP-22	ORNL	JAERI	J.E. Pawel	Similar to HFIR -JP-20			34	Dec-93	Jan-96	
HFIR-JP-23	PNL	MONBUSHO	D.S. Gelles	TEM	Austenitic and ferritic steels, Cu, Mo, V alloys, TiAl	300-600	8	Dec-93	Jun-94	
HFIR-HT-S1, -S7	ORNL		L.L. Snead	Thermal conductivity	Various insulators	80-350	0.01-1.0	Jun-95	Aug-95	
HFIR-HT-F Series	ORNL		L. L. Snead	Fiber tensile	SiC	80-800	0.001-1.0	Jan-95	Mar-96	

Summary of Reactor Irradiation Experiments

Experiment	Lead Lab	Collaborators	Responsible Person	Major Objectives	Materials	Temperature °C	Dose (dpa) or fluence	Irrad. Start	Irrad. Finish	Status
HFIR-TRIST-ER1	ORNL	MONBUSHO/ JAERI	S.J. Zinkle	In-situ electrical conductivity	Al2O3	450	3E+25 n/m2	Apr-96	Jun-96	
HFIR-RB-10J	ORNL	JAERI	J.E. Pawel	Tensile, fracture	Vanadium, 316LN-1G, J316	200, 500	5	Oct-98	Oct-99	
HFIR-RB-11J	ORNL	MONBUSHO/ JAERI	M. L. Grossbeck	Tensile, fracture, TEM	Low activation ferritics, V alloys, SiC	300	5	Feb-97	May-98	
HFIR-RB-12J	ORNL	MONBUSHO/ JAERI	M. L. Grossbeck	Tensile, fracture, TEM	Low activation ferritics, V alloys, SiC	500	5	Feb-97	May-98	
HFIR-RB-13J	ORNL	MONBUSHO/ JAERI	S. J. Zinkle	Varying temp. experiment	Ceramics, Fe-Cr-Ni, V alloys, ferritics, copper	200, 350, 500	5	Jul-98	Jul-99	
HFIR-RB-14J	ORNL	MONBUSHO	L. L. Snead	Strength, fracture, dim. stability, diffusivity	2nd generation SiC/SiC	300, 500, 800	5	Feb-99	Feb-00	
HFIR-TRIST-TC1	ORNL	MONBUSHO/ JAERI	L. L. Snead	In-situ thermal conductivity	SiC/SiC, SiC	150-700	3	Jan-99	Dec-99	
HFIR-CTR-62	ORNL	JAERI	R.L. Klueh	Charpy impact and He effects	and conventional ferritic steels	300, 400	13	Apr-95	Dec-95	
HFIR-CTR-63	ORNL	JAERI	R.L. Klueh	Charpy impact and tensile, TEM, He effects	and conventional ferritic steels	300, 400	13	Apr-95	Dec-95	
HFIR-JP25	ORNL	JAERI	R.L. Klueh	Tensile, fracture, TEM	Low activation ferritics	300, 500	20	Feb-99	Jan-00	
High Flux Beam Reactor, Brookhaven National Laboratory										
HFBR-ISEC-3	ORNL		L.L. Snead	In-situ electrical	WESGO Al2O3	450	1.5	Jul-95	Sep-95	
HFBR-V1	ORNL		L.L. Snead	Tensile, fracture	V-4Cr-4Ti	75, 150, 225	0.4	May-95	Jun-95	
HFBR-V2	ORNL		L.L. Snead	Tensile, fracture	V-4Cr-4Ti	75, 225, 300, 375	0.4	Jul-95	Aug-95	
HFBR-V3	ORNL		L.L. Snead	Tensile, fracture	V-4Cr-4Ti	160, 265, 315, 420	0.4	Aug-96	Sep-96	
HFBR-V4	ORNL		L.L. Snead	Tensile, fracture	V-4Cr-4Ti	105-505	0.1	Aug-96	Sep-96	

Summary of Reactor Irradiation Experiments

Experiment	Lead Lab	Collaborators	Responsible Person	Major Objectives	Materials	Temperature °C	Dose (dpa) or fluence	Irrad. Start	Irrad. Finish	Status
Advanced Test Reactor, Idaho Falls										
ATR-A1	ANL	MONBUSHO	D.L. Smith	Tensile, fracture toughness, TEM, creep	Vanadium alloys	200, 300	5	Dec-95	May-96	
BOR-60 Reactor, RIAR, Dimitrovgrad, Russia										
BOR-60-Fusion-1	ORNL, ANL	RDIPE, RIAR	A.F. Rowcliffe, D.L. Smith	Mechanical and microstructural properties	V alloys	350-380	10	Jul-95	Mar-96	
SM-2 Reactor, RIAR, Dimitrovgrad, Russia										
SM-2.1	ORNL, PNL	RIAR	S.J. Zinkle	Tensile, electrical, microstructural, and creep properties	Cu alloys	100, 200, 330	1, 5	Dec-93	Feb-94	
SM-2.2	PNL	SRIAR	D.J. Edwards	Mechanical behavior of bonded materials	Cu alloys/SS, Cu/Be	120, 300	0.2	Mar-96	May-96	
SM-2.3	PNL	SRIAR	D.J. Edwards	Mechanical behavior of bonded materials	Cu alloys/SS, Cu/Be	150, 300 200	0.4 2.0	Sep-97 Jul-98	Dec-97 Oct-98	

Irradiation complete

Irradiation in progress

Irradiation planned

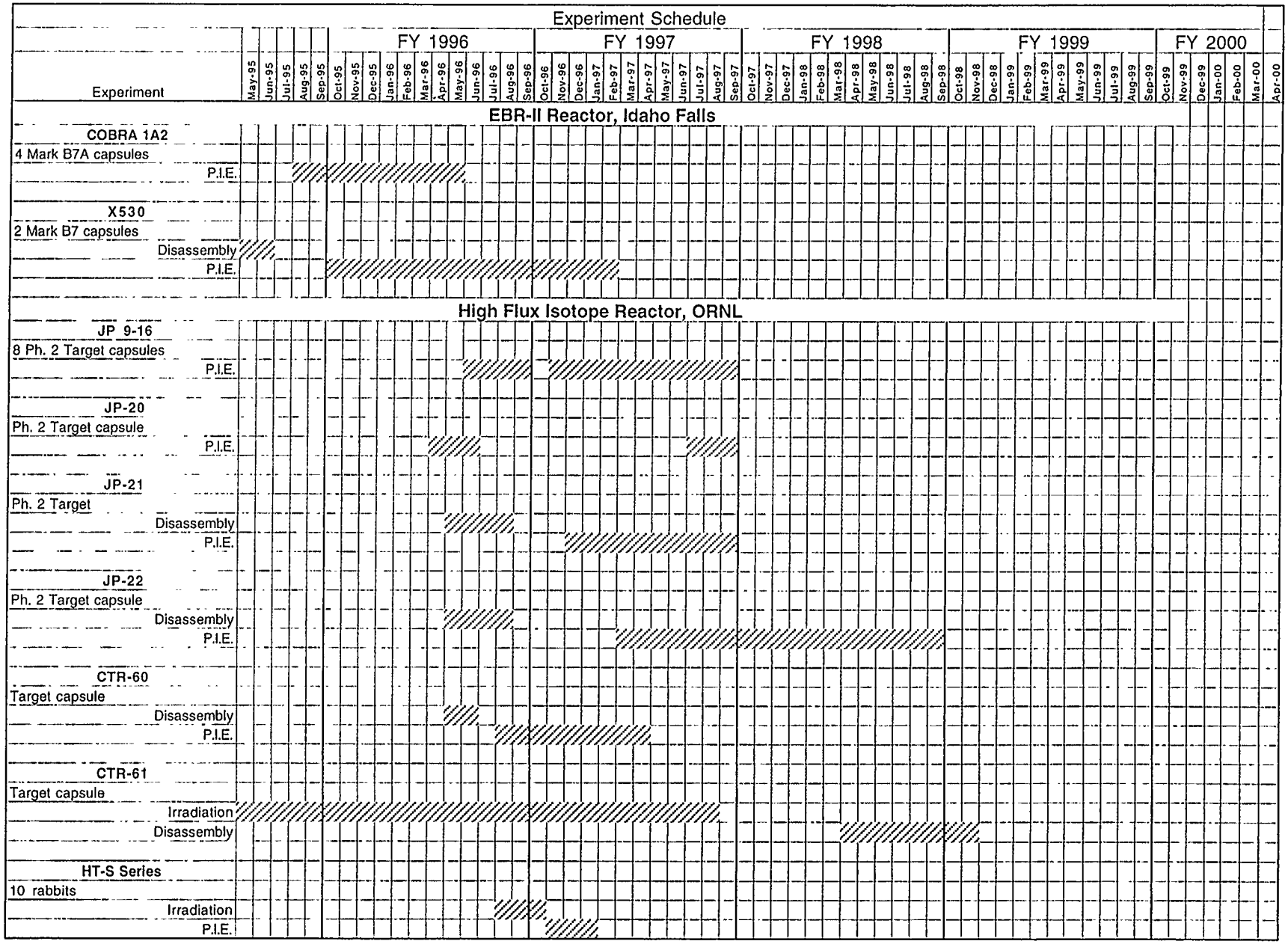
Experiment Schedule
FY 1996
FY 1997
FY 1998
FY 1999
FY 2000
Experiment
May-95 Jun-95 Jul-95 Aug-95 Sep-95 Oct-95 Nov-95 Dec-95 Jan-96 Feb-96 Mar-96 Apr-96 May-96 Jun-96 Jul-96 Aug-96 Sep-96 Oct-96 Nov-96 Dec-96 Jan-97 Feb-97 Mar-97 Apr-97 May-97 Jun-97 Jul-97 Aug-97 Sep-97 Oct-97 Nov-97 Dec-97 Jan-98 Feb-98 Mar-98 Apr-98 May-98 Jun-98 Jul-98 Aug-98 Sep-98 Oct-98 Nov-98 Dec-98 Jan-99 Feb-99 Mar-99 Apr-99 May-99 Jun-99 Jul-99 Aug-99 Sep-99 Oct-99 Nov-99 Dec-99 Jan-00 Feb-00 Mar-00 Apr-00
EBR-II Reactor, Idaho Falls
COBRA 1A2
4 Mark B7A capsules
P.I.E.
X530
2 Mark B7 capsules
Disassembly
P.I.E.
High Flux Isotope Reactor, ORNL
JP 9-16
8 Ph. 2 Target capsules
P.I.E.
JP-20
Ph. 2 Target capsule
P.I.E.
JP-21
Ph. 2 Target
Disassembly
P.I.E.
JP-22
Ph. 2 Target capsule
Disassembly
P.I.E.
CTR-60
Target capsule
Disassembly
P.I.E.
CTR-61
Target capsule
Irradiation
Disassembly
HT-S Series
10 rabbits
Irradiation
P.I.E.

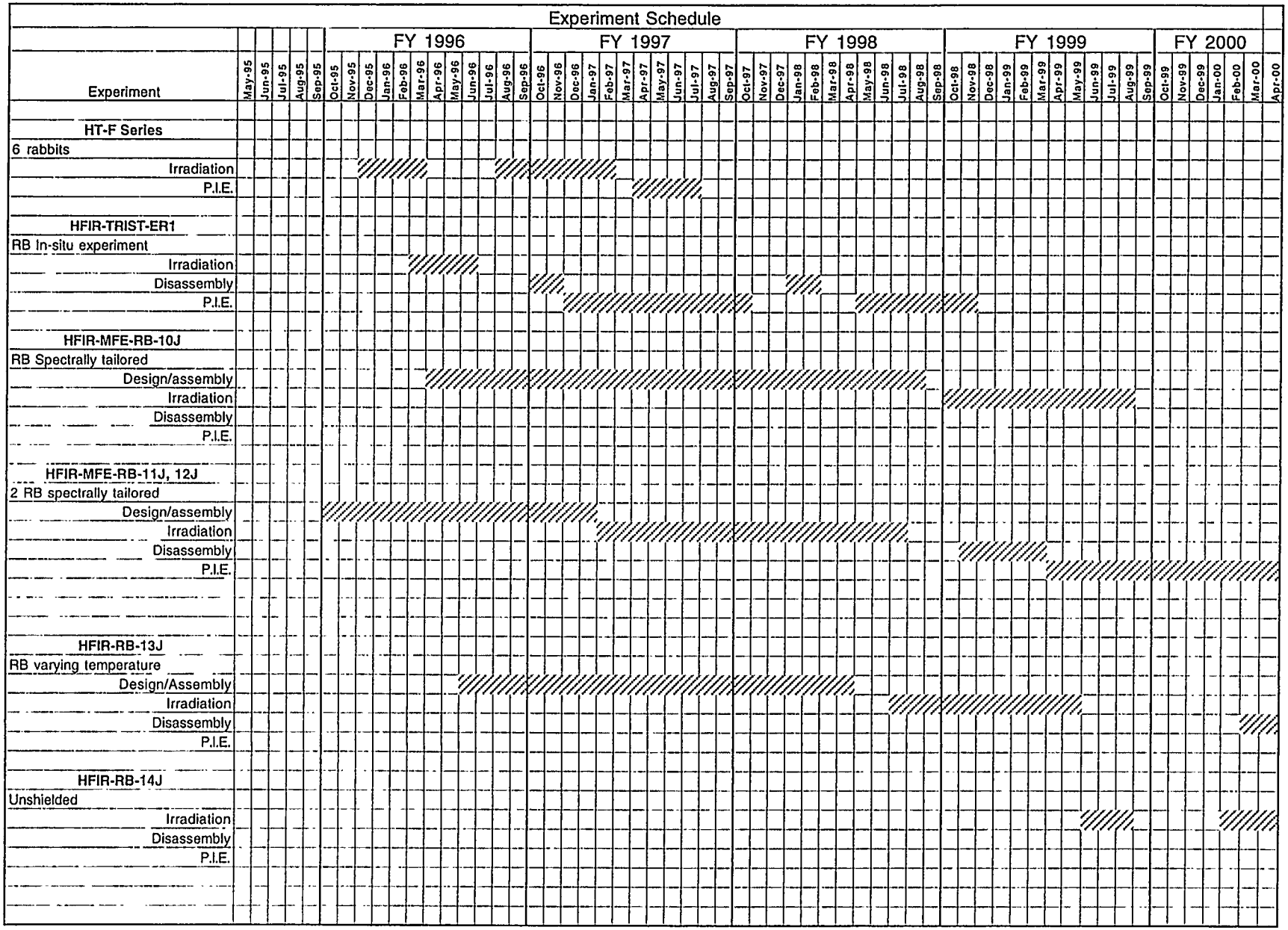
Experiment Schedule
FY 1996
FY 1997
FY 1998
FY 1999
FY 2000
Experiment
May-95
Jun-95
Jul-95
Aug-95
Sep-95
Oct-95
Nov-95
Dec-95
Jan-96
Feb-96
Mar-96
Apr-96
May-96
Jun-96
Jul-96
Aug-96
Sep-96
Oct-96
Nov-96
Dec-96
Jan-97
Feb-97
Mar-97
Apr-97
May-97
Jun-97
Jul-97
Aug-97
Sep-97
Oct-97
Nov-97
Dec-97
Jan-98
Feb-98
Mar-98
Apr-98
May-98
Jun-98
Jul-98
Aug-98
Sep-98
Oct-98
Nov-98
Dec-98
Jan-99
Feb-99
Mar-99
Apr-99
May-99
Jun-99
Jul-99
Aug-99
Sep-99
Oct-99
Nov-99
Dec-99
Jan-00
Feb-00
Mar-00
Apr-00
HT-F Series
6 rabbits
Irradiation
P.I.E.
HFIR-TRIST-ER1
RB In-situ experiment
Irradiation
Disassembly
P.I.E.
HFIR-MFE-RB-10J
RB Spectrally tailored
Design/assembly
Irradiation
Disassembly
P.I.E.
HFIR-MFE-RB-11J, 12J
2 RB spectrally tailored
Design/assembly
Irradiation
Disassembly
P.I.E.
HFIR-RB-13J
RB varying temperature
Design/Assembly
Irradiation
Disassembly
P.I.E.
HFIR-RB-14J
Unshielded
Irradiation
Disassembly
P.I.E.

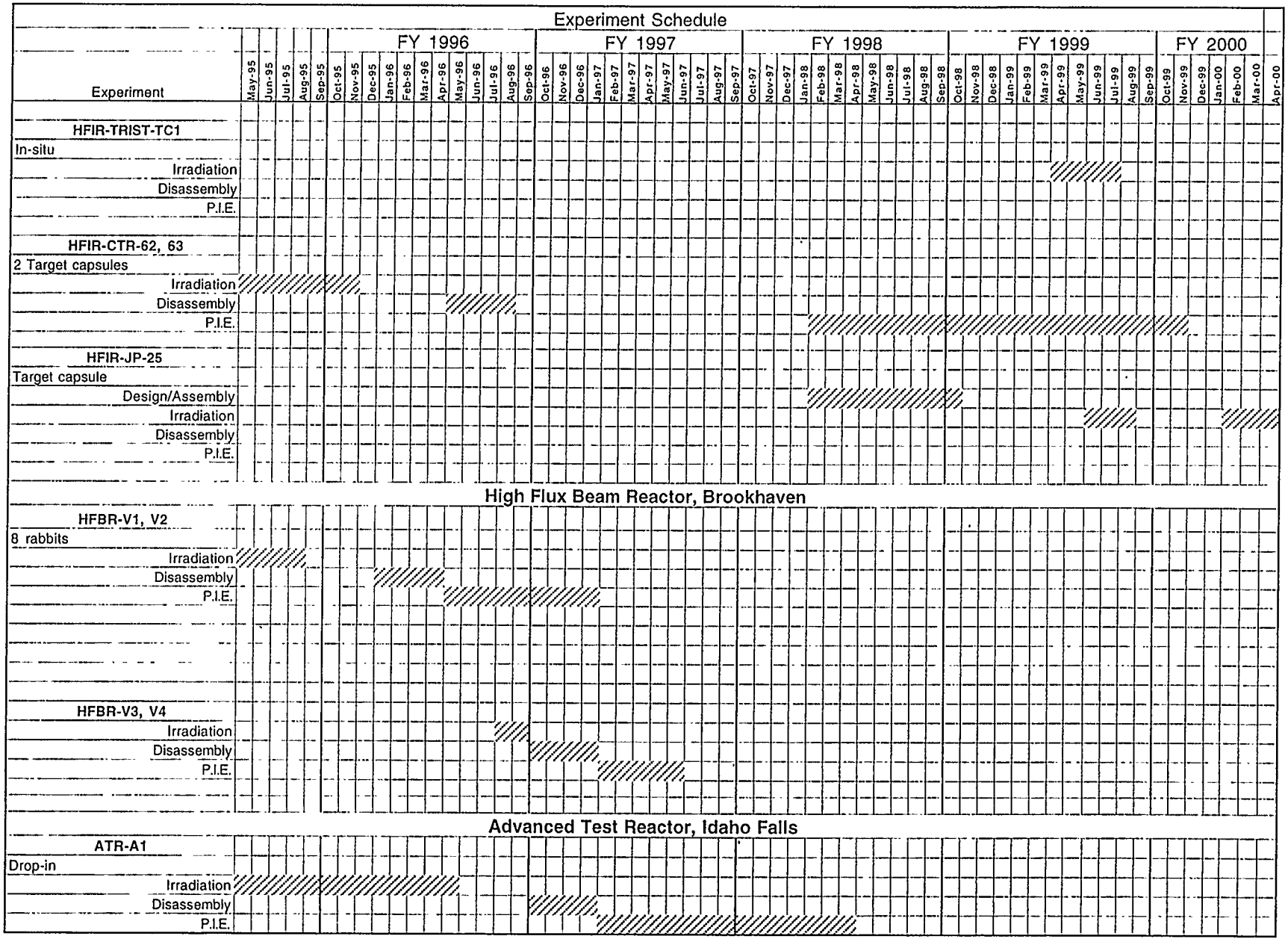
Experiment Schedule
FY 1996
FY 1997
FY 1998
FY 1999
FY 2000
Experiment
May-95
Jun-95
Jul-95
Aug-95
Sep-95
Oct-95
Nov-95
Dec-95
Jan-96
Feb-96
Mar-96
Apr-96
May-96
Jun-96
Jul-96
Aug-96
Sep-96
Oct-96
Nov-96
Dec-96
Jan-97
Feb-97
Mar-97
Apr-97
May-97
Jun-97
Jul-97
Aug-97
Sep-97
Oct-97
Nov-97
Dec-97
Jan-98
Feb-98
Mar-98
Apr-98
May-98
Jun-98
Jul-98
Aug-98
Sep-98
Oct-98
Nov-98
Dec-98
Jan-99
Feb-99
Mar-99
Apr-99
May-99
Jun-99
Jul-99
Aug-99
Sep-99
Oct-99
Nov-99
Dec-99
Jan-00
Feb-00
Mar-00
Apr-00
HFIR-TRIST-TC1
In-situ
Irradiation
Disassembly
P.I.E.
HFIR-CTR-62, 63
2 Target capsules
Irradiation
Disassembly
P.I.E.
HFIR-JP-25
Target capsule
Design/Assembly
Irradiation
Disassembly
P.I.E.
High Flux Beam Reactor, Brookhaven
HFBR-V1, V2
8 rabbits
Irradiation
Disassembly
P.I.E.
HFBR-V3, V4
Irradiation
Disassembly
P.I.E.
Advanced Test Reactor, Idaho Falls
ATR-A1
Drop-in
Irradiation
Disassembly
P.I.E.

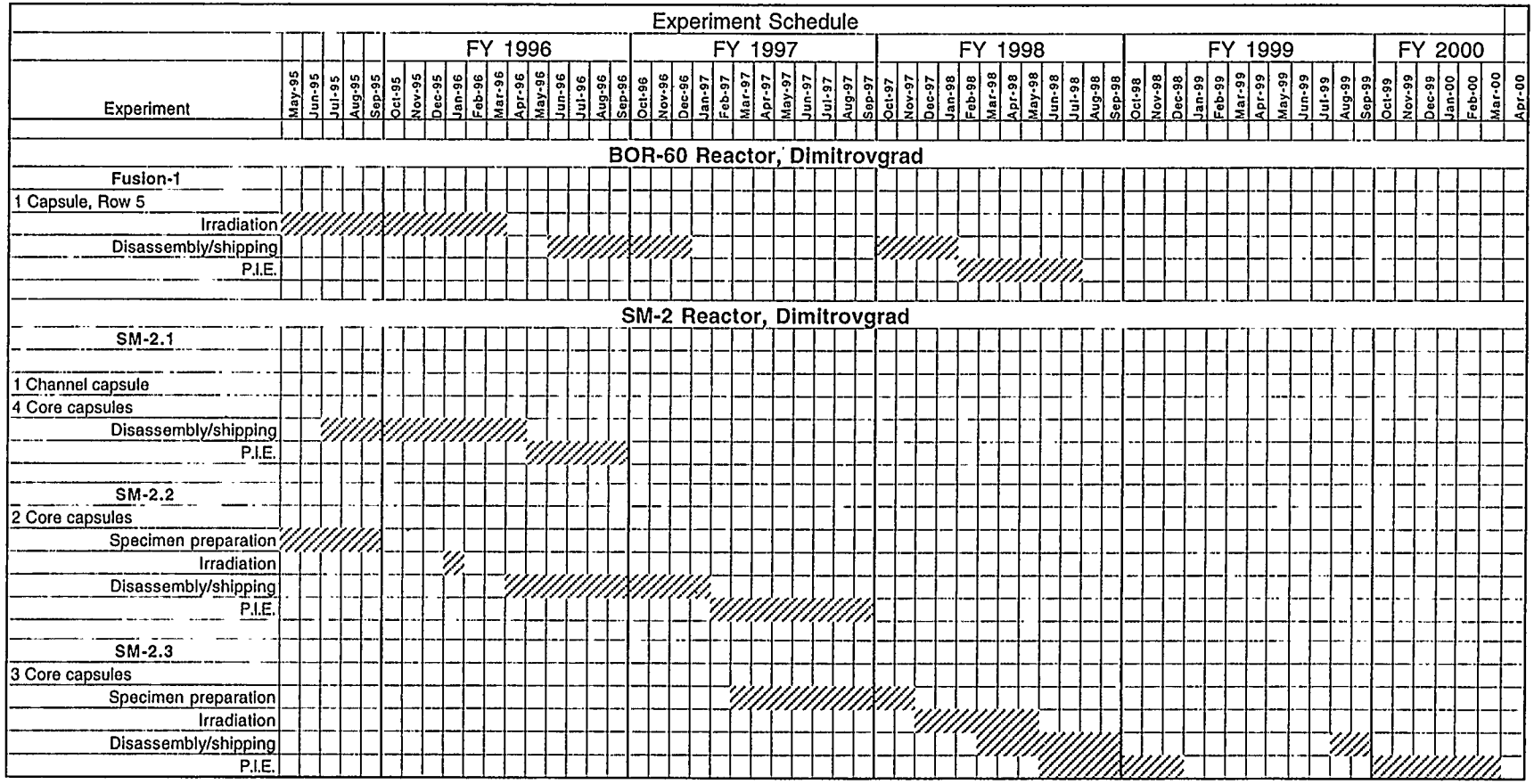
Experiment Schedule
FY 1996
FY 1997
FY 1998
FY 1999
FY 2000
Experiment
May-95 Jun-95 Jul-95 Aug-95 Sep-95 Oct-95 Nov-95 Dec-95 Jan-96 Feb-96 Mar-96 Apr-96 May-96 Jun-96 Jul-96 Aug-96 Sep-96 Oct-96 Nov-96 Dec-96 Jan-97 Feb-97 Mar-97 Apr-97 May-97 Jun-97 Jul-97 Aug-97 Sep-97 Oct-97 Nov-97 Dec-97 Jan-98 Feb-98 Mar-98 Apr-98 May-98 Jun-98 Jul-98 Aug-98 Sep-98 Oct-98 Nov-98 Dec-98 Jan-99 Feb-99 Mar-99 Apr-99 May-99 Jun-99 Jul-99 Aug-99 Sep-99 Oct-99 Nov-99 Dec-99 Jan-00 Feb-00 Mar-00 Apr-00
BOR-60 Reactor, Dimitrovgrad
Fusion-1
1 Capsule, Row 5
Irradiation
Disassembly/shipping
P.I.E.
SM-2 Reactor, Dimitrovgrad
SM-2.1
1 Channel capsule
4 Core capsules
Disassembly/shipping
P.I.E.
SM-2.2
2 Core capsules
Specimen preparation
Irradiation
Disassembly/shipping
P.I.E.
SM-2.3
3 Core capsules
Specimen preparation
Irradiation
Disassembly/shipping
P.I.E.

Distribution

1. Advanced Micro Devices, Inc., 5204 E. Ben White Blvd., MS-613, PCAL-Analytical TEM Section, Austin TX 78741
   J. Gazda

2-15. Argonne National Laboratory, 9700 South Cass Avenue, Argonne, IL 60439

M. C. Billone	C. E. Johnson	C. B. Reed
T. S. Bray	S. Majumdar	D. L. Smith
O. K. Chopra	R. F. Mattas	H. C. Tsai
H. M. Chung	K. Natesan	Y. Yan
A. B. Hull	J. H. Park	

16-17. Argonne National Laboratory, EBR-II Division, P.O. Box 2528, Idaho Falls, ID 83403-2528
   H. P. Planchon D. L. Porter

18. Auburn University, Department of Mechanical Engineering, 201 Ross Hall, Auburn, AL 36849
   B. A. Chin

19-20. Boeing, Mail Code S 106 7220, P.O. Box 516, St. Louis, MO 63166-0516
   J. W. Davis G. W. Wille

21. Carnegie Institute of Technology, Carnegie-Mellon University, Schenley Park, Pittsburgh, PA 15213
   W. M. Garrison, Jr.

22. Commissariat à l'Energie Atomique, Direction des Technologies Advancées, M2R1/DECM Cen-Saclay, Gif Sur Yvette, Cedex, France
   F. Tavassoli

23. Dow Corning Corporation, 3901 S. Saginaw Rd., MS-500, Midland, MI 48686-0995
   R. E. Jones

24-26. General Atomics, P.O. Box 85608, San Diego, CA 92138

W. R. Johnson	K. R. Schultz	C. Wong

27. Georgia Institute of Technology, Fusion Research Center, 0225, Atlanta, GA 30332
   W. M. Stacey

28. Grand Canyon University, Department of Natural Science, 3300 W. Camelback Rd., Phoenix, AZ 85017
   W. A. Coghlan

29-31. Idaho National Engineering Laboratory, Fusion Safety Program, P.O. Box 1625, Idaho Falls, ID 83415-3523
   G. Longhurst K. McCarthy D. Petti

32. Knolls Atomic Power Laboratory, P.O. Box 1072, Schenectady, NY 12301
   G. Newsome

33-35. Lawrence Livermore National Laboratory, P.O. Box 808, Livermore, CA 94550
   T. Diaz de la Rubia W. G. Wolfer J. Perkins

36-42. Los Alamos National Laboratory, Los Alamos, NM 87545
J. L. Anderson, R. G. Castro, D. W. Cooke, E. H. Farnum, R. E. Siemon, W. F. Sommer, K. E. Sickafus

43-45. Massachusetts Institute of Technology, Department of Metallurgy and Materials Science, Cambridge, MA 02139
L. W. Hobbs, N. J. Grant, K. C. Russell

46. Massachusette Institute of Technology, Plasma Fusion Center Headquarters, Cambridge, MA 02139
D. B. Montgomery

47. McMaster University, Engineering Physics, Hamilton, Ontario, Canada L8S 4L7
D. P. Jackson

48 MER Corp., 7960 South Kolb Rd., Tucson, AZ 85706
W. Kowbel

49. Merrimack College, Dept. of Physics, 315 Turnpike Street, North Andover, MA 01845
D. P. White

50. M. J. Schiff & Associates, 1291 N. Indian Hill Blvd., Claremont, CA 91711-3897
G.E.C. Bell

51-52. NASA Lewis Research Center, MS-106-5, Cleveland, OH 44135
J. DiCarlo, G. Morscher

53-55. National Institute of Standards and Technology, Boulder, CO 80302
F. R. Fickett, H. I. McHenry, R. P. Reed

56-57. Naval Research Laboratory, Code 6506, Washington, DC 20375
D. L. Griscom, J. A. Sprague

58-97. Oak Ridge National Laboratory, P.O. Box 2008, Oak Ridge, TN 37831
Central Research Library
Document Reference Section
Laboratory Records-RC
J. Bentley
E. E. Bloom
T. D. Burchell
T. S. Byun
S. D. Connery
J. R. DiStefano
R. H. Goulding
M. L. Grossbeck
N. Hashimoto
D. T. Hoelzer
N. Igawa
J. F. King
E. A. Kenik
R. L. Klueh
E. H. Lee
L. K. Mansur
P. J. Maziasz
S. Milora
B. A. Pint
A. L. Qualls
T. C. Reuther
J. P. Robertson
A. F. Rowcliffe (10)
J. Sheffield
L. L. Snead
R. E. Stoller
K. R. Thoms
S. J. Zinkle

98-111. Pacific Northwest National Laboratory, P.O. Box 999, Richland, WA 99352
D. J. Edwards, F. A. Garner (5), D. S. Gelles, L. R. Greenwood, M. L. Hamilton, H. L. Heinisch, G. W. Hollenberg, R. H. Jones, R. J. Kurtz, J. Youngblood

112. Oregon Graduate Institute, Dept. of Materials Science & Engineering, 19600 N.W. Von Neumann Drive, Beaverton, OR 97006
J. M. McCarthy

113-115. Princeton University, Princeton Plasma Physics Laboratory, P.O. Box 451, Princeton, NJ 08540
R. Goldston Long-Poe Ku D. M. Meade

116-117. Rensselaer Polytechnic Institute, Troy, NY 12181
D. Duquette D. Steiner

118-120. Sandia National Laboratories, Fusion Technology Dept., Dept. No 6531, P.O. Box 5800, Albuquerque, NM 87185-5800
M. J. Davis M. Ulrickson R. D. Watson

121-122. Sandia National Laboratories, Livermore Division 8316, Livermore, CA 94550
W. Bauer K. Wilson

123. San Diego State University, Mechanical Engineering Dept., San Diego, CA 92182-0191
L. D. Thompson

124. Texas A&M University, Box 397, Prairie View, TX 77446
D. Baker

125. TSI Research, 225 Stevens Ave., #110, Solana Beach, CA 92075
E. T. Cheng

126. University of California at San Diego, U.S. ITER Project Office, 9500 Gilman Drive, Bldg. 302, La Jolla, CA 92093-0035
C. C. Baker

127. University of California at San Diego, Fusion Energy Research Program, 9500 Gilman Drive, MC0417, La Jolla, CA 92093-0417
M. Tillack

128-129. University of California at Santa Barbara, Dept. of Mechanical and Environmental Engineering, Engineering II, Room 2355, Santa Barbara, CA 93106-5070
G. E. Lucas G. R. Odette

130-132. University of California at Los Angeles, Dept. of Chemical, Nuclear, and Thermal Engineering, Los Angeles, CA 90024
M. A. Abdou N. M. Ghoniem S. Sharafat

133. University of Illinois, Dept. of Nuclear Engineering, Urbana, IL 61801
J. Stubbins

134. University of Michigan, Dept. of Nuclear Engineering, Ann Arbor, MI 48109
T. Kammash

135. University of Missouri, Department of Nuclear Engineering, Rolla, MO 65401
A. Kumar

136-137. University of Tennessee, Dept. of Materials Science and Engineering, 427-B Dougherty Bldg., Knoxville, TN 37996-2200
P. K. Liaw C. J. McHargue

138-139. University of Wisconsin, Nuclear Engineering Dept., 1500 Johnson Drive, Madison, WI 53706
J. B. Blanchard G. L. Kulcinski

140. Helsinki University of Technology, Laboratory of Engineering Materials, Puumiehenkuja 3, SF-02150 Espoo, Finland
H. Hänninen

141-142. Hokkaido University, Center for Advanced Research of Energy Technology, Kita 13, Nishi 8, Kita-ku, Sapporo 060-8628, Japan
Tamaki Shibayama Heischichiro Takahashi

143-145. Hokkaido University, Faculty of Engineering, Kita 13, Nishi 8, Kita-ku, Sapporo 060-8628, Japan
Somei Ohnuki Akira Okada Seiichi Watanabe

146-150. Japan Atomic Energy Research Institute, Tokai Research Establishment, Tokai-mura, Naka-gun, Ibaraki-ken 319-1195, Japan
Akimichi Hishinuma Tatsuo Kondo R. Yamada
S. Jitsukawa Kenji Noda

151-153. Kyoto University, Institute of Advanced Energy, Gokasho, Uji, Kyoto 611-0011, Japan
Yutai Katoh Akihiko Kimura Akira Kohyama

154-155. Kyushu University, Dept. of Nuclear Engineering, Faculty of Engineering, Kyushu University, Hakozaki, Fukuoka 812-8582, Japan
Chiken Kinoshita Kenichi Shiiyama

156-157. Kyushu University, Research Institute for Applied Mechanics, Kasuga, Fukuoka 816-8580, Japan
Hideo Watanabe Naoaki Yoshida

158. Muroran Institute of Technology, Dept. of Metallurgical Engineering, 27-1 Mizumoto-cho, Mororan 050-8585, Hokkaido, Japan
Toshihei Misawa

159. Nagoya University, Dept. of Nuclear Engineering, Furo-Cho, Chikusa-ku, Nagoya 464-8603, Japan
Tetuo Tanabe

160-163. National Institute for Fusion Science, Oroshi, Toki, Gifu 509-5292, Japan
Osamu Motojima Chusei Namba
Takeo Muroga Nobuaki Noda

164-167. National Research Institute for Metals, Tsukuba Branch, Sengen, Tsukuba-shi, Ibaraki-ken, 305-0047, Japan
Fujio Abe Tetsuji Noda
Josei Nagakawa Haruki Shiraishi

168. PNC Oarai, 4002 Narita, Oarai, Ibaraki 311-1393, Japan
S. Ukai

169. Science University of Tokyo, Dept. of Materials Science & Technology, 2641 Yamazaki, Noda-shi, Chiba 278-8510, Japan
Naohiro Igata

170. Teikyo University, 359 Otsuka, Hachioji, Tokyo 192-0395, Japan
Akira Miyahara

171. Tohoku University, Institute for Materials Research, Katahira 2-2-1, Aoba-ku, Sendai 980-8577, Japan
Hideki Matsui

172-173. Tohoku University, Institute for Materials Research, Oarai Branch, Oarai-machi, Ibaraki 311-13, Japan
Hiroaki Kurishita Tatsuo Shikama

174-176. Tohoku University, Dept. of Quantum Science & Energy Engineering, Aoba, Aramaki, Sendai 980-8579, Japan
Katsunori Abe Akira Hasegawa Manabu Satou

177. Tokai University, Dept. of Nuclear Engineering, 1117 Kitakaname, Hiratsuka-shi, Kanagawa-ken 259-1292, Japan
Shiori Ishino

178. University of Tokyo, Dept. of Nuclear Engineering, 3-1, Hongo 7-Chome, Bunkyo-Ku, Tokyo 113-8654, Japan
Naoto Sekimura

179. University of Tokyo, Dept. of Materials Science, 3-1, Hongo 7-Chome, Bunkyo-ku, Tokyo 113-8654, Japan
Yutaka Kohno

180. VTT Manufacturing Technology, P.O. Box 1704, FIN-02044 VTT, Finland
P. Aaltonen

181. Commission of European Communities, Directorate-General for Research Science and Education, Fusion Programme, RUE De La Loi 200, B-1049 Brussels, Belgium
F. Cozzani

182. Southwestern Institute of Physics, P.O. Box 432, Chenedu 610041, Sichuan, P.R. China
Zeng Yu Xu

183. Southwestern Institute of Physics, P.O. Box 9819, Beijing 100029, P.R. China
J. P. Qian

184. Institute of Atomic Energy, Academia Sinica, P.O. Box 275-51, Beijing 102413, P.R. China
J. Yu

185. Riso National Laboratory, Materials Dept., P.O. Box 49, DK-4000, Roskilde, Denmark
B. N. Singh

186. CEA-CEREM-CEA, Saclay, CE2M/LECMA, Commissariat a l'Energie Atomique, 91191 Gif-Sur-Yvette, Cedex, France
N. Roux

187. Commission for European Communities, Joint Research Centre, I.A.M. Ispra Establishment, 21020 Ispra (Varese), Italy
P. Fenici

188. EURATOM/CIEMAT Fusion Association, Avenida Complutense 22, 28040, Madrid, Spain
E. R. Hodgson

189. Netherlands Energy Research Foundation ECN, Westerduinweg 3, P.O. Box 1, NI 1755 LE Petten, Netherlands
B. Van der Schaaf

190. Paul Scherrer Institute, CH-5232 Villigen, Wuerenlingen PSI, Switzerland
M. Victoria

191. Harwell Laboratory, B393, Radiation Damage Dept., Oxfordshire, OX11 ORA, United Kingdom
C. A. English

192. Metallurgical and Nuclear Consultant, 9A Cumnor Rise Road, Cumnor Hill, Oxford OX2 9HD, United Kingdom
D. R. Harries

193. Hahn-Mietner-Institut fur Kernforschung Berlin, Postfach 390128, Glienicker Str. 100, D-14109, Germany
H. Wollenberger

194. Institut fur Festkorperforschung Forschungszentrum Jülich, Postfach 1913, D-52425 Jülich, Germany
H. Ullmaier

195-196. ITER Garching Joint Work Site, Max-Planck-Institute für Plasmaphysik, Boltzmannstrasse 2, D-85748 Garching bei München, Germany
V. Barabash G. Kalinin

197-198. ITER Naka Joint Work Site, 801-1 Mukouyama, Naka-machi, Naka-gun, Ibaraki-Ken, 311-01, Japan
M. Huguet (2)

199-201. Kernforschungszentrum Karlsruhe, Postfach 3640, 75 Karlsruhe 1, Germany
M. Dalle-Donne (INR) A. Moeslang
K. Ehrlich (IMF-II)

202. Max-Planck-Institut für Plasmaphysik, Boltzmannstrasse 2, D-85748 Garching bei München, Germany
Patrick Lorenzetto

203. A. A. Baikov Institute of Metallurgy, USSR Academy of Sciences, Leninsky Prospect 49, Moscow, Russia
L. I. Ivanov

204. CRISM "Prometey," Naberezhnava r. Monastyrick 1, 193167, St. Petersburg, Russia
V. V. Rybin

205. D. V. Efremov Institute of Electro-Physical Apparatus, Scientific Technical Center "Sintez,"189631, St. Petersburg, Russia
S. A. Fabritsiev

206. Kharkov Institute of Physics & Technology, Radiation Damage and Materials Dept., Akademicheskaya 1, 310108 Kharkov, Ukraine
I. M. Neckludov

207-209. V. I. Lenin Research Institute of Atomic Reactors, 433510 Dimitrovgrad-10, Ulyanovsk Region, Russia
V. Kazakov A. S. Pokrovsky V. K. Shamardin

210. Korea Advanced Institute of Science and Technology, Department of Nuclear Engineering, DaeDukDanji, Taejon, 305-701, Korea
I-S. Kim

211. Korean Atomic Energy Research Institute, P.O. Box 105, Yusung, Taejon, 305-600, Korea
Jun Hwa Hong

212. Seoul National University, Dept. of Nuclear Engineering, 56-1 Shinrim-Dong, Kwanak-Ku Seoul, 151-742, Korea
K. H. Chung

213. Sung Kyun Kwan University, Dept. of Metallurgical Engineering, 300 Chunchun-dong, Jangan-gu, Suwon, 440-746, Korea
J. G. Han

214. Department of Energy, DOE Oak Ridge Field Office, P.O. Box 2008, Oak Ridge, TN 37831-6269
Assistant Manager for Energy Research and Development

215. Department of Energy, DOE Oak Ridge Field Office, P.O. Box 2008, Oak Ridge, TN 37831-6269
S. D. Frey

216. Department of Energy, Office of Basic Energy Sciences, Washington, D.C. 20585
R. J. Gottschall

217-221. Department of Energy, Office of Fusion Energy, Germantown, MD 20874
S. E. Berk W. Marton F. W. Wiffen
N. A. Davies R. McKnight

222. Department of Energy, Richland Operations Office, P.O. Box 550, MS-K850, Richland, WA 99352
J. Turner